CHARLES UNIVERSITY

Faculty of Science

Department of Physical and Macromolecular Chemistry

STRUCTURAL STUDIES OF 14-3-3 PROTEIN COMPLEXES AND THEIR STABILIZATION BY SMALL MOLECULE COMPOUNDS

Domenico Lentini Santo

Doctoral thesis

of study program Physical Chemistry

Supervisor: prof. RNDr. Tomáš Obšil, Ph.D.

Consultant: RNDr. Veronika Obšilová, Ph.D.

Prague 2021

Declaration

I declare that I carried out this doctoral thesis independently under the guidance of my supervisor prof. RNDr. Tomáš Obšil, Ph.D. and only with the cited sources, literature and other professional sources.

I understand that my work relates to the rights and obligations under the Act No. 121/2000 Coll., the Copyright Act, as amended, in particular the fact that the Charles University in Prague has the right to conclude a license agreement on the use of this work as a school work pursuant to Section 60 paragraph 1 of the Copyright Act.

In Prague, date 19. 4. 2021 _____

Signature

Acknowledgement

I would like to thank to my supervisor Tomáš Obšil and my consultant Veronika Obšilová for the help and supervision during these years, what I have learned as person is priceless. During these years I've learned the person I want be in the future and how I will lead myself in my future carrier. I would like to thank all my colleagues who helped me during this journey Olívia Petrvalská, Kateřina Pšenáková and Nicola Koupilová. Even if my last year was not as I expected, I cannot neglect who was with me anyway noticing what I felt, because this is the true friendship, that's why I have to thank with each pieces of me Ayoub, probably the best person and loyal I have ever met; Francesco, who I wish the success he deserves; Davide, who inspired me the Iron man spirit; Manal, you know what we are, words are useless after all these years; Thomas, who was able to motivate me across my craziness; Dario, Joao and Madita for the great partnership and support. I cannot neglect to thank you even if we are not together anymore because you were the best part of me.

Unlimited thanks to my family who believed in me even when I was close to give up this journey, their words were like fresh air for my person.

I would like to dedicate this goal to my grandparents, only god knows how much I love you.

At the end I want to thank all of people who I met in this year, because as probably know, I am keeping every time some pieces from all of you to build up a better of me. I am not perfect; I am simply unique because I have all of you in me.

This is for YOU

ABSTRAKT

Protein-proteinové interakce (PPI) hrají klíčovou roli téměř ve všech biologických procesech. Mnoho proteinů vyžaduje pro své fungování dynamické interakce s dalšími proteiny či biomolekulami. Proteomické studie naznačily, že lidský proteinový interaktom zahrnuje několika set tisíc proteinových komplexů. Detailní charakterizace PPI je proto nezbytná pro plné pochopení procesů zprostředkovaných proteinovými komplexy. Mnoho PPI je také zapojeno do procesů spojených s přenosem signálu (signálních drah) v rámci řady patologických stavů a tyto PPI představují důležité cíle pro vývoj nových léků, zejména v situacích, kdy nelze použít běžnější strategie, např. obsazení aktivního místa enzymu či vazebné místo receptoru.

Tato disertační práce se zaměřuje na proteiny 14-3-3, rodinu adaptorových proteinů účastnících se regulace mnoha signálních drah. 14-3-3 proteiny fungují jako tzv. interakční uzly a kritické regulátory mnoha enzymů, receptorů a strukturních proteinů. Hlavním cílem této práce bylo strukturně charakterizovat vybrané komplexy proteinů 14-3-3 a zkoumat možnost jejich stabilizace nízkomolekulárními látkami. Pomocí kombinace proteinové krystalografie, diferenční skenovací fluorimetrie, fluorescenční polarizace a analytické ultracentrifugace byly studovány PPI mezi proteiny 14-3-3 a jejich dvěma fyziologicky důležitými vazebnými partnery: Ca^{2+}/kalmodulin-dependentní protein kinasou kinasou 2 (CaMKK2) a inhibitorem nukleárního faktoru NFκB (IκBα). Dále byla studována stabilizace komplexu CaMKK2:14-3-3 pomocí derivátů Fusicoccinu A. Výsledky práce ukázaly, že stabilizace komplexu CaMKK2:14-3-3 by mohla být alternativní strategií inhibice CaMKK2. Screening knihovny fragmentů navíc umožnil identifikovat tři molekuly, které se váží na dva různé povrchy proteinu 14-3-3 mimo vazebný žlábek, což naznačuje nové možnosti pro selektivní modulaci komplexů proteinů 14-3-3.

ABSTRACT

Protein-protein interactions (PPIs) play a crucial role in almost all biological processes. Many proteins require a number of dynamic interactions with other proteins and/or biomolecules to function. Proteomic studies have suggested that human protein-protein interactome consists of several hundred thousands of protein complexes. A detailed insight into these PPIs is essential for a complete understanding of the processes mediated by these protein complexes. Because many PPIs are involved in disease-related signaling pathways, such PPIs are important targets for pharmaceutical interventions, especially in situations where a more conventional target (e.g. the active site of an enzyme, the binding site of a receptor) cannot be used.

This doctoral thesis focuses on 14-3-3 proteins, a family of eukaryotic adaptor and scaffolding proteins involved in the regulation of many signaling pathways. The 14-3-3 proteins function as interaction hubs and critical regulators of many enzymes, receptors and structural proteins. The main aim was to structurally characterize selected 14-3-3 protein complexes and investigate their stabilization by small molecule compounds. Using combination of protein crystallography, differential scanning fluorimetry, fluorescence polarization and analytical ultracentrifugation, the PPIs between 14-3-3 and two physiologically important binding partners the Ca^{2+}/calmodulin-dependent protein kinase kinase 2 (CaMKK2) and the nuclear factor of kappa light polypeptide gene enhancer in B-cells inhibitor, alpha (IκBα) have been characterized. The stabilization of PPIs between 14-3-3 and CaMKK2 by fusicoccins have been investigated and we showed that the targeting of the fusicoccin binding site by small-molecule compounds could be an alternative way how to suppress CaMKK2 activity by stabilizing its phosphorylation-dependent inhibited state. In addition, the screening of a fragment library designed to target the 14-3-3 protein surface enabled us to identify three molecules that bind to two different surfaces of the 14-3-3 protein outside the usual binding groove, thus highlighting new possibilities for selective modulation of 14-3-3 complexes.

ABBREVIATIONS

AANAT	Aralkylamine N-acetyltransferase
AID	Autoinhibitory domain
AIDS	Acquired Immune Deficiency Syndrome
AMPK	AMP-activated protein kinase activity
ATP	Adenosine triphosphate
AUC	Analytical Ultracentrifugation
BCL-3	B-cell lymphoma 3-encoded protein
Bmh1	14-3-3 gene in Saccharomyces cerevisiae
CaM	Calmodulin
CaMK	Ca^{2+}/calmodulin-dependent protein kinase
cAMP	Cyclic adenosine monophosphate
CaMKK	Ca^{2+}/calmodulin -dependent protein kinase kinase
CBP	CREB-binding protein
CD	Catalytic domain
CFTR	Cystic Fibrosis Trans-membrane conductance Regulator
CKII	Casein kinase II
cryo-EM	Cryogenic electron microscopy
Da	Dalton
DEAE	Diethylamonietil cellulose
Dmax	Maximum distance among molecules
DMSO	Dimethyl Sulfoxide
DNA	Deoxyribonucleic acid
ER	Endoplasmic reticulum
ERK	Extracellular signal-regulated kinase
Eq.	Equation
ExoS	Exoenzyme S from Pseudomonas aeruginosa
FAC	Florigen activation complex
FAM	5-carboxyfluorescein
FC	Fusicoccin
Fig.	Figure
FITC	Fluorescein isothiocyanate

FP	Fluorescence Polarization
GFP	Green fluorescent protein
GST	Glutathione S-transferase
H^+-ATPase	Plasma membrane H+-ATPase
HPLC	High performance liquid chromatography
HTS	High-Throughput Screening
I	Intensity
IC50	half maximal Inhibitory Concentration
IκB	Inhibitor of Kb
IKK	IκB kinase
ITC	Isothermal Titration Calorimetry
KD	Kinase domain
K_D	Dissociation Constant
LPS	Lipopolysaccharide molecules
MAPK	Mitogen-activated protein kinase
MAP3K5	Mitogen-Activated Protein Kinase Kinase Kinase 5
MEK	Mitogen-activated protein kinase kinase
MKK	Mitogen-activated kinase kinase
MS	Mass spectrometry
NEMO	NF-kappa-B essential modulator
NMR	Nuclear magnetic resonance
MR	Molecular Replacement
NF-κB	Nuclear factor kappa B
noW	no Trp
NPY	Neuropeptide Y
Nth1	Neutral trehalase
PCR	Polymerase Chain Reaction
PEG	Polyethylene glycol
PMA2	Plasma Membrane H^+-ATPase 2
PDB	Protein Data Bank
PKA	Protein Kinase A
PMA	Plasma Membrane H^+-ATPase
PP2A	protein phosphatase 2
PPI	Protein-protein interaction

pSer	Phosphoserine
pThr	Phosphothreonine
PTM	Post-translational modification
Rg	Radius gyration
ROS	Reactive oxygen species
SAXS	Small angle X-ray scattering
S.D	Standard deviation
SEC	Size exclusion chromatography
SV-AUC	Sedimentation velocity analytical ultracentrifugation
TAK1	Mitogen-activated protein kinase kinase kinase 7
TASK3	Potassium channel subfamily K member 9
TLR	Toll-like receptors
TNFα	Tumor necrosis factor α
TNFR	Tumor necrosis factor receptor
TPL2	Tumor progression locus 2
TRX	Thioredoxin-1
TSA	Thermal Shift Assay
Vp	Porod volume
WAT	White Adipose Tissue

LIST OF PUBLICATIONS

Publications enrolled in this thesis:

1. **Lentini Santo D.**, Petrvalska O., Obsilova V., Ottmann C. and Obsil T. Stabilization of protein-protein interactions between CaMKK2 and 14-3-3 by fusicoccins. *ACS Chem. Biol.* **15**(11):3060-3071 (2020).

2. Wolter M.*, **Lentini Santo D.***, Herman P., Ballone A., Centorrino F, Obsil T., and Ottmann C. Interaction of an IκBα Peptide with 14-3-3. *ACS Omega* **5**(10): 5380–5388 (2020).
   *contributed equally

3. Psenakova K., Petrvalska O., Kylarova S., **Lentini Santo D.,** Kalabova D., Herman P., Obsilova V. & Obsil T. 14-3-3 protein directly interacts with the kinase domain of calcium/calmodulin-dependent protein kinase kinase (CaMKK2). *Biochim. Biophys. Acta - Gen. Subj.* **1862**(7), 1612–1625 (2018).

4. Valenti D., Neves J.F., Cantrelle F.X., Hristeva S., **Lentini Santo, D.**, Obsil T., Hanoulle X., Levy L.M., Tzalis D., Landrieu I., Ottmann C. Set-up and Screening of a Fragment Library Targeting the 14-3-3 Protein Interface. *Medchemcomm* **10**(10):1796-1802 (2019).

Other publications:

5. Alblova M., Smidova A., Kalabova D., **Lentini Santo D.,** Obsil T., Obsilova V. Allosteric Activation of Yeast Enzyme Neutral Trehalase by Calcium and 14-3-3 Protein. *Physiol Res.* **68**(2):147-160 (2019).

Funding

This study was supported by the Czech Science Foundation (Projects 16-02739S, 19-00121S) and the Initial Training Network, funded by the H2020 Marie Curie Actions of the European Commission under Grant Agreement 675179.

TABLE OF CONTENTS

1 Introduction

1.1 14-3-3 proteins

Reversible phosphorylation, a post-translational modification, is one of the most relevant and deeply studied function, which plays a central role for the regulation of many key cellular processes [1]. One of the possible mechanisms of protein complex formation is based on the phosphorylation of specific serine/threonine residues, which are later recognized by scaffold molecules altering the target protein function. One of the first scaffold molecules identified for their ability to selectively bind phosphoserine/phosphothreonine (pSer/pThr) containing motifs were 14-3-3 proteins [2].

14-3-3 proteins are expressed in all eukaryotic cells and belong to a highly conserved protein family. Their uncommon name is derived from the elution positions on gel permeation chromatography (fraction 14) and migration pattern on two-dimensional DEAE-cellulose chromatography (position 3.3) [3]. Diversity of 14-3-3 protein isoforms is different in various organisms: while lower eukaryotes and e.g. yeast have two isoform Bmh1 and Bmh2, higher eukaryotes e.g. plants possess fifteen different 14-3-3 genes [4,5]. Seven 14-3-3 protein isoforms have been identified in mammals (β, γ, ε, ζ, η, σ, and τ), and all of them with the exception of sigma isoform form both homo- and heterodimers, the sigma isoform is strictly homodimeric [6,7]. The discovery that the 14-3-3 proteins can recognize and bind the specific pSer/pThr containing motifs of target proteins, suggested not only their important role in signal transduction, but also their role in the assembly of protein-protein complexes mediated by pSer/pThr phosphorylation [8]. Because of the large number of 14-3-3 binding partners and their variability, the members of 14-3-3 protein family play a crucial role in the regulation and coordination of many biological processes such as apoptosis, cell cycle progression, metabolism, DNA transcription/damage control and more [9].

1.1.2 14-3-3 protein structure and target recognition

First two structures of human 14-3-3ζ [10] and τ [11] isoforms showed that 14-3-3 proteins form highly helical dimers, where each protomer consists of nine anti-parallel α-helices and contains a characteristic target/ligand binding groove formed by four α-helices ***(Fig. 1.1 A)***.

Nowadays, the crystal structures of all seven human 14-3-3 isoforms are available [12]. They share a high percentage of sequence homology, the only difference is in the C-

terminal part (last 20-40 amino acid residues). Ligand binding induces several structural changes within the 14-3-3 dimer such as the small change in the position of protomers causing "opening" of the 14-3-3 dimer ***(Fig. 1.1 B)*** [7,12]. This conformational flexibility may facilitate the binding of ligands with various sizes and shapes. Another important difference observed among 14-3-3 isoforms, which may play a role in the isoform-specific functions, is the presence of salt bridges at the dimer interface. For example, the dimer formation of 14-3-3ζ is facilitated through three salt bridges and few hydrophobic and polar contacts between H1-H2 helices from one protomer and H3-H4 helices from the second protomer [10]. However, only one of these three salt bridges is conserved among human 14-3-3 isoforms [6–11,13].

As mentioned above, the largest sequence variability between the isoforms occurs in the C-terminal stretch. In terms of protein-protein interactions it has been shown that the C-terminus prevents the binding of unsuitable ligands by occupying the ligand binding groove, but it was also shown that the absence of its C-terminal domain, called ΔC, may enhance the binding of the target protein [10,14–16].

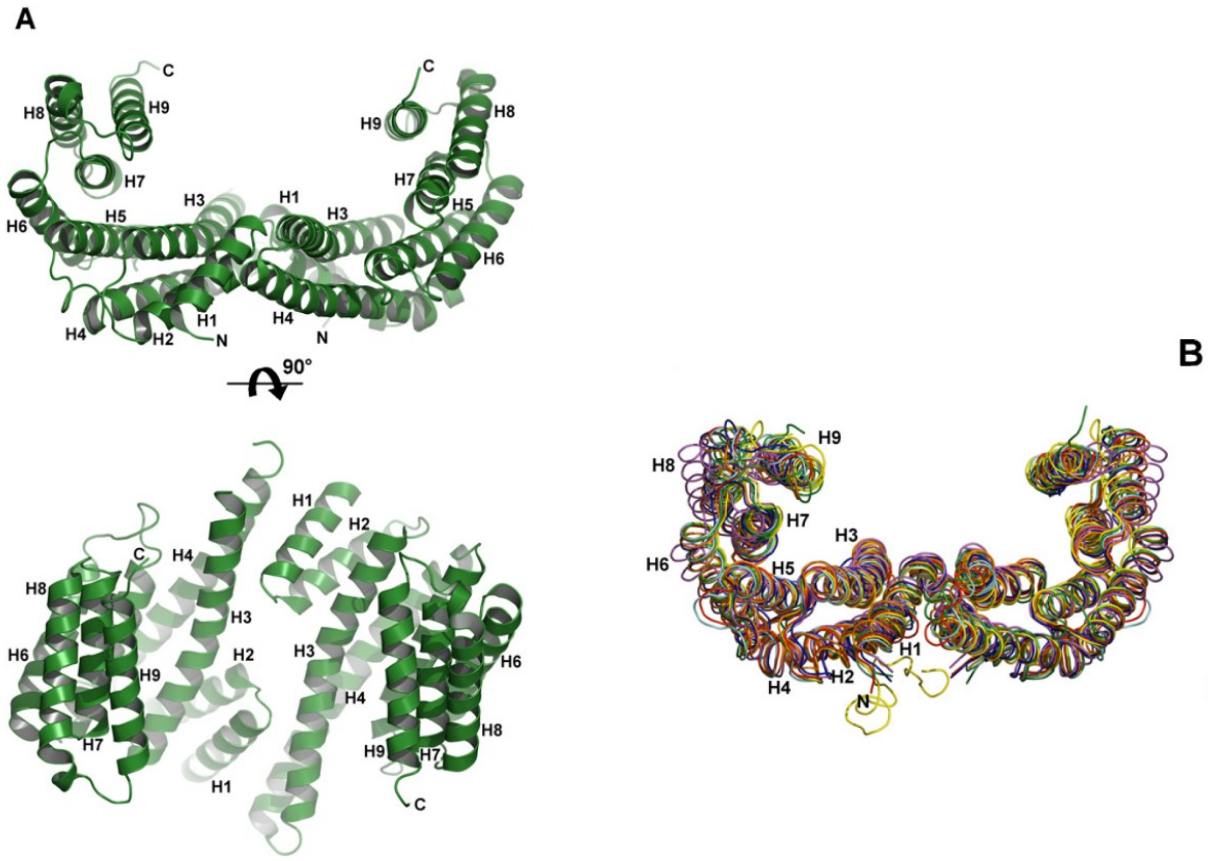

Fig. 1.1 (A) Crystal structure of 14-3-3ζ isoform (PDB ID 1QJB [17])presented as green ribbon. (B) Superimposition of all human 14-3-3 isoforms. The β isoform (PDB ID 2C23) is shown in magenta, γ (2B05) in red, ε (2BR9) in orange, ζ (1QJB) in green, η (2C74) in cyan, σ (1YWT) in

blue and τ (2BTP) in yellow. This figure was taken from [18].

The ability of 14-3-3 proteins to bind phosphoserine-containing motifs [8] was characterized using a peptide library screening and three optimal binding motifs were identified: (I) RSX(pS/T)XP, (II) RX(F/Y)X(pS)XP) and (III) C-terminal pS/pT-X_{1-2}-COOH [2,17,19,20]. However, these motifs are not absolute and many 14-3-3 binding partners contain different motifs [21].

The first structures of the 14-3-3 proteins with bound synthetic phosphopeptides showed only a small structural change of the 14-3-3 dimer compared to the free forms. The conformational change of 14-3-3 is likely caused by the interaction with the phosphopeptide, which makes polar contacts with residues Lys^{49}, Arg^{56}, Arg^{127} and Tyr^{128} (14-3-3ζ numbering) that form a positively charged pocket within the 14-3-3 ligand binding groove ***(Fig. 1.2)*** [10,17,19,22]. Phosphopeptides bind in similar extended conformations and besides contacts mediated by the phosphoresidue they also make several additional contacts with residues from the 14-3-3 ligand binding groove [2,12,17]. These structures also showed that the basic residues (Arg or Lys) frequently located at the -3 and -4 positions with the respect to the pSer or pThr appear to stabilize the conformation of the phosphopeptide through salt bridges with the phosphate of pSer/pThr. In addition, the frequent presence of proline at +2 position with respect to pSer likely allows the change in the direction of the phosphopeptide main chain ***(Fig. 1.2)*** [2,17]. Furthermore, several crystallographic studies have shown that the presence of an additional small molecule compound within the 14-3-3 ligand binding groove may change the conformation of the bound phosphopeptide [23–26].

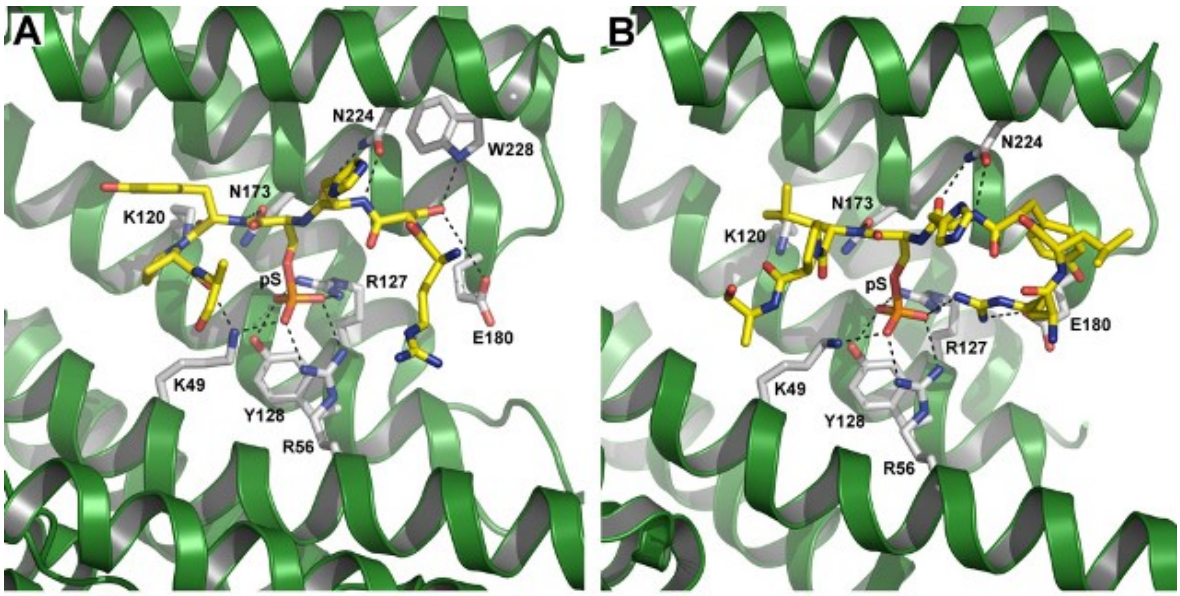

Fig. 1.2 Detailed view of contacts within the 14-3-3 ligand binding groove. (A) Phosphopeptide containing the "mode 1" motif (ARSHpSYPA) bound to 14-3-3 [17]. (B) Phosphopeptide containing the "mode 2" motif (RLYHpSLPA) bound to 14-3-3 [17]. This figure was taken from [18].

The third binding motif pS/pT-X_{1-2}-COOH is considered weaker in terms of binding affinity compared to mode 1 and 2 motifs. However, this motif enables the binding of an additional small molecule compound, which can significantly enhance the stability of the complex between 14-3-3 and the phosphopeptide**.** A typical compound used for this purpose is a diterpene glycoside toxin produced by fungi called fusicoccin. This compound has been shown to bind to and stabilize the 14-3-3:H^+-ATPase complex ***(Fig. 1.3)*** and it even enables the formation of the complex between 14-3-3 and the unphosphorylated H^+-ATPase [24,27]**.** The discovery of fusicoccin's ability to stabilize the 14-3-3 protein complexes suggested the possibility of development of new more potent compounds that could be used as modulators of interactions between 14-3-3ζ and their targets [18,27–29].

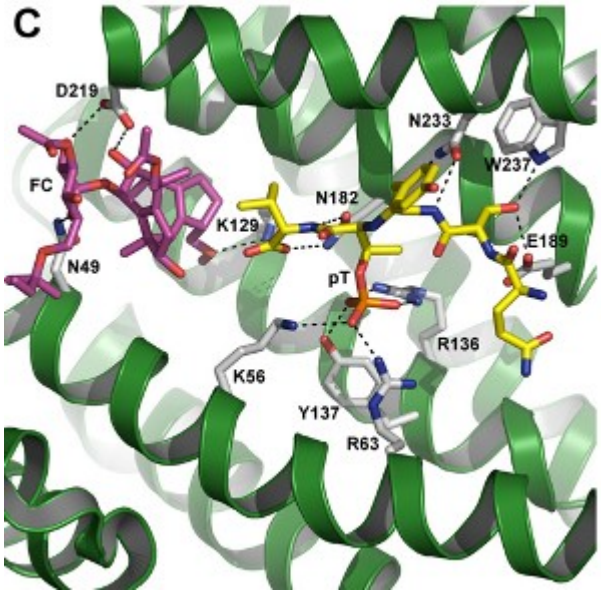

Fig. 1.3 The crystal structure of the mode 3 14-3-3 binding motif from the C-terminus of H^+-ATPase (QSYpTV) bound to 14-3-3C [24]. Fusicoccin (FC) is highlighted in magenta. This figure was taken from [18].

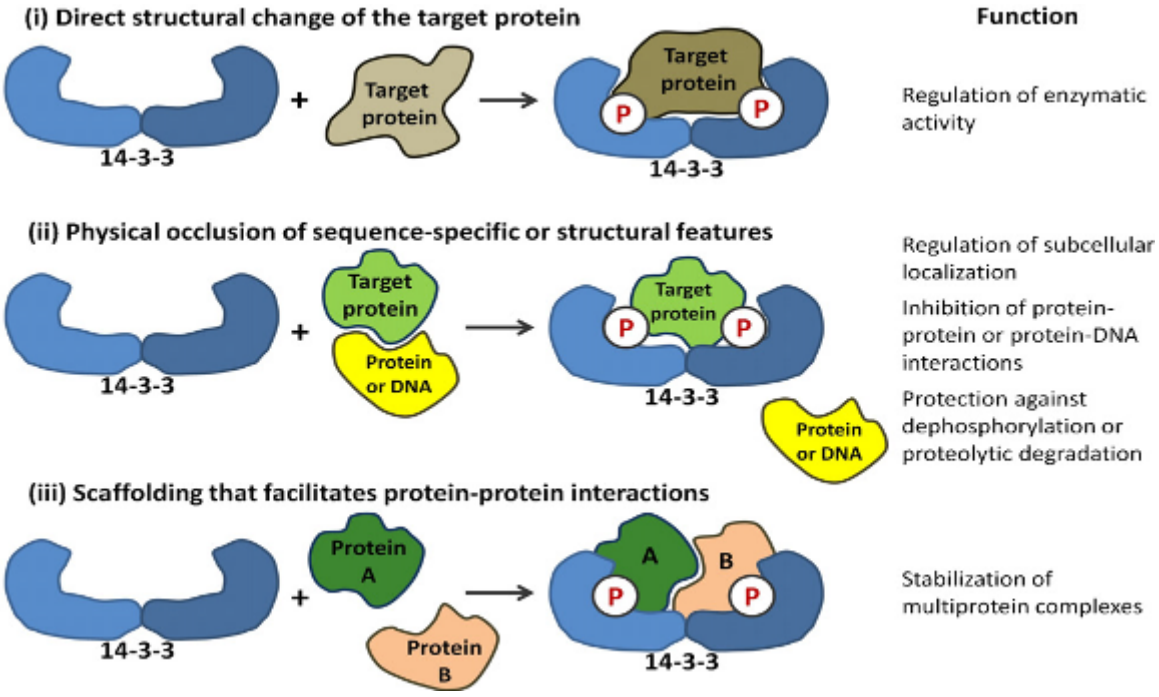

Fig. 1.4 Modes of action of 14-3-3 proteins. 14-3-3 is an adaptor scaffolding protein able to: (i) cause change in the conformation of target proteins; (ii) blocks the specific surface in protein; (iii) enhance the interaction of two selected proteins. This figure was taken from [18].

1.1.3 Mechanisms of 14-3-3 protein functions

During last past 30 years the study focused on 14-3-3 protein functions has revealed several mechanisms. It is possible to define three main functional roles (modes of action) of the 14-3-3 proteins: (I) 14-3-3 binding induces a structural change of the bound client protein; (II) physical obstruction of a specific sequence or structural feature; (III) scaffolding function, which promotes protein-protein interaction between two 14-3-3 binding partners ***(Fig. 1.4)*** [11,16,30–32]**.** Unfortunately, the detailed mechanisms of these modes of action are still unclear in most cases and the majority of structural data available today are crystal structures of 14-3-3 complexes with short phosphopeptides, which cannot give us a detailed insight into these processes. Nevertheless, available data revealed several common features important for the 14-3-3-mediated regulation of the target activities: (i) the rigid nature of the 14-3-3 protein molecule, (ii) the simultaneous presence of two (or more) specific motifs recognized by 14-3-3 proteins within the binding partner, and (iii) the location of 14-3-3 binding motifs within long disordered regions of target proteins [18,28].

1.1.4 Known structures of 14-3-3 protein complexes

The most important function of the 14-3-3 proteins is to act as scaffold/chaperone molecules able to modulate the structure and the function of the bound partner and to mediate interaction of two simultaneously bound partners. Examples of these two mechanisms were provided by solving the crystal structures of 14-3-3 in complex with serotonin N-acetyltransferase (AANAT) [33] and H^+-ATPase [34]. In both complexes the 14-3-3 dimer is able to anchor two chains of the target protein in its central cavity [33]. In the case of AANAT, the14-3-3 protein binding stabilizes the flexible part of the active site thus enhancing the substrate binding affinity and enzyme activity. In the case of H^+-ATPase, the 14-3-3 protein binding stabilizes the quaternary structure of the pump, thus also increasing its activity. More recently, additional structures of 14-3-3 protein complexes with full-length binding partners were reported. Taoka et al. [35] solved the crystal structure of the complex between plant 14-3-3 and florigen, which suggested the mechanism responsible for induction of flowering with 14-3-3 protein acting as intracellular receptor for florigen in shoot apical cells. Alblova at al. [36] reported the crystal structure of Bmh1 (yeast 14-3-3 isoform) in complex with neutral trehalase Nth1, which showed how 14-3-3s allosterically modulate the structure of a binding partner with multiple domains. In the complex, the 14-

3-3 protein stabilizes the flexible part of the active site through the proper positioning of the regulatory and catalytic domains. In addition, Sluchanko et al. [37] solved the crystal structure of the 14-3-3 protein in complex with the heat shock protein HSPB6, which showed that several intrinsically disordered HSPB6 regions are transformed into a well-defined asymmetric structure.

More recently structures of additional 14-3-3 protein complexes have been reported: the crystal structure of the complex between 14-3-3 and ExoS (Exoenzyme S from Pseudomonas aeruginosa) and the cryo-EM and crystal structures of the complex between 14-3-3 and B-RAF kinase. The structure of the 14-3-3:ExoS complex solved by Karlberg et al. [38] revealed that the complex formation is driven by an extensive hydrophobic surface of ExoS, which seems to be essential for the activation of the toxin. The structure suggested that the 14-3-3 binding masks this hydrophobic surface, thus protecting ExoS against aggregation. Reported structures of the 14-3-3:B-RAF and 14-3-3:B-RAF:MEK complexes revealed insights into how the 14-3-3 protein regulate B-RAF activity [3940]. The structure of the autoinhibited complex showed that 14-3-3 simultaneously binds phosphorylated Ser^{365} and Ser^{729} residues of one B-RAF molecule and blocks the dimerization interface of the B-RAF. On the other hand, the structure of the active 14-3-3:B-RAF:MEK complex revealed that an active B-RAF dimer is stabilized by the 14-3-3 dimer through the interaction with phosphorylated Ser^{729} motifs located at the C-termini of two B-RAF molecules.

1.1.5 14-3-3 protein complexes as targets for the modulation of protein-protein interactions

The fact that 14-3-3 proteins interact and regulate hundreds of binding partners involved in many disease-relevant signaling pathways makes these complexes interesting targets for pharmaceutical intervention. The targeting of these protein-protein interactions (PPI) will be particularly valuable for situations where it is difficult or impossible to directly target conventional molecules such as enzymes or receptors. However, the development of such modulators of PPI requires detailed knowledge of corresponding binding interfaces. Unfortunately, the majority of structures of 14-3-3 complexes available in the PDB databank are complexes with short phosphopeptides representing the 14-3-3 binding motifs of binding partners and only few structures of 14-3-3 complexes with full-length partners were reported so far. As already mentioned above, the 14-3-3 binding motifs are frequently located within the long disordered regions and the 14-3-3 binding partners are often multi-

domain and highly flexible proteins. Thus, during the complex formation the 14-3-3 protein dimer anchors only the phosphorylated regions and a large part of the target protein stays often disordered and structurally heterogeneous, thus preventing the crystal growth. Therefore, a common approach adopted to study such problematic 14-3-3 complexes is based on using synthetic phosphopeptides (10-40 amino acid residues long) to study at least interactions between 14-3-3 and 14-3-3 binding motifs of these targets. This approach enabled development of various potent modulators of 14-3-3 PPI, which were shown to either inhibit or stabilize specific 14-3-3 protein complexes [29,34].

1.1.6 Small-molecule modulators of 14-3-3 PPI

Fusicoccin A, a diterpene glycoside, is a natural compound produced by the phytopathogenic fungus *Phomopsis (Fusicoccum) amygdali,* which was firstly described for its ability to release a wilt-inducing toxin [41]. Latter it was shown that this compound stabilizes the complex between the plasma membrane H^+-ATPase (PMA) and the 14-3-3 protein, acting as a 'molecular activator' for the complex [42]. From this starting point, few Fusicoccin analogues, like Cotylenin A [43] or Fusicoccin THF [26], were prepared and tested and proved to behave as 'molecular modulator' for the stabilization of 14-3-3 binary complexes, especially those containing the C-terminal mode III binding motif ***(Fig. 1.5)***. However, the Fusicoccin A stabilizes not only 14-3-3 complexes with targets possessing the C-terminal 14-3-3 binding site, but also complexes with other motifs, for example, the 14-3-3 complex with the cystic fibrosis trans-membrane conductance regulator (CFTR) [44]. Cotylenin A, a Fusicoccin analogues also produced by a fungus (Cladosporium), behaves as a bioactive molecule in plants [42]. This compound also affects cell differentiation in human acute myeloid leukemia in mouse models and *in vitro* cell cultures [44,45]. The crystal structure of 14-3-3 in complex with the N-terminal 14-3-3 binding motif of the protein kinase C-RAF and cotylenin A (PDB ID: 4IEA) showed how this molecule stabilizes PPI between 14-3-3 and C-RAF and suggested it could possess an anti-tumor activity [25].

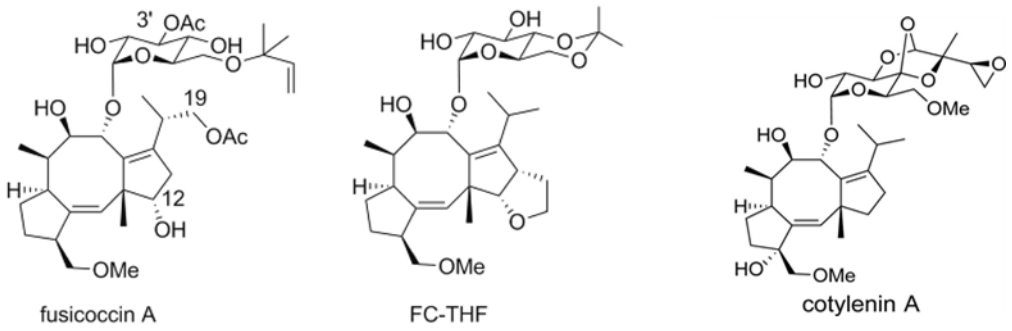

Fig. 1.5 Natural or semi-synthetic Fusicoccin analogues, that stabilize 14-3-3 binary complexes. This picture was taken from [29].

The 5-8-5-fused ring in the Fusicoccin scaffold makes the synthesis of new derivatives to improve selectivity and/or potency challenging. Nevertheless, new potent analogues of Fusicoccin have been described, for example, Fusicoccin-THF ***(Fig. 1.6),*** which was designed to selectively stabilize 14-3-3 complexes with the "mode III' motifs. This compound was shown to modulate the interaction between 14-3-3 and the potassium channel TASK3 [26].

The screening of a library of 37,000 small-molecules enabled identification of two new compounds: Epibestatin and Pyrrolidone 1 [46]. Pyrrolidone 1 interacts with the same 14-3-3 region as fusicoccin [47]. While Fusicoccin fills almost the whole volume of the cavity within the 14-3-3 binding groove, Pyrrolidone 1 occupies only part of it [47]. The binding conformation suggests that Pyrrolidone1, if its structure is modified, can be considered as a starting point for development of new inhibitors that would completely fill the gap in the two proteins interface. Epibestatin, similarly as fusicoccin, fills almost the whole binding site [46].

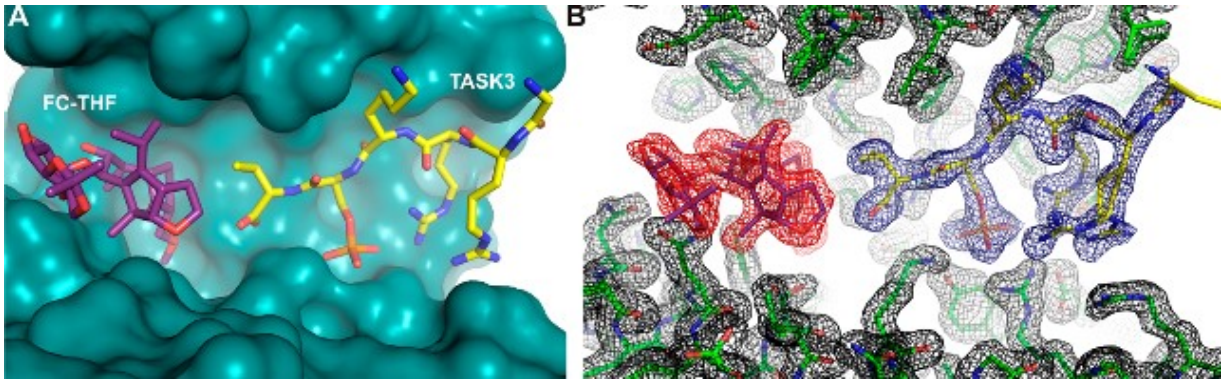

Fig. 1.6 Fusicoccin semi-synthetic derivative (FC-THF) stabilizes the 14-3-3σ/TASK3 peptide complex [26]. (A) FC-THF (purple sticks) and the TASK3 C-Terminal peptide (yellow sticks) are

located within the 14-3-3σ binding groove. (B) Electron density (red, blue, and black mesh, $2F_O$-F_C, contoured at 1.0 σ) around FC-THF (purple sticks), C-terminus of TASK3 peptide (yellow sticks), and 14-3-3σ (green sticks). This figure was taken from [29].

1.2 Nuclear Factor kappa B (NF-κB)

NF-κB signaling pathway has a crucial role in the development, maintenance, and progression of most chronic diseases. NF-κB regulates the gene expression and thus various physiological responses, such as immune inflammatory, acute-phase inflammatory and oxidative stress responses, cell adhesion, differentiation, and apoptosis [48]. NF-κB dysregulation has been shown in recent works that is connected to many diseases including asthma, diabetes, AIDS, stroke, viral infections, and other [49–56]. The role of NF-κB in inflammation and cancer progression suggested the potential use of NF-κB -specific drugs in hematological malignancies and solid tumors treatments [57,58].

There are five members in the NF-κB family: NF-κB1 (p50 and its precursor p105), and NF-κB2 (p52 and its precursor p100), ReIA (p65), ReIB and c-ReI, able to form hetero- or homodimers [59–61]. NF-κB activation is connected with its localization. In relaxed cells, NF-κB proteins are preserved in the cytoplasm bound to the inhibitor of κB (IκB) proteins: the most abundant are IκBα, IκBβ, and IκBε [59]. NF-κB activation occurs via both canonical and non-canonical mechanisms **(Fig. 1.7)**.

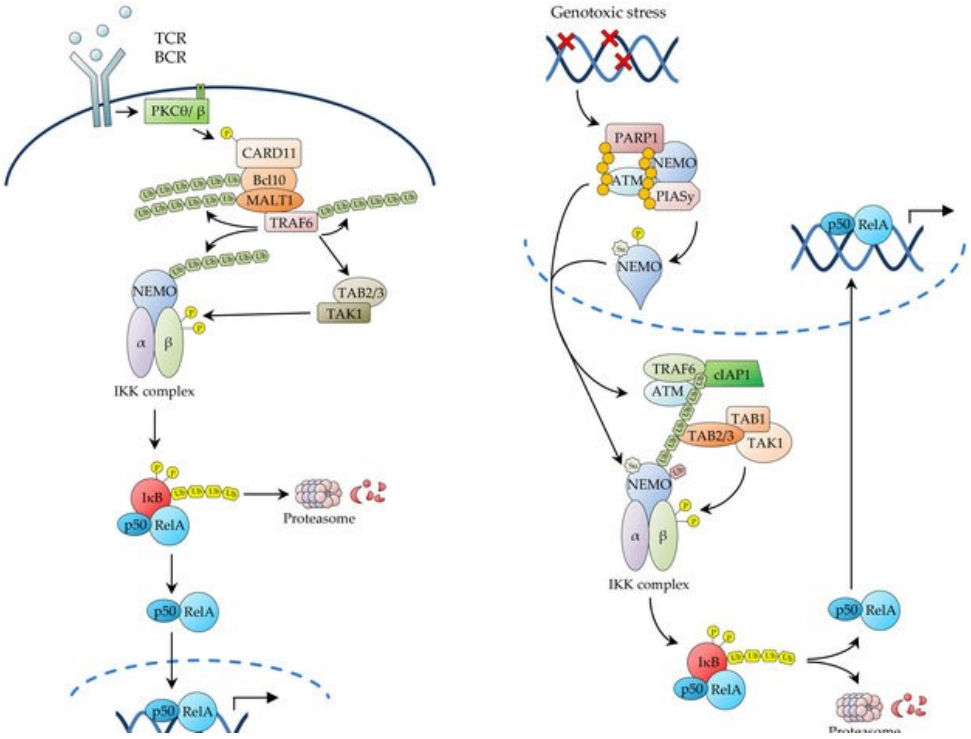

Fig. 1.7 Schematic view of main pathways of canonical NF-κB activation. In response to activating stimuli (e.g. genotoxic stress), protein NEMO is enrolled to the respective proximal signaling com-

plexes and bound to the receptors using non-degradative polyubiquitin chains. The enrollment of the IKK complex via NEMO permits the TAK1 kinase to phosphorylate and thus activate IκKβ. This triggers the IκBs' phosphorylation and degradation, thereby releasing the active NF-κB dimers. NF-κB, nuclear factor κB; TLR, toll-like receptor; NEMO, NF-κB essential modulator; IKK, IκB kinase; TAK1, Transforming growth factor β-activated kinase 1. This figure was taken from [62].

The activated NF-κB is located in the nucleus, where it undergoes a series of posttranslational modifications, such as phosphorylation, acetylation, and methylation, thus regulating the NF-κB activity with the ReIA/p65 regulation being the most relevant. Once this complex is formed, it is strictly phosphorylated by cAMP-dependent protein kinase (PKA), casein kinase II (CKII) and IKK [63,64]. The dephosphorylation of ReIA by the protein phosphatase 2A (PP2A) has been shown to reduce the NF-κB activity [65]. ReIA is also acetylated by p300/CBP, and acetylated ReIA has been shown to bind weakly to IκBα [66,67], thus promoting its nuclear localization and NF-κB transcriptional response.

Activated NF-κB controls the transcription of several hundreds of genes that participate in immunoregulation, growth regulation, inflammation, carcinogenesis, and apoptosis [68] ***(Fig. 1.8)***. Because of the multiple levels of regulation, NF-κB signaling pathway is potentially targeted at many levels including kinases, phosphatases, ubiquitination, nuclear translocation, DNA binding, protein acetyl transferases and methyl transferases ***(Fig. 1.9)***. Moreover, due to its ability to control multiple disease-relevant genes, the NF-κB signaling pathway is considered an important target for the development of new therapy approaches [49,69].

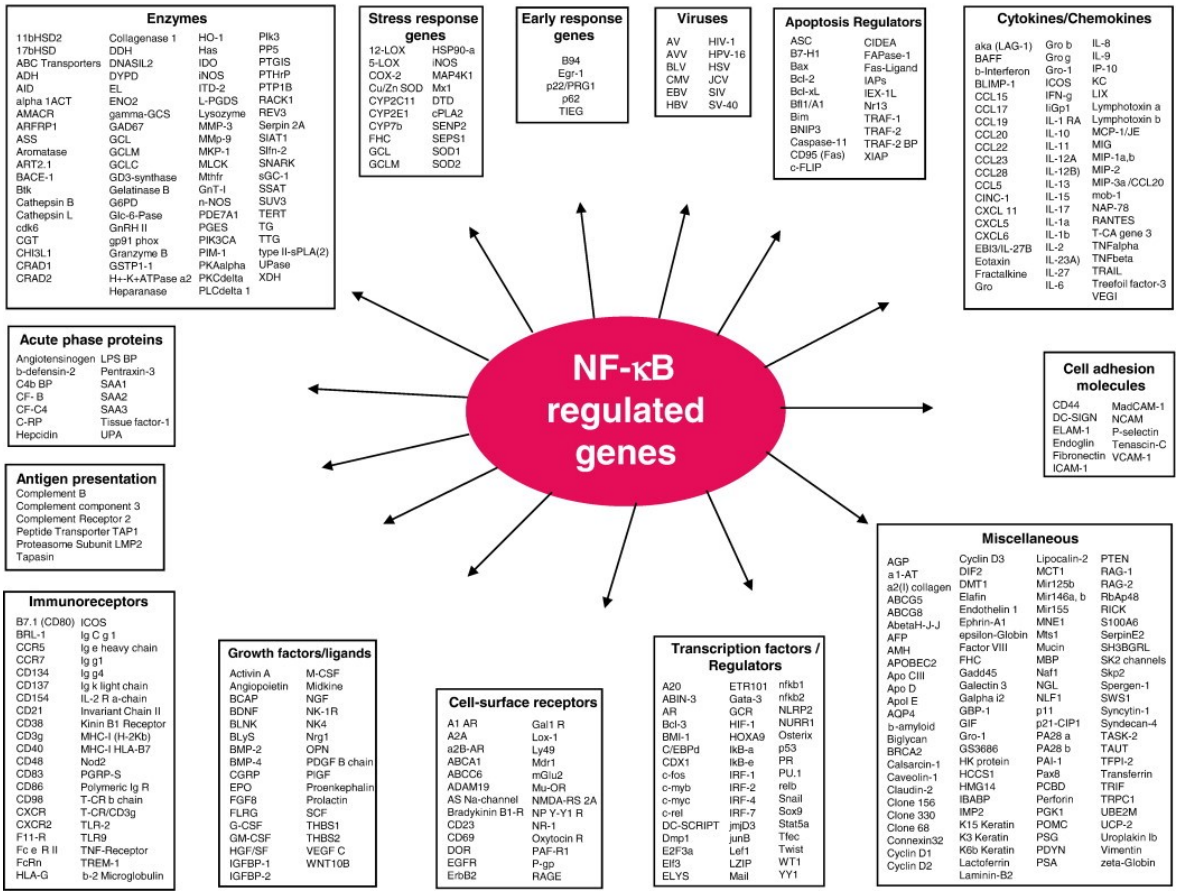

Fig. 1.8 Overview of genes regulated by NF-κB. This list includes transcription factors, cell-surface receptors, growth factors, immunoreceptors, acute phase proteins, enzymes, stress response genes, early response genes, viruses, apoptosis regulators, cytokines/chemokines and cell adhesion molecules. This figure was taken from [68].

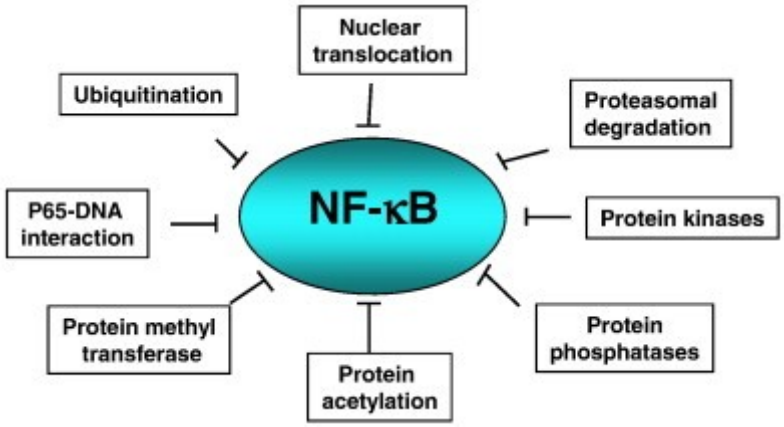

Fig. 1.9 Potential strategies of NF-κB pathway inhibition. NF-κB can be inhibited at various steps including kinases, phosphatases, ubiquitination, acetylation, methylation, nuclear translocation and DNA binding. This figure was taken from [68]

1.2.1 Inhibitor of Nuclear Factor kappa B (IκB)

The NF-κB protein family is known from many years to be involved in key biological processes including cell proliferation, cell survival, apoptosis and regulation of immune response [59,70–72]. The main characteristics of NF-κB pathway is its regulation by IκB proteins. IκB family consists of eight members containing the typical ankyrin repeat domains. The most studied member of IκB family is IκBα, which primarily targets the NF-κB heterodimer p50/p65 thus keeping the NF-κB in cytoplasm [73–76].

The key step in the activation of NF-κB is the phosphorylation of IκB at conserved Ser32 and Ser36, which leads to the IκBα ubiquitination and its proteasomal degradation [77,78]. In addition, it has been shown that the nuclear export of the IκBα/p65 complex requires a scaffolding protein 14-3-3 [79]. Physical interaction between 14-3-3 and IκBα was demonstrated by co-immunoprecipitation, however, the precise mechanism of the 14-3-3-mediated regulation of IκBα/p65 localization remains elusive [79].

1.3 Calcium/Calmodulin-dependent protein kinase kinase (CaMKK2)

Calcium/calmodulin (Ca^{2+}/CaM) signaling is directly connected with obesity and insulin resistance [80,81]. Several epidemiological studies highlighted Ca^{2+} signaling as a determinant cause in obesity, able to seriously alter system metabolism [81–84]. The Ca^{2+}/CaM signaling pathway starts with the formation of a complex between Ca^{2+} and its ubiquitous receptor, CaM. The Ca^{2+}/CaM complex then activates a set of Ca^{2+}/CaM-dependent protein kinases. In this kinase "cascade", one of the main actors is the Ca^{2+}/CaM-dependent protein kinase kinase 2 (CaMKK2), which, upon its activation, activates the downstream Ca^{2+}/CaM-dependent protein kinases I and IV (CaMKI and CaMKIV) ***(Fig. 1.10)*** [85]. Furthermore, CaMKK2 acts as an upstream activator of the AMP-activated protein kinase (AMPK) [86]**.** The CaMKK2:AMPK complex also controls energy equilibrium by acting in hypothalamus neurons, thus controlling the production of the hormone neuropeptide Y (NPY) [87]. CaMKK2 activity influences several physiological processes such as regulation of glucose balance, hematopoiesis, inflammation and cancer, in fact, CaMKK2 has been validated as potential target for pharmaceutical intervention [85].

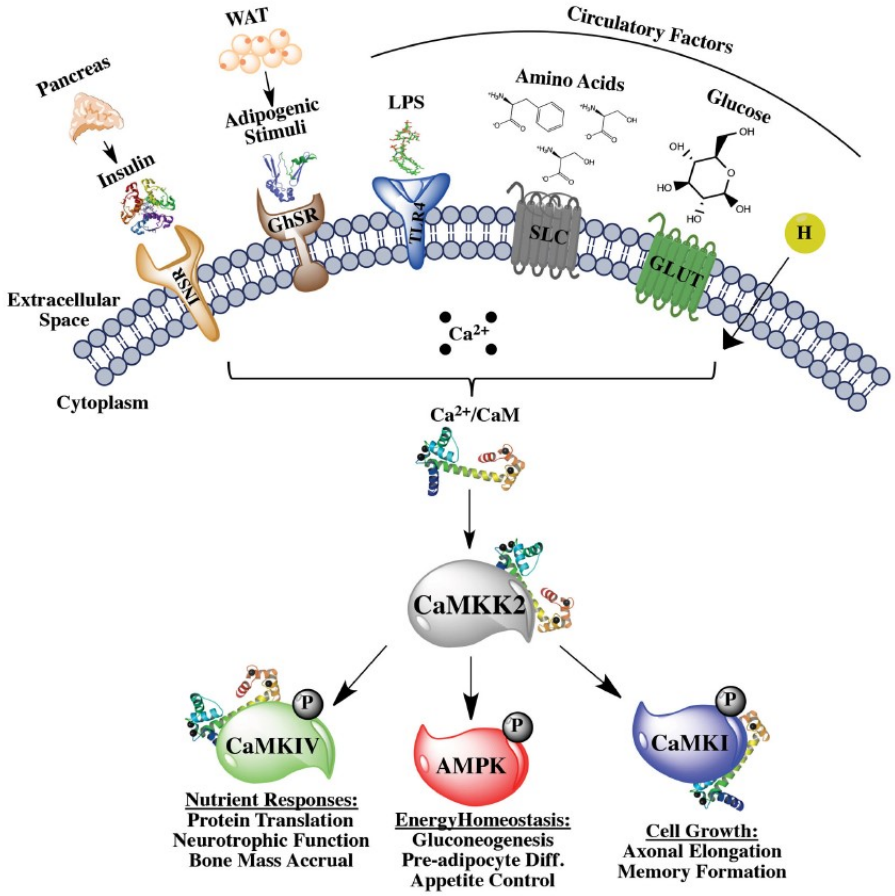

Fig. 1.10 The Ca^{2+}/CaM-dependent kinase cascade induces various metabolic responses to patho/physiologic stimuli. Upstream extracellular signals interact with their respective receptors, causing an increase in intracellular Ca^{2+} concentration and the formation of the Ca^{2+}/CaM complex, which interacts with many target proteins including CaMKK2. The Ca^{2+}/CaM binding activates CaMKK2, which in turn phosphorylates and activates downstream targets CaMKIV, AMPK and CaMKI. This figure was taken from [88].

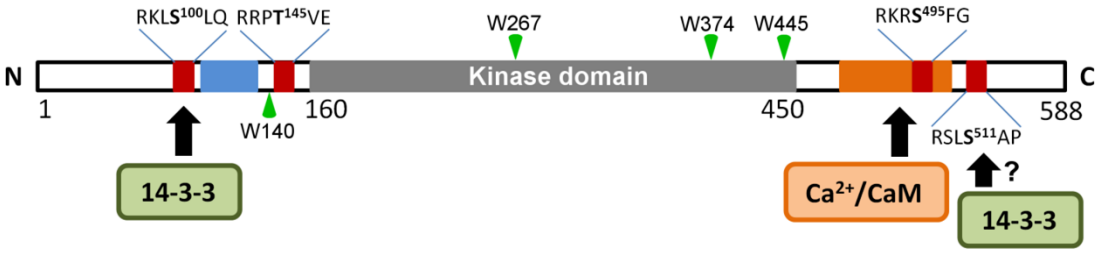

Fig. 1.11 CaMKK2 structure domain: the PKA phosphorylation sites are shown in red, the regulatory site and the CaM binding site are colored in blue and orange, respectively. This picture was taken from [89].

The members of the Ca^{2+}/CaM-dependent protein kinases (CaMK) family share a similar domain structure with the catalytic kinase domain followed by an autoinhibitory domain, which overlaps with the CaM-binding region ***(Fig. 1.11)*** [90]. The autoinhibitory segment interacts with the kinase domain and occupies the active site. The Ca^{2+}/CaM binding to the CaM-binding region of CaMK changes conformation of the autoinhibitory domain and releases it from the kinase domain, thus, in turn, enabling the kinase activity [89,91].

Mammalian cells express two CaMKK isoforms: CaMKK1 and 2, which share high degree of sequence similarity ***(Fig. 1.12)***, but differ in their biochemical properties. While CaMKK1 is regulated only through the autoinhibitory mechanism, CaMKK2 also exhibits considerable Ca^{2+}/CaM-independent activity. This autonomous activity is regulated by 23 amino acid region at the N-terminal end of the catalytic domain [92] containing three sites recognized by cyclin-dependent kinase 5 and glycogen synthase kinase 3 and also one specific site phosphorylated by cAMP-dependent protein kinase [93,94].

CaMKK1 possesses five PKA phosphorylation residues, Ser52, Ser74, Thr108, Ser458 and Ser475, four of those are also in CaMKK2 (Ser100, Thr145, Ser495 and Ser511) ***(Fig. 1.11).*** Both CaMKK1 and 2 are partially inhibited by PKA-mediated phosphorylation [93–95].

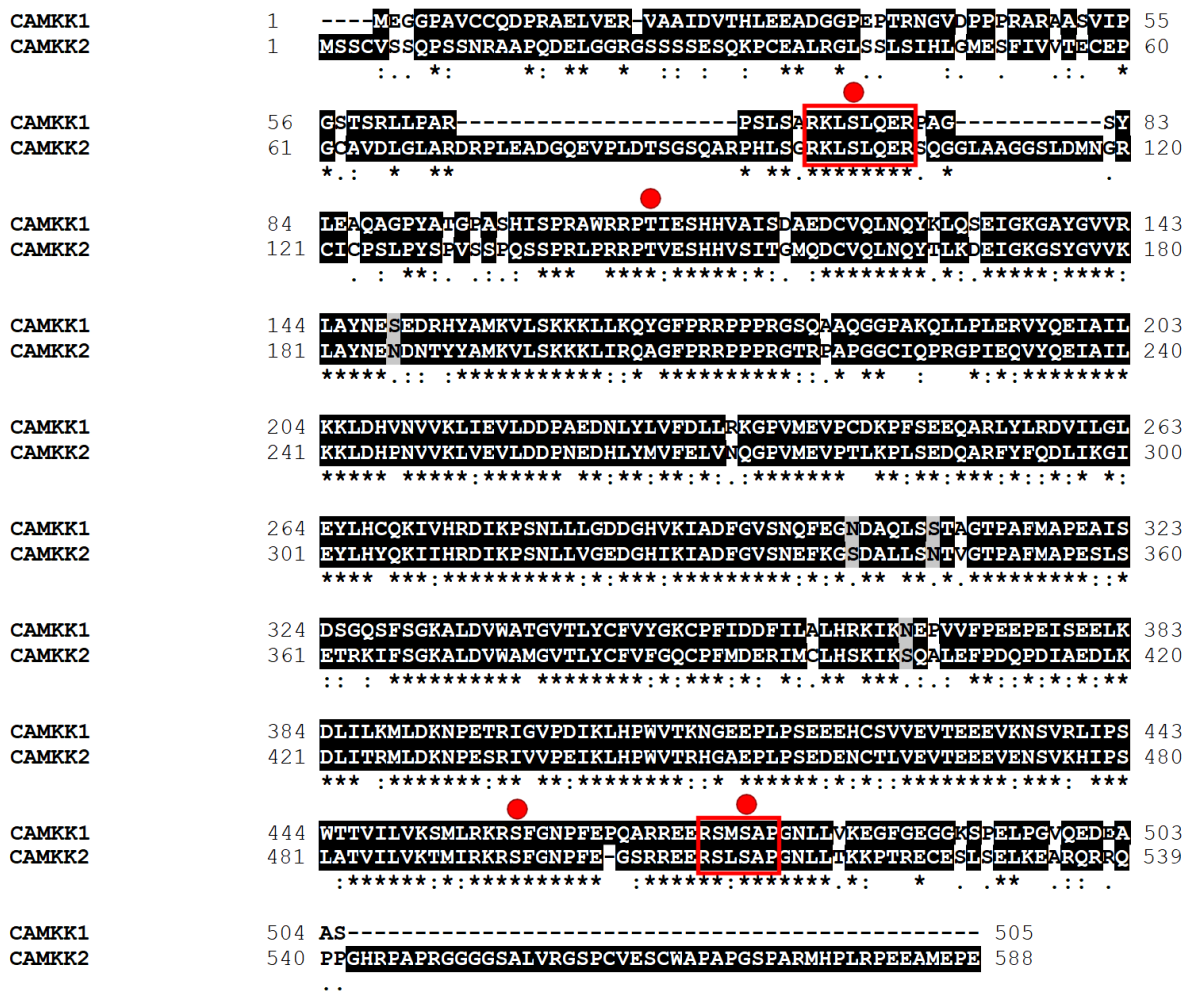

Fig. 1.12 Comparison of human CaMKK1 (Q8N5S9) and CaMKK2 (Q96RR4) sequences. Red circles denote PKA phosphorylation sites. Red squares denote the 14-3-3 binding motifs. This picture was taken from [89].

1.3.1 Interaction between CaMKKs and the 14-3-3 protein

The GST pull-down and co-immunoprecipitation experiments revealed that both CaMKKs can bind to 14-3-3 protein isoforms, particularly to isoform γ, upon the PKA-mediated phosphorylation [96,97]. The residue Ser[74] of CaMKK1 has been suggested to be the main 14-3-3 binding site, which corresponds to Ser[100] in CaMKK2 [97] (***Figs. 1.11 and 1.12***). On the other hand, Ser[475], which corresponds to Ser[511] in CaMKK2, is considered to be a secondary 14-3-3 binding site [97]. The PKA-mediated phosphorylation of the second site, however, is lower and requires the presence of the Ca^{2+}/CaM complex [96,98,99].

The role of 14-3-3 in the regulation of CaMKK activity is still unclear. Davare at al. [96] suggested that the 14-3-3 binding to CaMKK1 reduces the kinase activity through two

different mechanism: (i) protection of Thr^{108} against dephosphorylation, thus maintaining CaMKK1 in the PKA-mediated inhibited state, and (ii) through direct inhibition of the kinase activity. Another study by Ichimura et al. [97] showed that the 14-3-3 protein suppresses the maximum velocity (V_{max}) of CaMKK1. Therefore, both these studies indicated that the 14-3-3 protein act as a physiological inhibitor of CaMKK1. The role of 14-3-3 in the regulation of the second CaMKK isoform CaMKK2 was totally elusive.

2 Aims of this doctoral thesis

The main goal of this doctoral thesis was to structurally characterize 14-3-3 protein complexes with phosphopeptides containing 14-3-3 binding motifs of CaMKK2 and IκBα and investigate their stabilization by small molecule compounds.

Specific aims were:

1. to investigate the interaction between 14-3-3 and the phosphopeptide containing 14-3-3 binding motif of IκBα,
2. to investigate the interaction between 14-3-3 and phosphopeptides containing both 14-3-3 binding motifs of CaMKK2,
3. to evaluate the stabilization of the 14-3-3:CaMKK2 complex by Fusicoccin A and its derivatives,
4. to perform screening of a fragment library targeting the 14-3-3 protein interface.

Protein crystallography, fluorescence polarization (FP) assay, Thermal shift assay (TSA), analytical ultracentrifugation (AUC), tryptophan fluorescence measurement and nuclear magnetic resonance (NMR) spectroscopy were used as principal tools to achieve the specific aims.

3 Methods

This chapter lists only those methods that were the focus of my experimental work.

3.1 Expression and purification of 14-3-3 proteins

Human 14-3-3γ and ξ isoforms and their mutant forms were expressed and purified as previously described [33]. Purified 14-3-3s in a buffer containing 20 mM Tris-HCl (pH 7.5), 150 mM NaCl, 1 mM TCEP, and 10% (w/v) glycerol was concentrated to a final concentration of 30 $mg.mL^{-1}$, frozen in liquid nitrogen, and stored in aliquots at −80 °C (193.15 K).

3.2 Protein crystallization

3.2.1 Crystallization of binary 14-3-3:peptide complexes

14-3-3ζΔC or 14-3-3γΔC proteins and pepS100 or pepS511 peptides (sequences RKLpSLQER and RSLpSAPGN, respectively) were mixed in a 1:2 molar ratio. The buffer used was composed of 20 mM HEPES (pH 7), 2 mM $MgCl_2$ and 1 mM TCEP. Crystallization was performed using the hanging-drop vapor-diffusion method at 291 K. The crystals of the 14-3-3ζΔC:pepS100 peptide complex were grown in 2.5 µL drops of 16.2 $mg.mL^{-1}$ protein and 2.5 µL of 100 mM Tris-HCl (pH 7), 20.8% (*w*/*v*) PEG 2000 and 50 mM sodium fluoride. The crystals of the 14-3-3γΔC:pepS511 peptide complex were grown in drops of 1 µL of 16.5 $mg.mL^{-1}$ protein and 2 µL of 100 mM sodium citrate (pH 5.6), 200 mM potassium sodium tartrate, and 1.8 M ammonium sulfate. Crystals were cryoprotected by 30% (*v*/v) PEG 400 and then flash frozen in liquid nitrogen before data collection.

3.2.2 Crystallization of ternary 14-3-3:peptide:compound complexes

The ternary complex of 14-3-3 and CaMKK2 14-3-3 binding motif was prepared as fallows: 14–3–3γ protein and the pepS100 peptide (sequence RKLpSLQER) were mixed in a 1:2 molar ratio in buffer composed of 20 mM HEPES (pH 7), 2 mM $MgCl_2$, and 1 mM TCEP. Crystallization was performed using the hanging-drop vapor-diffusion method at 291 K, the 14–3–3γ:pepS100 binary complex's crystals were grown in drops of 2 µL of 16

mg mL^{-1} protein and 4 µL of 100 mM HEPES (pH 7.5), 200 mM $MgCl_2$, 32% (w/v) PEG400, and 1% (v/v) hexafluoro-propanol. Ternary complexe's crystals were obtained by soaking with 0.5 mM FC-A or 16-*O*-Me-FC-H for 3 h at 291 K. Soaked crystals were flashly frozen in liquid nitrogen.

3.3 Fluorescence polarization assay (FP assay)

3.3.1 FP assay with the binary 14-3-3 complexes

14-3-3γ (0-80 µM) was incubated for 1 h together with 100 nM of FAM (5-carboxyfluorescein)-conjugated synthetic peptides GSLSARKL(pS)LQER (FAM-CaMKK2-S100) or SRREERSLpSAPGN (FAM-CaMKK2-S511), where pS denotes phosphoserine, where a fluorofore, the fluorescein, was attached to the N-terminal part (Pepscan Presto BV, The Netherlands). Fluorescence polarization was recorded using a CLARIOstar microplate reader (BMG Labtech) in buffer composed of 10 mM HEPES (pH 7.4), 150 mM NaCl, 0.1% (*v*/v) Tween 20 and 0.1% (*w*/*v*) BSA. Excitation and emission wavelengths were 482 nm and 530 nm, respectively. To calculate the apparent K_D values of the peptide:14-3-3 interaction, the measured FP data were fitted to a one-site-binding model using OriginPro 2018b (OriginLab Corp. MA, USA).

3.3.2 FP assay with the ternary 14-3-3 complexes

14-3-3γ (0-80 µM) was incubated for 1 h together with 100 nM of FAM-CaMKK2-S100 or FAM-CaMKK2-S511 and 500 µM compound before the FP measurement. To determine the stabilization potency (EC_{50} values), a solution of 100 nM FAM-pepS100 and 20 µM 14-3-3 was titrated with the specific compound. To calculate K_D and EC_{50} values, the data were fitted to one-site-binding and dose-response models, respectively, using OriginPro 2018b (OriginLab Corp. MA, USA).

3.4 Thermal shift assay (TSA)

3.4.1 Sample preparation binary complex

Differential scanning fluorimetry (DSF) was performed using a LightCycler® 480 (Roche, Switzerland) on 96-well plates with samples containing 7 µM 14-3-3 in the pres-

ence or absence of each cocktail (2500 μM per fragment), in buffer containing 100 mM Hepes, pH 7.5, 150 mM NaCl and 4% (v/v) DMSO. The fluorescent probe SYPRO Orange (Sigma Aldrich) was included into the solution at a dilution of 1:600.

4 Results and Discussion

4.1 Structural and functional characterization of the interaction between 14-3-3 and human CaMKK2

Psenakova, K., Petrvalska, O., Kylarova, S., **Lentini Santo, D.,** Kalabova, D., Herman, P., Obsilova, V. & Obsil, T. 14-3-3 protein directly interacts with the kinase domain of calcium/calmodulin-dependent protein kinase kinase (CaMKK2). *Biochim. Biophys. Acta - Gen. Subj.* 1862, 1612–1625 (2018).

My contribution: Expression and purification of 14-3-3γΔC and 14-3-3ζΔC, evaluation of the phosphopeptide binding using the fluorescence polarization assay, crystallization and refinement of the 14-3-3γΔC:CaMKK2 pS100 and 14-3-3γΔC:CaMKK2 pS511 complexes.

4.1.1 Motivation of the study

Previous studies have shown that the kinase activity of CaMKKs is inhibited by PKA-mediated phosphorylation in a process involving the binding of the scaffolding 14-3-3 protein [96,97]. However, the exact role of the 14-3-3 protein binding in the inhibition of CaMKKs is elusive, mainly due to the lack of structural data. Moreover, the 14-3-3 proteins appear to be physiological inhibitors of CaMKKs, thus suggesting that the stabilization of PPIs between 14-3-3 and CaMKKs by small molecule compounds may be an alternative strategy in inhibiting these two kinases. Therefore, the main goal of this work was to perform the structural and biophysical characterization of interactions between 14-3-3 and CaMKK2.

4.1.2 Interactions between 14-3-3 and 14-3-3 binding motifs of CaMKK2

First, the interaction between 14-3-3γ (gamma isoform has been described as interaction partner of CaMKK1 [96,97] and phosphorylated CaMKK2 was characterized using analytical ultracentrifugation experiments. The data analysis showed that a dimer of 14-3-3γ is able to bind to CaMKK2 phosphorylated at Ser100 (CaMKK2-S^{100}) with an affinity of 1 ± 0.5 μM. On the other hand, the CaMKK2 phosphorylated at both Ser100 and Ser511 (Ser511 was phosphorylated only partially) (CaMKK2-$S^{100,511}$) can bind to 14-3-3γ protein with a higher affinity (K_D < 0.4 μM), indicating that the 14-3-3 binding site within the C-terminal segment, when phosphorylated, can enhance the complex stability.

To characterize interactions between 14-3-3 and both 14-3-3 binding motifs of

CaMKK2 at atomic level, two complexes between 14-3-3 and phosphopeptides representing the 14-3-3 binding motifs of CaMKK2 were crystallized. The 14-3-3ζΔC (without the highly flexible C-terminal loop) isoform was crystalized in the presence of the phosphopeptide containing the N-terminal CaMKK2-S^{100} 14-3-3 binding site, RKLpSLQER. The zeta isoform was used as we were unable to obtain well diffracting crystals of this complex with the gamma isoform. The 14-3-3γΔC isoform was crystalized with a phosphopeptide containing the C-terminal CaMKK2-S^{511} 14-3-3 binding site, RSLpSAPGN. Both structures were solved using molecular replacement using the structures of 14-3-3ζ (PDB ID: 4FJ3) and 14-3-3γ (PDB ID: 2B05) as search models, and refined at resolutions of 2.68 and 2.84 Å, respectively. Both structures revealed that phosphopeptides adopt within the 14-3-3 ligand binding groove extended conformations, which are highly similar to those observed in the other 14-3-3:phosphopeptide complexes. In detail, the phosphate moiety of $pSer^{100}$ in $pepS^{100}$ interacts with the side chains of 14-3-3ζ residues Lys^{49}, Arg^{56}, Arg^{127}, and Tyr^{128} ***(Fig. 4.1 A,B)***. The side-chain of the Glu residue at the +3 position with respect to $pSer^{100}$ is establishing a salt-bridge with the Lys^{120} of 14-3-3ζ protein. Interestingly, the side-chain of the Gln residue at +2 is makes hydrogen-bonds with the phosphate group and the main-chain carbonyl group of $pSer^{100}$. These interactions appear to change the direction of the phosphopeptide main chain, thus acting as the Pro residue, which is frequently located in 14-3-3 binding motifs at +2 position with respect to pSer/pThr [36]. As a result of that, the part of the 14-3-3 ligand binding groove, called fusicoccin binding cavity, stays empty, thus suggesting that this protein-protein interaction might be stabilized by small-molecule compounds ***(Fig. 4.1 F)*** [24].

In the case of the pS^{511} peptide, which possesses the canonical "mode I" 14-3-3 motif, the recognition of the $pSer^{511}$ and all other interactions ***(Fig. 4.1 C,D)*** are similar to those in other 14-3-3 complexes with peptides possessing the "mode I" motif [17,19].

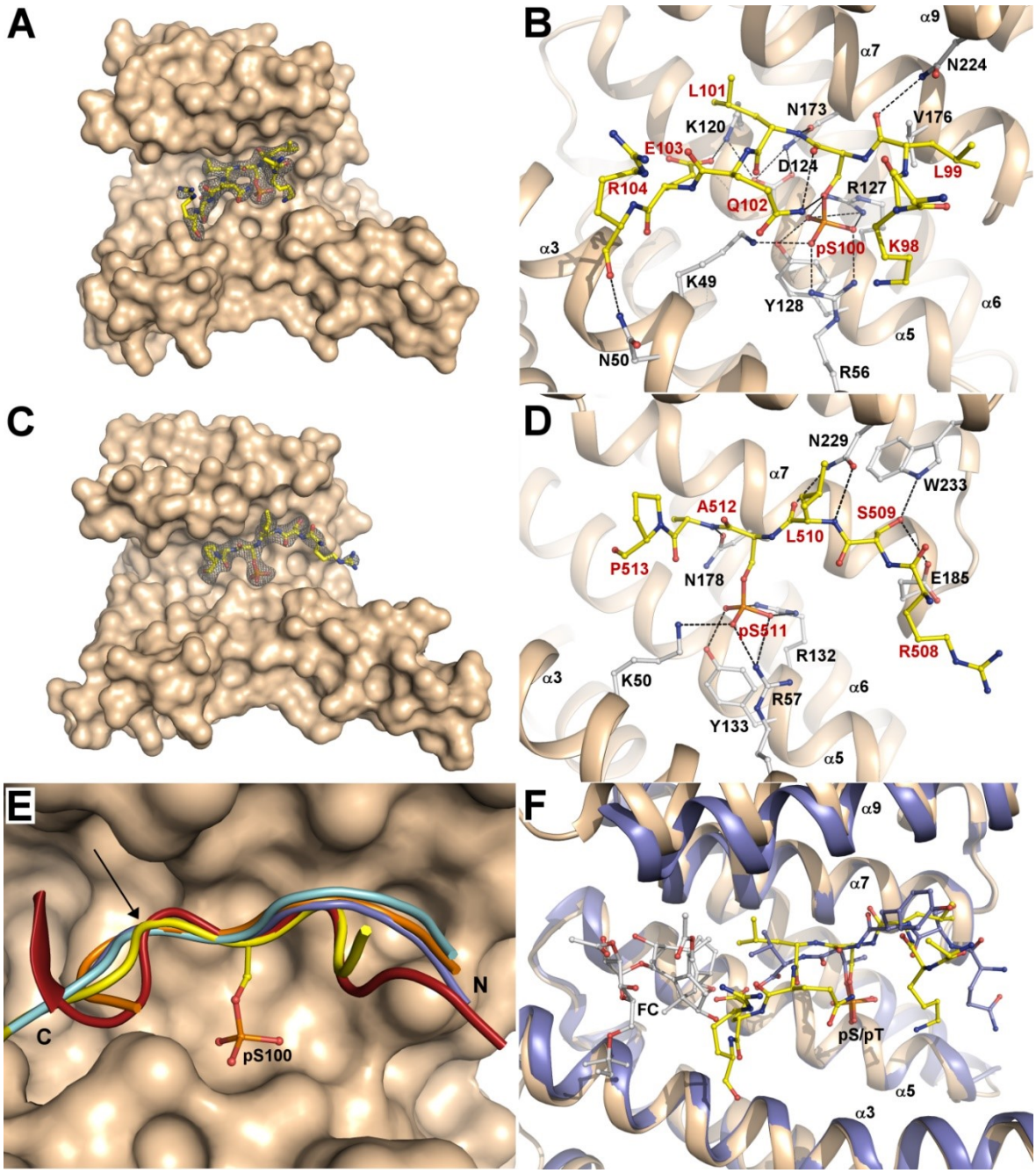

Fig. 4.1 Structural analysis of interactions between 14-3-3 and the 14-3-3 binding motifs of pCaMKK2. (A) Crystal structure of the 14-3-3ζ:pepS100 complex. The $2F_o$-F_c electron density map is shaped at 1σ. (B) In details contacts view between 14-3-3ζ and the $pepS^{100}$ peptide. The corresponding CaMKK2 residues are highlighted in red, and the 14-3-3ζ residues are highlighted in black. (C) Crystal structure of the 14-3-3γ:pepS511 complex. The $2F_o$-F_c electron density map is shaped at 1σ. (D) In details contacts view between 14-3-3γ and the pepS511 peptide. The CaMKK2 residues are highlighted in red, and the 14-3-3γ residues are highlighted in black. (E) Comparison of the main-chain conformation of pS^{100} (yellow) and pS^{511} (violet) peptides with a "mode 1" 14-3-3 peptide (sequence RSHpSYPA, PDB ID 1QJB, orange) [17], the 14-3-3 binding motifs of AANAT (sequence RRHpTLPA, PDB ID 1IB1, cyan) [33] and neutral trehalase Nth1 (sequence

TRRGpSEDDT, PDB ID 5N6N, red) [36]. The C-terminal portion of the 14-3-3 binding motifs is showed up with a black arrow. (F) Superimposition of the 14-3-3ζ:pepS^{100} complex (pepS100 is showed up in yellow) presenting a ternary complex which is a mix between the "mode 3" phosphopeptide resulted from the C-terminus of plant plasma membrane H^+-ATPase (sequence QSYpTV, blue), plant 14-3-3C and fusicoccin (FC, PDB ID 1O9F) [24].

4.1.3 14-3-3 protein directly interacts with the kinase domain of CaMKK2

Next, the interaction between the 14-3-3γ protein and CaMKK2 was investigated using small angle X-ray scattering (SAXS). CaMKK2 interacts with 14-3-3 through the N-terminal pSer^{100} motif (and potentially also through the C-terminal pSer^{511} motif when it is phosphorylated). However, it is unclear whether the other parts of CaMKK2, e.g. the kinase domain and/or CaM-binding region, are also involved in interactions with the 14-3-3 dimer (***Fig. 3.2***). Such contacts, if present, could explain the inhibitory effect of 14-3-3 binding on CaMKK activity. Therefore, SAXS measurements were performed to investigate the architecture of the 14-3-3γ:CaMKK2 complex.

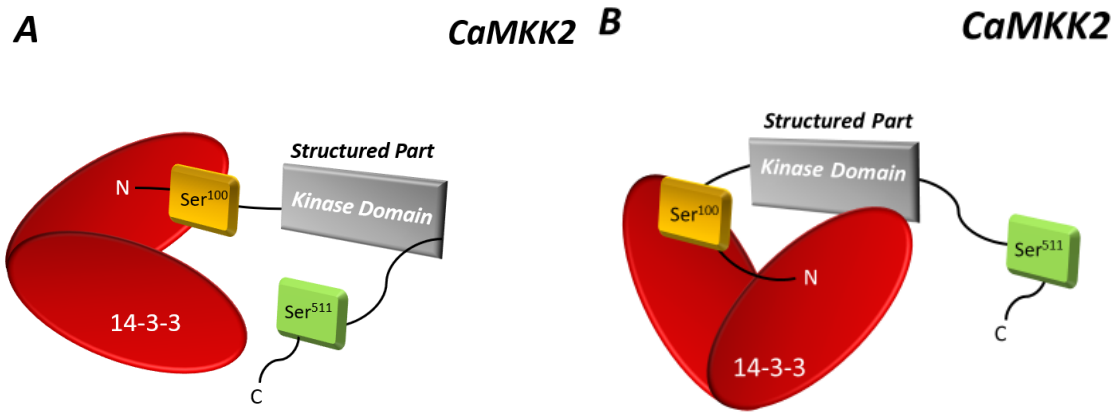

Fig. 4.2 Two possible architectures of the 14-3-3:CaMKK2 complex. (A) Extended arrangement in which the CaMKK2 is attached to 14-3-3 only through the N-terminal pSer100 motif and there are no additional contacts between 14-3-3 and other regions of CaMKK2. (B) Compact arrangement in which the CaMKK2 is attached to 14-3-3 through the N-terminal pSer100 motif and the kinase domain of CaMKK2 makes additional contacts with the 14-3-3 dimer.

Small angle X-ray scattering data were collected for 14-3-3γΔC and CaMKK2-S^{100} alone and for the complex between 14-3-3γΔC and CaMKK2-S^{100} and CaMKK2-S^{100,511} ***(Table 4.1 and Fig. 4.3 A)***. The absence of attractive inter-particle interactions in all samples was verified by the linear character of Guinier plots ***(Fig. 4.3 B)***. The prepared

complexes were sufficiently stable as the forward scattering intensity $I(0)$, the Porod volume V_p, and the radius of gyration R_g showed no significant concentration dependence ***(Table 4.1)***. $P(r)$ function for the 14-3-3γΔC dimer alone showed shorter inter-particle distances and a smaler maximum distance (D_{max}) compared to CaMKK2 alone and both complexes thus suggesting that CaMKK2 is a more extended molecule ***(Fig. 4.3 C)***. The dimensionless Kratky plot ($(sR_g)^2I(s)/I(0)$ versus sR_g) suggested the increased conformational heterogeneity of CaMKK2 and both complexes compared to 14-3-3γΔC alone ***(Fig. 4.3 D)***. In the case of the 14-3-3γΔC:CaMKK2-$S^{100-511}$ complex, the lower values of R_g and D_{max} indicate that this complex is more compact compared to that of CaMKK2-S^{100}.

Table 4.1 Structural parameters derived from SAXS data.

	c (mg·mL^{-1})	R_g (Å)[a]	R_g (Å)[b]	D_{max} (Å)	V_p[c] (nm^3)	M_w[d,f] (kDa)	M_w[e,f] (kDa)
14-3-3γΔC	3.0	28.7 ± 0.4	28.6 ± 0.4	89	77.8	54 ± 1	49
	1.5	29.0 ± 0.4	29.0 ± 0.4	89	82.8	55 ± 1	52
CaMKK2	2.8	32.6 ± 0.3	32.7 ± 0.3	126	95.6	48 ± 1	60
	2.1	32.1 ± 0.3	32.2 ± 0.3	125	94.0	46 ± 1	59
Complex (S^{100})	16.9	42.3 ± 0.6	42.4 ± 0.6	146	160.4	92 ± 1	100
	12.6	42.5 ± 0.6	42.6 ± 0.6	144	163.4	95 ± 1	102
	9.9	42.4 ± 0.6	42.5 ± 0.6	146	161.1	94 ± 1	101
Complex ($S^{100,511}$)	11.9	39.9 ± 0.7	40.0 ± 0.7	141	164.8	97 ± 1	103
	6.5	39.1 ± 0.6	39.2 ± 0.6	141	159.6	94 ± 1	100

[a]Calculated using Guinier approximation.

[b]Calculated using the program GNOM.

[c]The excluded volume of the hydrated particle (the Porod volume).

[d]Molecular weight estimated by comparing the forward scattering intensity $I(0)$ with that of the reference solution of bovine serum albumin.

[e]Molecular weight estimated from the Porod volume ($Mw \approx Vp \times 0.625$)[77].

[d]Theoretical molecular weights of the 14-3-3γΔC dimer, CaMKK2s and the CaMKK2:14-3-3γΔC complex with 2:1 stoichiometry are 54.3, 48.0 and 102.3 kDa, respectively.

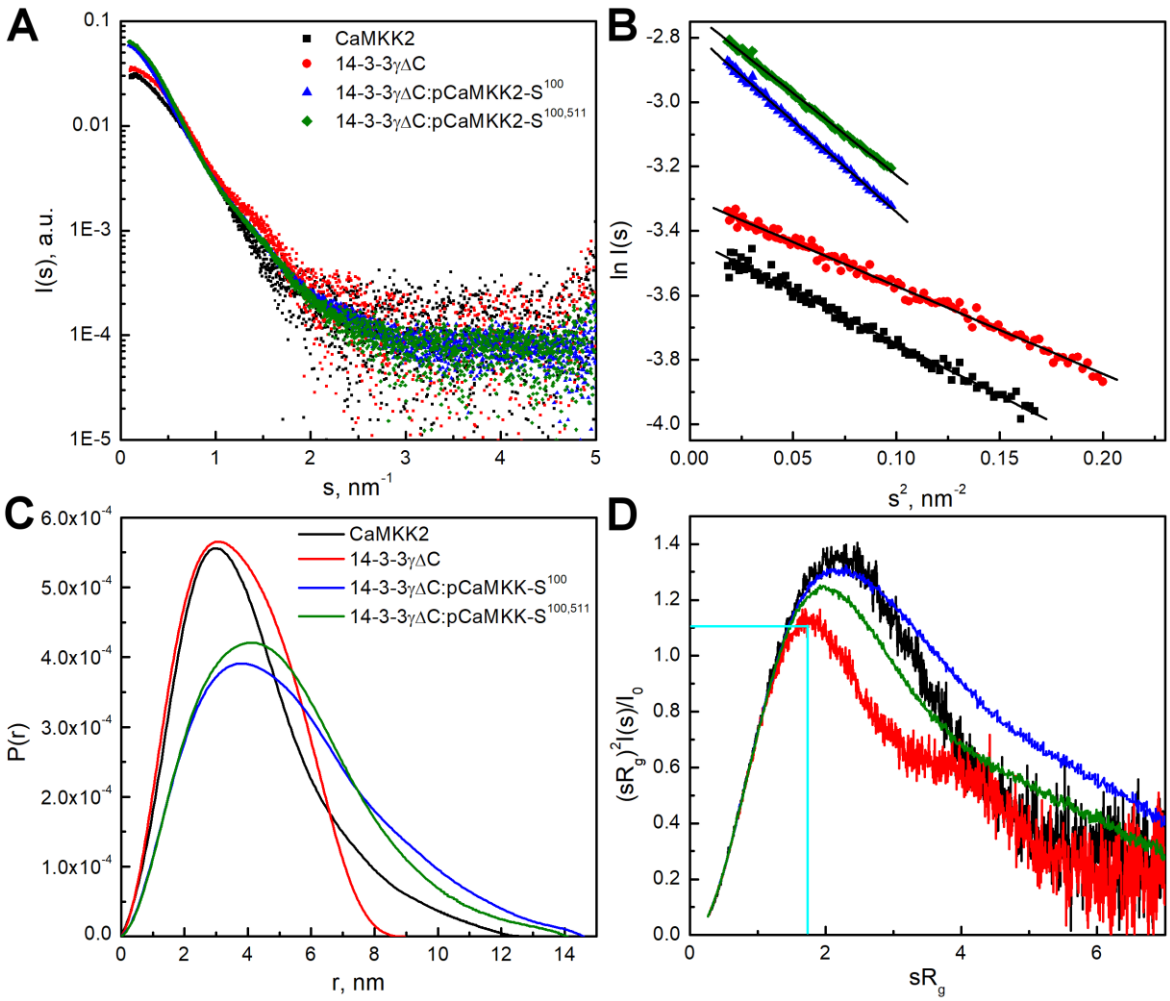

Fig. 4.3 SAXS analysis of the CaMKK2 alone and in complex with 14-3-3. A) Scattering intensity profiles of 14-3-3γΔC alone, CaMKK2-S^{100} alone, the 14-3-3γΔC:CaMKK2-S^{100} and the 14-3-3γΔC:CaMKK2-S^{100,511} complexes mixed at 2:1 molar stoichiometry ratio. B) Guinier plots for scattering curves from panel A). C) Distance distribution functions *P*(*r*) [100]. D) Dimensionless Kratky plots. Cyan line displays the compact globular protein's maximum [101].

Next, the low-resolution shape of the 14-3-3γΔC:CaMKK2-S^{100} complex was calculated using the MONSA program [102]. This approach was based on a multiphase modeling with an *ab initio* bead model, which consisted of two phases representing 14-3-3 and CaMKK2 within a low-resolution molecular envelope [103]. The obtained envelope revealed an asymmetric shape with the kinase domain attached to the side of the 14-3-3 dimer, instead of being located within the central channel of the 14-3-3 dimer **(*Fig. 4.4 A*)**. The rigid body modeling of the 14-3-3γΔC:CaMKK2-S^{100} complex was performed using the CORAL program [104]. For this purpose, the crystal structures of the 14-3-3γΔC (PDB ID: 2B05) and the CaMKK2 kinase domain (PDB ID: 2ZV2) were used and the missing flexible segments were modeled as chains of dummy residues. The resulting CORAL model of the complex also showed an asymmetric shape with the kinase domain interacting with 14-3-3γ outside

the central channel ***(Fig. 4.4 B)***. The SAXS curve calculated from the CORAL model fitted the experimental SAXS profile with χ^2 of 1.3. Therefore, the SAXS-based structural modeling indicated that CaMKK2-S^{100} binds to 14-3-3γ not only through the $pSer^{100}$-containing motif but also *via* the kinase domain.

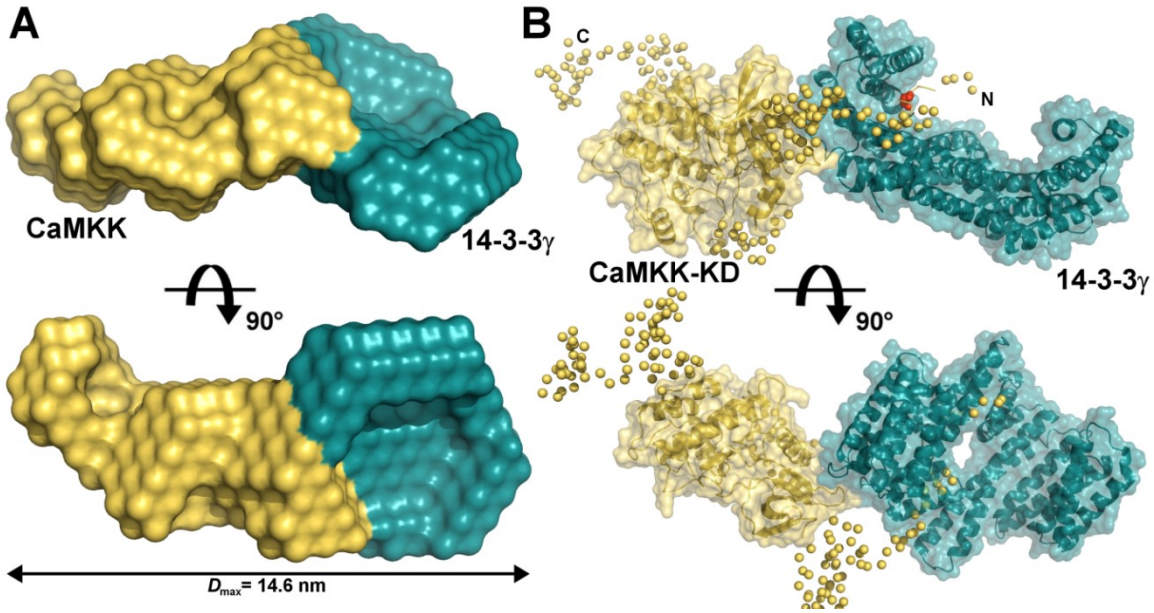

Fig. 4.4 Modeling of the 14-3-3γ:CaMKK2- S^{100} complex. A) The MONSA model of the complex. B) The CORAL model of the complex. The flexible parts of CaMKK2 missing in the crystal structure were modeled as chains of dummy residues. The Ser^{100} is highlighted in red.

4.1.4 14-3-3 binding does not affect the interaction between Ca^{2+}/CaM and CaMKK2

Next, we investigated whether the 14-3-3 protein binding affects the interaction between Ca^{2+}/CaM and CaMKK2. The CaMKK2 activity is triggered by the Ca^{2+}/CaM binding and the interference with this interaction might be another factor contributing to the 14-3-3-mediated regulation of CaMKK2. The binding of the dansyl-labeled CaM (dans-CaM) to CaMKK2 was studied in the absence and presence of 14-3-3γ using time-resolved fluorescence measurements. The summary of obtained data is listed in ***Table 4.2.***

Table 4.2 Summary of the time-resolved dans-CaM fluorescence measurements.

Sample	τ_{mean} [a,b] (ns)	K_{SV} [e] (M^{-1})	k_i ($\times 10^{-5}$) ($M^{-1}s^{-1}$) [f]	ϕ_1 [d] (ns)	β_1 [c]	ϕ_2 (ns)	β_2	ϕ_3 (ns)	β_3	ϕ_4 (ns)	β_4
Dansyl-CaM	15.2	0.18	120	< 0.1	0.03	0.6	0.02	2.5	0.10	9.3	0.12
+ 14-3-3γ	15.9	0.19	120	< 0.1	0.03	0.5	0.02	1.9	0.08	8.4	0.15
+ S^{100}	20.5	0.01	4			2.5	0.01	12	0.11	49	0.15
+ S^{100} + 14-3-3γ	20.5	0.00	0			3.0	0.01	11	0.10	49	0.16
+ $S^{100,511}$	20.6	0.01	3			4.7	0.03	16	0.10	52	0.15
+ $S^{100,511}$ + 14-3-3γ	20.2	0.11	53			2.8	0.02	12	0.08	88	0.16

[a]Mean lifetimes were calculated as $\tau mean = \Sigma_i f_i \tau_i$, where fi is an intensity fraction of the i-th lifetime component τ_i.

[b]S.D. value is ±0.1 ns.

[c]The anisotropies $r(t)$ were analyzed for a series of exponentials by a model-independent maximum entropy method.

[d]Fast unresolved component.

[e]Stern-Volmer constant of acrylamide quenching.

[f]Bimolecular quenching constant for acrylamide collisional quenching.

The fluorescence measurements revealed that the interaction between Ca^{2+}/CaM and CaMKK2 increased values of the mean excited-state lifetime (τ_{mean}) and the longest correlation time ϕ_4 of the dans-CaM. The 14-3-3γ binding did not cause any changes in the mobility of dans-CaM ***(Fig. 4.5 A)***. Conversely, the interaction between 14-3-3γ and CaMKK2-$S^{100,511}$ induced a shift of the anisotropy decay tail ***(Fig. 4.5 B)***, thus indicating that the binding of 14-3-3 does not affect the interaction between Ca^{2+}/CaM and CaMKK2.

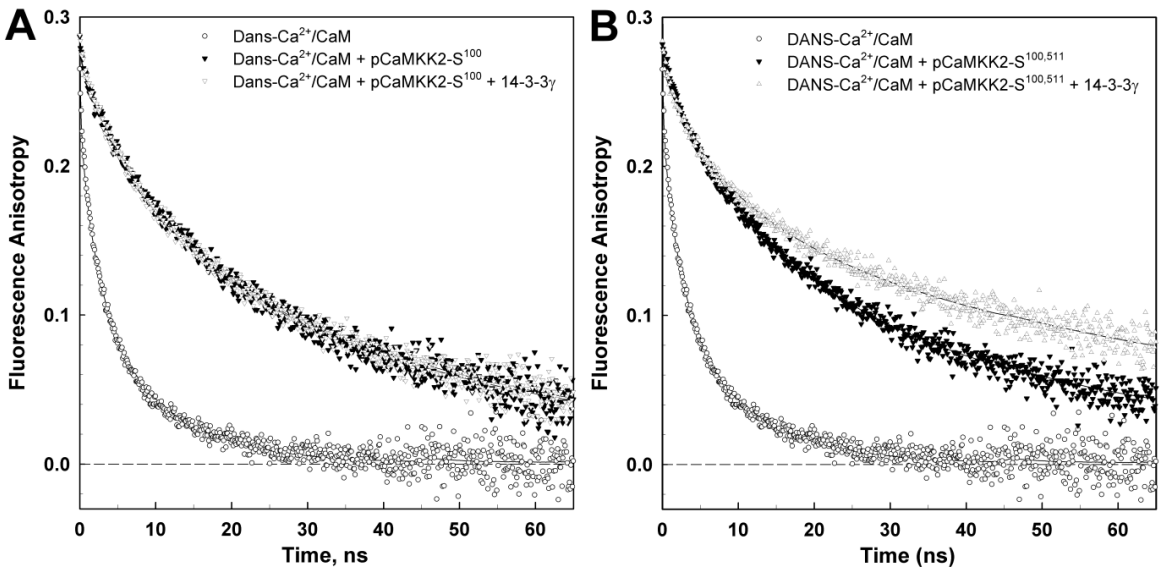

Fig. 4.5 Time-resolved dansyl fluorescence measurements. A) Fluorescence anisotropy decays of free dansyl-Ca^{2+}/CaM (o) in the presence of CaMKK2-S^{100} (▼), and in the presence of CaMKK2-S^{100} with 14-3-3γ (Δ). **B)** Fluorescence anisotropy decays of free dansyl-Ca^{2+}/CaM (o) in the

presence of CaMKK2-$^{100\text{-}511}$ (▼), and in the presence of CaMKK2-S $^{100\text{-}511}$ with 14-3-3 γ (Δ).

4.1.5 14-3-3 protein binding induces conformational changes of CaMKK2

To investigate whether CaMKK2 undergoes conformational changes upon the 14-3-3 binding, four mutants of CaMKK2 with single tryptophan residue located in different regions of CaMKK2 molecule (positions 140, 267, 374, 445) were designed and purified. The conformational behavior of CaMKK2 in the presence and absence of 14-3-3 was investigated using time-resolved fluorescence measurements with 14-3-3γ noW mutant, which contains no tryptophan residues [105].

Analyses of the tryptophan fluorescence data showed that the presence of 14-3-3γ noW induced an increase in τ_{mean} of Trp^{140} and Trp^{445} (***Fig. 4.6 and Table 4.3***). On the other hand, no significant changes were observed for mutants with Trp^{267} and Trp^{374}. The increase in τ_{mean} can be interpreted as a decrease in quenching interactions and/or polarity in the vicinity of Trp residue upon the 14-3-3γ binding. Next, segmental motions of inserted tryptophans were investigated using polarized fluorescence measurements. These experiments revealed small but significant increase in protein flexibility in regions surrounding Trp^{140} and Trp^{445} as judged from the sum of amplitudes of fast anisotropy decay components β_1 and β_2 (***Table 4.3***).

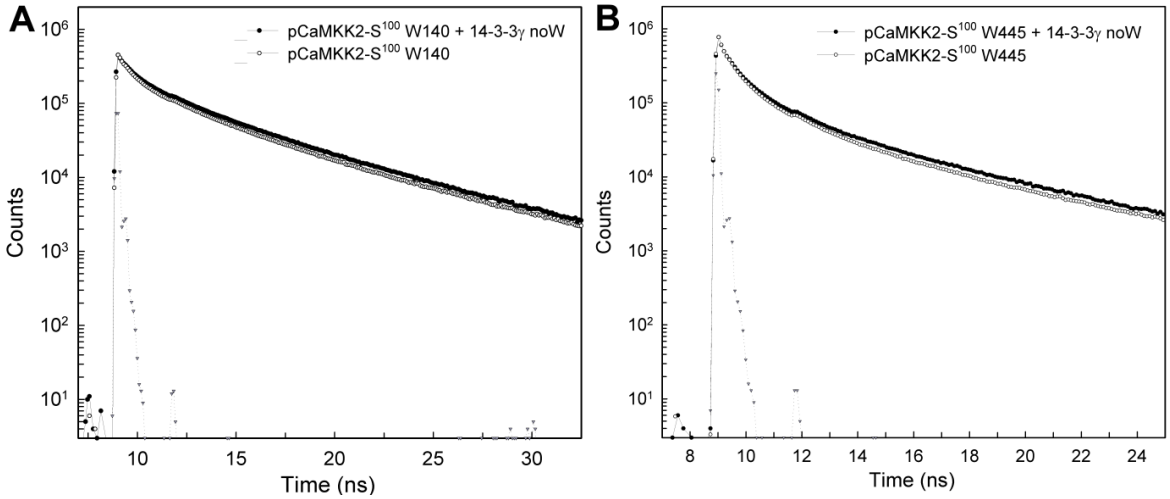

Fig. 4.6 Time-resolved tryptophan fluorescence measurements. A) Normalized fluorescence intensity decays of CaMKK2-S^{100} mutant characterized by single Trp^{140}, in the absence (o) and presence (●) of 14-3-3γ noW. The instrument response function is shown as triangles. B) Same as A) for the CaMKK2-S^{100} mutant characterized by single Trp^{445}.

Table 4.3 Summary of time-resolved tryptophan fluorescence measurements

pCaMKK-S[100] mutant	τ_{mean} [a,b] (ns)	ϕ_1 (ns)	β_1	ϕ_2 (ns)	β_2	ϕ_3 [c] (ns)	β_3
W140	4.19	1.4	0.037			72	0.170
W140 + 14-3-3γ noW	4.34	0.8	0.021	3.5	0.029	100	0.161
W267	4.88	0.9	0.014			53	0.200
W267 + 14-3-3γ noW	4.97	0.9	0.004	5.3	0.006	79	0.197
W445	2.47	2.3	0.026			84	0.184
W445 + 14-3-3γ noW	2.59	2.8	0.041			>100[d]	0.171
W374	4.39	0.9	0.004			44	0.205
W374 + 14-3-3γ noW	4.37	0.5	0.005			61	0.206

[a]Mean lifetimes were calculated as $\tau_{mean}=\Sigma_i f_i \tau_i$, where f_i is an intensity fraction of the *i-th* lifetime component τ_i.
[b]S.D. value is ± 0.05 ns.
[c]S.D. value is about ± 10ns
[d]Poorly resolved correlation time of the overall protein rotation; SD is highly asymmetric to longer values. The resolution is primarily limited by a short lifetime value.

4.1.6 Conclusions

Main goal of this study was to characterize the role of 14-3-3 binding in the regulation of CaMKK2. The AUC analysis showed that 14-3-3γ binds full-length CaMKK2 phosphorylated at Ser[100] with affinity in micromolar range. The presence of the secondary C-terminal 14-3-3 binding motif (Ser[511]) increased the stability of the complex. In contrast to CaMKK1, the catalytic activity of CaMKK2 is not inhibited by the 14-3-3 protein binding. Instead, the 14-3-3 protein appears to protect CaMKK2 against dephosphorylation, thus keeping the enzyme in its phosphorylation-dependent inhibited state. Structural analysis indicated that the interaction between 14-3-3 and the N-terminal 14-3-3 binding motif may be improved by small molecule compounds that target the fusicoccin binding site in the 14-3-3 ligand binding groove. SAXS-based analysis revealed that the 14-3-3:CaMKK2 complex is flexible and that the kinase domain of CaMKK2 is positioned outside the central channel of the 14-3-3γ dimer. In addition, the 14-3-3γ protein interacts with and affects the structure of various regions of CaMKK2 but without interfering with the Ca^{2+}/CaM binding to CaMKK2.

4.2 Biophysical characterization of the complex between 14-3-3 and the 14-3-3 binding motif of IκBα

Madita Wolter, **Domenico Lentini Santo**, Petr Herman, Alice Ballone, Federica Centorrino, Tomas Obsil and Christian Ottmann. Interaction of an IκBα peptide with 14-3-3. *ACS Omega* 5(10):5380-5388 (2020).

My contribution: Expression and purification of 14-3-3ζ noW for time-resolved tryptophan fluorescence measurements, sample preparation for tryptophan measurements.

4.2.1 Motivation of the study

The transcription factor NF-κB is a key regulator of the inflammatory response regulation and it has also been implicated in auto-immune diseases and cancer. The activation of NF-κB involves the phosphorylation of IκB at conserved Ser^{32} and Ser^{36}, which leads to the IκBα ubiquitination and its proteasomal degradation [77,78]. The export of the IκBα/p65 complex from the nucleus requires the interaction with the 14-3-3 protein [79] (***Fig. 4.7 A***). Although the complex formation between 14-3-3 and IκBα was demonstrated by co-immunoprecipitation, the structural details concerning the 14-3-3-mediated regulation of IκBα/p65 localization remain elusive.

The main goal of this work was biophysical and structural analysis of the complex between the 14-3-3 binding motif of IκBα and 14-3-3σ. The complex stability was investigated using fluorescence polarization assay and time-resolved tryptophan fluorescence. The structural characterization was performed by solving the crystal structure of the complex.

4.2.2 Sample preparation

14-3-3ζ noW was expressed and purified as reported previously [14]. To avoid any interference from inpurities during time-resolved tryptophan fluorescence measurements, only SEC-HPLC fractions without any detectable contaminants on SDS-PAGE gels were selected.

4.2.3 The IκBα 14-3-3 binding motif

The IκBα protein has only one canonical 14-3-3 binding motif, 57-PRGSEP-66. To elucidate the binding affinity of this motif for 14-3-3, the unphosphorylated (IκBαS63) and phosphorylated (IκBαpS63) binding motif peptides have been synthetized ***(Fig. 4.7 B).***

Both peptides were labeled at their N-termini with a fluorescein isothiocyanate (FITC) dye and their binding to all seven human 14-3-3 isoforms was investigated using fluorescence polarization (FP) ***(Fig. 4.7 C,D)***. These measurements showed no binding in the case of unphosphorylated peptide compared to the phosphorylated one, which displayed a weak binding to all 14-3-3 isoforms. The K_D values of 14-3-3/IκBαpS63 complexes are hypothetically in the range of high micromolar to millimolar and the best binding was detected for the 14-3-3η isoform ***(Fig. 4.7 D)***.

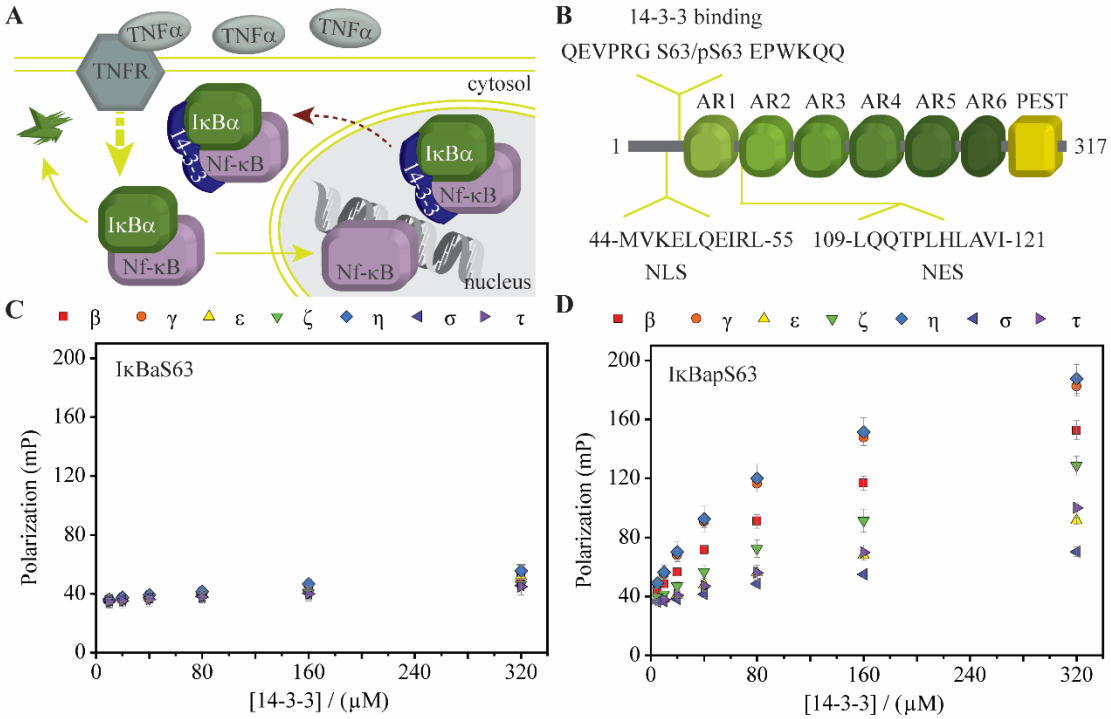

Fig. 4.7 Phosphorylated IκBα peptide binds to 14-3-3. A) The NF-κB pathway. Under inflammatory signal (through TNFα and its receptor TNFR), a cascade response (thick dashed arrow) guides IκBα to proteasomal degradation, thus NF-κB is translocated of into the nucleus. When 14-3-3 is bound to IκBα, NF-κB is essential for nuclear exportation or cytosolic preservation of IκBα/NF-κB complex (red dashed arrow). B) The IκBα protein is composed of an unstructured N-terminus, six helical ankyrin repeats and the PEST domain. 14-3-3 is predicted to bind to Ser^{63} at the unstructured N-terminal region. C) FP of IκBαS63 peptide with all human 14-3-3 isoforms. D) FP of IκBαpS63 peptide with all human 14-3-3 isoforms.

4.2.4 Crystal structure of IκBα-peptide with 14-3-3σΔC

All seven 14-3-3 isoforms were co-crystallized with the IκBαpS63 peptide. The best diffraction data (with the resolution of 1.13 Å) were collected for crystals of the IκBαpS63/14-3-3σΔC complex. Only 7 of 13 residues of IκBαpS63 were visible in the final electron density map ***(Fig. 4.8 A-B-C-D)***. Similarly as in other 14-3-3/phospho-peptide structures, 14-3-3 residues Arg^{56}, Arg^{129} and Tyr^{130} form polar contacts with the IκBαpS63 phosphate-group and the phosphoserine makes an additional polar contact with Lys^{67} of the peptide and Glu^{14} of the 14-3-3 protein ***(Fig. 4.8 E)***. Furthermore, contacts between the 14-3-3 protein and the IκBαpS63 peptide also involve several water-mediated contacts and a few hydrophobic interactions ***(Fig. 4.8 F)***.

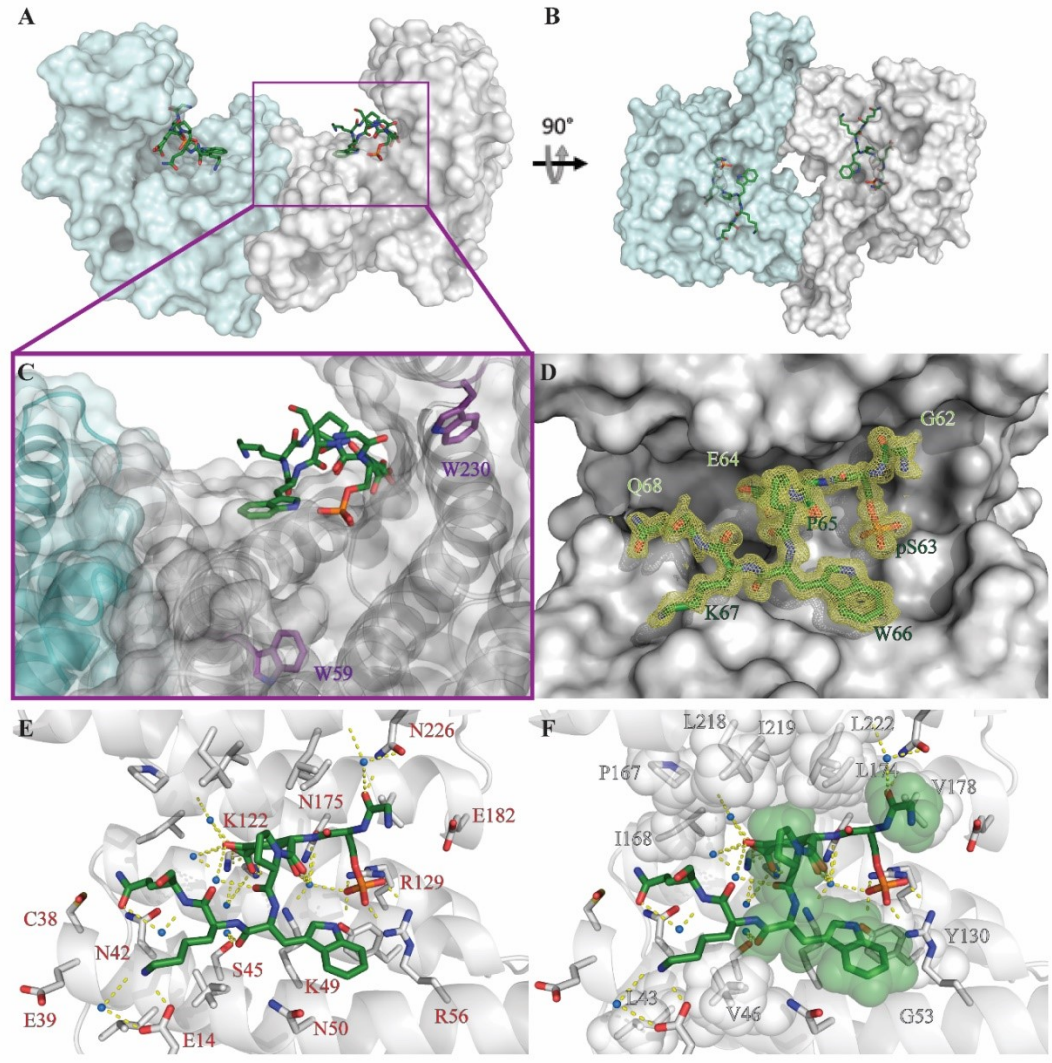

Fig. 4.8 Crystal structure of 14-3-3σΔC and IκBαpS63 peptide. Side A) and from the top B) surface representation of a 14-3-3 dimer with bound IκBαpS63 peptide (in green sticks) located within the binding cavity of each 14-3-3 protomer. C) A detailed view of transparent 14-3-3σ surface with the Trp^{59} and Trp^{230} residues highlighted in violet. D) 7 of 13 amino acid residues of the IκBαpS63

peptide with the final electron density map with (yellow mesh, σ = 1, carve = 1.3 Å). E) Polar contacts (shown as yellow dashed lines) between IκBαpS63, 14-3-3σΔC and the water molecules (blue spheres). F) Detailed view of hydrophobic interactions shown using sphere representation of hydrophobic residues.

4.2.5 Binding affinity measurements using tryptophan fluorescence lifetime

The crystal structure of the complex formed between 14-3-3σΔC and IκBαpS63 highlighted a wide-ranging of interactions between the IκBα Trp^{66} residue and the 14-3-3 binding groove with the indole portion lying in a non-polar environment. This binding mode indicated that τ_{mean} of Trp^{66} could be affected by complex formation and thus can be used to quantify the association without a synthetic fluorescence labeling. To distinguish fluorescence of the peptide from the Trp fluorescence of 14-3-3, we generated fluorescently silent 14-3-3ζ (designated as 14-3-3ζnoW) by mutating its two tryptophan residues Trp^{59} and Trp^{228} (equivalent to Trp^{59} and Trp^{230} in 14-3-3σ) to phenylalanine. Thus only the tryptophan fluorescence from the peptide could have been analyzed.

Time resolved fluorescence decays confirmed the IκBαpS63/14-3-3ζnoW complex formation by a significant increase in the Trp^{66} τ_{mean} upon the 14-3-3ζnoW addition ***(Fig. 4.9 A)***. Conversely, the unphosphorylated IκBαS63 exhibited much weaker affinity for 14-3-3ζnoW ***(Fig. 4.9 B)***. Thus, these measurements corroborated the polarization assay results and confirmed the phosphorylation-dependent interaction between IκBαS63 and 14-3-3.

The change of τ_{mean} was used to estimate the binding affinity of IκBαpS63 to 14-3-3ζnoW. Fitting the data using the 1:1 ratio binding model, the K_D value of 370±50 μM was obtained. To cross-validate this result, the FP assay was performed with 14-3-3ζnoW and both peptides. The FP as also revealed an incomplete saturation and the fitting indicated K_D values of ~380±1 μM and 415±30 μM for IκBα with 14-3-3ζWT and 14-3-3ζnoW, respectively ***(Fig. 4.9 D)***.

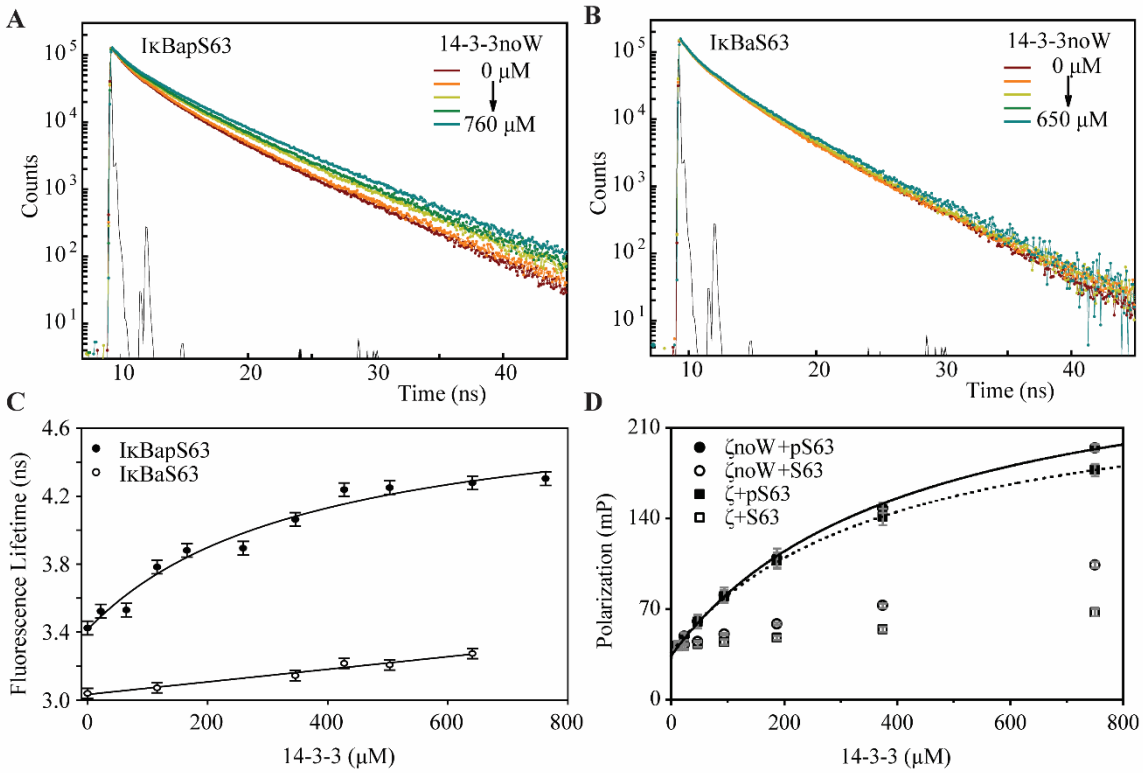

Fig. 4.9 Interaction between IκBα peptides and 14-3-3 analyzed by Trp^{66} fluorescence measurement. Panels A) and B) show peak-normalized fluorescence decays of IκBαpS63 and IκBαp63, respectively, with different 14-3-3ζnoW concentrations. C) τ_{mean} of IκBαS63 and IκBαpS63 as a function of the 14-3-3ζnoW concentration. D) FP assay using 14-3-3ζnoW and 14-3-3ζWT and FITC-labeled IκBαpS63 and IκBαS63.

4.2.6 Conclusion

This work was designed to extend our knowledge on the interaction between IκBα and 14-3-3. FP measurements with fluorescently labeled peptides clearly showed that the phosphorylation of the IκBα peptide is essential for its binding to 14-3-3. However, due to the low binding affinity we were unable to reliably determine the binding affinity. The low binding affinity of IκBαS63 indicates that the interaction between 14-3-3 and IκBα is likely mediated not only through Ser^{63}-containing motif but also a second still unidentified motif. The simultaneous presence of two binding motifs can dramatically increase the binding affinity as has been shown previously for several 14-3-3 binding partners [44,106].

The 14-3-3 amphipathic binding groove enables the presence of aromatic residues within the binding motifs ***(Fig. 4.8)***. Different structures have been reported for motifs containing aromatic residues at the -1 or +1 position with respect to the phosphorylated residue (***Fig. 4.10***) [24,107–109]. The IκBα tryptophan residue Trp^{66}, which is nicely visible in the electron density map, enabled direct biophysical affinity measurements without an

artificial probe. Both extrinsic and intrinsic fluorescence measurements gave similar results confirming the role of the IκBα phosphorylation in this low affinity interaction. Future research should be focused on finding the secondary 14-3-3 binding motif of IκBα and characterizing the role of 14-3-3 binding in the nuclear export mechanism of IκBα and p65 in detail.

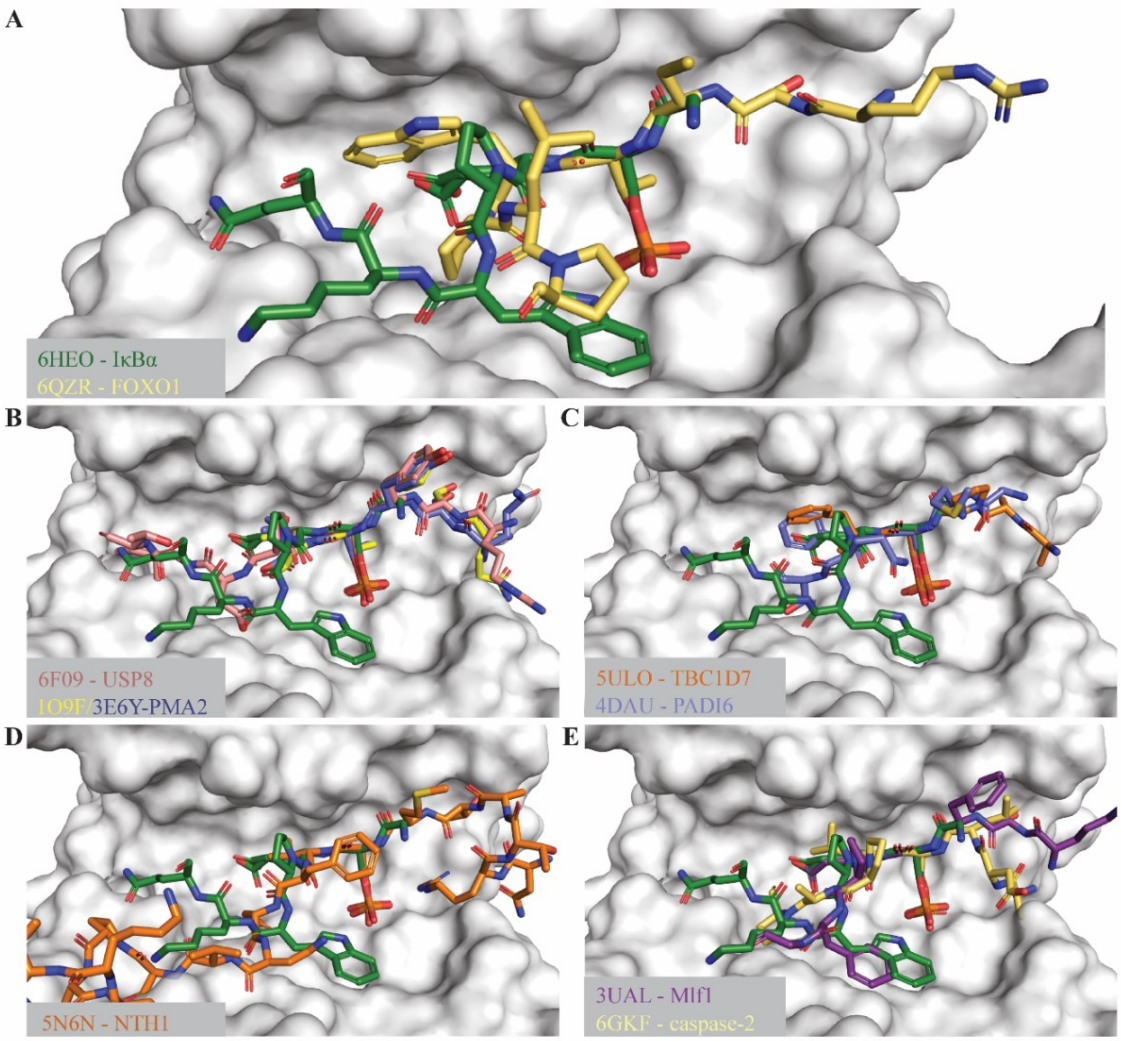

Fig. 4.10 Comparison of the IκBαpS63 binding motif with other 14-3-3 binding motifs. A) Comparison between the two 14-3-3 interaction motifs that host a tryptophan residue placed in the binding groove. All other binding motifs possess at least one aromatic residues at -1 position (B), +1 position (C), +2 position (D) or +3 position (E) compared to the phosphorylated residue. The IκBαpS63 peptide is shown as green sticks. Other peptides are shown as colored sticks.

4.3 Set-up and screening of a fragment library targeting the 14-3-3 protein interface

Dario Valenti, João Filipe Neves, François-Xavier Cantrelle, Stanimira Hristeva, **Domenico Lentini Santo**, Tomáš Obšil, Xavier Hanoulle, Laura M. Levy, Dimitrios Tzalis, Isabelle Landrieu, and Christian Ottmann. Set-up and screening of a fragment library targeting the 14-3-3 protein interface. *Medchemcomm* **10**(10):1796-1802 (2019).

My contribution: Evaluation of fragments using the thermal shift assay experiments.

4.3.1 Motivation of the study

Protein-protein interactions (PPIs) are considered as central for regulatory mechanisms in biological pathways and nowadays evolved as a captivating target for drug development. The scaffolding 14-3-3 proteins, which form complexes with a wide range of biologically interesting partner proteins, are thus considered as a very promising target for the drug development.

In this work, a fragment library screening was performed with the goal to identify fragments able to bing to the 14-3-3 sigma isoform. Nuclear magnetic resonance (NMR) spectroscopy and thermal shift assay (TSA) were used as main techniques. Identified fragments able to bind to 14-3-3 could be used as a starting point in the development of new compounds to interfere with PPIs of 14-3-3 proteins.

4.3.2 Sample preparation

14-3-3σ (for TSA experiments) or 14-3-3σΔC17 (cleaved after T231 – used for NMR experiments to improve the quality of spectra) were expressed and purified as described in [110].

4.3.3 How to set up a fragment screening

The aim of this study was to identify novel small-molecules that can be used as starting point in the development of new modulators (stabilizers or destabilizers) selective for 13-3-3σ interactions. To this end, we first prepared the appropriate fragment library using the collection of compound available at the Taros Company (Germany).

The selection of fragments was based on the Congreve's "Rule of Three" (Ro3) [111]. This is considered as one of the principal guidelines to identify molecules with appropriate physico-chemical properties. These features can be summarized as follows: molecular weight (MW) ≤ 300 Da, clogP ≤ 3 as well as the number of rotatable bonds and hydrogen-bond acceptors (HBAs) and donors (HBDs), Polar Surface Area (PSA) ≤ 60 $Å^2$. However, based on surfaces formed in 14-3-3 PPIs, we considered a higher tolerance regarding the selection of parameters. Thus, we used MW ≤ 330 Da, clogP ≤ 3.4, number of rotatable bonds ≤ 4 as well as HBAs and HBDs, and at last PSA ≤ 70 $Å^2$. Never then less, we also included highly attractive and chemically accessible structures to help the passage through the filtering phase, and a pre-filtering on the total Taros internal compounds collection (ca. 20000 entries) was performed by fixing a threshold of 350 Da for the MW.

The screening started from the Taros' small-molecules collection and after the two runs of physico-chemical properties filtering we ended up with a range of ca. 4000 compounds. Internal validation of all novel structures was performed, the numbers of entities decreased to 3200, which were further considered. The goal of this second step was to dismiss compounds which present unwanted structural properties.

The HPLC-MS was used to check all samples and, if required, purification by HPLC was enrolled. Through this workflow, we set up a library consisting of circa 900 entities. After adding newly designed fragments, the final number of compounds selected for screening was 1230 (***Fig. 4.11***).

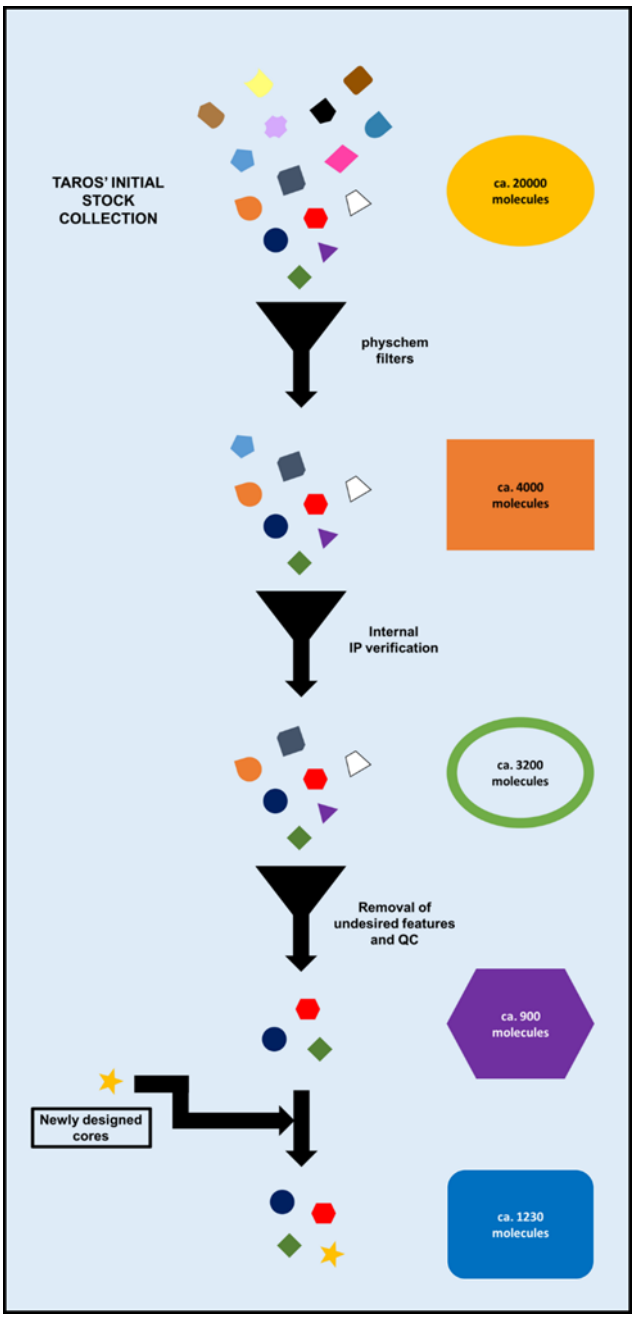

Fig. 4.11 Scheme applied to set up the Taros' PPIs fragment library.

4.3.4 Results and discussion

New compounds included into our library were derived from the nicotine ***(Fig. 4.12 a)***, a natural alkaloid almost unknown in drug discovery for its active ability on the cholinergic apparatus. This compound consists of one heteroaromatic ring (pyridine) linked to an aliphatic heterocycle (N-methylpyrrolidine) creating a chiral point with S-configuration. The *1,4-disubstituted triazoles* series ***(Fig. 4.12 c)*** enabled us to generate analogues where the link between the two rings is direct or mediated by one methylene. Moreover, it was possible to selectively generate the 1,4-regioisomer with good yields using the Cu-catalysed Huisgen cycloaddiction [112], with numerous terminal alkynes. We also decided to

add a third diversification point, which included *1,2,4-trisubstrituted triazoles* ***(Fig. 4.12 d)***.

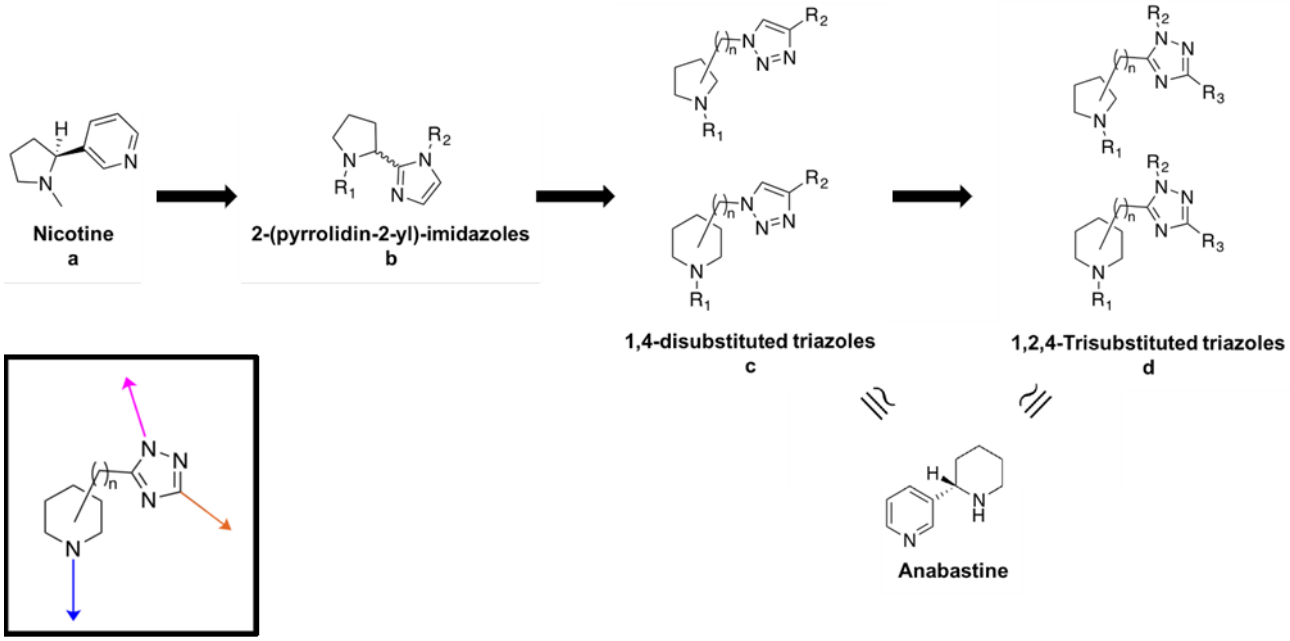

Fig. 4.12 New core's design example: Nicotine evolution (n between 0 and 3). In the black panel is heighted an example of BioCore (n between 0 and 3) where are displayed the changed points lay on different spatial vectors.

4.3.5 Fragment screening approach

Anoter selection approach thouth ChemAxon JChem for Excel (version 16.10.1700.1231) was used in order to selectivly reduse the numer of molecules considering Physico-chemical properties which helped to reach the final small-molecule entities based on 14-3-3 surface charateristics, from 1230 up to 785. Assembled in 157 cocktails of 5 compounds, a library of 785 small-molecules was screened to verify their binding to 14-3-3σ using TSA and NMR. TSA screening was applied on 156 out of the 157 cocktails. In addition, 102 cocktails were screened using WaterLOGSY NMR measurements and 55 cocktails using ^{1}H-^{15}N TROSY-HSQC experiments. ^{1}H-^{15}N TROSY-HSQC measurements were then used to characterize binding sites of compounds from cocktails identified by WaterLOGSY or TSA as containing potential binders. A diagram showing this screening approach is summarized in ***Fig. 4.13***.

4.3.6 Primary phase of the screening by WaterLOGSY

WaterLOGSY is a ligand-based NMR screening technique that enables the fast screening of small-molecule libraries characterized by the Nuclear Overhauser Effect (NOE)

(Dalvit, Fogliatto, Stewart, Veronesi, & Stockman, 2001). WaterLOGSY can be used for the first screening because requires small amount of protein, compared with protein-based NMR methods. WaterLOGSY was used for the 102 cocktails screening, which were not directly screened by ^{1}H-^{15}N TROSY-HSQC. The presence of binders was indicated for 43 out of the 102 cocktails, which were picked out for secondary screening by ^{1}H-^{15}N TROSY-HSQC.

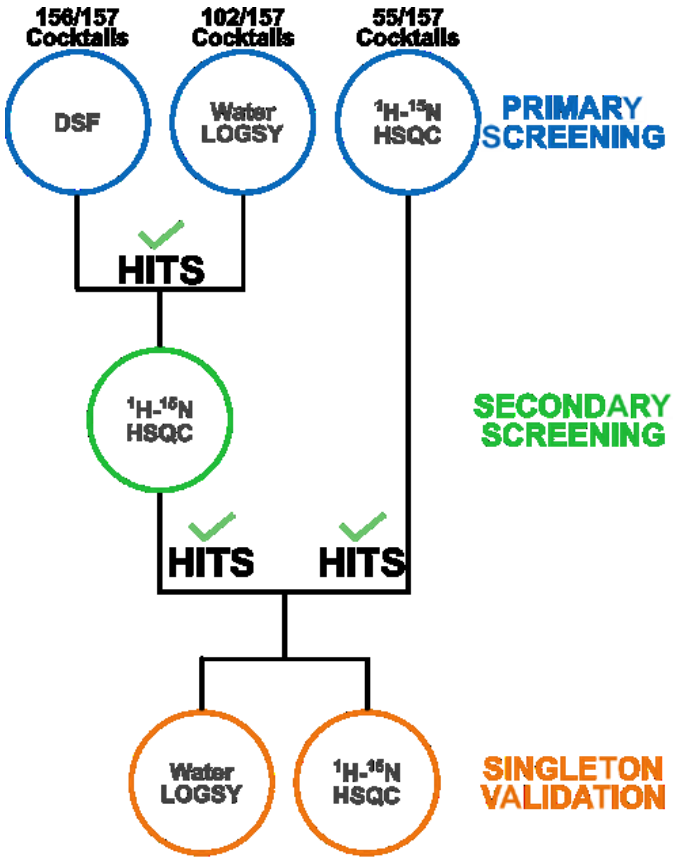

Fig. 4.13 Fragment screening summary scheme. TSA (also called DSF- Differential scanning fluorimetry, but in this thesis we will keep TSA as main acronym), Water LOGSY and ^{1}H-^{15}N TROSY-HSQC were used for primary screening. Secondary screening by ^{1}H-^{15}N TROSY-HSQC was chosen for the cocktails that highlighted binding by either TSA or WaterLOGSY. Instead, Water LOGSY and ^{1}H-^{15}N TROSY-HSQC for singleton validation were performed as final step.

4.3.7 Primary/secondary phase of the screening by ^{1}H-^{15}N TROSY-HSQC

^{1}H-^{15}N HSQC was used to screen of 55 out of 157 cocktails and as a secondary screening method for the 50 cocktails selected by WaterLOGSY (43), TSA (22) or both (15). Six cocktails showed strong effect on the ^{1}H-^{15}N TROSY-HSQC when 14-3-3σ was present.

All six cocktails were positive by WaterLOGSY, whereas four out of six were positive based on TSA.

At the final step, three fragments were confirmed as binders and further validated using both the ligand-based and the protein-based NMR methods. Two fragments interacted with the top of 14-3-3σ helices αH and αI and the binding site of the third fragment is located at the 14-3-3 dimer interface (***Fig. 4.14***).

4.3.8 Conclusions

The aim of this work was to prepare a fragment library and to identify fragments able to interact with 14-3-3σ. Three fragments were successfully identified, two interacting with the surface of helices αH and αI and the third one with the 14-3-3 dimer interface. Interestingly, both these sites are outside of the amphipathic ligand binding groove of 14-3-3σ. The surface of 14-3-3 helices αH and αI has been shown to be a common part of the binding interface in 14-3-3 complexes [33–35,37,113,114]. Therefore, fragments targeting this region outside the amphipathic binding groove may represent a promising opportunity to design and develop new compounds for selectively modulation of these PPIs.

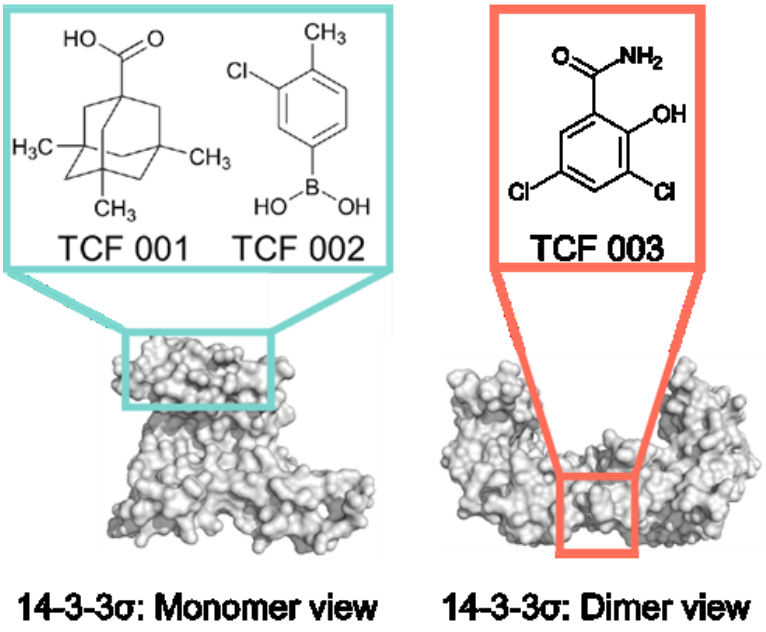

Fig. 4.14 Binding sites of identified fragments based on ^{1}H-^{15}N TROSY-HSQC. The 14-3-3σ crystal structure is shown as gray surface (PDB ID: 1YZ5). Fragments TCF 001 and TCF 002 caused chemical shift perturbations in resonances of residues from the top of helices αH and αI. Fragment TCF 003 induced chemical shift perturbations in resonances of residues located at the 14-3-3σ dimer interface.

4.4 Stabilization of protein-protein interactions between CaMKK2 and 14-3-3 by fusicoccanes

Domenico Lentini Santo, Olivia Petrvalska, Veronika Obsilova, Christian Ottmann, and Tomas Obsil. Stabilization of Protein-Protein Interactions between CaMKK2 and 14-3-3 by Fusicoccins. *ACS Chem. Biol.* **15**(11):3060-3071 (2020).

My contribution: Preparation of CaMKK2, 14-3-3γΔC and 14-3-3ξΔC, crystallization of ternary complexes, structure refinement, FP assay for K_D and IC_{50} determination.

4.4.1 Motivation of the study

Dysregulation of Ca^{2+}/calmodulin-dependent protein kinase kinase 2 (CaMKK2) is involved in several pathophysiological processes. CaMKK2 is inhibited through the phosphorylation and the interaction with 14-3-3 protein, which keeps CaMKK2 in the phosphorylation-dependent inhibited form. The previous work has suggested that the 14-3-3 protein binding to phosphorylated CaMKK2 might be improved by small-molecule compounds, which bind to the interface between the first 14-3-3 binding motif and the 14-3-3 ligand binding groove. Such stabilization might offer an alternative way of CaMKK2 inhibition. Therefore, in this work, we explored this possibility and studied the stabilization of the CaMKK2:14-3-3γ complex by Fusicoccin A and its analogues.

4.4.2 Sample preparation

Human 14-3-3γΔC and 14-3-3ξΔC were expressed and purified as described in [33]. Human CaMKK2 (residues 93-517) was expressed and purified as described in [89].

4.4.3 Fusicoccanes increase the stability of the complex between 14-3-3γ and the N-terminal 14-3-3 binding motif of CaMKK2

In [89] we showed that the $pSer^{100}$ 14-3-3-binding motif of CaMKKs bound to 14-3-3 adopts an unusual conformation. This, in turn, leaves portion of the 14-3-3 binding groove (so called fusicoccin binding site) empty. Therefore, we decided to study the stabilization of the 14-3-3:CaMKK complex by fusicoccin-like compounds.

For this purpose, five different fusicoccanes FC-A, FC-J, FC-THF, FC-H and 16-*O*-

Me-FC-H ***(Fig. 4.15 A)*** were tested. FC-A, FC-J, FC-H and 16-*O*-Me-FC-H are naturally produced compounds [115,116]. On the other hand, FC-THF was originally synthesized to specifically stabilize complexes between 14-3-3 and mode III 14-3-3 recognition motifs [26]. The capacity of fusicoccanes to interact with the 14-3-3γ:CaMKK2 $pSer^{100}$ complex was studied by FP with the $pSer^{100}$ motif-containing phosphopeptide labeled by 5-carboxyfluorescein (denoted as FAM-pepS100) ***(Fig. 4.15 B,C and Table 4.4)***.

FC-A improved the complex formation only negligibly and decreased the K_D value of FAM-pepS100 peptide from 25.5 ± 1 μM to 17.1 ± 0.5 μM at 500 μM concentration. On the other hand, other derivatives exhibited higher potency for the 14-3-3γ:FAM-pepS100 complex stabilization. The best stabilization effect was observed for FC-H and 16-*O*-Me-FC-H. These derivatives do not possess the hydroxyl group at the cyclopentene ring C and they were able to decrease the K_D of FAM-pepS100 for 14-3-3γ by factor 9.1 and 51, respectively. Moreover, the low stabilization potency observed for synthetic FC-THF confirmed that this derivative can selectively stabilize only the interaction between 14-3-3 and mode III binding sites [26].

Finally, the stabilization potency of two selected molecules (FC-A and 16-*O*-Me-FC-H) for the 14-3-3γ and the second 14-3-3 binding motif of CaMKK2 (sequence R^{508}SL-pS-AP^{513}) was characterized using the same approach ***(Fig. 4.15 D and Table 4.4)***. As expected, no evident stabilization was detected, and when FC-A was added, a destabilization has been observed. This is in line with the reported structure of the complex between CaMKK2 $pSer^{511}$ 14-3-3 binding motif and 14-3-3γ, which showed interactions typical for mode I motif [89].

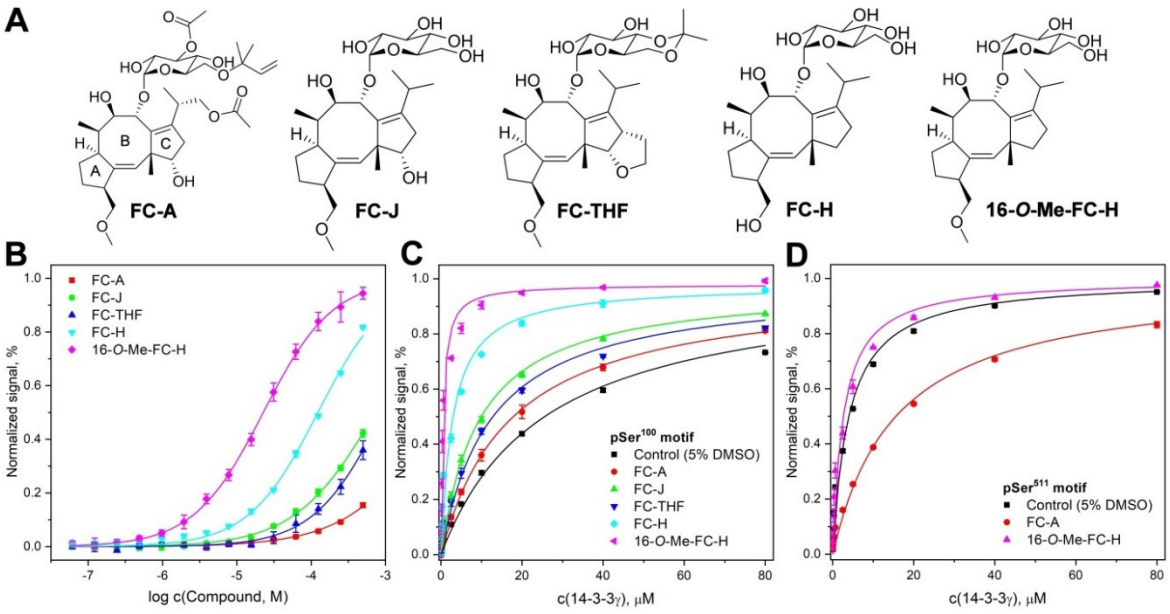

Fig. 4.15 Stabilization of the 14-3-3γ:CaMKK2 peptide complexes by fusicoccanes. A) Studied fusicoccanes. B) FP assay with the FAM-labeled pepS100 peptide (100 nM), 14-3-3γ (20 μM) and tested fusicoccanes. Data points are the means ± SD of three experiments. To get EC_{50} values, the FP data were fitted using the four-parameter dose-response function. C,D) FP of FAM-labeled pepS100 and pepS511 peptides in the presence of 500 μM of the study fusicoccanes titrated by 14-3-3γ. To obtain the apparent K_D values of the peptide:14-3-3γ interaction, the FP data were fitted considering one-site-binding model. Data points are set in means ± SD of triplicated measurements.

Table 4.4 Fusicoccanes stabilize interactions between CaMKK2 peptides and 14-3-3γ

Compound	EC_{50}, μM[1]	K_D, μM[2]	Factor[3]
FAM-pepS100 peptide			
Control (5% DMSO)	-	25.5 ± 1	-
FC-A	5600 ± 900	17.1 ± 0.5	1.5
FC-J	730 ± 30	9.5 ± 0.5	2.7
FC-THF	930 ± 50	12.3 ± 0.7	2.1
FC-H	123 ± 4	2.8 ± 0.3	9.1
16-*O*-Me-FC-H	23 ± 1	0.5 ± 0.05	51
FAM-pepS511 peptide			
Control (5% DMSO)		4.0 ± 0.4	-
FC-A		15.6 ± 0.9	0.25
16-*O*-Me-FC-H		2.6 ± 0.3	1.5

[1]The EC_{50} values were assessed by FP measurements of FAM-labeled pepS100 peptide (100 nM) and 14-3-3γ (20 μM) titrated with different fusicoccanes.

[2]The apparent K_D values of the interaction between the peptide and 14-3-3γ were determined by FP of FAM-labeled pepS100 and pepS511 peptides titrated with 14-3-3γ in the presence of the study

fusicoccanes (500 μM).

[3]Stabilization factor calculated from the apparent K_D values. Value lower than one express destabilization.

4.4.4 Structural insight into the stabilization potencies of fusicoccanes

Next, we crystallized and solved the structure of ternary complexes between 14-3-3γ, pSer[100] peptide (pepS100) and FC-A/16-*O*-Me-FC-H ***(Table 4.5)***. Both fusicoccanes bind to the same area of the 14-3-3 ligand binding cavity, formed by 14-3-3γ helices H3, H5, H7 and H9 (***Fig. 4.16***), interacting with 14-3-3γ mostly through hydrophobic contacts. The sugar moiety and the hydroxyl group of the B ring of FC-A interact with the 14-3-3γ residues Asn[43] and Asp[218]. Interestingly, no polar interactions between FC-A and the pepS100 were observed. On the other hand, the hydroxyl group at the ring C ***(labeled by an arrow in Fig. 4.16 C)*** is involved in a van der Waals interaction with Glu[103] from the C-terminus of the CaMKK2 peptide.

The binding pose of 16-*O*-Me-FC-H is identical to that of FC-A and the compound forms hydrogen bonds with the same 14-3-3γ residues ***(Fig. 4.16 D-F)***. In contrast to FC-A, 16-*O*-Me-FC-H, missing the hydroxyl group at the ring C, induces smaller shift (by ~0.6 Å) of the pepS100 peptide within the 14-3-3 ligand binding groove. This appears to be the reason of the considerable higher potency of 16-*O*-Me-FC-H to stabilize the interaction between the pepS100 and 14-3-3γ compared to FC-A.

Table 4.5 Crystallographic data collection and refinement statistic

Complex	14-3-3γ:pepS100:FC-A (6Y4K)	14-3-3γ:pepS100:16-*O*-Me-FC-H (6Y6B)
Wavelength (Å)	0.9184	0.9184
Space group	P6(3)22	P6(3)22
Unit-cell parameters		
a, *b*, *c* (Å)	225.85 225.85 72.96	226.27 226.27 72.99
α, β, γ (°)	90.0 90.0 120.0	90.0 90.0 120.0
Asymmetric unit contents	One dimer of 14-3-3γ with bound phosphopeptides and one molecule of FC-A	One dimer of 14-3-3γ with bound phosphopeptides and one molecule of 16-*O*-Me-FC-H
Resolution range (Å)[a]	48.62 - 3.00 (3.18 - 3.00)	48.99 - 3.08 (3.26 - 3.08)
Unique reflections	22485 (3562)	20904 (3285)
Data multiplicity	21.83 (21.01)	21.72 (22.04)
Completeness (%)	99.8 (99.8)	99.9 (99.7)
$\langle I/\sigma(I)\rangle$	18.91 (1.01)	11.53 (0.69)
R_{meas}[b]	16.5% (304.8%)	28.0% (497.0%)
R_{work}	0.2599 (0.3913)	0.2419 (0.4011)
R_{free}[c]	0.2920 (0.4308)	0.2815 (0.4272)
No. of protein atoms	3482	3634
No. of ligand atoms	48	35
No. of waters	0	0
Average B factors (Å^2)		
Protein	105.53	113.84
Ligand	121.97	119.89
R.m.s.[d] deviations from ideal values		
Bond lengths (Å)	0.003	0.001
Bond angles (°)	0.59	0.36
Ramachandran favored (%)	96.11	99.13
Ramachandran allowed (%)	3.89	0.87
Ramachandran outliers (%)	0	0

[a]Values in parentheses are for the highest resolution shell.

[b]$R_{meas} = \sum_{hkl}\{N(hkl)/[N(hkl)-1]\}^{1/2} \times \sum_{i}\left|I_i(hkl)-\langle I(hkl)\rangle\right| / \sum_{hkl}\sum_{i} I_i(hkl)$, where $I(hkl)$ is the intensity of reflection hkl, $\langle I(hkl)\rangle = \frac{1}{N(hkl)}\sum_i I_i(hkl)$, and $N(hkl)$ the multiplicity.

[c]The free *R* value (R_{free}) was calculated using 5% of the reflections, which were omitted from the refinement.

[d]R.m.s., root mean square.

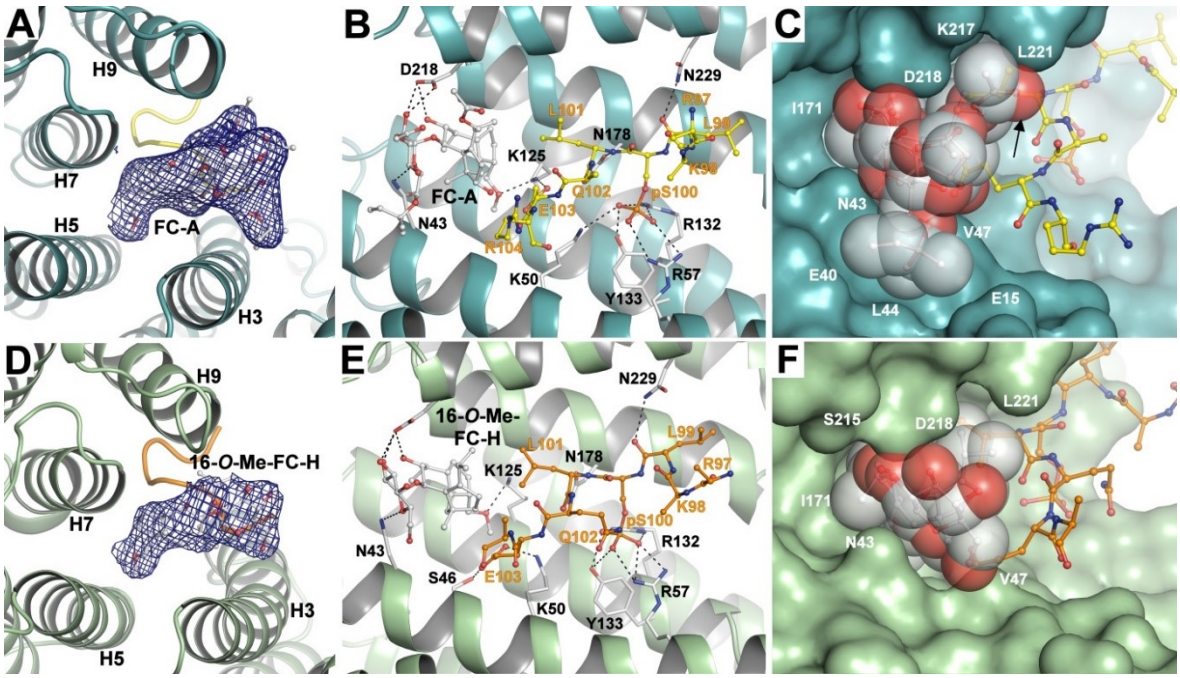

Fig. 4.16 Structure of complexes between 14-3-3γ, the pepS100 peptide and FC-A/16-*O*-Me-FC-H. A) FC-A bound to 14-3-3γ. The 14-3-3γ and the pepS100 peptide are shown in dark cyan and yellow, respectively. The final $2F_O$-F_C electron density map is contoured at 0.7σ. B) Contacts between 14-3-3ζ, the pepS100 peptide and FC-A. Polar interactions are shown as black dotted lines. C) The FC-A binding site. The 14-3-3 ligand binding groove is shown as dark cyan surface, the pepS100 peptide as yellow sticks and FC-A as spheres. The hydroxyl group at the ring C of FC-A is shown by a black arrow. D) 16-*O*-Me-FC-H bound within the 14-3-3γ ligand binding groove. The $2F_O$-F_C electron density map is contoured at 0.7σ. E) Interactions between 14-3-3ζ, the pepS100 peptide and 16-*O*-Me-FC-H. Polar interactions are highlighted by black dotted lines. F) The 16-*O*-Me-FC-H binding site. The 14-3-3 is shown as green surface, the pepS100 peptide as orange sticks and 16-*O*-Me-FC-H as spheres.

4.4.5 Fusicoccanes stabilize the complex between full-length CaMKK2 and 14-3-3γ

Next, the effect of FC-A and 16-*O*-Me-FC-H on the dpCaMKK2 binding to 14-3-3γ was investigated by SV-AUC. These experiments revealed that dpCaMKK2 and 14-3-3γ interact with an apparent K_D of 130 ± 20 nM ***(left panel in Fig. 4.17 A)***. Then, the same measurements were done with 500 µM FC-A and 16-*O*-Me-FC-H. The obtained s_w isotherms and $c(s)$ distributions are shown in ***Fig. 4.17 B,C***. These data showed that 16-*O*-Me-FC-H reduced the K_D value by a factor ~4 ***(Fig. 4.17 C)***, whereas FC-A destabilized the dpCaMKK2:14-3-3γ complex ***(Fig. 4.17 B)***.

This corroborated the FP results and revealed that 16-*O*-Me-FC-H improves the interaction between the full-length dpCaMKK2 and 14-3-3γ.

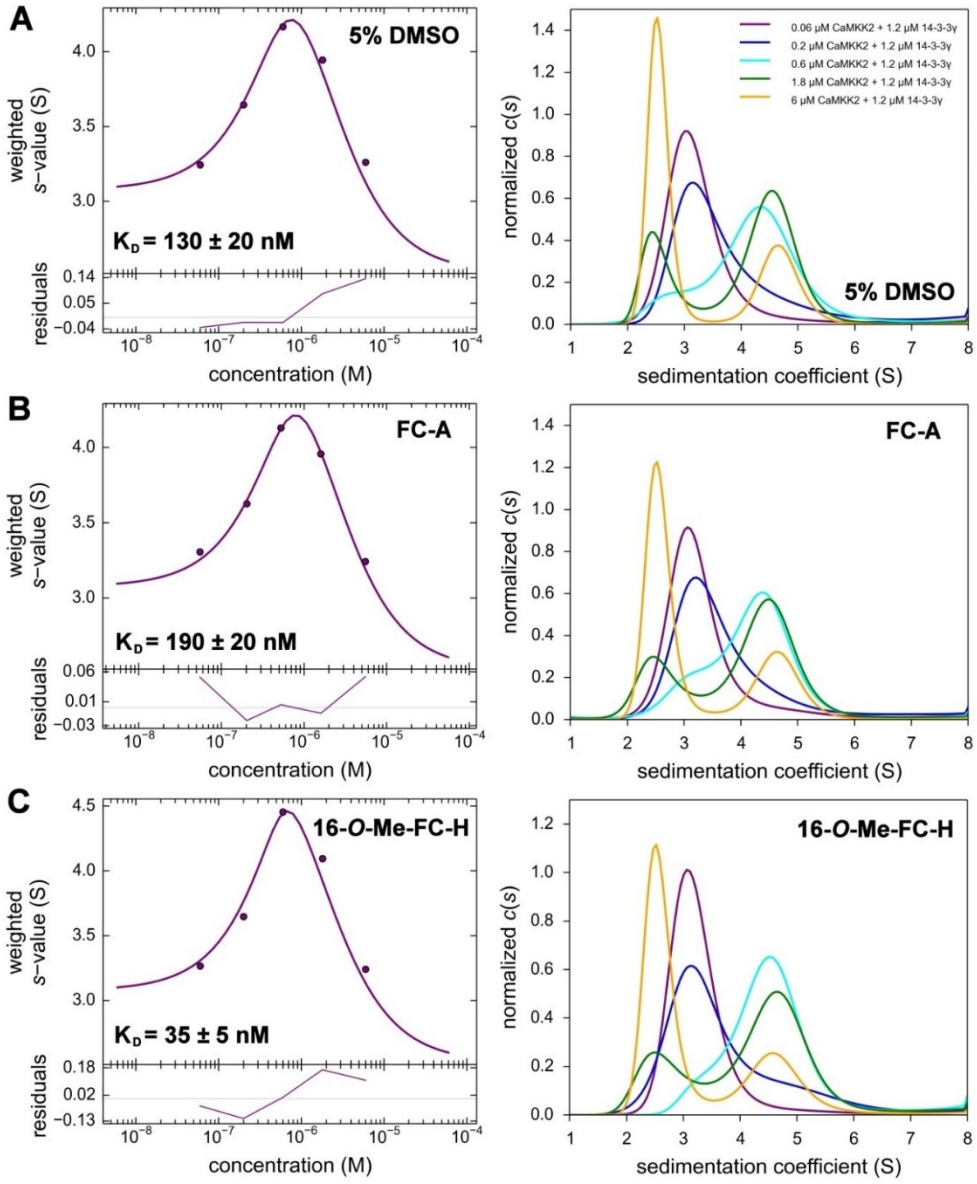

Fig. 4.17 Characterization of the dpCaMKK2:14-3-3γ complex by SV-AUC. A) 14-3-3γ and dpCaMKK2 in the presence of 5% DMSO. B) 14-3-3γ and dpCaMKK2 in the presence of 500 µM FC-A. C) 14-3-3γ and dpCaMKK2 in the presence of 500 µM 16-*O*-Me-FC-H. Isotherms of s_w were obtained by analyzing samples of 1.2 µM 14-3-3γ with 0.06–6 µM dpCaMKK2. The c(s) distributions underlying the s_w data points are displayed on the right.

4.4.6 Conclusion

In this work, we have shown that interactions between CaMKK2 and 14-3-3γ can be improved by selected fusicoccanes, which fill a gap in the binding interface. Differences in stabilization potency of tested compounds were caused by the contacts between the C-terminus of the 14-3-3 binding motif and the ring C of fusicoccane molecules. This provides foundations for the future design of more potent and specific stabilizers.

The two 14-3-3 binding motifs of CaMKK2 border the kinase domain and the motif within the N-terminal part acts as the main 14-3-3 binding site [89,96,97]. When both motifs are phosphorylated, CaMKK2 binds to 14-3-3γ with a significantly higher binding affinity compared to the form possessing only the N-terminal motif, thus suggesting that the C-terminal motif plays an important role in the stability of the CaMKK2:14-3-3γ complex. However, our data showed that only the N-terminal (pSer100) motif can be stabilized by fusicoccanes, whereas the binding of the C-terminal motif was either unaffected or even destabilized. Thus, this complex is a nice example demonstrating that the understanding of structural differences between various 14-3-3 binding motifs within one client protein is necessary for the development of small molecule stabilizers, where the specificity for a selected motif may be crucial for the overall stabilization potency.

5 Conclusions

The main aim of this doctoral thesis was to structurally characterize selected 14-3-3 protein complexes and investigate their stabilization by small molecule compounds using various biophysical approaches including protein crystallography, NMR, fluorescence polarization assay, thermal shift assay and time-resolved fluorescence spectroscopy.

1. Structural analysis of complexes between phosphopeptides containing both 14-3-3 binding motifs of CaMKK2 and 14-3-3 has been performed. Obtained results indicated that the interaction between 14-3-3 and the N-terminal 14-3-3 binding motif may be stabilized by small molecule compounds.
2. The interactions between phosphorylated CaMKK2 and 14-3-3γ can be stabilized by fusicoccanes, which fill a gap in the binding interface. Differences in stabilization potency of tested compounds were caused by the steric contacts between the groups decorating the ring C of fusicoccane molecules and the C-terminal part of the 14-3-3 binding motif.
3. The biophysical and structural analysis of interaction between the IκBα 14-3-3 binding motif and 14-3-3 has been performed. Obtained data revealed that this interaction is very weak, thus suggesting that the IκBα binding to 14-3-3 requires a second still unidentified motif. In addition, tryptophan residue Trp66 from the 14-3-3 binding motif of IκBα enabled direct biophysical affinity measurements without an artificial probe.
4. Three fragments able to interact with 14-3-3σ were identified. Two of them interact with the surface of helices αH and αI of 14-3-3 and the third one with the 14-3-3 dimer interface. Both these sites are outside of the amphipathic ligand binding groove of 14-3-3σ. Because the surface of 14-3-3 helices αH and αI is a common part of the binding interface in 14-3-3 complexes, fragments which bind to this region outside of the ligand binding groove may represent a promising opportunity to develop new compounds for selectively modulation of 14-3-3 PPIs.

6 References

1. Cohen, J. The immunopathogenesis of sepsis. *Nature* vol. 420 885–891 (2002).
2. Yaffe, M. B. & Elia, A. E. H. Phosphoserine/threonine-binding domains. *Curr. Opin. Cell Biol.* vol. 13 131–138 (2001).
3. Grasso, A., Roda, G., Hogue-Angeletti, R. A., Moore, B. W. & Perez, V. J. Preparation and properties of the brain specific protein 14-3-2. *Brain Res.* **124**, 497–507 (1977).
4. Wang, W. & Shakes, D. C. Molecular evolution of the 14-3-3 protein family. *J. Mol. Evol.* **43**, 384–398 (1996).
5. Rosenquist, M., Alsterfjord, M., Larsson, C. & Sommarin, M. Data mining the Arabidopsis genome reveals fifteen 14-3-3 genes. Expression is demonstrated for two out of five novel genes. *Plant Physiol.* **127**, 142–149 (2001).
6. Wilkert, E. W., Grant, R. A., Artim, S. C. & Yaffe, M. B. A structural basis for 14-3-3σ functional specificity. *J. Biol. Chem.* **280**, 18891–18898 (2005).
7. Gardino, A. K., Smerdon, S. J. & Yaffe, M. B. Structural determinants of 14-3-3 binding specificities and regulation of subcellular localization of 14-3-3-ligand complexes: A comparison of the X-ray crystal structures of all human 14-3-3 isoforms. *Semin. Cancer Biol.* **16**, 173–182 (2006).
8. Muslin, A. J., Tanner, J. W., Allen, P. M. & Shaw, A. S. Interaction of 14-3-3 with signaling proteins is mediated by the recognition of phosphoserine. *Cell* **84**, 889–897 (1996).
9. Pozuelo Rubio, M. *et al.* 14-3-3-Affinity purification of over 200 human phosphoproteins reveals new links to regulation of cellular metabolism, proliferation and trafficking. *Biochem. J.* **379**, 395–408 (2004).
10. Liu, D. *et al.* Crystal structure of the zeta isoform of the 14-3-3 protein. *Nature* **376**, 191–194 (1995).
11. Xiao, B. *et al.* Structure of a 14-3-3 protein and implications for coordination of multiple signalling pathways. *Nature* **376**, 188–191 (1995).
12. Yang, X. *et al.* Structural basis for protein-protein interactions in the 14-3-3 protein family. *Proc. Natl. Acad. Sci. U. S. A.* **103**, 17237–17242 (2006).
13. Verdoodt, B., Benzinger, A., Popowicz, G. M., Holak, T. A. & Hermeking, H. Characterization of 14-3-3sigma dimerization determinants: Requirement of homodimerization for inhibition of cell proliferation. *Cell Cycle* **5**, 2920–2926 (2006).

14. Obsilova, V. *et al.* 14-3-3ζ C-terminal Stretch Changes Its Conformation upon Ligand Binding and Phosphorylation at Thr232. *J. Biol. Chem.* **279**, 4531–4540 (2004).
15. Silhan, J. *et al.* 14-3-3 Protein C-terminal stretch occupies ligand binding groove and is displaced by phosphopeptide binding. *J. Biol. Chem.* **279**, 49113–49119 (2004).
16. Truong, A. B., Masters, S. C., Yang, H. & Fu, H. Role of the 14-3-3 C-terminal loop in ligand interaction. *Proteins Struct. Funct. Genet.* **49**, 321–325 (2002).
17. Rittinger, K. *et al.* Structural analysis of 14-3-3 phosphopeptide complexes identifies a dual role for the nuclear export signal of 14-3-3 in ligand binding. *Mol. Cell* **4**, 153–166 (1999).
18. Obsil, T. & Obsilova, V. Structural basis of 14-3-3 protein functions. *Semin. Cell Dev. Biol.* **22**, 663–672 (2011).
19. Yaffe, M. B. *et al.* The structural basis for 14-3-3:phosphopeptide binding specificity. *Cell* **91**, 961–971 (1997).
20. Coblitz, B., Wu, M., Shikano, S. & Li, M. C-terminal binding: An expanded repertoire and function of 14-3-3 proteins. *FEBS Letters* vol. 580 1531–1535 (2006).
21. Johnson, C. *et al.* Bioinformatic and experimental survey of 14-3-3-binding sites. *Biochem. J.* **427**, 69–78 (2010).
22. Petosa, C. *et al.* 14-3-3ζ binds a phosphorylated raf peptide and an unphosphorylated peptide via its conserved amphiphatic groove. *J. Biol. Chem.* **273**, 16305–16310 (1998).
23. Lentini Santo, D., Petrvalska, O., Obsilova, V., Ottmann, C. & Obsil, T. Stabilization of protein−protein interactions between CaMKK2 and 14−3−3 by fusicoccins. *ACS Chem. Biol.* **15**, 3060–3071 (2020).
24. Würtele, M., Jelich-Ottmann, C., Wittinghofer, A. & Oecking, C. Structural view of a fungal toxin acting on a 14-3-3 regulatory complex. *EMBO J.* **22**, 987–994 (2003).
25. Molzan, M. *et al.* Impaired Binding of 14-3-3 to C-RAF in Noonan Syndrome Suggests New Approaches in Diseases with Increased Ras Signaling. *Mol. Cell. Biol.* **30**, 4698–4711 (2010).
26. Anders, C. *et al.* A semisynthetic fusicoccane stabilizes a protein-protein interaction and enhances the expression of K+ channels at the cell surface. *Chem. Biol.* **20**, 583–593 (2013).
27. Svennelid, F. *et al.* Phosphorylation of Thr-948 at the C terminus of the plasma membrane H+-ATPase creates a binding site for the regulatory 14-3-3 protein. *Plant*

Cell **11**, 2379–2391 (1999).

28. Sijbesma, E. *et al.* Identification of Two Secondary Ligand Binding Sites in 14-3-3 Proteins Using Fragment Screening. *Biochemistry* **56**, 3972–3982 (2017).
29. Stevers, L. M. *et al.* Modulators of 14-3-3 Protein-Protein Interactions. *J. Med. Chem.* **61**, 3755–3778 (2018).
30. Aitken, A. *et al.* Specificity of 14-3-3 isoform dimer interactions and phosphorylation. in *Biochem. Soc. Trans.* vol. 30 351–360 (Biochem Soc Trans, 2002).
31. Tzivion, G. & Avruch, J. 14-3-3 Proteins: Active cofactors in cellular regulation by serine/threonine phosphorylation. *J. Biol. Chem. vol*. 277 3061–3064 (2002).
32. Bridges, D. & Moorhead, G. B. G. 14-3-3 proteins: a number of functions for a numbered protein. *Science's STKE : signal transduction knowledge environment* vol. 2004 (2004).
33. Obsil, T., Ghirlando, R., Klein, D. C., Ganguly, S. & Dyda, F. Crystal structure of the 14-3-3ζ:serotonin N-acetyltransferase complex: A role for scaffolding in enzyme regulation. *Cell* **105**, 257–267 (2001).
34. Ottmann, C. *et al.* Structure of a 14-3-3 Coordinated Hexamer of the Plant Plasma Membrane H+-ATPase by Combining X-Ray Crystallography and Electron Cryomicroscopy. *Mol. Cell* **25**, 427–440 (2007).
35. Taoka, K. I. *et al.* 14-3-3 proteins act as intracellular receptors for rice Hd3a florigen. *Nature* **476**, 332–335 (2011).
36. Alblova, M. *et al.* Molecular basis of the 14-3-3 protein-dependent activation of yeast neutral trehalase Nth1. *Proc. Natl. Acad. Sci. U. S. A.* **114**, E9811–E9820 (2017).
37. Sluchanko, N. N. *et al.* Structural Basis for the Interaction of a Human Small Heat Shock Protein with the 14-3-3 Universal Signaling Regulator. *Structure* **25**, 305–316 (2017).
38. Karlberg, T. *et al.* 14-3-3 proteins activate Pseudomonas exotoxins-S and -T by chaperoning a hydrophobic surface. *Nat. Commun.* **9**, 1–11 (2018).
39. Park, E. *et al.* Architecture of autoinhibited and active BRAF–MEK1–14-3-3 complexes. *Nature* **575**, 545–550 (2019).
40. Kondo, Y. *et al.* Cryo-EM structure of a dimeric B-Raf:14-3-3 complex reveals asymmetry in the active sites of B-Raf kinases. *Science (80-.).* **366**, 109–115 (2019).
41. Ballio, A. *et al.* Fusicoccin: A new wilting toxin produced by Fusicoccum amygdali

Del. [13]. *Nature* vol. 203 297 (1964).

42. Oecking, C., Eckerskorn, C. & Weiler, E. W. The fusicoccin receptor of plants is a member of the 14-3-3 superfamily of eukaryotic regulatory proteins. *FEBS Lett.* **352**, 163–166 (1994).
43. Sassa, T., Tojyo, T. & Munakata, K. Isolation of a new plant growth substance with cytokinin-like activity. *Nature* **227**, 379 (1970).
44. Stevers, L. M. *et al.* Characterization and small-molecule stabilization of the multisite tandem binding between 14-3-3 and the R domain of CFTR. *Proc. Natl. Acad. Sci. U. S. A.* **113**, E1152–E1161 (2016).
45. Honma, Y., Ishii, Y., Yamamoto-Yamaguchi, Y., Sassa, T. & Asahi, K. I. Cotylenin A, a differentiation-inducing agent, and IFN-α cooperatively induce apoptosis and have an antitumor effect on human non-small cell lung carcinoma cells in nude mice. *Cancer Res.* **63**, 3659–3666 (2003).
46. Rose, R. *et al.* Identification and structure of small-molecule stabilizers of 14-3-3 protein-protein interactions. *Angew. Chemie - Int. Ed.* **49**, 4129–4132 (2010).
47. Rose, R. *et al.* Identification and Structure of Small-Molecule Stabilizers of 14-3-3 Protein-Protein Interactions. *Angew. Chemie Int. Ed.* **49**, 4129–4132 (2010).
48. Pahl, H. L. Activators and target genes of Rel/NF-κB transcription factors. *Oncogene* vol. 18 6853–6866 (1999).
49. Karin, M., Yamamoto, Y. & Wang, Q. M. The IKK NF-κB system: A treasure trove for drug development. *Nat. Rev. Drug Discov.* vol. 3 17–26 (2004).
50. Haefner, B. NF-κB: Arresting a major culprit in cancer. *Drug Discov. Today* vol. 7 653–663 (2002).
51. Richmond, A. NF-κB, chemokine gene transcription and tumour growth. *Nat. Rev. Immunol.* vol. 2 664–674 (2002).
52. Aggarwal, B. B. Nuclear factor-κB: The enemy within. *Cancer Cell* vol. 6 203–208 (2004).
53. Clevers, H. At the crossroads of inflammation and cancer. *Cell* vol. 118 671–674 (2004).
54. Balkwill, F., Charles, K. A. & Mantovani, A. Smoldering and polarized inflammation in the initiation and promotion of malignant disease. *Cancer Cell* vol. 7 211–217 (2005).
55. Li, Q., Withoff, S. & Verma, I. M. Inflammation-associated cancer: NF-κB is the lynchpin. *Trends in Immunol.* vol. 26 318–325 (2005).
56. Luo, J. L., Kamata, H. & Karin, M. IKK/NF-κB signaling: Balancing life and death

- A new approach to cancer therapy. *J. Clin. Investig.* vol. 115 2625–2632 (2005).
57. Shaffer, A. L., Rosenwald, A. & Staudt, L. M. Lymphoid malignancies: The dark side of B-cell differentiation. *Nat. Rev. Immunol*. vol. 2 920–932 (2002).
58. Panwalkar, A., Verstovsek, S. & Giles, F. Nuclear Factor-KappaB Modulation As a Therapeutic Approach in Hematologic Malignancies. *Cancer* vol. 100 1578–1589 (2004).
59. Ghosh, S., May, M. J. & Kopp, E. B. NF-κB and rel proteins: Evolutionarily conserved mediators of immune responses. *ANNU REV IMMUNOL* vol. 16 225–260 (1998).
60. Ghosh, S. & Karin, M. Missing pieces in the NF-κB puzzle. *Cell* vol. 109 (2002).
61. Hayden, M. S. & Ghosh, S. Signaling to NF-κB. *Genes Dev.* vol. 18 2195–2224 (2004).
62. Begalli, F. *et al.* Unlocking the NF-κB Conundrum: Embracing complexity to achieve specificity. *Biomedicines* **5**, (2017).
63. Zhong, H., SuYang, H., Erdjument-Bromage, H., Tempst, P. & Ghosh, S. The transcriptional activity of NF-κB is regulated by the IκB- associated PKAc subunit through a cyclic AMP-independent mechanism. *Cell* **89**, 413–424 (1997).
64. Wang, D., Westerheide, S. D., Hanson, J. L. & Baldwin, J. Tumor necrosis factor α-induced phosphorylation of RelA/p65 on Ser529 is controlled by casein kinase II. *J. Biol. Chem.* **275**, 32592–32597 (2000).
65. Yang, J., Fan, G. H., Wadzinski, B. E., Sakurai, H. & Richmond, A. Protein Phosphatase 2A Interacts with and Directly Dephosphorylates RelA. *J. Biol. Chem.* **276**, 47828–47833 (2001).
66. Chen, L. F., Fischle, W., Verdin, E. & Greene, W. C. Duration of nuclear NF-κB action regulated by reversible acetylation. *Science (80-.).* **293**, 1653–1657 (2001).
67. Chen, L. feng, Mu, Y. & Greene, W. C. Acetylation of RelA at discrete sites regulates distinct nuclear functions of NF-κB. *EMBO J.* **21**, 6539–6548 (2002).
68. Gupta, S. C., Sundaram, C., Reuter, S. & Aggarwal, B. B. Inhibiting NF-κB activation by small molecules as a therapeutic strategy. *BBA - Gene Regulatory Mechanisms* vol. 1799 775–787 (2010).
69. Nagashima, K. *et al.* Rapid TNFR1-dependent lymphocyte depletion in vivo with a selective chemical inhibitor of IKKβ. *Blood* **107**, 4266–4273 (2006).
70. Hayden, M. S. & Ghosh, S. NF-κB, the first quarter-century: Remarkable progress and outstanding questions. *Genes Dev.* **26**, 203–234 (2012).
71. Viatour, P., Merville, M. P., Bours, V. & Chariot, A. Phosphorylation of NF-κB and

IκB proteins: Implications in cancer and inflammation. *Trends Biochem Sci* vol. 30 43–52 (2005).

72. Baldwin, A. S. The NF-κB and IκB proteins: New discoveries and insights. *Annu. Rev. Immunol.* **14**, 649–681 (1996).
73. Mulero, M. C., Bigas, A. & Espinosa, L. IκBa beyond the NF-κB dogma. *Oncotarget* **4**, 1550–1551 (2013).
74. Simeonidis, S., Liang, S., Chen, G. & Thanos, D. Cloning and functional characterization of mouse IκBε. *Proc. Natl. Acad. Sci. U. S. A.* **94**, 14372–14377 (1997).
75. Malek, S., Chen, Y., Huxford, T. & Ghosh, G. IκBβ, but Not IκBα, Functions as a Classical Cytoplasmic Inhibitor of NF-κB Dimers by Masking Both NF-κB Nuclear Localization Sequences in Resting Cells. *J. Biol. Chem.* **276**, 45225–45235 (2001).
76. Tran, K., Merika, M. & Thanos, D. Distinct functional properties of IkappaB alpha and IkappaB beta. *Mol. Cell. Biol.* **17**, 5386–5399 (1997).
77. DiDonato, J. *et al.* Mapping of the inducible IkappaB phosphorylation sites that signal its ubiquitination and degradation. *Mol. Cell. Biol.* **16**, 1295–1304 (1996).
78. Gonen, H. *et al.* Identification of the ubiquitin carrier proteins, E2s, involved in signal-induced conjugation and subsequent degradation of IκBα. *J. Biol. Chem.* **274**, 14823–14830 (1999).
79. Aguilera, C. *et al.* Efficient nuclear export of p65-IκBα complexes requires 14-3-3 proteins. *J. Cell Sci.* **119**, 3695–3704 (2006).
80. Schrager, S. Dietary calcium intake and obesity. *J. Am. Board Fam. Med*. vol. 18 205–210 (2005).
81. dos Santos, L. C., de Pádua Cintra, I., Fisberg, M. & Martini, L. A. Calcium intake and its relationship with adiposity and insulin resistance in post-pubertal adolescents. *J. Hum. Nutr. Diet.* **21**, 109–116 (2008).
82. Da Silva Ferreira, T., Torres, M. R. S. G. & Sanjuliani, A. F. Dietary calcium intake is associated with adiposity, metabolic profile, inflammatory state and blood pressure, but not with erythrocyte intracellular calcium and endothelial function in healthy pre-menopausal women. *Br. J. Nutr.* **110**, 1079–1088 (2013).
83. Parikh, S. J. & Yanovski, J. A. Calcium intake and adiposity. *Am. J. Clin. Nutr.* **77**, 281–287 (2003).
84. Torres, M. R. S. G., da Silva Ferreira, T., Carvalho, D. C. & Sanjuliani, A. F. Dietary calcium intake and its relationship with adiposity and metabolic profile in hypertensive patients. *Nutrition* **27**, 666–671 (2011).

85. Racioppi, L. & Means, A. R. Calcium/calmodulin-dependent protein kinase kinase 2: Roles in signaling and pathophysiology. *J. Biol. Chem. J BIOL CHEM* vol. 287 31658–31665 (2012).
86. Hurley, R. L. *et al.* The Ca2+/calmodulin-dependent protein kinase kinases are AMP-activated protein kinase kinases. *J. Biol. Chem.* **280**, 29060–29066 (2005).
87. Anderson, K. A. *et al.* Hypothalamic CaMKK2 Contributes to the Regulation of Energy Balance. *Cell Metab.* **7**, 377–388 (2008).
88. Marcelo, K. L. *et al.* Research resource: Roles for calcium/calmodulin- dependent protein kinase kinase 2 (caMKK2) in systems metabolism. *Mol. Endocrinol.* **30**, 557–572 (2016).
89. Psenakova, K. *et al.* 14-3-3 protein directly interacts with the kinase domain of calcium/calmodulin-dependent protein kinase kinase (CaMKK2). *Biochim. Biophys. Acta - Gen. Subj.* **1862**, 1612–1625 (2018).
90. Kukimoto-Niino, M. *et al.* Crystal structure of the Ca2+/calmodulin-dependent protein kinase kinase in complex with the inhibitor STO-609. *J. Biol. Chem.* **286**, 22570–22579 (2011).
91. Tokumitsu, H. & Soderling, T. R. Requirements for calcium and calmodulin in the calmodulin kinase activation cascade. *J. Biol. Chem.* **271**, 5617–5622 (1996).
92. Tokumitsu, H., Iwabu, M., Ishikawa, Y. & Kobayashi, R. Differential regulatory mechanism of ca2+/calmodulin-dependent protein kinase kinase isoforms. *Biochemistry* **40**, 13925–13932 (2001).
93. Green, M. F. *et al.* Ca 2+/calmodulin-dependent protein kinase kinase β is regulated by multisite phosphorylation. *J. Biol. Chem.* **286**, 28066–28079 (2011).
94. Wayman, G. A., Tokumitsu, H. & Soderling, T. R. Inhibitory cross-talk by cAMP kinase on the calmodulin-dependent protein kinase cascade. *J. Biol. Chem.* **272**, 16073–16076 (1997).
95. Matsushita, M. & Nairn, A. C. Inhibition of the Ca2+/calmodulin-dependent protein kinase I cascade by cAMP-dependent protein kinase. *J. Biol. Chem.* **274**, 10086–10093 (1999).
96. Davare, M. A., Saneyoshi, T., Guire, E. S., Nygaard, S. C. & Soderling, T. R. Inhibition of Calcium/Calmodulin-dependent Protein Kinase Kinase by Protein 14-3-3. *J. Biol. Chem.* **279**, 52191–52199 (2004).
97. Ichimura, T., Taoka, M., Hozumi, Y., Goto, K. & Tokumitsu, H. 14-3-3 Proteins directly regulate Ca2+/calmodulin-dependent protein kinase kinase α through phosphorylation-dependent multisite binding. *FEBS Lett.* **582**, 661–665 (2008).

98. Matsushita, M. & Nairn, A. C. Inhibition of the Ca2+/calmodulin-dependent protein kinase I cascade by cAMP-dependent protein kinase. *J. Biol. Chem.* **274**, 10086–10093 (1999).
99. Okuno, S., Kitani, T. & Fujisawa, H. Regulation of Ca2+/calmodulin-dependent protein kinase kinase α by cAMP-dependent protein kinase: I. Biochemical analysis. *J. Biochem.* **130**, 503–513 (2001).
100. Svergun, D. I. Determination of the regularization parameter in indirect-transform methods using perceptual criteria. *J. Appl. Crystallogr.* **25**, 495–503 (1992).
101. Receveur-Brechot, V. & Durand, D. How Random are Intrinsically Disordered Proteins? A Small Angle Scattering Perspective. *Curr. Protein Pept. Sci.* **13**, 55–75 (2012).
102. Svergun, D. I. Restoring low resolution structure of biological macromolecules from solution scattering using simulated annealing. *Biophys. J.* **76**, 2879–2886 (1999).
103. Rambo, R. P. Resolving individual components in protein-RNA complexes using small-angle X-ray scattering experiments. in *Methods in Enzymol.* vol. 558 363–390 (Academic Press Inc., 2015).
104. Petoukhov, M. V. *et al.* New developments in the ATSAS program package for small-angle scattering data analysis. *J. Appl. Crystallogr.* **45**, 342–350 (2012).
105. Rezabkova, L. *et al.* 14-3-3 protein interacts with and affects the structure of RGS domain of regulator of G protein signaling 3 (RGS3). *J. Struct. Biol.* **170**, 451–461 (2010).
106. Stevers, L. M. *et al.* Structural interface between LRRK2 and 14-3-3 protein. *Biochem. J.* **474**, 1273–1287 (2017).
107. Centorrino, F., Ballone, A., Wolter, M. & Ottmann, C. Biophysical and structural insight into the USP8/14-3-3 interaction. *FEBS Lett.* **592**, 1211–1220 (2018).
108. Ottmann, C. *et al.* A Structural Rationale for Selective Stabilization of Anti-tumor Interactions of 14-3-3 proteins by Cotylenin A. *J. Mol. Biol.* **386**, 913–919 (2009).
109. Rose, R., Rose, M. & Ottmann, C. Identification and structural characterization of two 14-3-3 binding sites in the human peptidylarginine deiminase type VI. *J. Struct. Biol.* **180**, 65–72 (2012).
110. Neves, J. F. *et al.* Backbone chemical shift assignments of human 14-3-3σ. *Biomol. NMR Assign.* **13**, 103–107 (2019).
111. Congreve, M., Carr, R., Murray, C. & Jhoti, H. A 'Rule of Three' for fragment-based lead discovery? *Drug Discov. Today* vol. 8 876–877 (2003).
112. Meldal, M. & Tomøe, C. W. Cu-catalyzed azide - Alkyne cycloaddition. *Chem. Rev.*

vol. 108 2952–3015 (2008).

113. Alblova, M. *et al.* Molecular basis of the 14-3-3 protein-dependent activation of yeast neutral trehalase Nth1. *Proc. Natl. Acad. Sci. U. S. A.* **114**, E9811–E9820 (2017).

114. Kalabova, D. *et al.* Human procaspase-2 phosphorylation at both S139 and S164 is required for 14-3-3 binding. *Biochem. Biophys. Res. Commun.* **493**, 940–945 (2017).

115. De Boer, A. H. & Leeuwen, I. J. d. V. van. Fusicoccanes: Diterpenes with surprising biological functions. *Trends Plant Sci* vol. 17 360–368 (2012).

116. Toyomasu, T. *et al.* Fusicoccins are biosynthesized by an unusual chimera diterpene synthase in fungi. *Proc. Natl. Acad. Sci. U. S. A.* **104**, 3084–3088 (2007).

7 Supplements

7.1 Supplement S1

7.1.1 14-3-3 protein directly interacts with the kinase domain of calcium/calmodulin-dependent protein kinase kinase (CaMKK2).

Psenakova, K., Petrvalska, O., Kylarova, S., **Lentini Santo, D.,** Kalabova, D., Herman, P., Obsilova, V. & Obsil, T. 14-3-3 protein directly interacts with the kinase domain of calcium/calmodulin-dependent protein kinase kinase (CaMKK2). *Biochim. Biophys. Acta - Gen. Subj.* **1862**, 1612–1625 (2018).

My contribution: Expression and purification of 14-3-3γΔC and 14-3-3ζΔC, evaluation of the phosphopeptide binding using the fluorescence polarization assay, crystallization and refinement of the 14-3-3γΔC:CaMKK2 pS100 and 14-3-3γΔC:CaMKK2 pS511 complexes.

BBA - General Subjects 1862 (2018) 1612–1625

Contents lists available at ScienceDirect

BBA - General Subjects

journal homepage: www.elsevier.com/locate/bbagen

14-3-3 protein directly interacts with the kinase domain of calcium/calmodulin-dependent protein kinase kinase (CaMKK2)

Katarina Psenakova[a,b,1], Olivia Petrvalska[a,b,1], Salome Kylarova[a,b,1], Domenico Lentini Santo[a], Dana Kalabova[b], Petr Herman[c], Veronika Obsilova[b,*], Tomas Obsil[a,b,**]

[a] Department of Physical and Macromolecular Chemistry, Faculty of Science, Charles University, Prague, Czech Republic
[b] BioCeV – Institute of Physiology, The Czech Academy of Sciences, Vestec, Czech Republic
[c] Institute of Physics, Faculty of Mathematics and Physics, Charles University, Prague, Czech Republic

ARTICLE INFO

Keywords:
14-3-3 protein
CaMKK
Protein-protein interaction
SAXS
Fluorescence spectroscopy

ABSTRACT

Background: Calcium/calmodulin-dependent protein kinase kinase 2 (CaMKK2) is a member of the Ca^{2+}/calmodulin-dependent kinase (CaMK) family involved in adiposity regulation, glucose homeostasis and cancer. This upstream activator of CaMKI, CaMKIV and AMP-activated protein kinase is inhibited by phosphorylation, which also triggers an association with the scaffolding protein 14-3-3. However, the role of 14-3-3 in the regulation of CaMKK2 remains unknown.

Methods: The interaction between phosphorylated CaMKK2 and the 14-3-3γ protein, as well as the architecture of their complex, were studied using enzyme activity measurements, small-angle x-ray scattering (SAXS), time-resolved fluorescence spectroscopy and protein crystallography.

Results: Our data suggest that the 14-3-3 protein binding does not inhibit the catalytic activity of phosphorylated CaMKK2 but rather slows down its dephosphorylation. Structural analysis indicated that the complex is flexible and that CaMKK2 is located outside the phosphopeptide-binding central channel of the 14-3-3γ dimer. Furthermore, 14-3-3γ appears to interact with and affect the structure of several regions of CaMKK2 outside the 14-3-3 binding motifs. In addition, the structural basis of interactions between 14-3-3 and the 14-3-3 binding motifs of CaMKK2 were elucidated by determining the crystal structures of phosphopeptides containing these motifs bound to 14-3-3.

Conclusions: 14-3-3γ protein directly interacts with the kinase domain of CaMKK2 and the region containing the inhibitory phosphorylation site Thr^{145} within the N-terminal extension.

General significance: Our results suggested that CaMKK isoforms differ in their 14-3-3-mediated regulations and that the interaction between 14-3-3 protein and the N-terminal 14-3-3-binding motif of CaMKK2 might be stabilized by small-molecule compounds.

1. Introduction

Calcium/calmodulin-dependent protein kinase kinase (CaMKK), a member of the Ca^{2+}/calmodulin-dependent kinase (CaMK) family, specifically phosphorylates Thr residues within the activation loop of two downstream kinases, CaMKI and CaMKIV, considerably increasing their catalytic efficiency, resulting in phosphorylation of multiple downstream targets [1]. Two CaMKK isoforms (CaMKK1 and CaMKK2) have been identified in mammals, which are both highly expressed in the brain. CaMKK2 is also an upstream activator of the AMP-activated protein kinase (AMPK) [2], and studies have shown that the AMPK:-CaMKK2 complex regulates energy balance by acting in the hypothalamus [3]. In fact, CaMKK2 is one of the most versatile CaMKs, which is involved in adiposity regulation, glucose homeostasis, hematopoiesis, inflammation, and cancer, and is considered a potential target for therapeutic intervention (reviewed in [4]).

The members of the CaMK family share a common domain organization consisting of the catalytic domain followed by an autoinhibitory region, which overlaps with the CaM-binding region (Fig. 1A and C) [5]. Although CaMKK1 and CaMKK2 share high similarity and

Abbreviations: AMPK, AMP-activated protein kinase; AUC, Analytical ultracentrifugation; CaM, Calmodulin; CaMKK2, Calcium/calmodulin-dependent protein kinase kinase 2; SAXS, Small-angle x-ray scattering; SV, Sedimentation velocity

* Correspondence to: V. Obsilova, BioCeV – Institute of Physiology, The Czech Academy of Sciences, Prague, Czech Republic.
** Correspondence to: T. Obsil, Department of Physical and Macromolecular Chemistry, Faculty of Science, Charles University, Prague, Czech Republic.
E-mail addresses: veronika.obsilova@fgu.cas.cz (V. Obsilova), obsil@natur.cuni.cz (T. Obsil).

[1] The first three authors KP, OP and SK contributed equally to this work.

https://doi.org/10.1016/j.bbagen.2018.04.006
Received 16 January 2018; Received in revised form 5 April 2018; Accepted 6 April 2018
Available online 10 April 2018
0304-4165/ © 2018 Elsevier B.V. All rights reserved.

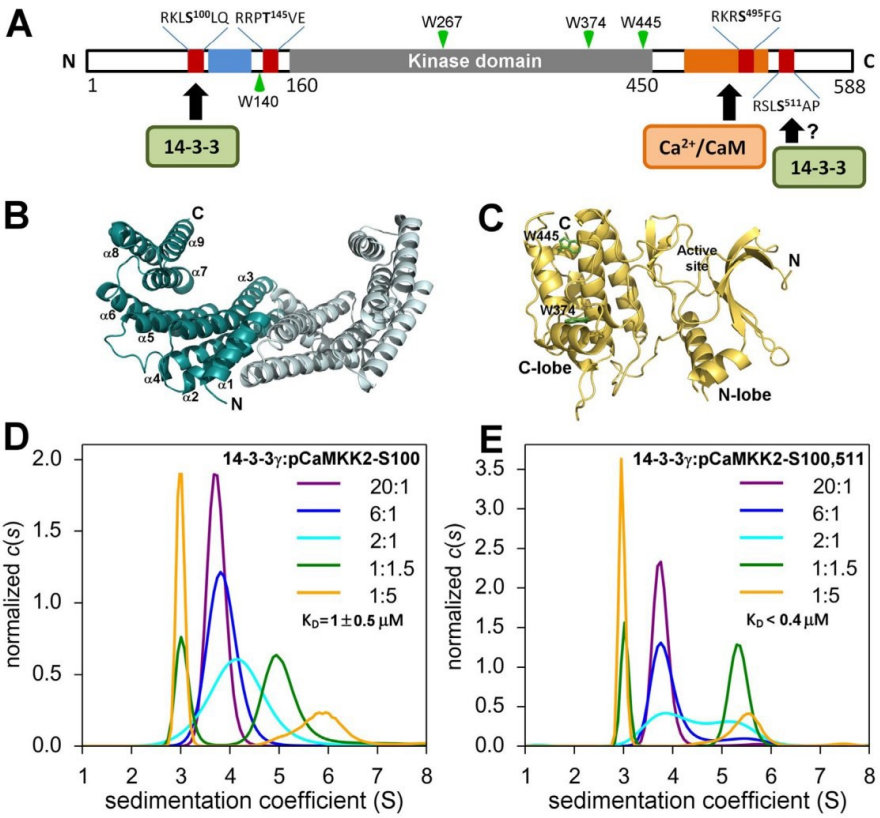

Fig. 1. Phosphorylated CaMKK2 Forms a Stable Complex with 14-3-3γ. (A) Domain structure of CaMKK2. The positions of PKA phosphorylation sites, the N-terminal regulatory site and the CaM binding region are indicated by red, blue and orange rectangles, respectively. The positions of tryptophan residues used in the time-resolved fluorescence experiments are indicated by green triangles. (B) Crystal structure of the 14-3-3γ protein dimer (PDB ID: 2B05) Each protomer is shown in different color. (C) Crystal structure of the kinase domain of CaMKK2 [35]. Tryptophan residues located in the C-lobe are shown as sticks. (D, E) Series of area-normalized $c(s)$ distributions of mixtures of pCaMKK2 and 14-3-3γ at various molar ratios, using 6 μM 14-3-3γ and 0.3 − 30 μM pCaMKK2.

identity in their amino acid sequences (Fig. S1), they differ in their biochemical properties. CaMKK1 activity is strictly regulated by an autoinhibitory mechanism, and Ca^{2+}/CaM binding relieves this autoinhibition [6]. However, in contrast to CaMKK1, CaMKK2 is significantly active in the absence of Ca^{2+}/CaM [7]. This autonomous activity is regulated by a stretch of 23 amino acids (residues 129–151 in rat CaMKK2), which is located N-terminally to the catalytic domain and apparently participates in the release of the autoinhibitory region from the catalytic domain [8]. Moreover, this regulatory region contains three phosphorylation sites targeted by cyclin-dependent kinase 5 and glycogen synthase kinase 3 and one site recognized by cAMP-dependent protein kinase (PKA) [9,10].

Both CaMKKs are partly inhibited upon phosphorylation by PKA [10–12]. CaMKK1 contains five PKA phosphorylation sites, Ser^{52}, Ser^{74}, Thr^{108}, Ser^{458}, and Ser^{475}, four of which are also present in CaMKK2 (Ser^{100}, Thr^{145}, Ser^{495}, and Ser^{511}) (Figs. 1A and S1). Ser^{458} phosphorylation has been shown to block Ca^{2+}/CaM-binding, whereas Thr^{108} phosphorylation plays a role in the regulation of CaMKK1 activity toward CaMKI and CaMKIV [10,13].

In addition to direct, PKA-mediated inhibition, CaMKK1 activity is further regulated through a PKA-dependent mechanism based on interaction with 14-3-3 proteins [14,15]. 14-3-3 proteins, a family of highly conserved dimeric proteins ubiquitously expressed in all eukaryotic cells (Fig. 1B), function as scaffold and chaperone molecules that interact with and regulate the function of several hundred partner proteins by recognizing phosphoserine- (pS) or phosphothreonine (pT)-containing motifs [16]. Mechanistically, 14-3-3 proteins constrain the conformation, occlude sequence-specific and structural features, promote protein-protein interactions, or prevent the aggregation of their binding partners (reviewed in [17,18]). GST pull-down and co-immunoprecipitation assays, together with site-directed mutagenesis, have shown that both CaMKK isoforms bind to various 14-3-3 protein isoforms (mainly γ isoform) and that the conserved motif containing phosphorylated Ser^{74} in CaMKK1 (corresponding to Ser^{100} in CaMKK2, Figs. 1A and S1) functions as the primary 14-3-3 binding site [14,15]. Furthermore, a second 14-3-3 binding motif containing phosphorylated Ser^{475} in CaMKK1 (Ser^{511} in CaMKK2) has also been suggested [15]. The phosphorylation of this site by PKA, however, is low and mainly occurs in the presence of Ca^{2+}/CaM [11,12,14]. The functional role of 14-3-3 binding in CaMKK regulation is apparently twofold. Davare et al. [14] suggested that the 14-3-3 binding inhibits CaMKK1 through two mechanisms, namely inhibition of Thr^{108} dephosphorylation, thus maintaining the kinase in the PKA-mediated inhibited state, and direct inhibition of the kinase activity. Accordingly, Ichimura et al. [15] showed that binding to 14-3-3 decreases the maximum velocity (V_{max}) of CaMKK1. However, the molecular mechanism of this interaction as well as the role of 14-3-3 in the regulation of CaMKK2 remains unclear.

Thus, in this study, we used enzyme activity measurements, small-

analysis based on the ensemble optimization method was performed using the program EOM [28].

2.9. Fluorescence polarization assay

Various concentrations of 14-3-3γ were incubated for 1 h with 20 nM of FITC-conjugated synthetic peptide GSLSARKL(pS)LQER (FITC-CaMKK2-S100), where pS denotes phosphoserine, with a fluorescein attached to the N-terminus (Pepscan Presto BV, The Netherlands). Fluorescence polarization was measured using a CLARIOstar microplate reader (BMG Labtech) in 10 mM HEPES (pH 7.4), 150 mM NaCl, 0.1% (*v*/v) Tween 20 and 0.1% (*w*/*v*) BSA buffer after incubating for 1 h in a 96-well black plate. Excitation and emission wavelengths were 482 nm and 530 nm, respectively, and K_D was determined using Origin (OriginLab Corp., MA, USA).

2.10. Time-resolved fluorescence measurements

Time-resolved tryptophan fluorescence intensity and anisotropy decay measurements as well as data analysis were performed as previously described [29]. Tryptophan emission was excited at 298 nm by a tripled output of the Ti:Sapphire laser. Tryptophan fluorescence was isolated at 355 nm using a combination of monochromator and a stack of UG1 and BG40 glass filters (Thorlabs) placed in front of the input slit. Dansyl fluorescence was excited at 355 nm and collected at 550 nm. Samples were placed in a thermostatic holder, and all experiments were performed at 23 °C in buffer containing 50 mM Tris-HCl (pH 7.5), 150 mM NaCl, 1 mM TCEP, 1 mM $CaCl_2$ and 10% (*w*/*v*) glycerol. In tryptophan fluorescence experiments, the pCaMKK2 and 14-3-3γ noW concentrations were 12 and 60 μM, respectively. In dansyl fluorescence experiments, the DANS-CaM, CaMKK2 and 14-3-3γ concentrations were 25, 28 and 100 μM, respectively.

2.11. Crystallization, data collection and structure determination

The 14-3-3ζΔC or 14-3-3γΔC proteins and the pepS100 or pepS511 peptides (sequences RKLpSLQER and RSLpSAPGN, respectively) were mixed in a 1:2 M stoichiometry in buffer containing 20 mM HEPES (pH 7), 2 mM $MgCl_2$ and 1 mM TCEP. Crystallization was performed using the hanging-drop vapor-diffusion method at 291 K. Crystals of the 14-3-3ζΔC:pepS100 peptide complex were grown from drops consisting of 2.5 μL of 16.2 mg.mL^{-1} protein and 2.5 μL of 100 mM Tris-HCl (pH 7), 20.8% (*w*/*v*) PEG 2000 and 50 mM sodium fluoride. Crystals of the 14-3-3γΔC:pepS511 peptide complex were grown from drops consisting of 1 μL of 16.5 mg.mL^{-1} protein and 2 μL of 100 mM sodium citrate (pH 5.6), 200 mM potassium sodium tartrate, and 1.8 M ammonium sulfate. Crystals were cryoprotected using 30% (*v*/v) PEG 400 and flash frozen in liquid nitrogen before data collection in oscillation mode at beamline 14.1 of the BESSY synchrotron and the D8 Venture system (Bruker, MA, USA). Diffraction data processing was performed using the packages XDS and XDSAPP [30,31]. Crystal structures of the 14-3-3ζΔC:pepS100 and 14-3-3γΔC:pepS511 complexes were solved by molecular replacement in MOLREP [32], using the structures of 14-3-3ζ (PDB ID: 4FJ3 [33]) and 14-3-3γ (PDB ID: 2B05) as search models, and refined at resolutions of 2.68 and 2.84 Å, respectively, with PHENIX [34]. The atomic coordinates and structure factors of both complexes have been deposited in the RCSB PDB with accession codes 6EWW and 6FEL. All structural figures were prepared with PyMOL (https://pymol.org/2/).

3. Results

3.1. Preparation of phosphorylated CaMKK2

Because the 14-3-3 binding motifs of human CaMKK2 are located around pSer^{100} and pSer^{511}, flanking the kinase domain [14,15], we restricted our analysis to the residues 93 − 517 containing these two motifs, the kinase domain, and the Ca^{2+}/CaM binding region (hereafter referred to as CaMKK2). To prepare well-defined protein, suitable for structural analysis, the other two sites phosphorylated by PKA (Thr^{145} and Ser^{495}) were mutated to Ala. In addition, the mutation D^{330}A, of the catalytic aspartate residue, was introduced into the kinase domain to avoid autophosphorylation of the recombinant protein during expression and phosphorylation by PKA. Recombinantly expressed CaMKK2$_{93–517}$T^{145}A, D^{330}A, S^{495}A (hereafter referred to as CaMKK2-S^{100,511}) was phosphorylated in vitro by PKA, and the extent of the phosphorylation reaction was determined by mass spectrometry. HPLC-MS analysis confirmed the stoichiometric phosphorylation of Ser^{100} but only partial (approximately 50%) phosphorylation of Ser^{511} (Fig. S2). Neither the presence of Ca^{2+}/CaM nor the increased concentration of PKA improved the phosphorylation status of Ser^{511}. The weak phosphorylation of Ser^{511} by PKA is consistent with previous reports and indicates that, under physiological conditions, the N-terminal 14-3-3 binding motif would be significantly more phosphorylated than the C-terminal 14-3-3 binding motif [11,12,14]. Therefore, we also prepared a construct containing only the N-terminal 14-3-3 binding motif with Ser^{100} by inserting an additional mutation, Ser^{511} to Ala (hereafter referred to as CaMKK2-S^{100}).

3.2. Phosphorylated CaMKK2 forms a stable complex with 14-3-3γ

The formation of the complex between 14-3-3γ and pCaMKK2 (S^{100} and S^{100,511}) was studied using sedimentation velocity (SV) analytical ultracentrifugation (AUC) by analyzing their mixtures at various molar ratios (Fig. 1D and E). The normalized continuous sedimentation coefficient distributions *c*(*s*) based on the SV AUC experiments showed that 14-3-3γ and pCaMKK2-S^{100} formed a complex with a weight-averaged sedimentation coefficient (corrected to 20.0 °C and to the density of water), $s_{w(20,w)}$, of 6.17 S, with a frictional ratio f/f_o of 1.3, whereas 14-3-3γ and pCaMKK2-S^{100} alone showed single peaks, with $s_{w(20,w)}$ values of 3.91 and 3.16 S, respectively. The $s_{w(20,w)}$ value of the 14-3-3γ:pCaMKK2-S^{100} complex corresponds to a molecular mass of ~110 kDa, thus suggesting a 2:1 M stoichiometry for the complex (105.0 kDa theoretical molecular mass). The direct modeling of the SV AUC data using the Lamm equation showed best-fit apparent equilibrium dissociation constants (K_D) of 1 ± 0.5 μM using a Langmuir binding model with a pCaMKK2-S^{100} molecule interacting with a 14-3-3γ dimer.

SV-AUC analysis of mixtures of 14-3-3γ and pCaMKK2-S^{100,511} revealed the formation of a complex with an $s_{w(20,w)}$ value of 5.72 S and with a frictional ratio f/f_o of 1.4. This $s_{w(20,w)}$ value corresponds to a molecular mass of ~111 kDa, thus also suggesting the 2:1 M stoichiometry of the complex. The direct modeling of the SV AUC data showed a best-fit K_D of < 0.4 μM, thus suggesting that the C-terminal motif, when phosphorylated, increases the stability of the complex.

3.3. 14-3-3 Protein binding does not inhibit the activity of pCaMKK2 but slows down its Dephosphorylation

Previous studies have shown that the 14-3-3 binding inhibits the catalytic activity of phosphorylated CaMKK1 [14,15]. To test whether the catalytic activity of pCaMKK2 is also affected by interaction with 14-3-3, the kinase activity measurements were performed. Human CaMK1D and AMPKA2 (catalytic α2 subunit of AMPK) were used as specific substrates. As expected, the phosphorylation by PKA significantly suppressed the activity of pCaMKK2 relative to the non-phosphorylated protein by ~50% and ~30% for CaMK1D and AMPKA2 as substrates, respectively (Fig. 2). Interestingly, the addition of 14-3-3γ did not further suppress the activity of pCaMKK2 but rather resulted in its weak enhancement. When CaMK1D was used as a substrate, the effect was insignificant (the activity increased by 5% on a relative scale compared to the non-phosphorylated enzyme activity), but when

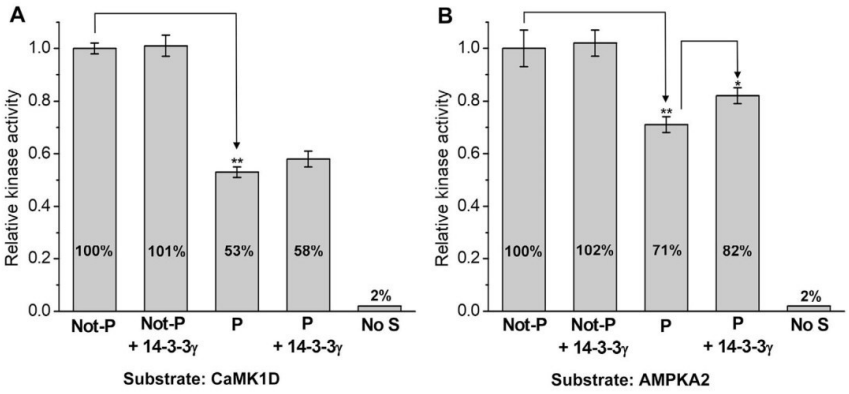

Fig. 2. 14-3-3 Protein Binding Does Not Inhibit the Catalytic Activity of Phosphorylated CaMKK2. The catalytic activity of CaMKK2 and pCaMKK2 both in the absence and the presence of 14-3-3γ was measured using human CaMK1D (kinase-dead mutant $D^{165}A$) and AMPKA2 (kinase-dead mutant $D^{157}A$) as specific substrates. The activities were normalized compared to the non-phosphorylated enzyme activity in the absence of 14-3-3γ (specific activities were 940 ± 20 and 740 ± 50 nmol.min^{-1}.mg^{-1} for CaMK1D and AMPKA2 as substrates, respectively). Results are the means ± S.D., $n = 3$. No S, no substrate; *, $p < 0.05$; **, $p < 0.005$.

AMPKA2 was used as a substrate the pCaMKK2 activity increased significantly by 11%. This indicates that the 14-3-3-mediated regulations of pCaMKK1 and pCaMKK2 differ.

Davare et al. [14] suggested that the 14-3-3 binding inhibits CaMKK1 mainly through inhibition of Thr^{108} (Thr^{145} in CaMKK2) dephosphorylation, thus maintaining the kinase in the PKA-mediated inhibited state. Therefore, we next compared time-dependent overall dephosphorylation of PKA-phosphorylated pCaMKK2 by type 1 protein phosphatase (PP1) in the absence and presence of 14-3-3γ using phos-tag SDS-PAGE. The kinase-dead mutant of pCaMKK2 $D^{330}A$ was used to avoid autophosphorylation of additional residues. Dephosphorylation was assessed by downward shift (Fig. S3) on a phos-tag SDS-PAGE gel. CaMKK2 shifted down gradually with incubation time through several discrete bands, which correspond to various partly phosphorylated forms of CaMKK2. As noticed, an incubation with PP1 for 7 and 30 min resulted in a substantial dephosphorylation of pCaMKK2 in the absence of 14-3-3γ. On the other hand, the presence of 14-3-3γ suppressed the overall dephosphorylation of pCaMKK2 as indicated by a lower abundance of bands corresponding to dephosphorylated CaMKK2 after 7 and 30 min of incubation time.

To assess dephosphorylation of specific regulatory sites Thr^{145} and Ser^{495} (Thr^{108} and Ser^{458} in CaMKK1) an HPLC-MS approach was used. Proteins treated by PP1 for 0, 1.5 and 7 min were collected and directly injected onto an immobilized protease column. After rapid online digestion and desalting, HPLC separation coupled with MS detection was done. Abundances of selected peptides containing Thr^{145} and Ser^{495} were then estimated from intensities of their extracted ion chromatograms (Table S1). The intensity ratios between non-phosphorylated and phosphorylated forms of selected peptides indicated slower dephosphorylation of both phosphoresidues for pCaMKK2 bound to 14-3-3γ compared with pCaMKK2 alone, especially $pSer^{495}$ whose non-phosphorylated form could not be detected. This suggests that the 14-3-3γ binding slows down the dephosphorylation of inhibitory PKA sites of pCaMKK2.

3.4. Structural characterization of the 14-3-3 binding motifs of CaMKK2

Although the putative C-terminal 14-3-3 binding motif (sequence RSLpSer^{511}AP) is a canonical "mode I" 14-3-3 binding site (RXX(pS/pT)XP, wherein pS/pT is phosphoserine or phosphothreonine and X is any residue [36,37]), the N-terminal motif (sequence RKLpS^{100}LQE) contains a Gln residue at the position +2 relative to the phosphorylated residue $pSer^{100}$ (Fig. 1A). Bioinformatics survey of 14-3-3 binding sites revealed that Gln is seldom found at +2 because the Pro residue and, to a lesser extent, Ser, Gly and Asp also, are frequently found at this position [38]. The frequent occurrence of proline at the +2 position is explained by the need to introduce a kink in the peptide chain and to direct the C-terminal portion out of the ligand binding groove of the 14-3-3 protein [36]. To elucidate the structural basis of interactions between 14-3-3 proteins and the 14-3-3 binding motifs of CaMKK2, we solved the crystal structures of phosphopeptides pepS100 (sequence RKLpSLQER) and pepS511 (sequence RSLpSAPGN) bound to 14-3-3ζΔC and 14-3-3γΔC, respectively (ΔC denotes C-terminally truncated versions missing the highly flexible ~15-residues-long C-terminal tail [39]). The 14-3-3 isoforms were selected based on quality of the resulting crystals. The crystal structures were solved by molecular replacement using the structures of 14-3-3ζ (PDB ID: 4FJ3 [33]) and 14-3-3γ (PDB ID: 2B05) as search models, and refined at a resolution of 2.68 and 2.84 Å, respectively (Table 1). The final electron densities allowed us to build seven residues (KLpSLQER, Fig. 3A and B) of pepS100 and six residues (RSLpSAP, Fig. 3C and D) of pepS511.

The main-chain conformations of both phosphopeptides in the 14-3-3 binding grooves are similar to those previously observed in other 14-3-3 protein complexes [33,37,40–42]. The 14-3-3ζ side chains coordinating the $pSer^{100}$ moiety of pepS100 include Arg^{56}, Arg^{127}, and Tyr^{128} (Fig. 3B). Although the side-chain of the Glu residue at the +3 position relative to $pSer^{100}$ is salt-bridged to the Lys^{120} of 14-3-3ζ, the side-chain of the Gln residue at +2 is hydrogen-bonded to the phosphate and to the main-chain carbonyl groups of $pSer^{100}$. These interactions apparently force the direction of the polypeptide chain to change, thus mimicking the role of the Pro residue, as previously observed, for example, in the 14-3-3 binding motifs of yeast neutral trehalase, which also lacks a Pro residue at the +2 position relative to the phosphorylated residue (Fig. 3E) [42]. In the case of pepS511, which contains the canonical "mode I" 14-3-3 binding motif, the coordination of the $pSer^{511}$ moiety and all other contacts are identical to those previously observed in other complexes of peptides with the "mode I" motif.

3.5. The 14-3-3γ:pCaMKK2 complex is flexible and elongated

Because all our attempts to grow crystals of the 14-3-3γ:pCaMKK2-S^{100} and 14-3-3γ:pCaMKK2-$S^{100,511}$ complexes failed, we used SAXS analysis to structurally characterize the interaction between 14-3-3γ and pCaMKK2 in solution. We and other researchers have previously used a similar approach to characterize various 14-3-3 protein complexes [22,41,45]. X-ray scattering data were collected for CaMKK2-S^{100}, 14-3-3γΔC and both complexes prepared with 2:1 M stoichiometry (Table 2). The linearity of the Guinier plots (Fig. 4B), the lack of a significant variation in forward scattering intensity $I(0)$ with the concentration, the Porod volume V_p and the radius of gyration R_g (Table 2) confirmed the absence of aggregation and the stability of the complexes within the concentration range tested. The apparent M_w values of ~47 and ~54 kDa for CaMKK2 and 14-3-3γΔC, respectively, estimated based

Table 1
Crystallographic data collection and refinement statistics.

Complex	14-3-3ζΔC:pepS100	14-3-3γΔC:pepS511
Wavelength (Å)	0.9184	1.3418
Space group	P212121	R3
Unit-cell parameters		
a, *b*, *c* (Å)	56.95, 60.31, 262.19	115.73, 115.73, 203.96
α, β, γ (°)	90, 90, 90	90, 90, 120
Asymmetric unit contents	Two dimers of 14-3-3ζΔC with bound phosphopeptides	Two dimers of 14-3-3γΔC with bound phosphopeptides
Resolution range (Å)[a]	47.71–2.68 (2.84–2.68)	26.82–2.84 (2.94–2.84)
Unique reflections	26,274 (4126)	22,801 (2424)
Data multiplicity	6.42 (6.23)	10.85 (10.81)
Completeness (%)	99.7 (98.9)	94.4 (99.4)
$\langle I/\sigma(I)\rangle$	17.37 (5.21)	11.19 (2.26)
R_{meas}[b]	0.08 (0.3)	0.26 (0.97)
R_{work}	0.208	0.228
R_{free}[c]	0.234	0.280
No. of protein atoms	7118	7402
No. of waters	114	35
Average B factors (Å^2)		
Protein	50.34	40.87
Water	41.77	34.55
R.m.s.[d] deviations from ideal values		
Bond lengths (Å)	0.009	0.004
Bond angles (°)	0.97	0.55
Ramachandran favored (%)	95.51	98.88
Ramachandran allowed (%)	4.49	1.12
Ramachandran outliers (%)	0	0

[a] Values in parentheses are for the highest resolution shell.

[b] $R_{meas} = \sum_{hkl}\{N(hkl)/[N(hkl)-1]\}^{1/2} \times \sum_i |I_i(hkl) - \langle I(hkl)\rangle| \sum_{hkl}\sum_i I_i(hkl)$, where $I(hkl)$ is the intensity of reflection hkl, $\langle I(hkl)\rangle = \frac{1}{N(hkl)}\sum_i I_i(hkl)$, and $N(hkl)$ the multiplicity.

[c] The free R value (R_{free}) was calculated using 5% of the reflections, which were omitted from the refinement.

[d] R.m.s., root mean square.

on the $I(0)$, correspond well with their expected M_w values of 48.0 and 54.3 kDa, respectively. The apparent M_w of 92 − 95 and 94 − 97 kDa of the 14-3-3γΔC:pCaMKK2-S^{100} and 14-3-3γΔC:pCaMKK2-S^{100,511} complexes, respectively, as well as their V_p (~160 nm^3), also indicate a 2:1 M stoichiometry (theoretical M_w 102.3 kDa), thus corroborating the SV AUC results (for globular proteins, $M_w \approx V_p \times 0.625$).

The comparison of the calculated distance distribution functions, $P(r)$, is shown in Fig. 4C. The $P(r)$ functions of CaMKK2 alone and of both complexes show significant asymmetry and longer intra-particle distances and a larger maximum particle distance (D_{max}) than those of the 14-3-3γΔC dimer alone, thus suggesting that their molecules are more extended. This is also supported by their R_g and D_{max} values (Table 2), which are significantly larger than those of spherical proteins consisting of 430 (CaMKK2) and 944 (the 14-3-3γΔC:pCaMKK2 complex) residues ($R_g \sim 3N^{1/3}$, where N is the number of residues; $D_{max} \sim 2.6R_g$). Moreover, the analysis of scattering data showed that the 14-3-3γΔC:pCaMKK2-S^{100,511} complex has lower R_g and D_{max} values than the 14-3-3γΔC:pCaMKK2-S^{100} complex (Table 2), thus indicating that CaMKK2 phosphorylated at both motifs forms a more compact complex with 14-3-3γ. However, it should be noted that the 14-3-3γΔC:pCaMKK2-S^{100,511} complex was prepared using pCaMKK2-S^{100,511}, which was not completely phosphorylated at Ser^{511} (Fig. S2). Therefore, the values of R_g and D_{max} were assessed in a mixture of two complexes where either the N-terminal motif or both motifs are docked within the binding grooves of the 14-3-3 dimer.

14-3-3 binding motifs are frequently located within long intrinsically disordered segments found in most 14-3-3 binding partners [46]. Apparently, CaMKK2 is not an exception because the analysis of protein disorder using the web servers PrDOS [47] and IUPred [48] suggested that its N- and C-terminal segments (residues 1 − 155 and 495 − 588) are significantly disordered (Fig. S4). These segments flank the structured kinase domain and contain both 14-3-3 binding motifs, as well as other regulatory regions (Fig. 1A). Indeed, the analysis of protein disorder using the dimensionless Kratky plot ($(sR_g)^2I(s)/I(0)$ versus sR_g) suggested that CaMKK2 and both complexes have higher conformational flexibility than 14-3-3γΔC (Fig. 4D). The scattering data for compact globular proteins in this plot show a maximum value of 1.104 at sR_g ~1.73 [49]. In addition, only 14-3-3γΔC showed a bell-shaped curve with an $(sR_g)^2I(s)/I(0)$ maximum of ~1.1 at an sR_g value of 1.7 (marked by cyan lines in Fig. 4D). Moreover, a more gradual decrease toward zero at higher sR_g and a higher maximum indicated that the 14-3-3γΔC:pCaMKK2-S^{100} complex has a higher conformational flexibility than the pCaMKK2-S^{100,511} complex, most likely resulting from the absence of interaction between 14-3-3 and the C-terminal segment of pCaMKK2-S^{100}.

3.6. Structural architecture of the 14-3-3γ:pCaMKK2 complex in solution

SAXS-based structural modeling was performed only for the 14-3-3γΔC:pCaMKK2-S^{100} complex. The 14-3-3γΔC:pCaMKK2-S^{100,511} complex was excluded from this analysis due to the heterogeneity caused by the incomplete phosphorylation of the C-terminal motif at Ser^{511} (Fig. S2). Moreover, the 14-3-3γΔC:pCaMKK2-S^{100} complex likely represents a physiologically more relevant form, considering the weak phosphorylation of Ser^{511} [11,12,14]. To determine the relative positions of 14-3-3 and CaMKK2 within the complex, multiphase modeling was performed to obtain ab initio bead models that include two phases representing individual components within a low-resolution shape [50]. Twenty independent models generated using the program MONSA [27] showed similar shape with a mean normalized spatial discrepancy (NSD) value of 0.61. The final model (Fig. 5A), the most typical model selected from all models calculated based on the lowest NSD value, showed a good approximation to the experimental SAXS data (Fig. S5). The calculated molecular envelope had an asymmetric shape, with most of the CaMKK2 phase located not in the central channel of the 14-3-3 dimer (a deep depression in the center of the 14-3-3 phase) but rather attached to the side of the 14-3-3 dimer and stretching out into the solution.

Subsequently, rigid-body modeling of the 14-3-3γΔC:pCaMKK2-S^{100} complex was performed using the program CORAL [25] and the crystal structures of 14-3-3γΔC (PDB ID: 2B05) and of the kinase domain of CaMKK2 [35]. The N-terminal 14-3-3 binding motif was restrained in the ligand-binding groove of 14-3-3γ, as previously observed in the crystal structure of the 14-3-3γΔC:pepS100 complex (Fig. 3A), and unstructured segments missing in the crystal structure were modeled as dummy residue chains. The final CORAL model fitted the SAXS data, with a χ^2 value of 1.33, and showed an asymmetric overall shape similar to that of the kinase domain of CaMKK2 located outside the central channel of the 14-3-3γ dimer (Fig. 5B and D). The model suggests that pCaMKK2-S^{100} interacts with 14-3-3γ not only through the phosphorylated N-terminal motif but also via a direct contact between the kinase domain and the 14-3-3 surface, in contrast to an extended state with CaMKK2 tethered to 14-3-3 only via a single phosphosite. Moreover, the presence of additional contacts between 14-3-3γ and pCaMKK2-S^{100}, outside the phosphorylated motif and the 14-3-3 binding groove, was corroborated by the binding affinity of pCaMKK2-S^{100} (K_D of ~1 μM, Fig. 1B), which was significantly higher than that of the synthetic phosphopeptide containing only the N-terminal 14-3-3 binding motif that binds 14-3-3γ with a K_D of 9 μM (Fig. S6).

Because the 14-3-3 binding motif and the kinase domain of pCaMKK-S^{100} are separated by a 60-residue-long segment, which is predicted to be unstructured (Figs. 1A and S4), in solution, the 14-3-

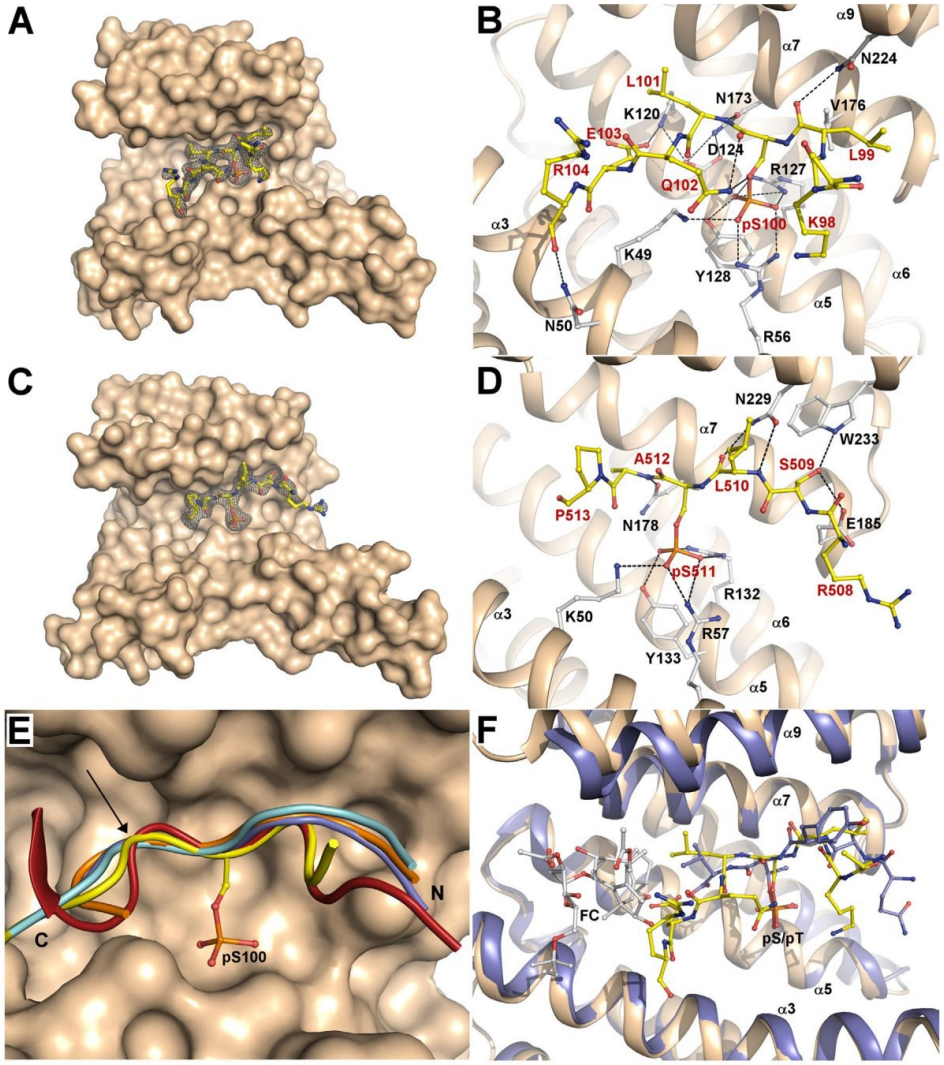

Fig. 3. Contacts between 14-3-3 and the 14-3-3 Binding Motifs of pCaMKK2. (A) Crystal structure of the 14-3-3ζ:pepS100 complex. The $2F_o$-F_c electron density map is contoured at 1σ. (B) Detailed view of contacts between 14-3-3ζ and the pepS100 peptide. The CaMKK2 residues are labeled in red, and the 14-3-3ζ residues are labeled in black. (C) Crystal structure of the 14-3-3γ:pepS511 complex. The $2F_o$-F_c electron density map is contoured at 1σ. (D) Detailed view of contacts between 14-3-3γ and the pepS511 peptide. The CaMKK2 residues are labeled in red, and the 14-3-3γ residues are labeled in black. (E) Comparison of the main-chain conformation of pepS100 (yellow) and pepS511 (violet) peptides with a "mode 1" 14-3-3 peptide (sequence RSHpSYPA, PDB ID: 1QJB, orange) [37], the 14-3-3 binding motifs of AANAT (sequence RRHpTLPA, PDB ID: 1IB1, cyan) [43] and neutral trehalase Nth1 (sequence TRRGpSEDDT, PDB ID: 5N6N, red) [42]. The C-terminal portion of the 14-3-3 binding motifs is indicated by a black arrow. (F) Superimposition of the 14-3-3ζ:pepS100 complex (pepS100 is shown in yellow) with the ternary complex between the "mode 3" phosphopeptide derived from the C-terminus of plant plasma membrane H^+-ATPase (sequence QSYpTV, shown as violet sticks), plant 14-3-3C (violet) and fusicoccin (FC, PDB ID: 1O9F) [44].

3γΔC:pCaMKK2-S^{100} complex may adopt different conformations. Moreover, the presence of conformational flexibility in the complex was indicated by the dimensionless Kratky plot (Fig. 4D). Therefore, we also attempted to model the complex as an ensemble of conformers using the program EOM [28]. The 14-3-3γΔC dimer, the 14-3-3 binding motif and the kinase domain of CaMKK2 were treated as rigid bodies and the flexible N- and C-terminal segments of CaMKK2 as chains of dummy residues. An initial pool of 10,000 conformers was generated and a genetic algorithm was then used to select an ensemble of conformers that collectively fit the experimental SAXS data. The selected ensemble of conformers fits the experimental scattering data with a χ^2 value of 1.22 (Fig. 5D). The R_g and D_{max} distributions calculated from the optimized ensemble are shown in Fig. 5C. The R_g distribution of the EOM-selected ensemble is biased toward more compact structures with lower R_g values than those of the pool. The average R_g and D_{max} values of the ensemble (42.4 and 149 Å, respectively) are consistent with values calculated from the scattering curves (Table 2). In addition, the R_g and D_{max} distributions of the 14-3-3γΔC:pCaMKK2-S^{100} complex have

Table 2
Structural parameters determined from SAXS data.

	c (mg.mL^{-1})	R_g (Å)[b]	R_g (Å)[c]	D_{max} (Å)	V_p[d] (nm^3)	M_w[e,g] (kDa)	M_w[f,g] (kDa)
14-3-3γΔC[a]	3.0	28.7 ± 0.4	28.6 ± 0.4	89	77.8	54 ± 1	49
	1.5	29.0 ± 0.4	29.0 ± 0.4	89	82.8	55 ± 1	52
CaMKK2	2.8	32.6 ± 0.3	32.7 ± 0.3	126	95.6	48 ± 1	60
	2.1	32.1 ± 0.3	32.2 ± 0.3	125	94.0	46 ± 1	59
Complex pSer^{100}	16.9	42.3 ± 0.6	42.4 ± 0.6	146	160.4	92 ± 1	100
	12.6	42.5 ± 0.6	42.6 ± 0.6	144	163.4	95 ± 1	102
	9.9	42.4 ± 0.6	42.5 ± 0.6	146	161.1	94 ± 1	101
Complex pSer^{100,511}	11.9	39.9 ± 0.7	40.0 ± 0.7	141	164.8	97 ± 1	103
	6.5	39.1 ± 0.6	39.2 ± 0.6	141	159.6	94 ± 1	100

[a] 14-3-3γ missing its C-terminal 13 residues.
[b] Calculated using Guinier approximation.
[c] Calculated using the programm GNOM.
[d] The excluded volume of the hydrated particle (the Porod volume).
[e] Molecular weight estimated by comparing the forward scattering intensity $I(0)$ with that of the reference solution of bovine serum albumin.
[f] Molecular weight estimated from the Porod volume ($M_w \approx V_p \times 0.625$) [25].
[g] Theoretical molecular weights of the 14-3-3γΔC dimer, pCaMKK2 and the pCaMKK2:14-3-3γΔC complex (with 2:1 stoichiometry) are 54.3, 48.0 and 102.3 kDa, respectively.

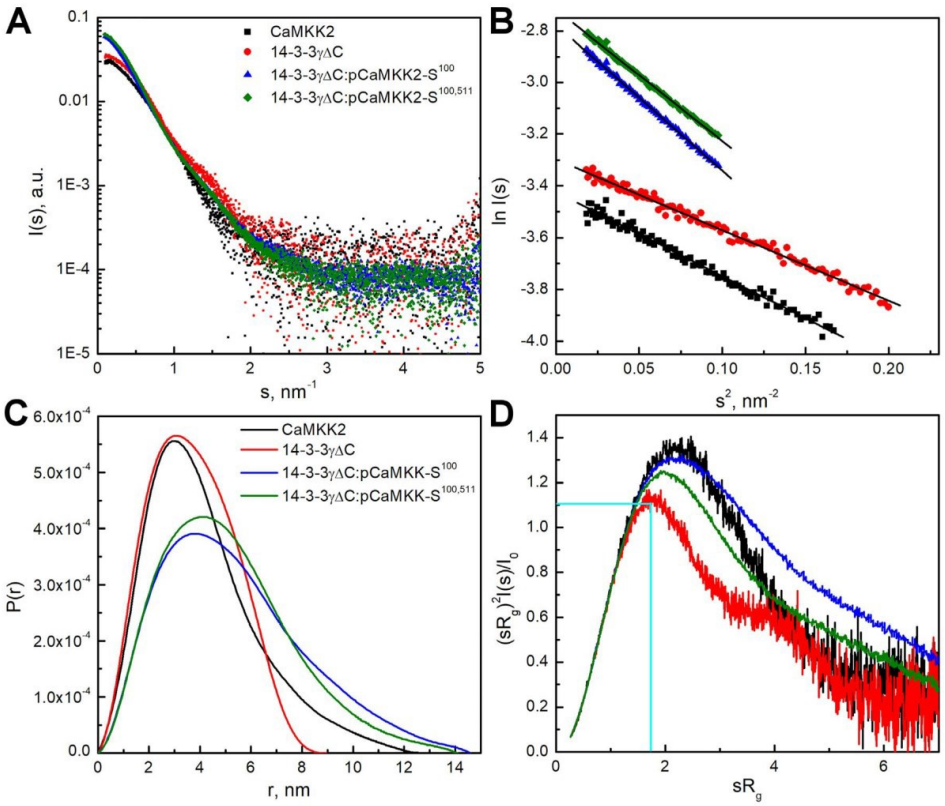

Fig. 4. SAXS Analysis of the 14-3-3ζ:pCaMKK2 Complexes. (A) Scattering intensity as a function of the scattering vector s ($s = 4\pi\sin(\theta/\lambda)$, where 2θ is the scattering angle, and λ is the wavelength) of 14-3-3γΔC, CaMKK-S^{100}, and the 14-3-3γΔC:pCaMKK2-S^{100} and 14-3-3γΔC:pCaMKK2-S^{100,511} complexes were mixed at 2:1 M stoichiometry. (B) Guinier plots for scattering curves shown in panel A. (C) Distance distribution functions P(r) calculated from scattering data using the program GNOM [24]. (D) Dimensionless Kratky plots. Cyan lines mark the maximum at a value of 1.104 for $sR_g = 1.73$, which is characteristic for the scattering data of compact globular proteins [49].

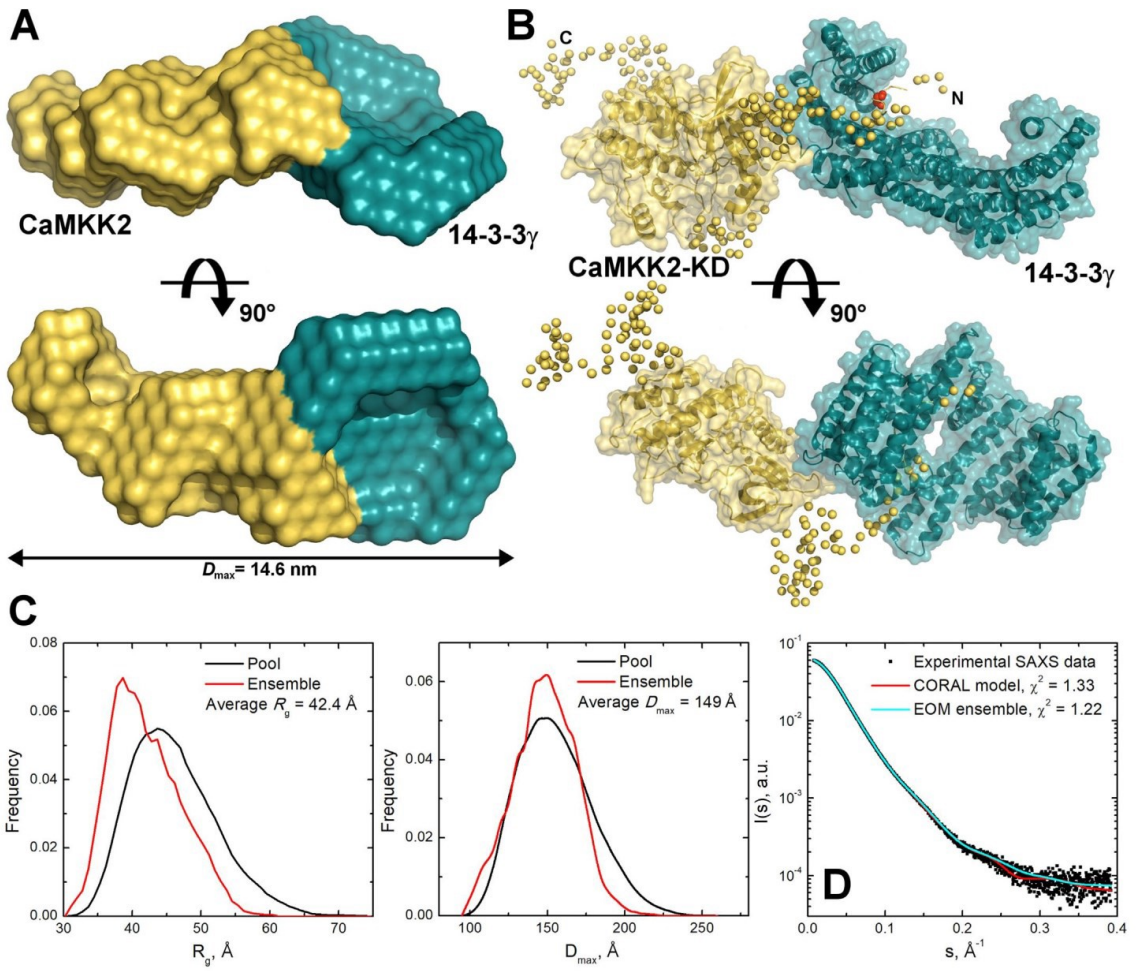

Fig. 5. SAXS-Based Structural Modeling of the 14-3-3γ:pCaMKK2 Complex. (A) Most typical multiphase reconstruction for the 14-3-3γΔC:pCaMKK2-S^{100} complex with the 14-3-3 phase colored in cyan and the CaMKK2 phase colored in yellow. (B) Typical conformation of the 14-3-3γΔC:pCaMKK2-S^{100} complex obtained in the program CORAL using the crystal structures of 14-3-3γΔC (PDB ID: 2B05) and the kinase domain of CaMKK2 (CaMKK-KD, PDB ID: 2ZV2 [35]). The unstructured segments missing in the crystal structure were modeled as dummy residue chains. The residue Ser^{100} is shown in red. (C) Distributions of R_g and D_{max} values of the 14-3-3γΔC:pCaMKK2-S^{100} complex conformations from ensemble selected by the program EOM [28]. (D) Experimental scattering curve of the complex superimposed with the calculated curves of the CORAL model shown in panel B (red) and the ensemble selected by the program EOM (cyan).

smaller extents than those of the pools, indicating that its accessible conformations are not fully randomly distributed and that the complex is unable to be fully extended in solution, thereby suggesting that 14-3-3γΔC interacts with the kinase domain and with pCaMKK2 linkers in solution. Thus, these results are consistent with the MONSA and the CORAL models.

3.7. 14-3-3γ binding does not affect Ca^{2+}/CaM binding to pCaMKK2

A common mechanism of action of the 14-3-3 protein is the interference with protein-protein interactions of its ligand. In the case of CaMKK, 14-3-3 could affect Ca^{2+}/CaM binding to the C-terminus of CaMKK. To test this hypothesis, Ca^{2+}/CaM binding to pCaMKK2-S^{100} and to pCaMKK2-S^{100,511} was investigated in the absence and presence of 14-3-3γ. For such purpose, dansyl-labeled CaM [51] was prepared, and its interaction with pCaMKK2 was monitored using time-resolved fluorescence intensity and anisotropy decay measurements (Table 3 and Fig. 6). The analysis of these measurements showed that Ca^{2+}/CaM binding to pCaMKK2 significantly increased the mean excited-state lifetime (τ_{mean}) and the longest correlation time ϕ_4 of the dansyl moiety, thus reflecting a decrease in the overall rotational diffusion coefficient upon complex formation, which indicates Ca^{2+}/CaM binding to both pCaMKK2 variants. The mutual interaction is clearly visible by the naked eye because the complexes have slower anisotropy decays than free Ca^{2+}/CaM, as shown in Fig. 6A, B. Although 14-3-3γ addition to the pCaMKK2-S^{100}:Ca^{2+}/CaM complex failed to induce any significant change in the dansyl anisotropy decay (open triangles in Fig. 6A), in the case of the pCaMKK2-S^{100,511}:Ca^{2+}/CaM complex, the presence of 14-3-3γ resulted in an additional increase of the rotational correlation time ϕ_4, as clearly seen in the raw data from the elevation of the anisotropy decay tail (open triangles in Fig. 6B). This indicates a significant change in the hydrodynamic properties of the complex,

Table 3
Summary of time-resolved Dans-CaM fluorescence measurements.

Sample	τ_{mean}[a,b] (ns)	K_{SV}[e] (M^{-1})	k_i ($\times 10^{-5}$) ($M^{-1}\,s^{-1}$)[f]	ϕ_1[d] (ns)	β_1[c]	ϕ_2 (ns)	β_2	ϕ_3 (ns)	β_3	ϕ_4 (ns)	β_4
Dansyl-CaM	15.2	0.18	120	< 0.1	0.03	0.6	0.02	2.5	0.10	9.3	0.12
+14-3-3γ	15.9	0.19	120	< 0.1	0.03	0.5	0.02	1.9	0.08	8.4	0.15
+S^{100}	20.5	0.01	4			2.5	0.01	12	0.11	49	0.15
+S^{100} + 14-3-3γ	20.5	0.00	0			3.0	0.01	11	0.10	49	0.16
+$S^{100,511}$	20.6	0.01	3			4.7	0.03	16	0.10	52	0.15
+$S^{100,511}$ + 14-3-3γ	20.2	0.11	53			2.8	0.02	12	0.08	88	0.16

[a] Mean lifetimes were calculated as $\tau_{mean} = \Sigma f_i \tau_i$, where f_i is an intensity fraction of the i-th lifetime component τ_i.
[b] S.D. value is ± 0.1 ns.
[c] The anisotropies $r(t)$ were analyzed for a series of exponentials by a model-independent maximum entropy method.
[d] Fast unresolved component.
[e] Stern-Volmer constant of acrylamide quenching.
[f] Bimolecular quenching constant for acrylamide collisional quenching.

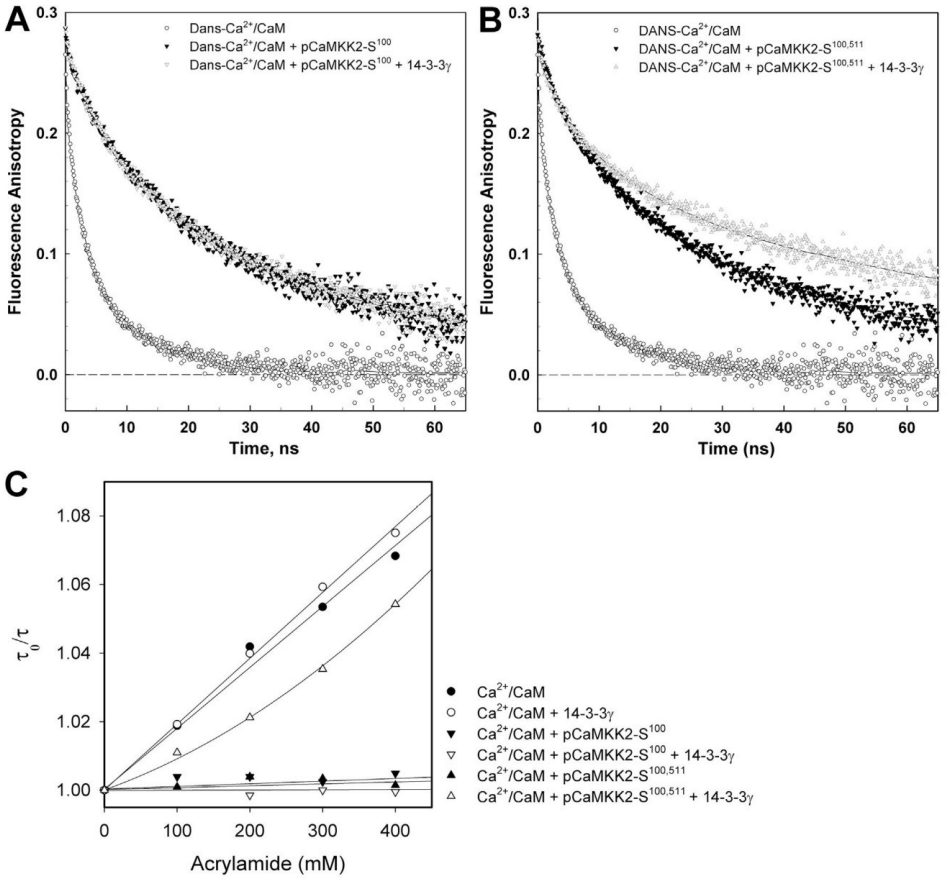

Fig. 6. Time-Resolved Dansyl Fluorescence Measurements. (A) Fluorescence anisotropy decays of free dansyl-Ca^{2+}/CaM (open circles) and dansyl-Ca^{2+}/CaM in the presence of pCaMKK2-S^{100} (closed triangles), and pCaMKK2-S^{100} and 14-3-3γ (open triangles). (B) Fluorescence anisotropy decays of free dansyl-Ca^{2+}/CaM (open circles) and dansyl-Ca^{2+}/CaM in the presence of pCaMKK2-$S^{100,511}$ (closed triangles) and pCaMKK2-$S^{100,511}$ and 14-3-3γ (open triangles). (C) Acrylamide quenching of dansyl-Ca^{2+}/CaM fluorescence. Quenching of free dansyl-Ca^{2+}/CaM (●) is dramatically reduced in the presence of pCaMKK2-S^{100} (▼) and pCaMKK2-$S^{100,511}$ (▲). Although 14-3-3γ addition to the dansyl-Ca^{2+}/CaM/pCaMKK2-S^{100} mixture only slightly increases the shielding of the dansyl fluorophore from the quencher (▽), its addition to the dansyl-Ca^{2+}/CaM/pCaMKK2-$S^{100,511}$ mixture significantly increases dansyl accessibility to acrylamide (△), indicating a conformational change of the complex. 14-3-3γ addition to dansyl-Ca^{2+}/CaM causes virtually no effect in the control sample (○).

likely reflecting the binding of the phosphorylated C-terminal motif of pCaMKK2-S^{100,511} to the binding groove of the second 14-3-3γ protomer that results in a formation of apparently larger rotor. Negligible changes in the τ_{mean} of the dansyl moiety, observed in the presence of 14-3-3γ, suggested that 14-3-3γ binding has no effect on the stability of the pCaMKK2:Ca^{2+}/CaM complex. This result was further corroborated by acrylamide quenching of dansyl-CaM fluorescence (Fig. 6C). More specifically, quenching of free dansyl-Ca^{2+}/CaM markedly decreased in the presence of both pCaMKK2 variants. Although 14-3-3γ addition to the pCaMKK2-S^{100}:Ca^{2+}/CaM complex caused only a slight increase in the shielding of the dansyl fluorophore from the quencher, 14-3-3γ addition to the pCaMKK2-S^{100,511}:Ca^{2+}/CaM complex resulted in a significant increase of dansyl accessibility to acrylamide, thus indicating a conformational change in the vicinity of bound Ca^{2+}/CaM, most likely due to the interaction between the C-terminal motif and 14-3-3γ.

3.8. Conformational behavior of CaMKK2 and its changes upon 14-3-3γ binding

Time-resolved tryptophan fluorescence measurements were then performed to investigate the conformational behavior of pCaMKK2-S^{100} upon 14-3-3γ binding. Four CaMKK2-S^{100} mutants containing a single tryptophan residue (Trp^{140}, Trp^{267}, Trp^{374} and Trp^{445}) were prepared (Fig. 1A). The sequence of CaMKK2$_{93-517}$ contains two tryptophan residues, Trp^{374} and Trp^{445}, both located within the C-lobe of the kinase domain (Fig. 1C). Therefore, mutants containing single Trp^{374} or Trp^{445} were created by mutating the other residue to Phe. Mutants containing Trp^{140} and Trp^{267} located within the N-terminal linker, close to the regulatory phosphorylation site Thr^{145}, and the N-lobe of the kinase domain, respectively, were generated by mutating both Trp^{374} and Trp^{445} to Phe and by introducing a single Trp residue at the desired position. The fluorescently silent 14-3-3γ noW missing all Trp residues was used in all tryptophan fluorescence measurements [52].

Fluorescence intensity decay measurements showed that the 14-3-3γ noW binding causes a small, albeit significant, increase in the τ_{mean} of Trp^{140} and Trp^{445}, whereas nonsignificant effects were assessed on mutants containing Trp^{267} and Trp^{374} (Table 4). The τ_{mean} prolongation of both mutants is clearly visible in the raw data shown in Fig. 7A and B, wherein the difference between fluorescence decays in the presence and absence of 14-3-3 is undoubtedly higher than the data noise level. The analysis of the lifetime distribution, shown in Fig. 7C and D, indicates an increase in the τ_{mean} of Trp^{140} upon 14-3-3 binding, mainly caused by the appearance of a new lifetime component centered around 8 ns, and a decrease in the intensity fractions associated with the shorter lifetime components. Similarly, 14-3-3 binding induced an increase in the τ_{mean} of Trp^{445}, mainly caused by the extension of the longest lifetime component around 5 ns and by the significant increase in its intensity fraction. The statistical significance of the observed difference is supported by the Monte Carlo confidence-interval analysis [53] shown in Fig. S7. The increase in τ_{mean} indicates a small 14-3-3γ binding-induced change of quenching interactions and/or polarity near these two Trp residues.

Table 4
Summary of time-resolved tryptophan fluorescence measurements.

pCaMKK-S^{100} mutant	τ_{mean} [a,b] (ns)	ϕ_1 (ns)	β_1	ϕ_2 (ns)	β_2	ϕ_3 [c] (ns)	β_3
W140	4.19	1.4	0.037			72	0.170
W140 + 14-3-3γ noW	4.34	0.8	0.021	3.5	0.029	100	0.161
W267	4.88	0.9	0.014			53	0.200
W267 + 14-3-3γ noW	4.97	0.9	0.004	5.3	0.006	79	0.197
W445	2.47	2.3	0.026			84	0.184
W445 + 14-3-3γ noW	2.59	2.8	0.041			> 100 [d]	0.171
W374	4.39	0.9	0.004			44	0.205
W374 + 14-3-3γ noW	4.37	0.5	0.005			61	0.206

[a] Mean lifetimes were calculated as $\tau_{mean} = \Sigma_i f_i \tau_i$, where f_i is an intensity fraction of the *i-th* lifetime component τ_i.
[b] S.D. value is ± 0.05 ns.
[c] S.D. value is about ± 10 ns.
[d] Poorly resolved correlation time of the overall protein rotation; SD is highly asymmetric to longer values. The resolution is primarily limited by a short lifetime value.

Subsequently, the segmental motions of inserted tryptophans were studied using the polarized time-resolved emission measurements. The fluorescence anisotropy decays of all four tryptophans revealed two classes of correlation times (Table 4). Short correlation times, with values up to few nanoseconds (ϕ_1), likely reflect fast segmental motion of the protein near the tryptophan residue, whereas significantly longer correlation times (ϕ_3 > 44 ns) likely reflect the overall rotational motion of pCaMKK2-S^{100}. In the case of the pCaMKK2-S^{100} W140 and W267 mutants, 14-3-3γ noW binding resulted in the appearance of a new correlation time component located around 3.5 − 5.3 ns (ϕ_2), which could reflect slightly modified internal dynamics of the pCaMKK2-S^{100} complex, induced by 14-3-3γ binding. Changes in the extent of segmental motion were assessed based on the change in the sum of amplitudes of fast anisotropy decay components ($\beta_{fast} = \beta_1 + \beta_2$) [54]. Similarly to the fluorescence lifetime measurements, small but significant changes in β_{fast} were observed only in mutants containing Trp^{140} and Trp^{445}, thus suggesting that complex formation increases protein flexibility in regions surrounding these two tryptophan residues.

Therefore, fluorescence lifetime and anisotropy results indicate that 14-3-3γ binding affects the conformation of CaMKK2 in several regions outside the N-terminal phosphorylated motif, including regions surrounding the Trp^{140} within the N-terminal extension and the Trp^{445} within the C-lobe of the kinase domain.

4. Discussion

The main aim of this study was to characterize the interaction between the 14-3-3 protein and CaMKK2. 14-3-3 proteins regulate the function of many enzymes through various mechanisms. For example, serotonin *N*-acetyltransferase and neutral trehalase Nth1 are activated through 14-3-3 protein-mediated structural modulation of their active sites [42,43]. In the case of phosphorylated tryptophan hydroxylase, 14-3-3 binding slows-down the dephosphorylation of key regulatory phosphosites [55]. Other mechanisms are based on the regulation of sub-cellular localization [56] and on the stabilization of the tertiary and/or quaternary structure of the bound enzyme [57]. Enzymes regulated in a 14-3-3-dependent manner also include many protein kinases [58], although the underlying mechanisms are not fully understood, primarily due to the lack of structural data.

Previous studies on phosphorylated CaMKK1 have shown that the 14-3-3 binding suppresses its catalytic activity [14,15]. Interestingly, enzyme activity measurements revealed that the activity of phosphorylated CaMKK2 is not suppressed but rather weakly enhanced upon complexation with 14-3-3γ (Fig. 2). This indicates that CaMKK isoforms differ in their 14-3-3-mediated regulations, maybe due to differences in their biochemical properties [6,7].

The SAXS results indicated that the complex formed between 14-3-3γ and pCaMKK2-S^{100} had an elongated and flexible conformation in which the kinase domain of CaMKK appears to directly interact with the 14-3-3γ dimer surfaces outside its central channel (Figs. 4C,D and 5A,B). The interaction between the kinase domain of pCaMKK2-S^{100} and 14-3-3γ was also indicated by the analysis, in terms of ensemble of conformations (Fig. 5C), which suggested that the 14-3-3γ:pCaMKK2-S^{100} complex is not as extended as the flexible linkers allow. Moreover,

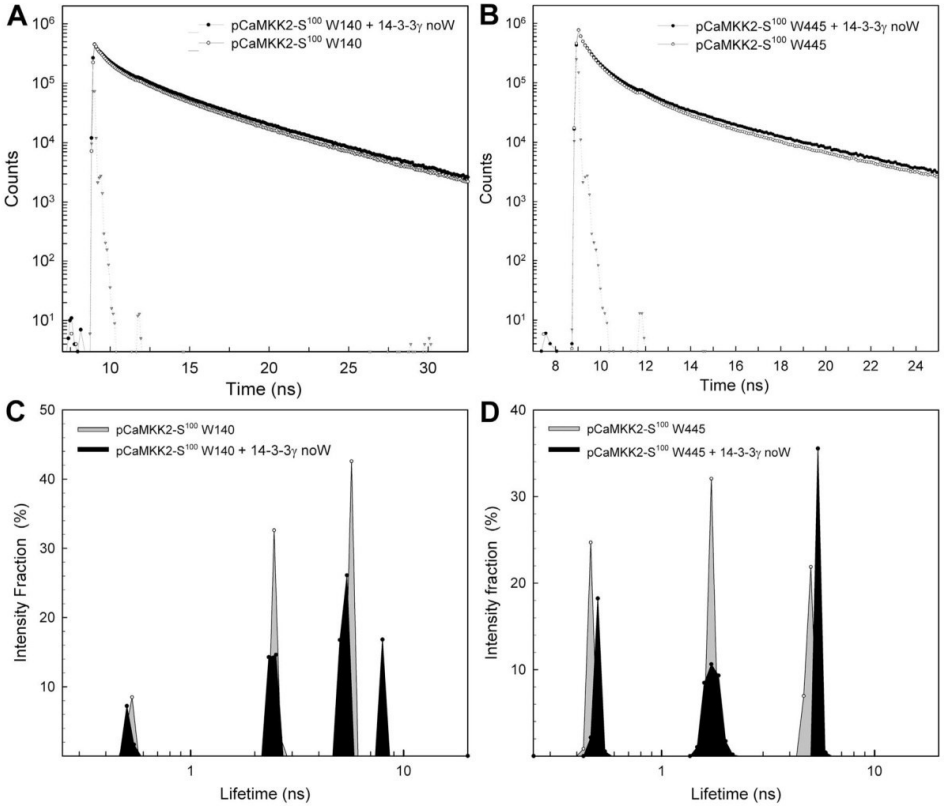

Fig. 7. Time-Resolved Tryptophan Fluorescence Measurements. (A) Normalized fluorescence intensity decays of pCaMKK2-S^{100} W140 mutant, in the absence (open circles) and presence (closed circles) of 14-3-3γ noW. Triangles denote instrument response function. (B) Same as (A) for pCaMKK2-S^{100} W445 mutant. (C) Excited state lifetime distribution of pCaMKK2-S^{100} W140 in the absence (gray-filled distribution) and presence of 14-3-3γ noW (black-filled distribution). (D) Same as (C) for pCaMKK2-S^{100} W445 mutant.

time-resolved fluorescence measurements of the pCaMKK2-S^{100} W445 mutant (Table 4 and Fig. 7) and the binding affinity of pCaMKK2-S^{100}, which was significantly higher than that of pepS100 phosphopeptide (Figs. 1D and S6), further corroborated the existence of contacts between 14-3-3γ and the kinase domain of CaMKK2. Although the second 14-3-3 binding motif at the C-terminus of CaMKK2 may not be significantly phosphorylated in vivo [11,12,14], the presence of this motif increased the overall stability of the complex and reduced its conformational flexibility (Figs. 1E and 4D, 6B). This most likely results from the immobilization of the C-terminal extension when the C-terminal motif is anchored to the second ligand binding groove of the 14-3-3γ dimer. The interaction between 14-3-3 and the kinase domain may be responsible for observed changes in the catalytic activity of CaMKK2 (Fig. 2). We may speculate that the 14-3-3γ binding affects the conformation of the CaMKK2 active site and/or changes its accessibility. Yet another possibility might be that the 14-3-3γ binding affects the interaction between the kinase domain and regulatory regions within the N- and C-terminal segments flanking the kinase domain.

CaMKK1 activity is inhibited by Thr^{108} phosphorylation (Thr^{145} in CaMKK2) [10,13]. In addition, a recent report indicated that the phosphorylation of this residue by AMPK suppresses the autonomous activity of rat CaMKK2 without significant effect on Ca^{2+}/CaM-dependent activity [59]. This threonine residue is located in the linker between the N-terminal 14-3-3 binding motif and the kinase domain (Fig. 1A) [10,13]. CaMKK2 also contains, in this region, serine residues Ser^{129}, Ser^{133}, Ser^{137} phosphorylated by cyclin-dependent kinase 5 and by glycogen synthase kinase 3, which are involved in the regulation of CaMKK2 autonomous activity and stability [9]. Time-resolved fluorescence measurements of the pCaMKK2-S^{100} W140 mutant showed that 14-3-3γ binding affects the structure of this region (Table 4 and Fig. 7). Therefore, structural changes in this region and/or its closeness to 14-3-3 may account for the previously reported protection of CaMKK1 Thr^{145} against dephosphorylation, which keeps CaMKK1 in the PKA-mediated inhibited state [14]. A similar mechanism may also be involved in the regulation of CaMKK2 as suggested by our observation that the 14-3-3γ binding slows down the dephosphorylation of pCaMKK2 by PP1 in vitro (Table S1 and Fig. S3). Alternatively, the 14-3-3 binding may inhibit CaMKK activity by affecting CaM binding to the C-terminus of CaMKK. However, fluorescence measurements with dansyl-CaM showed that this interaction is unaffected by 14-3-3 binding to the pCaMKK2:Ca^{2+}/CaM complex (Table 3 and Fig. 6).

The crystal structures of complexes between 14-3-3 and the 14-3-3 binding motifs of CaMKK showed that both phosphopeptides interact with the amphipathic groove of 14-3-3 similarly to other 14-3-3 complexes [33,37,40–42]. Nevertheless, in the case of the N-terminal motif, the interaction between the side-chain of Gln at the position +2 relative to pSer^{100} and the phosphate group appears to change the direction of the polypeptide chain (Fig. 3B). Interestingly, the superimposition of this structure with that of the ternary complex between the phosphopeptide derived from the C-terminus of plant plasma

membrane H^+-ATPase, plant 14-3-3C, and fusicoccin (Fig. 3F) [44] showed that the fusicoccin binding cavity stays empty due to the abrupt change in the direction of the C-terminal part of pepS100. Therefore, this protein-protein interaction might be stabilized by small-molecule compounds, as previously reported for other 14-3-3 complexes (reviewed in [60]), which is a potential strategy to inhibit the CaMKK activity.

Transparency document

The http://dx.doi.org/10.1016/j.bbagen.2018.04.006 associated this article can be found, in online version.

Acknowledgement

We thank Prof. Jaroslav Vecer for dansyl fluorescence data analysis, Dr. Petr Pompach and Dr. Petr Man for mass spectrometry analyses and Dr. Carlos V. Melo for proofreading the article.

Funding sources

This work was supported by the Czech Science Foundation (grant number 16-02739S), the Czech Academy of Sciences (Research Projects RVO: 67985823 of the Institute of Physiology), EU supported projects BIOCEV (CZ.1.05/1.1.00.02.0109) and Operational Programme "Research and Development for Innovation" (no. CZ.1.05/4.1.00/16.0340), Czech Infrastructure for Integrative Structural Biology (CIISB) project LM2015043, funded by MEYS CR, and by the H2020 Marie Curie Actions of the European Commission through the TASPPI project, Grant Agreement 675179.

Data deposition

The atomic coordinates and structure factors have been deposited in the Protein Data Bank, www.wwpdb.org (PDB ID codes 6EWW and 6FEL).

Author contributions

V.O. and T.O. designed research; K.P., O.P., S.K., D.K., D.L.S., P.H., and T.O. performed research; K.P., S.K., O.P., P.H., V.O., and T.O. analyzed data; and V.O. and T.O. wrote the paper.

Conflict of interest

The authors declare no conflict of interest.

Appendix A. Supplementary data

Supplementary data to this article can be found online at https://doi.org/10.1016/j.bbagen.2018.04.006.

References

[1] B. Haribabu, S.S. Hook, M.A. Selbert, E.G. Goldstein, E.D. Tomhave, A.M. Edelman, R. Snyderman, A.R. Means, Human calcium-calmodulin dependent protein kinase I: cDNA cloning, domain structure and activation by phosphorylation at threonine-177 by calcium-calmodulin dependent protein kinase I kinase, EMBO J. 14 (1995) 3679–3686.
[2] R.L. Hurley, K.A. Anderson, J.M. Franzone, B.E. Kemp, A.R. Means, L.A. Witters, The Ca2+/calmodulin-dependent protein kinase kinases are AMP-activated protein kinase kinases, J. Biol. Chem. 280 (2005) 29060–29066.
[3] K.A. Anderson, T.J. Ribar, F. Lin, P.K. Noeldner, M.F. Green, M.J. Muehlbauer, L.A. Witters, B.E. Kemp, A.R. Means, Hypothalamic CaMKK2 contributes to the regulation of energy balance, Cell Metab. 7 (2008) 377–388.
[4] L. Racioppi, A.R. Means, Calcium/calmodulin-dependent protein kinase kinase 2: roles in signaling and pathophysiology, J. Biol. Chem. 287 (2012) 31658–31665.
[5] H. Tokumitsu, T.R. Soderling, Requirements for calcium and calmodulin in the calmodulin kinase activation cascade, J. Biol. Chem. 271 (1996) 5617–5622.
[6] H. Tokumitsu, M. Muramatsu, M. Ikura, R. Kobayashi, Regulatory mechanism of Ca2+/calmodulin-dependent protein kinase kinase, J. Biol. Chem. 275 (2000) 20090–20095.
[7] K.A. Anderson, R.L. Means, Q.H. Huang, B.E. Kemp, E.G. Goldstein, M.A. Selbert, A.M. Edelman, R.T. Fremeau, A.R. Means, Components of a calmodulin-dependent protein kinase cascade. Molecular cloning, functional characterization and cellular localization of Ca2+/calmodulin-dependent protein kinase kinase beta, J. Biol. Chem. 273 (1998) 31880–31889.
[8] H. Tokumitsu, M. Iwabu, Y. Ishikawa, R. Kobayashi, Differential regulatory mechanism of Ca2+/calmodulin-dependent protein kinase kinase isoforms, Biochemistry 40 (2001) 13925–13932.
[9] M.F. Green, J.W. Scott, R. Steel, J.S. Oakhill, B.E. Kemp, A.R. Means, Ca2+/calmodulin-dependent protein kinase kinase beta is regulated by multisite phosphorylation, J. Biol. Chem. 286 (2011) 28066–28079.
[10] G.A. Wayman, H. Tokumitsu, T.R. Soderling, Inhibitory cross-talk by cAMP kinase on the calmodulin-dependent protein kinase cascade, J. Biol. Chem. 272 (1997) 16073–16076.
[11] M. Matsushita, A.C. Nairn, Inhibition of the Ca2+/calmodulin-dependent protein kinase I cascade by cAMP-dependent protein kinase, J. Biol. Chem. 274 (1999) 10086–10093.
[12] S. Okuno, T. Kitani, H. Fujisawa, Regulation of Ca(2+)/calmodulin-dependent protein kinase kinase alpha by cAMP-dependent protein kinase: I. Biochemical analysis, J. Biochem. 130 (2001) 503–513.
[13] T. Kitani, S. Okuno, H. Fujisawa, Regulation of ca(2+)/calmodulin-dependent protein kinase kinase alpha by cAMP-dependent protein kinase: II. Mutational analysis, J. Biochem. 130 (2001) 515–525.
[14] M.A. Davare, T. Saneyoshi, E.S. Guire, S.C. Nygaard, T.R. Soderling, Inhibition of calcium/calmodulin-dependent protein kinase kinase by protein 14-3-3, J. Biol. Chem. 279 (2004) 52191–52199.
[15] T. Ichimura, M. Taoka, Y. Hozumi, K. Goto, H. Tokumitsu, 14-3-3 proteins directly regulate Ca(2+)/calmodulin-dependent protein kinase kinase alpha through phosphorylation-dependent multisite binding, FEBS Lett. 582 (2008) 661–665.
[16] A.J. Muslin, J.W. Tanner, P.M. Allen, A.S. Shaw, Interaction of 14-3-3 with signaling proteins is mediated by the recognition of phosphoserine, Cell 84 (1996) 889–897.
[17] N.N. Sluchanko, N.B. Gusev, Moonlighting chaperone-like activity of the universal regulatory 14-3-3 proteins, FEBS J. 284 (2017) 1279–1295.
[18] T. Obsil, V. Obsilova, Structural basis of 14-3-3 protein functions, Semin. Cell Dev. Biol. 22 (2011) 663–672.
[19] F.H. Niesen, H. Berglund, M. Vedadi, The use of differential scanning fluorimetry to detect ligand interactions that promote protein stability, Nat. Protoc. 2 (2007) 2212–2221.
[20] V. Obsilova, P. Herman, J. Vecer, M. Sulc, J. Teisinger, T. Obsil, 14-3-3zeta C-terminal stretch changes its conformation upon ligand binding and phosphorylation at Thr232, J. Biol. Chem. 279 (2004) 4531–4540.
[21] B. Holakovska, L. Grycova, J. Bily, J. Teisinger, Characterization of calmodulin binding domains in TRPV2 and TRPV5 C-tails, Amino Acids 40 (2011) 741–748.
[22] O. Petrvalska, D. Kosek, Z. Kukacka, Z. Tosner, P. Man, J. Vecer, P. Herman, V. Obsilova, T. Obsil, Structural insight into the 14-3-3 protein-dependent inhibition of protein kinase ASK1 (apoptosis signal-regulating kinase 1), J. Biol. Chem. 291 (2016) 20753–20765.
[23] L. Rezabkova, P. Man, P. Novak, P. Herman, J. Vecer, V. Obsilova, T. Obsil, Structural basis for the 14-3-3 protein-dependent inhibition of the regulator of G protein signaling 3 (RGS3) function, J. Biol. Chem. 286 (2011) 43527–43536.
[24] D.I. Svergun, Determination of the regularization parameter in indirect-transform methods using perceptual criteria, J. Appl. Crystallogr. 25 (1992) 495–503.
[25] M.V. Petoukhov, D. Franke, A.V. Shkumatov, G. Tria, A.G. Kikhney, M. Gajda, C. Gorba, H.D. Mertens, P.V. Konarev, D.I. Svergun, New developments in the program package for small-angle scattering data analysis, J. Appl. Crystallogr. 45 (2012) 342–350.
[26] P.V. Konarev, V.V. Volkov, A.V. Sokolova, M.H.J. Koch, D.I. Svergun, PRIMUS: a windows PC-based system for small-angle scattering data analysis, J. Appl. Crystallogr. 36 (2003) 1277–1282.
[27] D.I. Svergun, Restoring low resolution structure of biological macromolecules from solution scattering using simulated annealing, Biophys. J. 76 (1999) 2879–2886.
[28] G. Tria, H.D. Mertens, M. Kachala, D.I. Svergun, Advanced ensemble modelling of flexible macromolecules using X-ray solution scattering, IUCrJ 2 (2015) 207–217.
[29] D. Kosek, S. Kylarova, K. Psenakova, L. Rezabkova, P. Herman, J. Vecer, V. Obsilova, T. Obsil, Biophysical and structural characterization of the thioredoxin-binding domain of protein kinase ASK1 and its interaction with reduced thioredoxin, J. Biol. Chem. 289 (2014) 24463–24474.
[30] W. Kabsch, Xds, Acta Crystallogr D Biol Crystallogr, 66 (2010), pp. 125–132.
[31] K.M. Sparta, M. Krug, U. Heinemann, U. Mueller, M.S. Weiss, Xdsapp2.0, J. Appl. Crystallogr. 49 (2016) 1085–1092.
[32] A. Vagin, A. Teplyakov, MOLREP: an automated program for molecular replacement, J. Appl. Crystallogr. 30 (1997) 1022–1025.
[33] M. Molzan, C. Ottmann, Synergistic binding of the phosphorylated S233- and S259-binding sites of C-RAF to one 14-3-3zeta dimer, J. Mol. Biol. 423 (2012) 486–495.
[34] P.D. Adams, P.V. Afonine, G. Bunkoczi, V.B. Chen, I.W. Davis, N. Echols, J.J. Headd, L.W. Hung, G.J. Kapral, R.W. Grosse-Kunstleve, A.J. McCoy, N.W. Moriarty, R. Oeffner, R.J. Read, D.C. Richardson, J.S. Richardson, T.C. Terwilliger, P.H. Zwart, PHENIX: a comprehensive python-based system for macromolecular structure solution, Acta Crystallogr. D Biol. Crystallogr. 66 (2010) 213–221.
[35] M. Kukimoto-Niino, S. Yoshikawa, T. Takagi, N. Ohsawa, Y. Tomabechi, T. Terada, M. Shirouzu, A. Suzuki, S. Lee, T. Yamauchi, M. Okada-Iwabu, M. Iwabu, T. Kadowaki, Y. Minokoshi, S. Yokoyama, Crystal structure of the ca(2)

(+)/calmodulin-dependent protein kinase kinase in complex with the inhibitor STO-609, J. Biol. Chem. 286 (2011) 22570–22579.
[36] M.B. Yaffe, K. Rittinger, S. Volinia, P.R. Caron, A. Aitken, H. Leffers, S.J. Gamblin, S.J. Smerdon, L.C. Cantley, The structural basis for 14-3-3: phosphopeptide binding specificity, Cell 91 (1997) 961–971.
[37] K. Rittinger, J. Budman, J. Xu, S. Volinia, L.C. Cantley, S.J. Smerdon, S.J. Gamblin, M.B. Yaffe, Structural analysis of 14-3-3 phosphopeptide complexes identifies a dual role for the nuclear export signal of 14-3-3 in ligand binding, Mol. Cell 4 (1999) 153–166.
[38] C. Johnson, S. Crowther, M.J. Stafford, D.G. Campbell, R. Toth, C. MacKintosh, Bioinformatic and experimental survey of 14-3-3-binding sites, Biochem. J. 427 (2010) 69–78.
[39] J. Silhan, V. Obsilova, J. Vecer, P. Herman, M. Sulc, J. Teisinger, T. Obsil, 14-3-3 protein C-terminal stretch occupies ligand binding groove and is displaced by phosphopeptide binding, J. Biol. Chem. 279 (2004) 49113–49119.
[40] R. Rose, M. Rose, C. Ottmann, Identification and structural characterization of two 14-3-3 binding sites in the human peptidylarginine deiminase type VI, J. Struct. Biol. 180 (2012) 65–72.
[41] N.N. Sluchanko, S. Beelen, A.A. Kulikova, S.D. Weeks, A.A. Antson, N.B. Gusev, S.V. Strelkov, Structural basis for the interaction of a human small heat shock protein with the 14-3-3 universal signaling regulator, Structure 25 (2017) 305–316.
[42] M. Alblova, A. Smidova, V. Docekal, J. Vesely, P. Herman, V. Obsilova, T. Obsil, Molecular basis of the 14-3-3 protein-dependent activation of yeast neutral trehalase Nth1, Proc. Natl. Acad. Sci. U. S. A. 114 (2017) E9811–E9820.
[43] T. Obsil, R. Ghirlando, D.C. Klein, S. Ganguly, F. Dyda, Crystal structure of the 14-3-3 zeta: serotonin N-acetyltransferase complex. A role for scaffolding in enzyme regulation, Cell 105 (2001) 257–267.
[44] M. Wurtele, C. Jelich-Ottmann, A. Wittinghofer, C. Oecking, Structural view of a fungal toxin acting on a 14-3-3 regulatory complex, EMBO J. 22 (2003) 987–994.
[45] M. Kacirova, J. Novacek, P. Man, V. Obsilova, T. Obsil, Structural basis for the 14-3-3 protein-dependent inhibition of Phosducin function, Biophys. J. 112 (2017) 1339–1349.
[46] D.M. Bustos, The role of protein disorder in the 14-3-3 interaction network, Mol. BioSyst. 8 (2012) 178–184.
[47] T. Ishida, K. Kinoshita, PrDOS: prediction of disordered protein regions from amino acid sequence, Nucleic Acids Res. 35 (2007) W460–464.
[48] Z. Dosztanyi, V. Csizmok, P. Tompa, I. Simon, IUPred: web server for the prediction of intrinsically unstructured regions of proteins based on estimated energy content, Bioinformatics 21 (2005) 3433–3434.
[49] V. Receveur-Brechot, D. Durand, How random are intrinsically disordered proteins? A small angle scattering perspective, Curr. Protein Pept. Sci. 13 (2012) 55–75.
[50] R.P. Rambo, Resolving individual components in protein-RNA complexes using small-angle X-ray scattering experiments, Methods Enzymol. 558 (2015) 363–390.
[51] R.L. Kincaid, M. Vaughan, J.C. Osborne Jr., V.A. Tkachuk, Ca2+ −dependent interaction of 5-dimethylaminonaphthalene-1-sulfonyl-calmodulin with cyclic nucleotide phosphodiesterase, calcineurin, and troponin I, J. Biol. Chem. 257 (1982) 10638–10643.
[52] L. Rezabkova, E. Boura, P. Herman, J. Vecer, L. Bourova, M. Sulc, P. Svoboda, V. Obsilova, T. Obsil, 14-3-3 protein interacts with and affects the structure of RGS domain of regulator of G protein signaling 3 (RGS3), J. Struct. Biol. 170 (2010) 451–461.
[53] P. Herman, J.C. Lee, The advantage of global fitting of data involving complex linked reactions, in: A.W.W. Fenton (Ed.), Allostery: Methods and Protocols, vol. 796, Humana Press Inc., New York, 2012, pp. 399–421.
[54] L. Rezabkova, M. Kacirova, M. Sulc, P. Herman, J. Vecer, M. Stepanek, V. Obsilova, T. Obsil, Structural modulation of phosducin by phosphorylation and 14-3-3 protein binding, Biophys. J. 103 (2012) 1960–1969.
[55] U. Banik, G.A. Wang, P.D. Wagner, S. Kaufman, Interaction of phosphorylated tryptophan hydroxylase with 14-3-3 proteins, J. Biol. Chem. 272 (1997) 26219–26225.
[56] A. Kumagai, W.G. Dunphy, Binding of 14-3-3 proteins and nuclear export control the intracellular localization of the mitotic inducer Cdc25, Genes Dev. 13 (1999) 1067–1072.
[57] C. Ottmann, S. Marco, N. Jaspert, C. Marcon, N. Schauer, M. Weyand, C. Vandermeeren, G. Duby, M. Boutry, A. Wittinghofer, J.L. Rigaud, C. Oecking, Structure of a 14-3-3 coordinated hexamer of the plant plasma membrane H +-ATPase by combining X-ray crystallography and electron cryomicroscopy, Mol. Cell 25 (2007) 427–440.
[58] M. Tinti, F. Madeira, G. Murugesan, G. Hoxhaj, R. Toth, C. Mackintosh, ANIA: ANnotation and integrated analysis of the 14-3-3 interactome, Database (Oxford) 2014 (2014) bat085, , http://dx.doi.org/10.1093/database/bat085.
[59] A. Nakanishi, N. Hatano, Y. Fujiwara, A. Sha'ri, S. Takabatake, H. Akano, N. Kanayama, M. Magari, N. Nozaki, H. Tokumitsu, AMP-activated protein kinase-mediated feedback phosphorylation controls the Ca(2+)/calmodulin (CaM) dependence of Ca(2+)/CaM-dependent protein kinase kinase beta, J. Biol. Chem. 292 19804–19813.
[60] L.M. Stevers, E. Sijbesma, M. Botta, C. MacKintosh, T. Obsil, I. Landrieu, Y. Cau, A.J. Wilson, A. Karawajczyk, J. Eickhoff, J. Davis, M. Hann, R.G. Mahony, L. Doveston, C. Ottmann Brunsveld, Modulators of 14-3-3 protein-protein interactions, J. Med. Chem. (2017 Oct. 19), http://dx.doi.org/10.1021/acs.jmedchem.7b00574 (Epub ahead of print).

Table S1

Dephosphorylation of CaMKK2 at pThr^{145} and pSer^{495} by PP1 in the presence and absence of 14-3-3γ.

Site	peptide form	m/z (charge)	Dephosphorylation time (min)					
			pCaMKK2			pCaMKK2 + 14-3-3γ		
			0	1.5	7	0	1.5	7
Thr145[a]	P	695,9556 (5+)	2.5E+07	2.8E+07	2.2E+07	2.0E+07	4.0E+07	1.6E+07
	not-P	679,9625 (5+)	1.3E+07	3.3E+07	3.7E+07	1.3E+07	1.3E+07	3.2E+07
	ratio non-P/P[c]		**0.52**	**1.2**	**1.7**	**0.65**	**0.33**	**2.0**
Ser495[b]	P	570,2900 (5+)	2.3E+07	2.5E+07	5.4E+06	1.8E+06	4.0E+06	4.2E+06
	not-P	554,2970 (5+)	0.0E+00	2.9E+06	6.2E+06	0.0E+00	0.0E+00	0.0E+00
	ratio non-P/P		**0**	**0.12**	**1.1**	**0**	**0**	**0**

[a]Peptide sequence PSLPYSPVSSPQSSPRLPRRPT^{145}VESHHVSIT

[b]Peptide sequence VKTMIRKRS^{495}FGNPFEGSRREERS

[c]Phosphorylated CaMKK2$_{93\text{-}517}$ D^{330}A (kinase dead mutant) in the presence and absence of 14-3-3γ was dephosphorylated by protein phosphatase 1 (PP1, catalytic subunit α-isoform from rabbit). Dephosphorylation by PP1 (Sigma-Aldrich, USA) with a specific activity 5,000 units/mg) was performed at 30 °C in buffer containing 50 mM HEPES (pH 7.5), 100 mM NaCl, 2 mM DTT, 1 mM $MnCl_2$, and 0.01% NP-40. The reaction mixture contained 11 μM CaMKK2 D^{330}A, 34 μM 14-3-3γ (where needed) and PP1 in an optimized molar ratio of 1:250 (enzyme/substrate). Reactions were stopped after 0, 1.5 and 7 min by adding 100 mM β-glycerolphosphate (Sigma-Aldroch, USA) and immediate freezing in liquid nitrogen. Analysis was started by an online digestion of sample solution containing 64 pmol of CaMKK2 on a pepsin column (66 μL bed volume, flow rate 100 μL.min^{-1}, 3 min). Generated peptides were trapped and desalted online on a Peptide microtrap column (Optimize Technologies, Oregon City, OR) and separated on a C18 reversed phase column (ZORBAX 300SB-C18 3.5 μm, 0.5 × 35 mm, Agilent, Santa Clara, CA) using a linear gradient 10–45% B in 40 min, where solvent A was 2% acetonitrile/0.4% formic acid in water, solvent B 95% acetonitrile/5% water/0.4% formic acid. The column was interfaced with the ESI source of a 15T FT-ICR mass spectrometer (SolariX XR, Bruker Daltonics, Bremen, Germany) operating in MS/MS mode. Peptides were identified by a MASCOT search against a database containing the sequence of human CaMKK2. Intensities of extracted ion chromatograms of first monoisotopes of phosphorylated (P) and non-phosphorylated (not-P) peptides were used to calculate ratios between non-phosphorylated and phosphorylated forms.

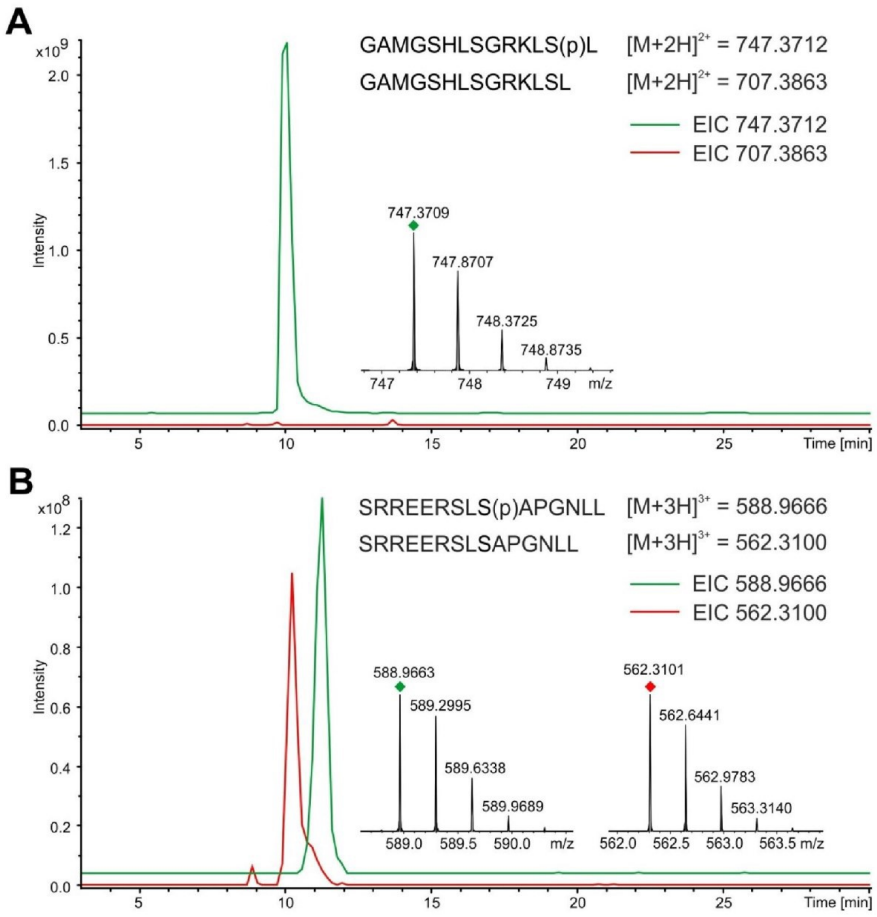

Figure S2. Related to Figure 1.

Detection of CaMKK-S^{100,511} phosphorylated peptides by FT-ICR mass spectrometry. (A) Extract ion chromatogram (EIC) of phosphorylated GAMGSHLSGRKLS^{100}L peptide shown in green, observed at m/z 747.3709 (2+). The red line represents the EIC of the non-phosphorylated form of the same peptide observed at m/z 707.3863 (2+). The inset shows the zoomed, high-resolution MS spectrum of phosphorylated GAMGSHLSGRKLS^{100}L. (B) Extract ion chromatograms of the phosphorylated SRREERSLS^{511}APGNLL peptide shown in green, observed at m/z 588.9663 (3+), and of non-phosphorylated form, observed at m/z 562.3101 (3+), which is shown in red. The inset shows the zoomed, high-resolution MS spectra of phosphorylated and non-phosphorylated SRREERSLS^{511}APGNLL peptides. The phosphorylation sites in both peptides were determined based on the collision-induced dissociation spectra. See also Figure S1A.

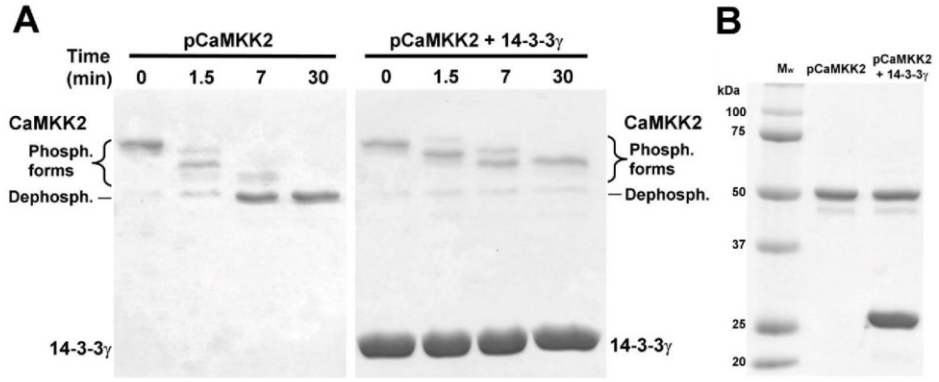

Figure S3. Related to Figure 2.

14-3-3γ Binding Slows Down Dephosphorylation of CaMKK2. (A) Phosphorylated $CaMKK2_{93\text{-}517}$ $D^{330}A$ (kinase dead mutant) in the presence and absence of 14-3-3γ was dephosphorylated by type 1 protein phosphatase (PP1, catalytic subunit α-isoform from rabbit). Dephosphorylation by PP1 (Sigma-Aldrich, USA) with a specific activity 5,000 units/mg) was performed at 30 °C in buffer containing 50 mM HEPES (pH 7.5), 100 mM NaCl, 2 mM DTT, 1 mM $MnCl_2$, and 0.01% NP-40. The reaction mixture contained 11 μM CaMKK2 $D^{330}A$, 34 μM 14-3-3γ (where needed) and PP1 in an optimized molar ratio of 1:250 (enzyme/substrate). Reactions were stopped after 0, 1.5 and 7 min by adding 100 mM β-glycerolphosphate (Sigma-Aldroch, USA), mixing with SDS reducing sample buffer and boiling for 5 min. Sample analysis was performed using 12% Phos-tag SDS-PAGE with 50 μM Phos-tag (FUJIFILM Wako Pure Chemical Corp., Japan). (B) Samples used in (A) resolved on 12% SDS-PAGE. See also Figure 2.

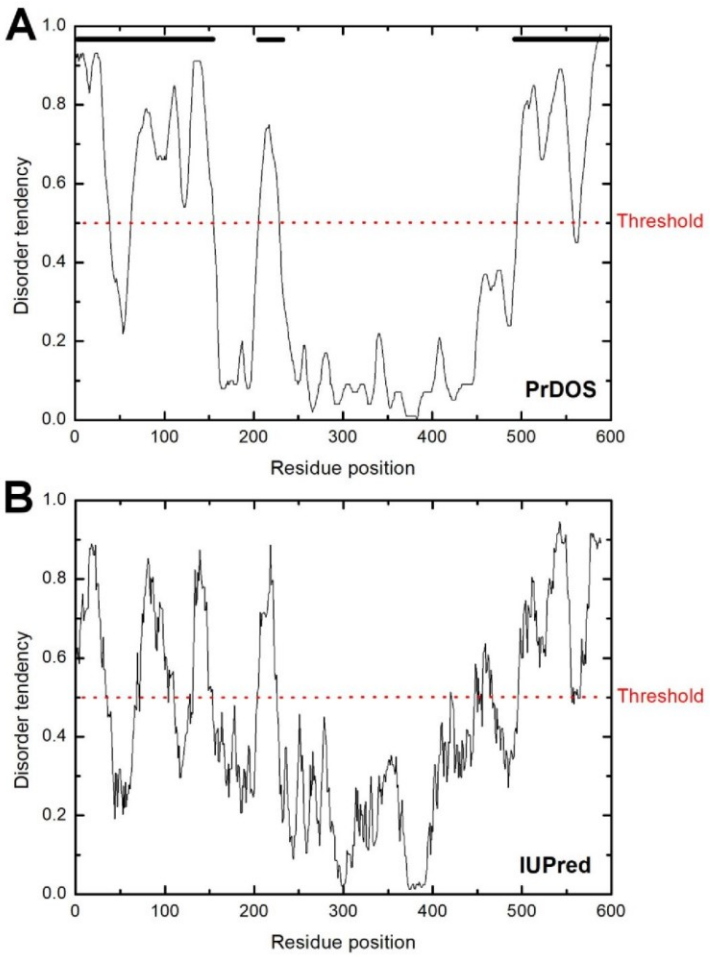

Figure S4. Related to Figure 4D.

Bioinformatics analysis of CaMKK2. Disorder prediction using PrDOS (A) (Ishida and Kinoshita, 2007) and IUPred (B) (Dosztanyi et al., 2005) predictors suggests that both the N-terminal (residues 1-125) and the C-terminal (residues 500-588) tails of CaMKK2 are unstructured. See also Figure 4D.

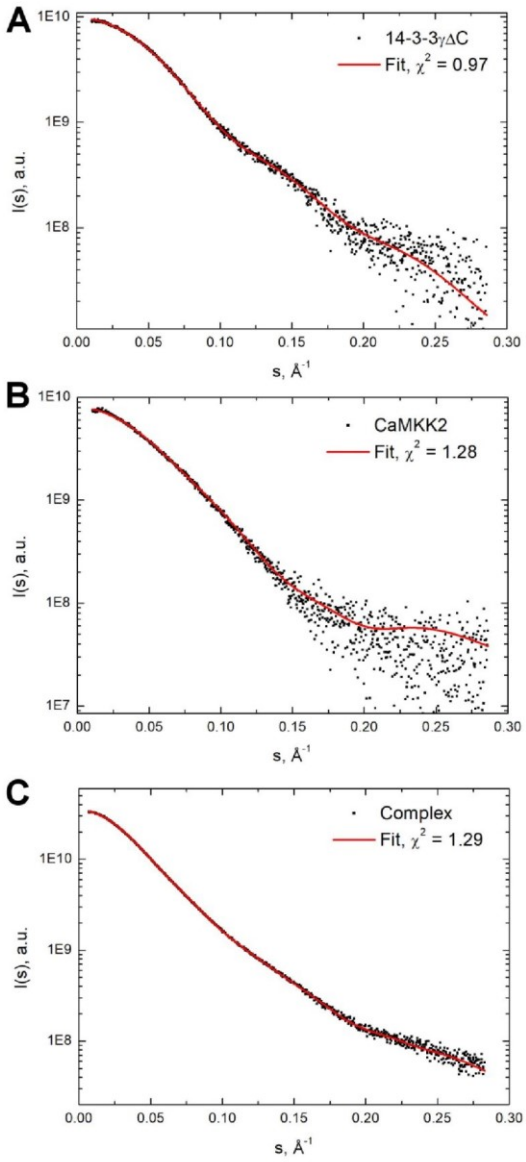

Figure S5. Related to Figure 5A.

Ab initio shape reconstruction of the pCaMKK2-S^{100}:14-3-3γ complex using MONSA. Fits of the simulated scattering curves versus the experimental SAXS data of 14-3-3γΔC (A), CaMKK2-S^{100} (B) and the 14-3-3γΔC:pCaMKK2-S^{100} (2:1) complex (C). See also Figure 5A.

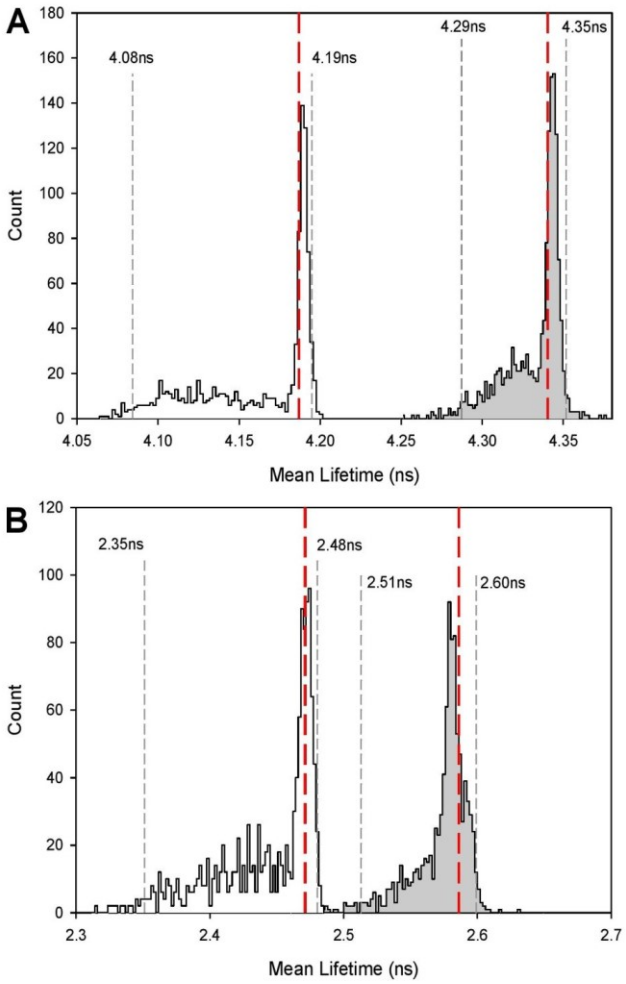

Figure S7. Related to Table 4 and Figure 7.

Statistical significance of observed differences in mean fluorescence lifetimes. Rigorous confidence-interval analysis of the mean fluorescence lifetime of the pCaMKK2-S^{100} W140 (A) and W445 (B) mutants in the absence (white-filled histogram) and presence (gray-filled histogram) of 14-3-3γ noW. Histograms constructed from 1000 Monte-Carlo MEM-fitting cycles (Herman and Lee, 2012) represent the probability of recovering a particular mean fluorescence lifetime from the data shown in Fig. 6 A,B. Dashed lines border 95% confidence intervals (2 standard deviations), the red line indicates the best-fitted value of Table 4. The histograms show that the mean fluorescence lifetime of the complex significantly increases in the presence of 14-3-3γ noW. See also Table 4 and Figure 7.

References

Dosztanyi, Z., Csizmok, V., Tompa, P., and Simon, I. (2005). IUPred: web server for the prediction of intrinsically unstructured regions of proteins based on estimated energy content. Bioinformatics *21*, 3433-3434.

Herman, P., and Lee, J.C. (2012). The advantage of global fitting of data involving complex linked reactions In Allostery: Methods and Protocols, A.W.W. Fenton, ed. (New York: Humana Press Inc.), pp. 399-421.

Ishida, T., and Kinoshita, K. (2007). PrDOS: prediction of disordered protein regions from amino acid sequence. Nucleic Acids Res *35*, W460-464.

7.2 Supplement S2

7.2.1 Interaction of an IκBα peptide with 14-3-3

Madita Wolter‡, **Domenico Lentini Santo**‡, Petr Herman, Alice Ballone, Federica Centorrino, Tomas Obsil and Christian Ottmann. Interaction of an IκBα peptide with 14-3-3. *ACS Omega* 5(10):5380-5388 (2020).

‡ Equal contribution

My contribution: Expression and purification of 14-3-3ζ noW for time-resolved tryptophan fluorescence measurements, sample preparation for tryptophan measurements.

ACS OMEGA

http://pubs.acs.org/journal/acsodf

Article

Interaction of an IκBα Peptide with 14-3-3

Madita Wolter, Domenico Lentini Santo, Petr Herman, Alice Ballone, Federica Centorrino, Tomas Obsil,* and Christian Ottmann*

Cite This: https://dx.doi.org/10.1021/acsomega.9b04413

Read Online

ACCESS | Metrics & More | Article Recommendations | Supporting Information

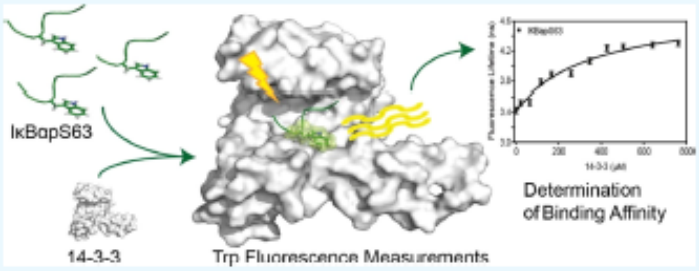

ABSTRACT: Inflammatory responses mediated by the transcription factor nuclear factor kappa-light-chain enhancer of activated B cells (NF-κB) play key roles in immunity, autoimmune diseases, and cancer. NF-κB is directly regulated through protein−protein interactions, including those with IκB and 14-3-3 proteins. These two important regulatory proteins have been reported to interact with each other, although little is known about this interaction. We analyzed the inhibitor of nuclear factor kappa B α (IκBα)/14-3-3σ interaction via a peptide/protein-based approach. Structural data were acquired via X-ray crystallography, while binding affinities were measured with fluorescence polarization assays and time-resolved tryptophan fluorescence. A high-resolution crystal structure (1.13 Å) of the uncommon 14-3-3 interaction motif of IκBα (IκBαpS63) in a complex with 14-3-3σ was evaluated. This motif harbors a tryptophan that makes this crystal structure the first one with such a residue visible in the electron density at that position. We used this tryptophan to determine the binding affinity of the unlabeled IκBα peptide to 14-3-3 via tryptophan fluorescence decay measurements.

INTRODUCTION

The κB-protein family is well known for their involvement in cell proliferation, cell survival, apoptosis, and regulation of the immune response.[1−4] The family is divided into transcription factors, summarized as nuclear factor kappa-light-chain enhancer of activated B cells (NF-κB), and their inhibitors (IκB). NF-κB is sequestered by IκB in the cytosol, and upon activation, IκB is phosphorylated and degraded, while NF-κB is translocated into the nucleus. The transcriptional activity of NF-κB regulates over 500 genes, and many of those are involved in a variety of diseases.[5] The most abundant representatives of this protein family are the heterodimer p50/p65 forming NF-κB and its inhibitor of nuclear factor kappa B α (IκBα), which is fundamental for the regulation of NF-κB activity.[6]

The most prominent regulatory pathway of IκBα is its phosphorylation at Ser32 and Ser36, which induces ubiquitination and proteasomal degradation of IκBα.[7,8] Several studies reported IκBα as an essential component for the inhibition of the transcriptional activity of NF-κB,[9−11] with the nuclear export of the IκBα/p65 complex depending on a third binding partner, the 14-3-3 proteins.[12] Overexpression of 14-3-3 increases the IκBα amount in the cytosol, while mutation of the possible IκBα motifs for 14-3-3 binding leads to an increased nuclear signal for both IκBα and NF-κB (Figure 1A).[12]

The 14-3-3 proteins are dimeric scaffold proteins that interact with several hundred different proteins.[13] The seven human isoforms (β, γ, ε, ζ, η, σ, and τ) are highly abundant in almost all human cells, and they exist as homo- or heterodimers.[14] The 14-3-3 monomer consists of nine helices that form an amphipathic binding groove. By binding one or two interaction partners within the two binding grooves of the 14-3-3 dimer, the activity or cellular localization of the target proteins is altered.[15] Interaction partners of 14-3-3 bind to 14-3-3 via distinguished phosphorylated motives in most often unstructured regions.[16]

Physical interaction of 14-3-3 and IκBα was demonstrated by co-immunoprecipitation, whereby the truncation analysis of

Received: December 22, 2019
Accepted: February 19, 2020

ACS Publications © XXXX American Chemical Society

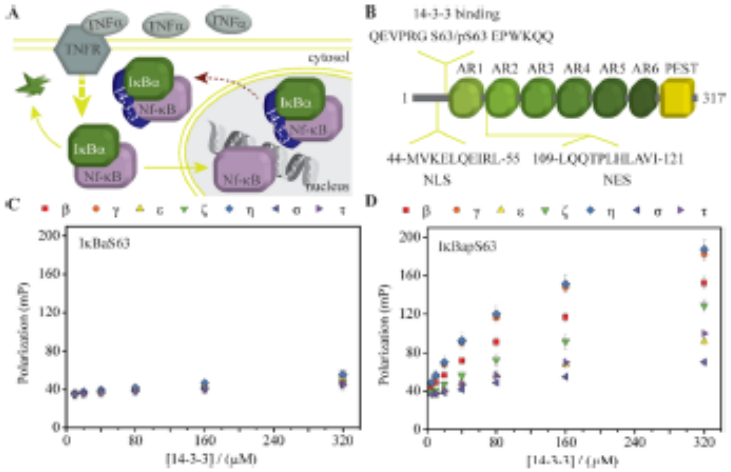

Figure 1. Phosphorylated IκBα peptide bound to 14-3-3. (A) Schematic representation of the key elements of the NF-κB pathway. In short, upon an inflammatory signal (here represented via TNFα and its receptor TNFR), a signaling cascade (thick dashed arrow) leads to proteasomal degradation of IκBα and translocation of NF-κB into the nucleus. Binding of 14-3-3 to IκBα and NF-κB is required for either nuclear export or cytosolic retention of the IκBα/NF-κB complex (red dashed arrow). (B) IκBα protein consists of an unstructured N-terminus, six helical ankyrin repeats, and the proline (P), glutamic acid (E), serine (S), and threonine (T) rich (PEST) domain. The 14-3-3 is supposed to bind to S63 at the unstructured N-terminal region. (C) Fluorescence polarization (FP) with the IκBαS63 peptide and all human 14-3-3 isoforms. (D) FP with the IκBαpS63 peptide and all human 14-3-3 isoforms.

IκBα suggested only one active 14-3-3 binding motif.[12] This motif, 59-PRGSEPW-67, follows the 14-3-3 binding motif RXpSXP, although phosphorylation of S63 is not yet reported. Co-immunoprecipitation of the IκBα/14-3-3 complex in the presence and absence of phosphatases revealed no significant differences, indicating that the phosphorylation of this residue might not be required for binding.[12] However, later studies showed that 14-3-3 binding protects its interaction partners from phosphatases,[17−19] wherefore further investigations are needed to confirm the phosphorylation status of S63 of IκBα. Nevertheless, this region of IκBα is most likely unstructured and therefore compatible with 14-3-3 binding. Fortunately, the binding sequence of IκBα contains a Trp residue at position 66. An aromatic amino acid at this position, +3 from the phosphosite, is rare within the known 14-3-3 interactome, which makes this Trp especially interesting. It has been well documented that Trp is an environmentally sensitive fluorophore that is able to reflect even subtle changes in its interaction network by spectral shifts and changes in its quantum yield and fluorescence lifetime.[20−22] The specific Trp response depends on a number of intramolecular and/or solvent interactions (e.g., Coulombic interaction, local polarity, H-bonding, Trp mobility, etc.), all of which depend on a detailed protein structure.[23,24] Trp emission can be therefore used for monitoring binding-induced conformational transitions and variations of microenvironmental polarity. Generally, increased hydrophobicity leads to blue spectral shift and prolonged fluorescence lifetime of indole emission.[25] We, therefore, utilized Trp66 fluorescence for the detection of interaction between IκBα peptides and the 14-3-3 protein.

In this study, the interaction of IκBα and 14-3-3 is characterized by a peptide-based approach. The binding of the IκBα peptide to 14-3-3 was measured by fluorescence polarization (FP) assay and the interface of IκBα and 14-3-3 was structurally characterized by X-ray crystallography. Furthermore, the intrinsic fluorescence of Trp66 of the peptide was used to establish a label-free method for the determination of binding affinities based on fluorescence decay. Our findings expand our knowledge of the IκBα/14-3-3 interaction and further provide a technique for the characterization of binding affinities.

RESULTS

14-3-3 Binding Motif of IκBα. The IκBα protein contains only one 14-3-3 binding site, which follows a typical 14-3-3 binding motif, 57-PRGSEP-66. To investigate the binding affinity of 14-3-3 and IκBα, two peptides were synthesized, representing the unphosphorylated (IκBαS63) and phosphorylated (IκBαpS63) binding motifs (Figure 1B). In both peptides, the centered Ser63 is flanked by six amino acids on each side of the wild-type sequence of IκBα.

For the initial measurements of the binding affinities, the peptides were N-terminally labeled with a fluorescein isothiocyanate (FITC) dye and fluorescence polarization (FP) assays were performed for both peptides with all seven human 14-3-3 isoforms (Figure 1C,D). The unphosphorylated peptide showed no affinity to either of the seven isoforms, whereas the phosphorylated peptide showed binding. No peptide reached sufficient binding for a reliable calculation of dissociation constant (K_D), although differences between the isoforms were detectable. The K_D values of IκBαpS63 and 14-3-3 are expected to be in the high micromolar to millimolar range, with the best binding to 14-3-3η and the weakest binding to 14-3-3σ (Figure 1D).

This binding behavior was previously reported in the literature for peptides representing 14-3-3 binding motifs.[26−28] In those cases, a second binding site was essential for sufficient representation of the bivalent binding to the 14-3-3 dimer. Therefore, we elaborated on a hypothetical presence of additional binding sites with the prediction server 14-3-3pred.[29] This server analyzes the amino acid sequence of 14-3-3 interaction partners with three different methods, resulting in

https://dx.doi.org/10.1021/acsomega.9b04413
ACS Omega XXXX, XXX, XXX−XXX

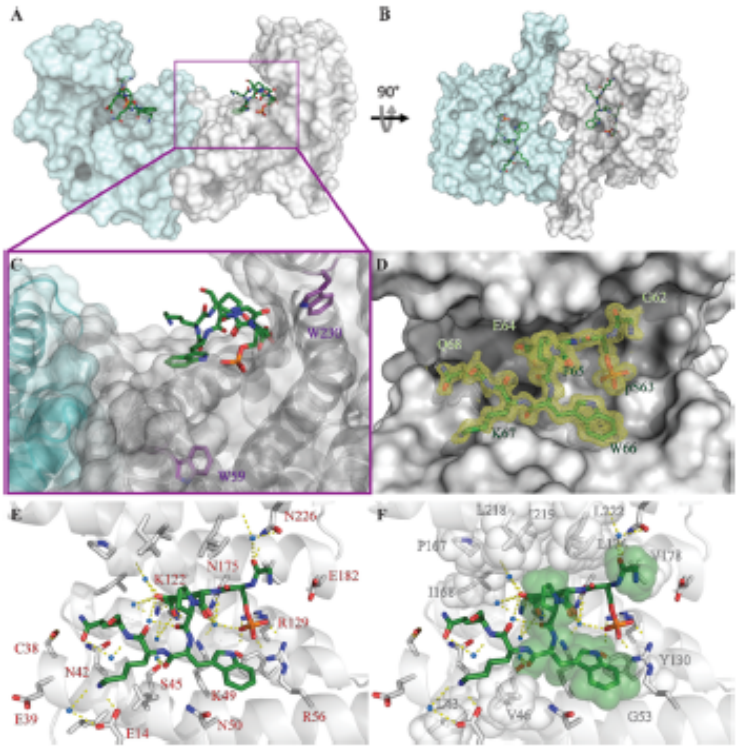

Figure 2. Crystal structure of the interface of the IκBαpS63 peptide and 14-3-3σΔC. Side (A) and top (B) views of the surface of a 14-3-3 dimer, with IκBαpS63 shown as green sticks in the binding groove of each monomer. (C) Zoom-in view shows the transparent surface and cartoon display of 14-3-3 with Trp59 and Trp230 of 14-3-3σ in violet. (D) IκBαpS63 peptide with eight of 13 amino acids covered by the electron density map (yellow mesh, $\sigma = 1$, carve = 1.3 Å). (E) Polar contacts (yellow dashed lines) between IκBαpS63, 14-3-3σΔC, and the water shell (blue spheres). (F) Possible hydrophobic contacts indicated via sphere representation of hydrophobic residue PDB ID: 6Y1J.

a score for each method plus an overall score. The IκBα sequence revealed only one site, pT168 (sequence: VLTQSCpT168TPHL; Supporting Information, Table 1), as a likely binding site. This residue is located next to the second ankyrin repeat of the IκBα protein (Supporting Information, Figure S1), and previous truncation assays did not reveal any effect on the 14-3-3 binding.[12] Therefore, we continued with the single phosphorylated IκBαpS63 peptide only.

Crystal Structure of IκBα Peptide with 14-3-3σ with Truncated C-Terminus ΔC232-248 (14-3-3σΔC). To obtain structural information on the binding interface, co-crystallization trials were performed. The complex of IκBαpS63 with 14-3-3σΔC was grown to the best diffracting crystals among all 14-3-3 isoforms, allowing to solve the structure with a high resolution of 1.13 Å (PDB ID: 6Y1J, Supporting Information, Table S2). The crystals belonged to the space group C2221, with one 14-3-3 monomer in the asymmetric unit. One peptide is binding in each of the two binding grooves of the 14-3-3 dimer (Figure 2A,B). The peptide is binding in the proximity of both tryptophan residues of 14-3-3, Trp59, and Trp230 (Figure 2C). In total, seven of the 13 amino acids of the peptide could be assigned to the electron density map (Figure 2D), whereas pSer63 till Trp66 is the most rigid amino acids with the lowest B factors (Supporting Information, Figure S2). Consistently with other 14-3-3/phosphopeptide structures Arg56, Arg129, and Tyr130 of the protein form polar contacts with the phospho group of IκBαpS63. Except for phosphoserine, the only additional direct polar contact detected by Pymol software appeared to be between Lys67 of the peptide and Glu14 of the protein (Figure 2E). Nevertheless, more polar contacts are mediated via waters, like Gly62 of the peptide with Asn226 and the backbone of Leu222 of the protein, Glu64 of the peptide and the backbone of Pro167 and Lys122 of the protein, and the backbone of Trp66 of the peptide and Ser45 of the protein. Additionally, there are hydrophobic contacts between Gly62 and Val178, Pro65 and Leu218, Ile219, Leu122, and Trp66, and the aliphatic chain of Lys46 and Gly53, Lys67 and Val46 (Figure 2F).

Measurement of K_D via Mean Tryptophan Fluorescence Lifetime. The crystal structures of IκBαpS63 and 14-3-3σΔC revealed extensive contacts between the Trp66 residue and the binding groove of 14-3-3, with the indole moiety being located in a more hydrophobic environment. This binding mode suggested that the mean fluorescence lifetime τ_{mean} of Trp66 might change upon peptide binding and can be therefore used to detect the binding of the peptide without an artificial fluorescence labeling. To separate the fluorescence of the peptide from the Trp fluorescence of 14-3-3ζ, we made 14-3-3ζ fluorescently silent by mutating its two tryptophan residues, Trp59 and Trp228 (equals Trp230 in 14-3-3σ), to phenylalanine (W59F and W228F double mutation of 14-3-3ζ (14-3-3ζnoW)). Then, only the fluorescence of the peptide is detected.

https://dx.doi.org/10.1021/acsomega.9b04413
ACS Omega XXXX, XXX, XXX−XXX

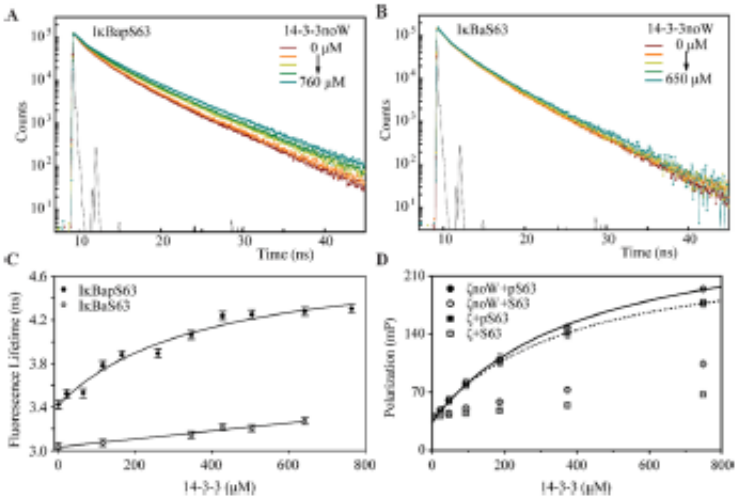

Figure 3. Binding of IκBα peptides to 14-3-3 monitored by Trp66 fluorescence. Panels (A) and (B) represent the peak-normalized fluorescence decays of IκBαpS63 and IκBαp63, respectively, in the presence of different concentrations of 14-3-3ζnoW. (C) τ_{mean} of IκBαS63 (opened circles) and IκBαpS63 (closed circles) as a function of 14-3-3ζnoW concentration. Solid lines represent the best fit to the simple two-state single-binding-site model: EC50 = min + (max − min)·[x]/(K_D + [x]), where [x] is a concentration of the titrant. (D) FP assay with 14-3-3ζnoW (circles) and 14-3-3ζ (squares) and FITC-labeled IκBαpS63 (closed) and IκBαS63 (open). Lines represent the best fit of peptide binding to 14-3-3ζnoW (solid) or 14-3-3ζ (dashed) to the equation described in (C).

Indeed, time-resolved fluorescence decays clearly indicate a progressive formation of IκBαpS63/14-3-3ζnoW complex by a significant increase of the Trp66 lifetime upon 14-3-3ζnoW addition (Figure 3A). This concentration-dependent increase of τ_{mean} ranges from 3.42 ns for the IκBαpS63 alone to 4.30 ns at 763 μM 14-3-3ζnoW (Figure 3A). In contrast, the unphosphorylated IκBαS63 indicated a much weaker interaction with 14-3-3ζnoW (Figure 3B). This finding is consistent with the results of the polarization assay shown in Figure 1. The τ_{mean} for the peptide alone was 3.04 ns, while it increased to 3.27 ns at a maximum protein concentration of 640 μM, confirming that the binding sequence needs to be phosphorylated for efficient binding.

The change in τ_{mean} due to different protein concentrations encouraged us to use this change for an estimation of the binding affinity of IκBαpS63 to 14-3-3ζnoW. Therefore, τ_{mean} was plotted as a function of the 14-3-3ζnoW concentration, which revealed a binding curve with incomplete saturation (Figure 3C). The data were fitted to a simple 1:1 binding model resulting in a K_D value of about 370 ± 50 μM for the IκBαpS63/14-3-3ζnoW complex. It has to be noted that the K_D values are slightly underestimated since the fitting model neglected the increased quantum yield of the Trp in the complex. To validate the obtained dissociation constant, FP assays with 14-3-3ζ and 14-3-3ζnoW were repeated with the highest possible protein concentrations and both are labeled as IκBαS63/pS63 peptides. The FP assay also showed incomplete saturation, but the fitting converged to the K_D of about 380 ± 1 and 415 ± 30 μM for IκBα with 14-3-3ζ and 14-3-3ζnoW, respectively (Figure 3D). Although the accuracy of such a fitting might be questionable, the similarity of the fitted dissociation constants is promising. Fortunately, due to the comparable molecular weight of the phosphorylated and unphosphorylated peptide, the plateau of all FP curves in Figure 3D, defined by the overall rotational diffusion of the complex, should be very similar. This makes the comparison of K_Ds more reliable.

Within the uncertainty, the fluorescence decay data agree well with the fluorescence polarization data, whereas both techniques revealed K_D values close to 400 μM for the analogous IκBαpS63/14-3-3ζnoW complex. Due to limits of protein solubility, very weak interaction, and thereof inability to reach saturation, the K_D for the unphosphorylated complex was not reliably quantifiable.

DISCUSSION

This study focuses on an extension of our knowledge of the IκBα interaction with 14-3-3 and establishing label-free measurements of dissociation constants via fluorescence decay on a difficult system. In the first part, we could validate the 14-3-3 binding motif of IκBα on the basis of an IκBα-peptide−14-3-3 interaction with the traditional FP assay. The biophysical assays showed that phosphorylation of the IκBα peptide is necessary for binding to 14-3-3, although the rather weak binding made a quantitative determination of affinity difficult. Regarding the bivalent binding mode due to the two phospho-accepting pockets of the 14-3-3 dimer, this low affinity is consistent with those of other 14-3-3 interactions. Several studies showed similar binding behaviors for single phosphorylated peptides, and double phosphorylated binding partners reached affinities in the low-micromolar to the high-nanomolar range.[26,27] The transition from a peptide motif to a protein domain or even full-length protein−protein interaction is expected to considerably enhance the binding affinity. In the case of 14-3-3 PPIs, only a few studies succeeded in the analysis of the complex formation of full-length domains due to the binding of 14-3-3 to unstructured regions of its interaction partners.[28,30−36] In the case of calcium/calmodulin-dependent protein kinase kinase 2 (CaMKK2), binding to 14-3-3 was established via unstructured peptide-like motifs, which could be crystallized in a complex with 14-3-3.[33] Complementary

https://dx.doi.org/10.1021/acsomega.9b04413
ACS Omega XXXX, XXX, XXX−XXX

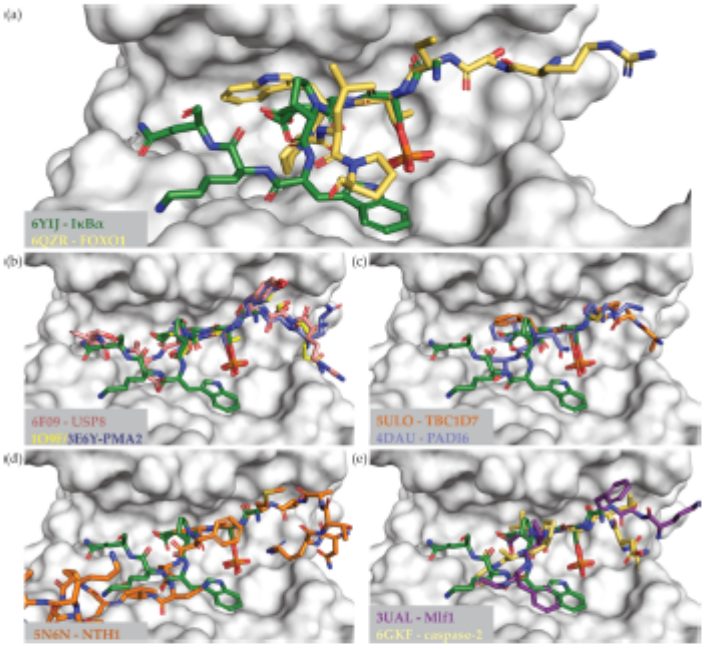

Figure 4. Comparison of the IκBαpS63 binding mode with other binding 14-3-3 partners. (a) Only two interaction motifs of 14-3-3 hosting a tryptophan residue within the binding groove. All other displayed binding modes contain at least one aromatic residues at (b) −1-position, (c) +1-position, (d) +2-position, or (e) +3-position in relation to the phosphorylated residue. The 14-3-3 is shown as a white surface and the IκBαpS63 peptide as green sticks. Other binding partners are displayed as colored sticks with the associated PDB ID and the name of the interaction partner. For sequence comparison and Cα distances, see Supporting Information Table S3.

small-angle X-ray scattering (SAXS) and binding affinity measurements showed that additional contacts were made with the outside of the 14-3-3 binding groove, while the peptide-like binding conformation in the binding groove was confirmed. Similarly, the crystal structure of the neutral trehalase of *Saccharomyces cerevisiae* (Nth1)/14-3-3 complex[30] revealed that there are extensive interactions between 14-3-3 and Nth1 beyond those involving the 14-3-3 binding grooves. Another example of a biphosphorylated interaction partner of 14-3-3 is procaspase-2.[28] In this case, both binding motifs were tested in fluorescence polarization assays, whereas only one site showed μM binding. However, both phosphorylation sites were necessary to establish a complex formation of the full-length proteins, while no complex formation could be observed for either single phosphorylated procaspase 2. These data suggest that an additional binding site is necessary for efficient binding of IκBα to 14-3-3. This can be either via a not yet identified 14-3-3 binding site of IκBα or a third binding partner that is simultaneously binding to IκBα and 14-3-3. A ternary complex formation has been reported among others for the A20/RAF proto-oncogene serine/threonine-protein kinase (C-Raf)/14-3-3[37] and glycogen synthase kinase-3 β (GSK3beta)/Tau/14-3-3 interactions.[38] A high-affinity binding of the second binding site might even mediate binding of the unphosphorylated IκBαS63 motif,[12] although the isolated motif needs to be phosphorylated to show activity in binding assays. For the IκBα/14-3-3 interaction, only one active binding motif could be identified via co-immunoprecipitation, and also the sequence analysis of the IκBα protein revealed only one additional possible, but in the structural context unlikely, binding site (pT168; Supporting Information, Table S1 and Figure S1). In this case, it is more likely that the additional binding partner NF-κB is essential to enhance the binding of IκBα to 14-3-3. Binding of 14-3-3 to the NF-κB subunit p65 and to IκBα is needed for sufficient export of the IκBα/NF-κB nuclear export or retention in the cytoplasm.[12]

Noteworthy is also the binding mode of the IκBαpS63 peptide as Trp66 at the +3-position of the phosphorylated residue shows a remarkable conformation. Multiple 14-3-3 binding sequences contain aromatic residues; however, even within the constantly growing collection of peptides crystallized in complex with 14-3-3, only a small number contain tryptophan residues. Lately, the first crystal structure was published with a Trp residue, which was actually covered in electron density, located at the +1-position (Figure 4A).[39] Two other examples of peptides binding to 14-3-3 and containing a tryptophan resides are the serine/threonine-protein kinase 26 (MST4) derived peptide (PDB ID: 5XY9) and the serine/threonine-protein kinase STK11 (LKB1) derived peptide (PDB ID: 5WXN). The tryptophan residue of MST4 is at the +4-position in relation to the phosphorylated residue, while that of LKB1 is at the −4-position; however, the indol moieties of both tryptophan residues were not visible in the electron density. That makes this study the second one with a Trp residue visible in a 14-3-3 crystal structure.

The amphipathic binding groove of 14-3-3 provides a lot of options for aromatic residues to bind (Figure 4). Multiple structures have been published with aromatic residues at the −1-position or +1-position of the phosphorylated residue, where they make contacts with the hydrophobic residues of the

https://dx.doi.org/10.1021/acsomega.9b04413
ACS Omega XXXX, XXX, XXX−XXX

binding groove of 14-3-3 (Figure 4B,C).[40−43] An aromatic residue at the +2-position is rare and for the structure shown, the interaction of the yeast Nth1 domain with 14-3-3, the phenylalanine does not make contact with 14-3-3 (Figure 4D).[50] It is only stable in the context of the full domain, which is not shown for clarity. Actually, there is no other structure published with tryptophan at the +3-position in addition to the IκBαpS63. However, there are at least two structures available with a phenylalanine at that position, whereby for one the side chain was not visible in the electron density map (PDB ID: 6GKF; Figure 4E).[44] Nevertheless, the peptide−protein interface of myeloid leukemia factor 1 (Mfl1) and 14-3-3ε comprises a phenylalanine at the +3-position with the same orientation as Trp66 of IκBαpS63 (PDB ID: 3UAL; Figure 4E).[45] The conformation of the binding motifs deviates C-terminally from the phospho site more than they do N-terminally, whereas the Mfl1 motif shows the only comparable conformation. Measurements of the distances of the Cα atoms, Trp66 of IκBα, and phenylalanine of Mfl1 are 1.5 Å apart, while in all other structures, the residues at the +3-position are more than 2.6 Å apart (Supporting Information Table S3). This demonstrates that not only the binding groove in general but also the environment of the phosphorylation site can accommodate bulky hydrophobic residues like aromatic amino acids.

The tryptophan, clearly visible in the electron density, offers a nice opportunity to use its environmentally sensitive emission for direct biophysical affinity measurements without a need for a bulky artificial dye that could eventually bias interactions between IκBα peptides and 14-3-3. For K_D quantification, we used the FP assay with externally labeled protein, which relies on changed hydrodynamic properties of the complex. In parallel, we applied intrinsic Trp fluorescence directly reflecting interaction-induced variations of the Trp micro-environment. For our system, both methods gave comparable results, proving the importance of the IκBα phosphorylation and yielding K_D of the IκBαpS63/14-3-3ζnoW complex formation in the 10^{-4} M range.

Future research will further evaluate the binding of IκBα/p65 to 14-3-3 and analyze the contribution of this complex regarding the nuclear export mechanism of IκBα and p65.

■ MATERIALS AND METHODS

Peptide Synthesis. Peptides were synthesized via Fmoc-solid-phase peptide synthesis with an automated Intavis MultiPep RSi peptide synthesizer with a Rink amide AM resin (Novabiochem; 0.59 mmol/g loading). After the synthesis was completed, the resin was split, with half of the peptide N-terminally acetylated (1:1:3 acetic anhydride (Ac_2O)/pyridine/*N*-methyl-2-pyrrolidone (NMP)) and the other one isothiocyanate (FITC)-labeled via a β-alanine linker as described above.[46] The peptides were cleaved with a 2.5:2.5:2.5:92.5 EDT/TIS/MQ/TFA mixture and purified with a preparative reversed-phase high-performance liquid chromatography (HPLC) system with mass spectrometry (MS) detection (Supporting Information, Figure S3). The purified peptide was lyophilized and stored at −30 °C.

14-3-3 Expression. The 14-3-3 isoforms were transiently expressed in *Escherichia coli* Nico21(DE3) or BL21(DE3) competent cells via a pPROEX HTb plasmid. The cells were grown to a density of OD_{600} = 0.8−1, and protein expression was induced with 0.4 mM isopropyl β-D-1-thiogalactopyranoside (IPTG) for 18 h by 18 °C. The proteins were purified following standard procedures for Ni-affinity chromatography. For crystallography, the His6-Tag was removed by TEV cleavage and an additional Ni-NTA column, followed by size-exclusion chromatography ensuring the highest purity. All proteins were dialyzed against 25 mM *N*-(2-hydroxyethyl)-piperazine-*N*′-ethanesulfonic acid (Hepes) pH 7.5, 100 mM NaCl, 10 mM $MgCl_2$, 0.5 mM tris(2-carboxyethyl)phosphine, and stored at −80 °C. The exact mass of the proteins was confirmed via hybrid quadrupole time-of-flight (QTOF) measurements, whereby the number of peaks in the chromatogram indicated the purity of the protein (Supporting Information, Figure S4).

Crystallography. 14-3-3σΔC232-248 and IκBαS63/pS63 complexes were mixed in a ratio of 1:2 in a final protein concentration of 12 mg/mL in crystallography buffer (20 mM Hepes pH 7.5, 2 mM $MgCl_2$, 2 mM β-mercaptoethanol) and incubated overnight at 4 °C. In a hanging drop approach, the peptide/protein complex was mixed in a 1:1 ratio with a precipitation buffer (0.95 mM Hepes pH 7.1, 28% PEG400, 5% glycerol, 0.19 M $CaCl_2$), crystals grew within one week. The crystals could be directly fished and flash-cooled in liquid nitrogen. The data set was measured at the Synchrotron DESY beamline P11, Hamburg, Germany.

For the indexing, integration, and molecular replacement, the CCP4 suite[47] was used (iMosflm,[48] Aimless,[49,50] and MolRep[51,52]). As a search model for molecular replacement, PDB ID code 4FR3 was used. The refinement was done with phenix[53] and the model building in Coot.[54]

Fluorescence Polarization (FP) Assay. The FP was measured with FITC-labeled peptides at a final concentration of 100 nM in fluorescence polarization buffer (10 mM Hepes, pH 7.4, 150 mM NaCl, 0.1% Tween 20, 1 mg/mL bovine serum albumin (BSA)). The 14-3-3 isoforms were titrated as indicated. All data sets were measured in at least three independent experiments in Corning black round-bottom 384-well plates with a Tecan Infinite F500 plate reader (excitation 485 nm, emission 535 nm).

Time-Resolved Tryptophan Fluorescence Measurements. Measurements of time-resolved Trp emission were performed on an apparatus comprised of a femtosecond Ti:sapphire laser (Chameleon Ultra II; Coherent) with the repetition rate reduced to 4 MHz by a pulse picker (APE). The fluorescence signal was collected using time-correlated single-photon counting detection SPC150 (Becker&Hickl) with a cooled MCP-PMT (R3809U-50; Hamamatsu). Trp fluorescence was excited at 298 nm by a tripled output of the laser and the emission was isolated under the "magic angle" conditions at 355 nm using a combination of a monochromator and a stack of UG1 and BG40 glass filters (Thorlabs) placed in front of the input slit. Fluorescence decays were typically accumulated in 1024 channels with a time resolution of 50 ps/channel until 105 counts in the decay maximum were reached. All experiments were performed at 23 °C in a buffer containing 20 mM Tris−HCl (pH 7.5), 150 mM NaCl, 1 mM ethylenediaminetetraacetic acid (EDTA), and 5 mM dithiothreitol (DTT). The IκBαS63/pS63 peptide and 14-3-3ζnoW concentrations were 1 and 0−763 μM, respectively. Fluorescence decays were analyzed by the model-independent maximum entropy method[55] allowing accurate determination of the mean fluorescence lifetime τ_{mean} calculated as $\tau_{mean} = \sum \alpha_i \tau_i^2 / \sum \alpha_i \tau_i$, where τ_i and α_i are the fluorescence lifetime components and the corresponding amplitudes revealed by the analysis, respectively.

https://dx.doi.org/10.1021/acsomega.9b04413
ACS Omega XXXX, XXX, XXX−XXX

■ ASSOCIATED CONTENT

Supporting Information

The Supporting Information is available free of charge at https://pubs.acs.org/doi/10.1021/acsomega.9b04413.

Results of the 14-3-3pred webserver for IκBα (uniprot ID: P25963) (Table S1); crystal structure of IκBα (Figure S1); B-factor coloring of 14-3-3σΔC and the IκBαpS63 peptide (Figure S2); crystallographic statistics of the X-ray structure of the IκBαpS63/14-3-3σΔC232-248 complex (PDB ID: 6Y1J) (Table S2); quantitative comparison of 14-3-3 binding motifs (Table S3); LC−MS analysis of the in-house synthesized and purified peptides (Figure S3); and QTOF measurements of the purified 14-3-3 isoforms (Figure S4) (PDF)

Accession Codes

Given are the accession codes of UniProt. 14-3-3β: P31946 (1433B_HUMAN) 14-3-3γ: P61981 (1433G_HUMAN) 14-3-3ε: P62258 (1433E_HUMAN) 14-3-3ζ: P63104 (1433Z_HUMAN) 14-3-3η: Q04917 (1433F_HUMAN) 14-3-3σ: P31947 (1433S_HUMAN) 14-3-3τ: P27348 (1433T_HUMAN) IκBα: P25963 (IKBA_HUMAN)

■ AUTHOR INFORMATION

Corresponding Authors

Tomas Obsil − *Department of Physical and Macromolecular Chemistry, Faculty of Science, Charles University, Prague 12843, Czech Republic;* orcid.org/0000-0003-4602-1272; Email: tomas.obsil@natur.cuni.cz

Christian Ottmann − *Department of Biomedical Engineering, Laboratory of Chemical Biology and Institute for Complex Molecular Systems, Eindhoven University of Technology, 5600 MB Eindhoven, The Netherlands; Department of Organic Chemistry, University of Duisburg-Essen, 45117 Essen, Germany;* orcid.org/0000-0001-7315-0315; Email: c.ottmann@tue.nl

Authors

Madita Wolter − *Department of Biomedical Engineering, Laboratory of Chemical Biology and Institute for Complex Molecular Systems, Eindhoven University of Technology, 5600 MB Eindhoven, The Netherlands*

Domenico Lentini Santo − *Department of Physical and Macromolecular Chemistry, Faculty of Science, Charles University, Prague 12843, Czech Republic*

Petr Herman − *Institute of Physics, Faculty of Mathematics and Physics, Charles University, Prague 12116, Czech Republic*

Alice Ballone − *Department of Biomedical Engineering, Laboratory of Chemical Biology and Institute for Complex Molecular Systems, Eindhoven University of Technology, 5600 MB Eindhoven, The Netherlands*

Federica Centorrino − *Department of Biomedical Engineering, Laboratory of Chemical Biology and Institute for Complex Molecular Systems, Eindhoven University of Technology, 5600 MB Eindhoven, The Netherlands*

Complete contact information is available at: https://pubs.acs.org/10.1021/acsomega.9b04413

Author Contributions

C.O. supervised the project and provided scientific guidance. T.O. supervised and provided scientific guidance for tryptophan fluorescence experiments. M.W. performed FP and crystallography. D.L.S. performed protein purification of 14-3-3noW and, together with P.H., fluorescence decay experiments. M.W., A.B., and F.C. performed peptide synthesis/purification and protein expression/purification. M.W. wrote the manuscript, followed by its revision by all. These authors contributed equally.

Notes

The authors declare no competing financial interest.

■ ACKNOWLEDGMENTS

This study was supported by the Initial Training Network, funded by the H2020 Marie Curie Actions of the European Commission under Grant Agreement 675179. P.H. acknowledges the EU Operational Program No. CZ.1.05/4.1.00/16.0340 and the institutional support UNCE/SCI/010.

■ ABBREVIATIONS

14-3-3ζnoW, W59F W228F double mutation of 14-3-3ζ; 14-3-3σΔC, 14-3-3σ with truncated C-terminus ΔC232-248; A20, TNF α induced protein 3, also known as TNFAIP3; CaMKK2, calcium/calmodulin-dependent protein kinase kinase 2; C-Raf, RAF proto-oncogene serine/threonine-protein kinase; DTT, dithiothreitol; EDT, 1,2-ethanedithiol; EDTA, ethylenediaminetetraacetic acid; FITC, fluorescein isothiocyanate; FP, fluorescence polarization; GSK3beta, glycogen synthase kinase-3 β; IκBα, inhibitor of nuclear factor kappa B α; K_D, dissociation constant; LKB1, serine/threonine-protein kinase STK11; Mfl1, myeloid leukemia factor 1; MST4, serine/threonine-protein kinase 26; NF-κB, nuclear factor kappa-light-chain-enhancer of activated B cells; Nth1, neutral trehalase of *Saccharomyces cerevisiae*; PEST, proline (P), glutamic acid (E), serine (S), and threonine (T) rich sequence; SAXS, small-angle X-ray scattering; τ_{mean}, mean fluorescence life

■ REFERENCES

(1) Hayden, M. S.; Ghosh, S. NF-κB, the first quarter-century: remarkable progress and outstanding questions. *Genes Dev.* **2012**, *26*, 203−234.

(2) Viatour, P.; Merville, M.-P.; Bours, V.; Chariot, A. Phosphorylation of NF-κB and IκB proteins: implications in cancer and inflammation. *Trends Biochem. Sci.* **2005**, *30*, 43−52.

(3) Ghosh, S.; May, M. J.; Kopp, E. B. NF-κB AND REL PROTEINS: Evolutionarily Conserved Mediators of Immune Responses. *Annu. Rev. Immunol.* **1998**, *16*, 225−260.

(4) Baldwin, A. S., Jr. The NF-kappa B and I kappa B proteins: new discoveries and insights. *Annu. Rev. Immunol.* **1996**, *14*, 649−683.

(5) Gupta, S. C.; Sundaram, C.; Reuter, S.; Aggarwal, B. B. Inhibiting NF-κB activation by small molecules as a therapeutic strategy. *Biochim. Biophys. Acta, Gene Regul. Mech.* **2010**, *1799*, 775−787.

(6) Mulero, M. C.; Bigas, A.; Espinosa, L. IκBα beyond the NF-kB dogma. *Oncotarget* **2013**, *4*, 1550−1551.

(7) DiDonato, J.; Mercurio, F.; Roette, C.; Wu-Li, J.; Suyang, H.; Ghosh, S.; Karin, M. Mapping of the Inducible IκB Phosphorylation Sites That Signal Its Ubiquitination and Degradation. *Mol. Cell. Biol.* **1996**, *16*, 1295−1304.

(8) Gonen, H.; Bercovich, B.; Orian, A.; Carrano, A.; Takizawa, C.; Yamanaka, K.; Pagano, M.; Iwai, K.; Ciechanover, A. Identification of the Ubiquitin Carrier Proteins, E2s, Involved in Signal-induced Conjugation and Subsequent Degradation of IκBα. *J. Biol. Chem.* **1999**, *274*, 14823−14830.

(9) Simeonidis, S.; Liang, S.; Chen, G.; Thanos, D. Cloning and functional characterization of mouse IκBε. *Proc. Natl. Acad. Sci. U.S.A.* **1997**, *94*, 14372−14377.

(10) Malek, S.; Chen, Y.; Huxford, T.; Ghosh, G. IκBβ, but not IκBα, functions as a classical cytoplasmic inhibitor of NF-κB dimers

https://dx.doi.org/10.1021/acsomega.9b04413
ACS Omega XXXX, XXX, XXX−XXX

by masking both NF-κB nuclear localization sequences in resting cells. *J. Biol. Chem.* **2001**, *267*, 45225−45235.
(11) Tran, K.; Merika, M.; Thanos, D. Distinct Functional Properties of IκBα and IκBε. *Mol. Cell. Biol.* **1997**, *17*, 5386−5399.
(12) Aguilera, C.; Fernández-Majada, V.; Inglés-Esteve, J.; Rodilla, V.; Bigas, A.; Espinosa, L. Efficient nuclear export of p65-IκBα complexes requires 14-3-3 proteins. *J. Cell Sci.* **2016**, *129*, 2472.
(13) Johnson, C.; Tinti, M.; Wood, N. T.; Campbell, D. G.; Toth, R.; Dubois, F.; Geraghty, K. M.; Wong, B. H. C.; Brown, L. J.; Tyler, J.; Gernez, A.; Chen, S.; Synowsky, S.; MacKintosh, C. Visualization and Biochemical Analyses of the Emerging Mammalian 14-3-3-Phosphoproteome. *Mol. Cell. Proteomics* **2011**, *10*, No. M110.005751.
(14) Fu, H.; Subramanian, R. R.; Masters, S. C. 14-3-3 Proteins: Structure, Function, and Regulation. *Annu. Rev. Pharmacol. Toxicol.* **2000**, *40*, 617−647.
(15) Aitken, A. 14-3-3 proteins: A historic overview. *Semin. Cancer Biol.* **2006**, *16*, 162−172.
(16) Yaffe, M. B.; Rittinger, K.; Volinia, S.; Caron, P. R.; Aitken, A.; Leffers, H.; Gamblin, S. J.; Smerdon, S. J.; Cantley, L. C. The Structural Basis for 14-3-3:Phosphopeptide Binding Specificity. *Cell* **1997**, *91*, 961−971.
(17) Palmer, D.; Jimmo, S. L.; Raymond, D. R.; Wilson, L. S.; Carter, R. L.; Maurice, D. H. Protein Kinase A Phosphorylation of Human Phosphodiesterase 3B Promotes 14-3-3 Protein Binding and Inhibits Phosphatase-catalyzed Inactivation. *J. Biol. Chem.* **2007**, *282*, 9411−9419.
(18) Sun, L.; Stoecklin, G.; Way, S. V.; Hinkovska-Galcheva, V.; Guo, R.-F.; Anderson, P.; Shanley, T. P. Tristetraprolin (TTP)-14-3-3 Complex Formation Protects TTP from Dephosphorylation by Protein Phosphatase 2a and Stabilizes Tumor Necrosis Factor-α mRNA. *J. Biol. Chem.* **2007**, *282*, 3766−3777.
(19) Zhang, J.; Chen, F.; Li, W.; Xiong, Q.; Yang, M.; Zheng, P.; Li, C.; Pei, J.; Ge, F. 14-3-3ζ Interacts with Stat3 and Regulates Its Constitutive Activation in Multiple Myeloma Cells. *PLoS One* **2012**, *7*, No. e29554.
(20) Obsilova, V.; Nedbalkova, E.; Silhan, J.; Boura, E.; Herman, P.; Vecer, J.; Sulc, M.; Teisinger, J.; Dyda, F.; Obsil, T. The 14-3-3 Protein Affects the Conformation of the Regulatory Domain of Human Tyrosine Hydroxylase. *Biochemistry* **2008**, *47*, 1768−1777.
(21) Herman, P.; Lee, J. C. Functional Energetic Landscape in the Allosteric Regulation of Muscle Pyruvate Kinase. 2. Fluorescence Study. *Biochemistry* **2009**, *48*, 9456−9465.
(22) Herman, P.; Vecer, J.; Scognamiglio, V.; Staiano, M.; Rossi, M.; D'Auria, S. A Recombinant Glutamine-Binding Protein from Escherichia coli: Effect of Ligand-Binding on Protein Conformational Dynamics. *Biotechnol. Prog.* **2004**, *20*, 1847−1854.
(23) Eftink, M. R. Intrinsic Fluorescence of Proteins. In *Topics in Fluorescence Spectroscopy*; Lakowicz, J. R., Ed.; Springer: US, Boston, MA, 2000; Vol. 6, pp 1−15.
(24) *Principles of Fluorescence Spectroscopy*; Lakowicz, J. R., Ed.; Springer: US, Boston, MA, 2006.
(25) Gryczynski, I.; Wiczk, W.; Johnson, M. L.; Lakowicz, J. R. Lifetime distributions and anisotropy decays of indole fluorescence in cyclohexane/ethanol mixtures by frequency-domain fluorometry. *Biophys. Chem.* **1988**, *32*, 173−185.
(26) Stevers, L. M.; de Vries, R. M. J. M.; Doveston, R.; Milroy, L.-G.; Brunsveld, L.; Ottmann, C. Structural interface between LRRK2 and 14-3-3 protein. *Biochem. J.* **2017**, *7*, 1273−1287.
(27) Stevers, L. M.; Lam, C. V.; Leysen, S. F. R.; Meijer, F. A.; van Scheppingen, D. S.; de Vries, R. M. J. M.; Carlile, G. W.; Milroy, L.-G.; Thomas, D. Y.; Brunsveld, L.; Ottmann, C. Characterization and small-molecule stabilization of the multisite tandem binding between 14-3-3 and the R domain of CFTR. *Proc. Natl. Acad. Sci. U.S.A.* **2016**, *113*, E1152−E1161.
(28) Kalabova, D.; Smidova, A.; Petrvalska, O.; Alblova, M.; Kosek, D.; Man, P.; Obsil, T.; Obsilova, V. Human procaspase-2 phosphorylation at both S139 and S164 is required for 14-3-3 binding. *Biochem. Biophys. Res. Commun.* **2017**, *493*, 940−945.
(29) Madeira, F.; Tinti, M.; Murugesan, G.; Berrett, E.; Stafford, M.; Toth, R.; Cole, C.; MacKintosh, C.; Barton, G. J. 14-3-3-Pred: improved methods to predict 14-3-3-binding phosphopeptides. *Bioinformatics* **2015**, *31*, 2276−2283.
(30) Alblova, M.; Smidova, A.; Docekal, V.; Vesely, J.; Herman, P.; Obsilova, V.; Obsil, T. Molecular basis of the 14-3-3 protein-dependent activation of yeast neutral trehalase Nth1. *Proc. Natl. Acad. Sci. U.S.A.* **2017**, *114*, E9811−E9820.
(31) Joo, Y.; Schumacher, B.; Landrieu, I.; Bartel, M.; Smet-Nocca, C.; Jang, A.; Choi, H. S.; Jeon, N. L.; Chang, K.-A.; Kim, H.-S.; Ottmann, C.; Suh, Y.-H. Involvement of 14-3-3 in tubulin instability and impaired axon development is mediated by Tau. *FASEB J.* **2015**, *29*, 4133−4144.
(32) Kacirova, M.; Novacek, J.; Man, P.; Obsilova, V.; Obsil, T. Structural Basis for the 14-3-3 Protein-Dependent Inhibition of Phosducin Function. *Biophys. J.* **2017**, *112*, 1339−1349.
(33) Psenakova, K.; Petrvalska, O.; Kylarova, S.; Lentini Santo, D.; Kalabova, D.; Herman, P.; Obsilova, V.; Obsil, T. 14-3-3 protein directly interacts with the kinase domain of calcium/calmodulin-dependent protein kinase kinase (CaMKK2). *Biochim. Biophys. Acta, Gen. Subj.* **2018**, *1862*, 1612−1625.
(34) Park, E.; Rawson, S.; Li, K.; Kim, B.-W.; Ficarro, S. B.; Pino, G. G.-D.; Sharif, H.; Marto, J. A.; Jeon, H.; Eck, M. J. Architecture of autoinhibited and active BRAF−MEK1−14-3-3 complexes. *Nature* **2019**, *575*, 545−550.
(35) Sluchanko, N. N.; Beelen, S.; Kulikova, A. A.; Weeks, S. D.; Antson, A. A.; Gusev, N. B.; Strelkov, S. V. Structural Basis for the Interaction of a Human Small Heat Shock Protein with the 14-3-3 Universal Signaling Regulator. *Structure* **2017**, *25*, 305−316.
(36) Tugaeva, K. V.; Kalacheva, D. I.; Cooley, R. B.; Strelkov, S. V.; Sluchanko, N. N. Concatenation of 14-3-3 with partner phosphoproteins as a tool to study their interaction. *Sci. Rep.* **2019**, *9*, No. 15007.
(37) Vincenz, C.; Dixit, V. M. 14-3-3 Proteins Associate with A20 in an Isoform-specific Manner and Function Both as Chaperone and Adapter Molecules. *J. Biol. Chem.* **1996**, *271*, 20029−20034.
(38) Agarwal-Mawal, A.; Qureshi, H. Y.; Cafferty, P. W.; Yuan, Z.; Han, D.; Lin, R.; Paudel, H. K. 14-3-3 Connects Glycogen Synthase Kinase-3β to Tau within a Brain Microtubule-associated Tau Phosphorylation Complex. *J. Biol. Chem.* **2003**, *278*, 12722−12728.
(39) Saline, M.; Badertscher, L.; Wolter, M.; Lau, R.; Gunnarsson, A.; Jacso, T.; Norris, T.; Ottmann, C.; Snijder, A. AMPK and AKT protein kinases hierarchically phosphorylate the N-terminus of the FOXO1 transcription factor, modulating interactions with 14-3-3 proteins. *J. Biol. Chem.* **2019**, *294*, 13106−13116.
(40) Centorrino, F.; Ballone, A.; Wolter, M.; Ottmann, C. Biophysical and structural insight into the USP8/14-3-3 interaction. *FEBS Lett.* **2018**, *592*, 1211−1220.
(41) Ottmann, C.; Weyand, M.; Sassa, T.; Inoue, T.; Kato, N.; Wittinghofer, A.; Oecking, C. A Structural Rationale for Selective Stabilization of Anti-tumor Interactions of 14-3-3 proteins by Cotylenin A. *J. Mol. Biol.* **2009**, *386*, 913−919.
(42) Würtele, M.; Jelich-Ottmann, C.; Wittinghofer, A.; Oecking, C. Structural view of a fungal toxin acting on a 14-3-3 regulatory complex. *EMBO J.* **2003**, *22*, 987−994.
(43) Rose, R.; Rose, M.; Ottmann, C. Identification and structural characterization of two 14-3-3 binding sites in the human peptidylarginine deiminase type VI. *J. Struct. Biol.* **2012**, *180*, 65−72.
(44) Smidova, A.; Alblova, M.; Kalabova, D.; Psenakova, K.; Rosulek, M.; Herman, P.; Obsil, T.; Obsilova, V. 14-3-3 protein masks the nuclear localization sequence of caspase-2. *FEBS J.* **2018**, *285*, 4196−4213.
(45) Molzan, M.; Weyand, M.; Rose, R.; Ottmann, C. Structural insights of the MLF1/14-3-3 interaction. *FEBS J.* **2012**, *279*, 563−571.
(46) Kim, Y.-W.; Grossmann, T. N.; Verdine, G. L. Synthesis of all-hydrocarbon stapled α-helical peptides by ring-closing olefin metathesis. *Nat. Protoc.* **2011**, *6*, 761−771.
(47) Winn, M. D.; Ballard, C. C.; Cowtan, K. D.; Dodson, E. J.; Emsley, P.; Evans, P. R.; Keegan, R. M.; Krissinel, E. B.; Leslie, A. G.

https://doi.org/10.1021/acsomega.9b04413
ACS Omega XXXX, XXX, XXX−XXX

689 W.; McCoy, A.; McNicholas, S. J.; Murshudov, G. N.; Pannu, N. S.;
690 Potterton, E. A.; Powell, H. R.; Read, R. J.; Vagin, A.; Wilson, K. S.
691 Overview of the CCP 4 suite and current developments. *Acta*
692 *Crystallogr., Sect. D: Biol. Crystallogr.* **2011**, *67*, 235−242.
693 (48) Battye, T. G. G.; Kontogiannis, L.; Johnson, O.; Powell, H. R.;
694 Leslie, A. G. W. iMOSFLM: a new graphical interface for diffraction-
695 image processing with MOSFLM. *Acta Crystallogr., Sect. D: Biol.*
696 *Crystallogr.* **2011**, *67*, 271−281.
697 (49) Evans, P. Scaling and assessment of data quality. *Acta*
698 *Crystallogr., Sect. D: Biol. Crystallogr.* **2006**, *62*, 72−82.
699 (50) Evans, P. R.; Murshudov, G. N. How good are my data and
700 what is the resolution? *Acta Crystallogr., Sect. D: Biol. Crystallogr.*
701 **2013**, *69*, 1204−1214.
702 (51) Lebedev, A. A.; Vagin, A. A.; Murshudov, G. N. Model
703 preparation in MOLREP and examples of model improvement using
704 X-ray data. *Acta Crystallogr., Sect. D: Biol. Crystallogr.* **2008**, *64*, 33−
705 39.
706 (52) Vagin, A.; Teplyakov, A. Molecular replacement with
707 MOLREP. *Acta Crystallogr., Sect. D: Biol. Crystallogr.* **2010**, *66*, 22−
708 25.
709 (53) Adams, P. D.; Afonine, P. V.; Bunkóczi, G.; Chen, V. B.; Davis,
710 I. W.; Echols, N.; Headd, J. J.; Hung, L.-W.; Kapral, G. J.; Grosse-
711 Kunstleve, R. W.; McCoy, A. J.; Moriarty, N. W.; Oeffner, R.; Read, R.
712 J.; Richardson, D. C.; Richardson, J. S.; Terwilliger, T. C.; Zwart, P.
713 H. *PHENIX*: a comprehensive Python-based system for macro-
714 molecular structure solution. *Acta Crystallogr., Sect. D: Biol. Crystallogr.*
715 **2010**, *66*, 213−221.
716 (54) Emsley, P.; Cowtan, K. Coot: model-building tools for
717 molecular graphics. *Acta Crystallogr., Sect. D: Biol. Crystallogr.* **2004**,
718 *60*, 2126−2132.
719 (55) Vecer, J.; Herman, P. Maximum Entropy Analysis of
720 Analytically Simulated Complex Fluorescence Decays. *J. Fluoresc.*
721 **2011**, *21*, 873−881.

https://doi.org/10.1021/acsomega.9b04413
ACS Omega XXXX, XXX, XXX−XXX

SI Table 1: Results of the 14-3-3pred webserver for IκBα (uniprot ID: P25963). Shown are the phosphorylated residue (site), the sequence of IκBα from position -6 to +4 of the WT sequence around the phosphorylated residue (peptide), the scores for three different methods to estimate the likeliness of an 14-3-3 binding motif (ANN, PSSM, SVM) and the overall score (consensus) based on a combination of the three scores named before. Finally, an indication is given if information about the phosphorylation status of the predicted phospho-site are available. These results were downloaded on the 30.01.2019.

Site	Peptide_[-6:4]	ANN	PSSM	SVM	Consensus	pSer/Thr
32	LDDRHDsGLDS	0.35	0.63	-0.324	0.219	Yes
36	HDSGLDsMKDE	0.078	-0.128	-1.268	-0.44	Yes
63	QEVPRGsEPWK	0.499	0.48	-0.112	0.289	-
71	PWKQQLtEDGD	0.325	0.11	-0.251	0.061	-
76	LTEDGDsFLHL	0.097	-0.198	-1.178	-0.426	-
90	HEEKALtMEVI	0.342	0.256	-0.384	0.071	-
113	QNNLQQtPLHL	0.023	-0.5	-1.848	-0.775	-
121	LHLAVItNQPE	0.134	-0.225	-1.259	-0.45	-
146	RDFRGNtPLHL	0.18	0.451	-0.591	0.013	-
159	EQGCLAsVGVL	0.17	0.027	-0.81	-0.204	-
164	ASVGVLtQSCT	0.046	-0.316	-1.79	-0.687	-
166	VGVLTQsCTTP	0.1	-0.079	-1.136	-0.372	-
168	VLTQSCtTPHL	0.842	0.742	0.837	0.807	-
169	LTQSCTtPHLH	0.108	-0.414	-1.365	-0.557	-
174	TTPHLHsILKA	0.063	-0.217	-1.46	-0.538	-
179	HSILKAtNYNG	0.133	-0.02	-1.256	-0.381	-
185	TNYNGHtCLHL	0.054	-0.073	-1.092	-0.37	-
191	TCLHLAsIHGY	0.243	-0.085	-0.872	-0.238	-
204	IVELLVsLGAD	0.645	0.155	0.206	0.335	-
219	EPCNGRtALHL	0.033	-0.185	-1.581	-0.578	-
234	QNPDLVsLLLK	0.153	-0.196	-1.015	-0.353	-
247	ADVNRVtYQGY	0.288	-0.055	-0.575	-0.114	-
252	VTYQGYsPYQL	0.066	-0.348	-1.086	-0.456	-
257	YSPYQLtWGRP	0.063	-0.183	-1.387	-0.502	-
262	LTWGRPsTRIQ	0.218	0.004	-0.784	-0.187	-
263	TWGRPStRIQQ	0.195	0.511	-0.389	0.106	-
273	QQLGQLtLENL	0.1	0.033	-0.828	-0.232	-
283	LQMLPEsEDEE	0.15	-0.056	-0.779	-0.228	Yes
288	ESEDEEsYDTE	0.104	-0.284	-1.373	-0.517	Yes
291	DEESYDtESEF	0.15	-0.206	-1.323	-0.46	Yes
293	ESYDTEsEFTE	0.089	-0.104	-1.18	-0.398	Yes
296	DTESEFtEFTE	0.266	-0.119	-0.93	-0.261	-
299	SEFTEFtEDEL	0.235	0.057	-0.944	-0.217	Yes
316	FGGQRLtL---	0.421	0.366	-0.091	0.232	-

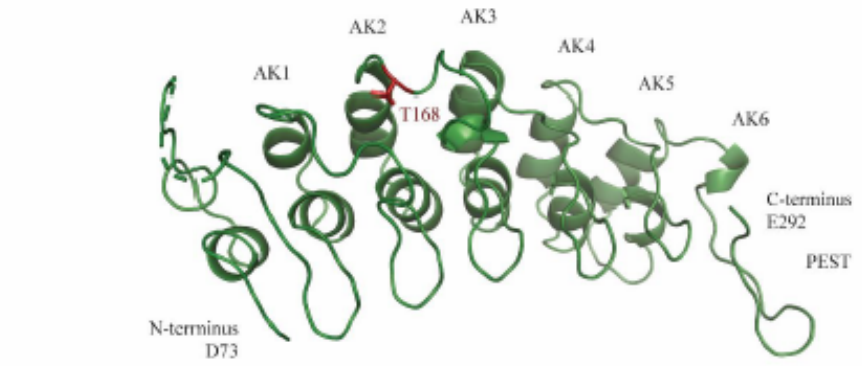

SI Figure 1: Crystal structure of IκBα (green cartoon; PDB: 1IKN). p65 and p50 are not shown for clarity. 219 out of 317 residues were visible in the electron density (D73 – E292) and structural features are indicated (AR: ankyrin repeat; PEST: proline, glutamate, serine and threonine rich sequence). Highlighted is the only predicted 14-3-3 binding site T168. (red sticks).

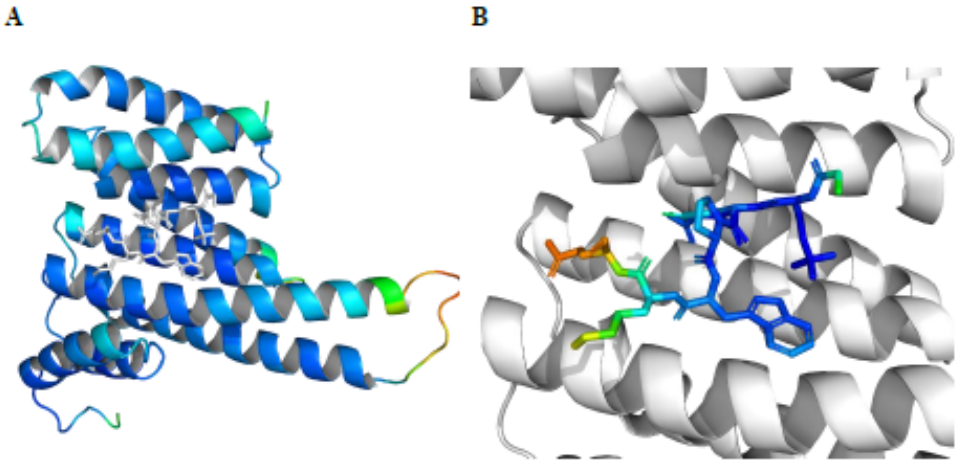

SI Figure 2: B-factor coloring of 14-3-3σΔC and the IκBαpS63 peptide. A The 14-3-3σΔC protein is represented as cartoon while the IκBαpS63 peptide is shown as white sticks. **B** The IκBαpS63 peptide is shown as sticks while the 14-3-3σΔC protein is shown as white cartoon. The B-factor coloring follows the rainbow color scheme with blue for low B-factors and red for high B-factors. The B-factors vary between 4.6 – 57.04 A^2.

SI Table 2: Crystallographic statistics of the X-ray structure of the IκBαpS63/14-3-3σΔC232-248 complex (PDB ID: 6HEO). Values in parentheses show statistics for the high resolution shell.

Property	Value	Source
Space group	C 2 2 21	phenix_table1
Cell constants a, b, c, α, β, γ	82.46Å 111.82Å 62.48Å 90.00° 90.00° 90.00°	phenix_table1
Resolution (Å)	45.49 - 1.13 (1.17-1.13) 45.49 - 1.13	phenix_table1 EDS
% Data completeness (in resolution range)	100.0 (99.97) 100.0	phenix_table1 EDS
Unique reflections	107826 (10678)	phenix_table1
Multiplicity	2.0 (2.0)	phenix_table1
< I/σ(I) >	15.53 (2.43)	Xtriage
CC1/2	1 (0.903)	phenix_table1
Wilson B-factor (A^2)	9.6	Xtriage
Rmerge	0.0217 (0.221)	phenix_table1
Rmeas	0.0307 (0.313)	phenix_table1
Rpim	0.0217 (0.221)	phenix_table1
Anisotropy	0.434	Xtriage
Bulk solvent ksol(e/ Å 3), Bsol(Å2)	0.40 , 44.5	EDS
L-test for twinning	< |L| > = 0.49, < L2 > = 0.33	Xtriage
Estimated twinning fraction	No twinning to report	Xtriage
Fo,Fc correlation	0.97	EDS
Refinement program	PHENIX (1.11.1_2,57,5)	Depositor
R, Rfree	0.170 (0.271), 0.183 (0.279) 0.171 , 0.182	phenix_table1 DCC
Rfree test set	5463 reflections (5.03%)	wwPDI3-VP
Total number of atoms	4545	wwPDI3-VP
Ramachandran favored (%)	97.86	phenix_table1
Ramachandran allowed (%)	2.14	phenix_table1
Ramachandran outliers (%)	0.00	phenix_table1
Rotamer outliers (%)	0.00	phenix_table1
RMS bonds, angles	0.008, 1.28	phenix_table1
Clashscore	2.83	phenix_table1
Average B, all atoms (Å2)	14.0 14.2	wwPDI3-VP phenix_table1
Average B, macromolecules	11.6	phenix_table1
Average B, ligands	50.1	phenix_table1
Average B, solvent	25.6	phenix_table1

SI Table 3: Quantitative comparison of 14-3-3 binding motifs. The analyzed structures are grouped based on the subpanels of Figure 4 and the peptide sequences were aligned via the phosphorylated residue of the binding motifs (position 0). The complete structures (14-3-3 protein and interaction partner) were aligned via the Cα atoms of the residues and the distances of corresponding amino acids were measured using the "Structural alignment – Gesamt" tool of the CCP4i2 suite. Due to the considerably different conformations of the peptides, the software aligned position +3 of 6F09 with position +4 of the reference structure (6HEO- IκBα) and position +4 of 5N6N0 with the position +5 of 6HEO (new positions are indicated in parentheses).

PDB ID\ position		-3	-2	-1	0	1	2	3	4	5
	Sequence									
reference model	6HEO			GLY	**SEP**	GLU	PRO	TRP	LYS	GLN
Figure 4A	6QZR	ARG	SER	CYS	**TPO**	PRO	LEU	PRO		
Figure 4B	6F09			TYR	**SEP**	SER	PRO	-	ASP (+3)	ILE (+4)
	1O9F	GLN	SER	TYR	**TPO**	VAL				
	3E6Y	GLN	SER	TYR	**TPO**	VAL				
Figure 4C	5ULO		SER	PRO	**SEP**	PHE				
	4DAU		ALA	MET	**SEP**	PHE	GLN	SER		
Figure 4D	5N6N	ARG	ARG	GLY	**SEP**	GLU	ASP	ASP	-	THR (+4)
Figure 4E	6GKF	TYR	ASP	LEU	**SEP**	LEU	PRO	PHE	PRO	
	3UAL	ARG	SER	PHE	**SEP**	GLU	PRO	PHE	GLY	
	Distance (Å)									
Figure 4A	6QZR			0.51	**0.53**	0.71	2.41	3.07		
Figure 4B	6F09			0.50	**0.25**	0.26	0.79	-	2.81	1.58
	1O9F			0.67	**0.71**	1.44				
	3E6Y			0.60	**0.72**	1.14				
Figure 4C	5ULO			0.91	**0.56**	0.63				
	4DAU			0.52	**0.38**	0.37	0.42			
Figure 4D	5N6N			1.48	**0.80**	0.81	3.09	2.64	-	1.58
Figure 4E	6GKF			1.36	**0.50**	0.81	1.61	2.63		
	3UAL			0.36	**0.22**	0.33	0.96	1.53	2.96	

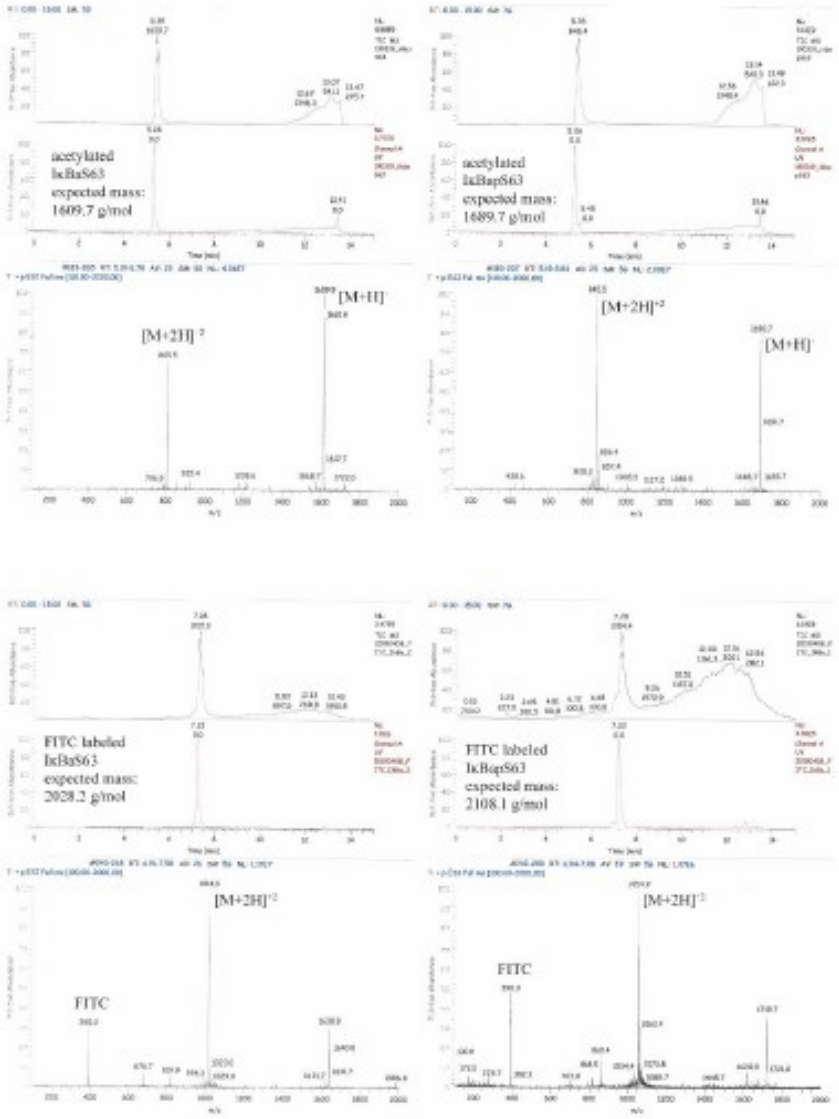

SI Figure 3: LC-MS analysis of the in-house prepared and purified peptides.

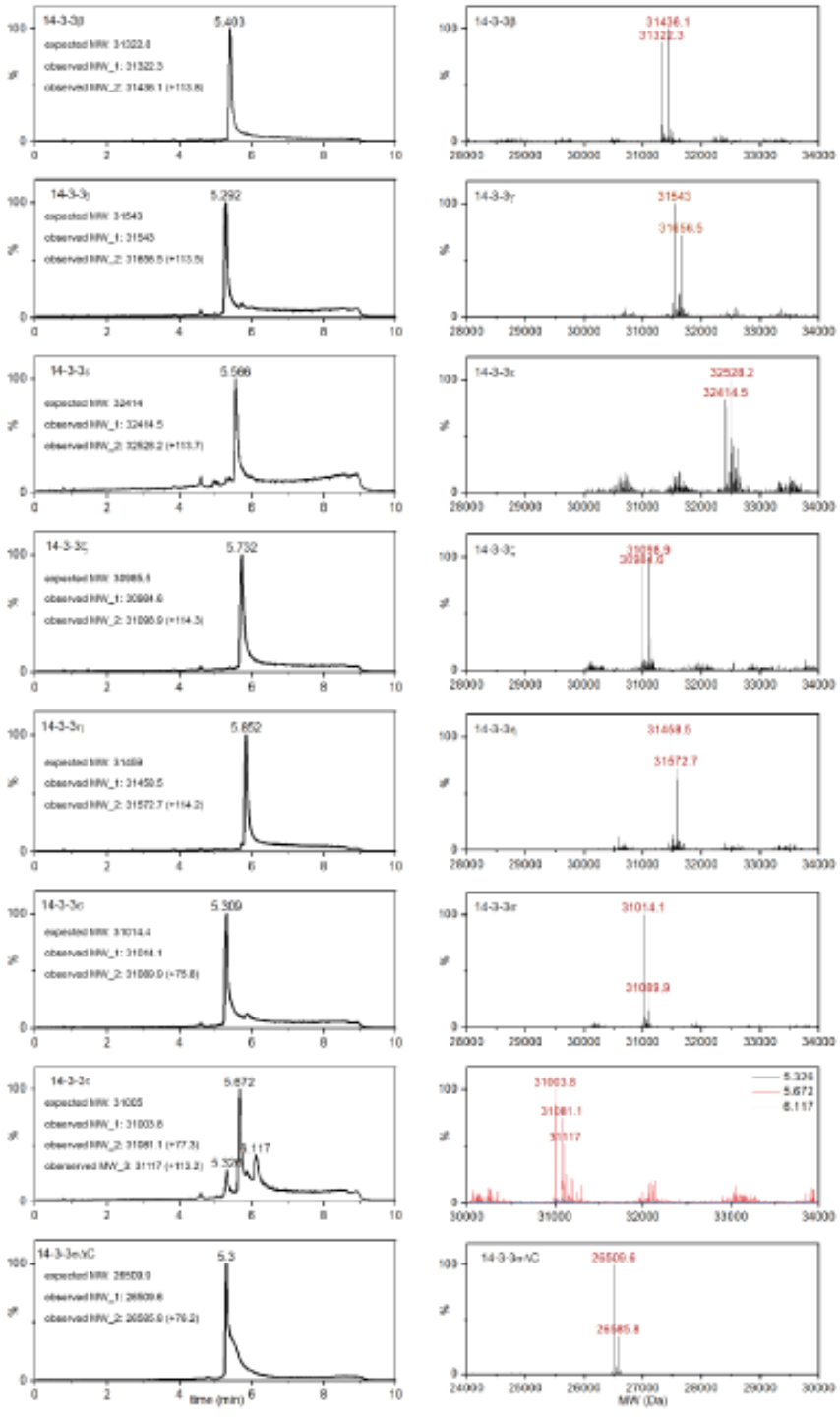

SI Figure 4: QTOF measurements of the purified 14-3-3 isoforms. The purity of the chromatogram (left panel) was taken as indication for the purity of the protein. The mass over charge distributions corresponding to the peak(s) in the chromatogram were deconvoluted to

a single mass using the the MaxEnt1 function of the MassLynx MS Software. Settings were chosen in the following way: the output mass range is shown on the x-axis, resolution was set to 0.1 Da/channel; a simulated isotope pattern model was used as damage model, while the blur width was determined via the peak width at half the of the peak height of the most abundant peak; the deconvolution was iterated until convergence and the mock results were compared with the initial mass spectra to ensure success of the deconvolution.

7.3 Supplement S3

7.3.1 Set-up and screening of a fragment library targeting the 14-3-3 protein interface

Dario Valenti, João Filipe Neves, François-Xavier Cantrelle, Stanimira Hristeva, **Domenico Lentini Santo**, Tomáš Obšil, Xavier Hanoulle, Laura M. Levy, Dimitrios Tzalis, Isabelle Landrieu, and Christian Ottmann. Set-up and screening of a fragment library targeting the 14-3-3 protein interface. *Medchemcomm* 10(10):1796-1802 (2019).

My contribution: Evaluation of fragments using the thermal shift assay experiments.

MedChemComm

RESEARCH ARTICLE

View Article Online
View Journal | View Issue

Check for updates

Cite this: Med. Chem. Commun., 2019, 10, 1796

Set-up and screening of a fragment library targeting the 14-3-3 protein interface†

Dario Valenti,‡[ab] João Filipe Neves,‡[c] François-Xavier Cantrelle,[c] Stanimira Hristeva,[a] Domenico Lentini Santo,[d] Tomáš Obšil,[de] Xavier Hanoulle,[c] Laura M. Levy,‡[a] Dimitrios Tzalis,*[a] Isabelle Landrieu‡*[c] and Christian Ottmann ‡*[bf]

Received 11th April 2019,
Accepted 20th July 2019

DOI: 10.1039/c9md00215d

rsc.li/medchemcomm

Protein–protein interactions (PPIs) are at the core of regulation mechanisms in biological systems and consequently became an attractive target for therapeutic intervention. PPIs involving the adapter protein 14-3-3 are representative examples given the broad range of partner proteins forming a complex with one of its seven human isoforms. Given the challenges represented by the nature of these interactions, fragment-based approaches offer a valid alternative for the development of PPI modulators. After having assembled a fragment set tailored on PPIs' modulation, we started a screening campaign on the sigma isoform of 14-3-3 adapter proteins. Through the use of both mono- and bi-dimensional nuclear magnetic resonance spectroscopy measurements, coupled with differential scanning fluorimetry, three fragment hits were identified. These molecules bind the protein at two different regions distant from the usual binding groove highlighting new possibilities for selective modulation of 14-3-3 complexes.

Published on 22 July 2019. Downloaded by Charles University on 7/7/2020 10:09:10 AM.

Introduction

Adapter proteins play a crucial role in the formation of complexes and their stabilization in regulatory pathways. Given their function – to mediate interactions between two proteins and therefore to regulate the activity or localization of their partners – this protein class represents an attractive point for therapeutic intervention. An example of adapter proteins is represented by the 14-3-3 protein family that – through its seven human isoforms[1] – is involved in the regulation of numerous biological functions such as cellular signalling,[2] protein translocation,[3] enzymatic activity modulation,[4] cell cycle regulation,[5] structural maintenance,[6] and many others. 14-3-3 proteins are dimers composed of two 30 kDa monomers constituted by 9 α helices, named αA–αI.[1] Nowadays, PPIs attract significant interest in the pharmaceutical industry but are also challenging targets in drug discovery. PPIs involved in regulation are generally weak, ensuring a turn-over and mainly corresponding to superficial interactions between two – or more – proteins. Nonetheless, the multiplicity of hydrogen bonds,[7] lipophilic interactions, π-stacking, π-cation stacking[8] and ionic interactions[9] observed in these interactions constitutes a complex and dynamic network that is hard to emulate. Their modulation has been studied intensively and several approaches have emerged to improve the discovery of small molecules able to offer therapeutic intervention.

In previous contributions,[10–13] the rise of fragment-based approaches in this field was discussed as a good opportunity for developing successful modulators. *Circa* one third of the clinical candidates or approved drugs modulating PPIs have been indeed developed by application of fragment-based campaigns.[10] The central idea of the fragment-based approach (FBA) is to develop a ligand for its own target, building it piece-by-piece from a low molecular weight (MW) molecule. Because of this principle, this strategy offers numerous advantages such as the possibility of constantly validating the molecules' evolution and of covering a very broad chemical space using one binding pharmacophore. This multidisciplinary strategy is generally constituted by a

[a] Medicinal Chemistry, Taros Chemicals GmbH & Co. KG, Emil-Figge-Straße 76a, 44227, Dortmund, Germany. E-mail: dtzalis@taros.de
[b] Department of Biomedical Engineering and Institute for Complex Molecular Systems, Technische Universiteit Eindhoven, Den Dolech 2, 5612 AZ Eindhoven, The Netherlands. E-mail: c.ottmann@tue.nl
[c] Univ. Lille, CNRS, UMR 8576 – UGSF, F-59000 Lille, France. E-mail: isabelle.landrieu@univ-lille.fr
[d] Department of Physical and Macromolecular Chemistry, Faculty of Science, Charles University, 12843 Prague, Czech Republic
[e] Department of Structural Biology of Signaling Proteins, Division BIOCEV, Institute of Physiology of the Czech Academy of Sciences, Prumyslova 595, 252 50 Vestec, Czech Republic
[f] Department of Chemistry, University of Duisburg-Essen, Universitätsstraße 7, 45117, Essen, Germany

† Electronic supplementary information (ESI) available: Statistical analysis of the fragment collection, DSF melting curves, DSF compound-induced thermal shifts, WaterLOGSY NMR spectra, ^{1}H–^{15}N TROSY-HSQC NMR spectra and chemical shift perturbation plots. See DOI: 10.1039/c9md00215d

‡ These authors contributed equally to this work.

This journal is © The Royal Society of Chemistry 2019

Published on 22 July 2019. Downloaded by Charles University on 7/7/2020 10:09:10 AM.

multistep workflow that allows scientists to go relatively fast from a fragment – an entity with a MW ≤ 300 Da – to a drug-like molecule ready to enter the clinical phase. The fragments' character – reported by Congreve *et al.* in 2003[14] – enhances the possibilities of finding key structural motifs able to address the target's binding site with higher ligand efficiency. However, as fragments do not contain many functional groups, the number of interactions with the target is also limited and therefore these compounds bind weakly (normally in the high μM–mM range). Among the broad range of biophysical techniques involved in the primary screening, nuclear magnetic resonance (NMR) is especially suitable to detect weak and very weak interactions (μM–mM range),[15] which is a major reason for its employment in the FBA. NMR fragment screening methods can be divided into two classes: ligand-based methods and protein-based methods. While ligand-based methods allow the fast and sensitive screening of fragment mixtures with little material consumption,[16] protein-based methods are more robust and allow, in cases where a protein assignment is available, the determination of the approximate binding site.[17]

In recent years, considerable effort has been put on the development of modulators of 14-3-3 PPIs, ranging from covalent[18] and non-covalent fragments,[19] peptidomimetic inhibitors,[20,21] semi-synthetic derivatives of natural compounds[22] and molecular tweezers.[23,24] Considering that 14-3-3 proteins have hundreds of different protein-partners with a variety of binding interfaces, the discovery of small attaching points in their structures is important towards the selective modulation of 14-3-3 PPIs. The results presented here contribute to the enrichment of the portfolio of 14-3-3 binders with three novel fragments binding to two different areas of 14-3-3σ.

Experimental

Set-up of the fragment collection

With the aim to identify novel chemical entities as a starting point in the development of modulators (either disruptive or stabilizing) of 14-3-3σ interactions, we performed a fragment screening campaign. The first step on this pathway is the set-up of a pool of fragments. Currently, Taros proprietorial fragment collection has a subdivision dedicated to the PPIs' modulation with *circa* 1230 entries comprising both commercially available and novel structures. In this paragraph, we describe the guidelines used for building up this fragments' set. In usual practice, Congreve's "Rule of Three" (Ro3) would be applied. It represents one of the main guidelines for identifying molecules presenting the optimal physico-chemical properties required to be considered as a reliable member of the set. These attributes can be listed as follows: molecular weight ≤ 300 Da and clog P ≤ 3 as well as the number of rotatable bonds and hydrogen-bond acceptors (HBAs) and donors (HBDs), and polar surface area (PSA) ≤ 60 Å^2. However, considering the superficial nature of PPIs as well as the dynamic behaviour of a pocket formed by two proteins, we decided to apply a higher tolerance regarding the previously mentioned selection parameters. Thus, we considered as optimal parameters molecular weight ≤ 330 Da, clog P ≤ 3.4, the number of rotatable bonds ≤4 as well as the hydrogen-bond acceptors (HBAs) and donors (HBDs) and finally a polar surface area ≤70 Å^2. Nonetheless, in order to include also very attractive and chemically accessible structures that otherwise would not have passed the filtering phase, we decided to perform pre-filtering on the whole Taros internal compound collection (*ca.* 20 000 entries) fixing a threshold of 350 Da for the MW. This pre-filtering phase was followed by a visual inspection of the molecules (*ca.* 300) with a mass between 330 Da (our parameters for the final physico-chemical filtering) and 350 Da. As anticipated, the process started from the whole Taros compound collection and after two rounds of physico-chemical property filtering we reached a pool of *ca.* 4000 entries. Internal verification of eventual intellectual property issues for all novel structures within this set decreased the number of molecules to 3200, which were submitted to additional considerations. The aim of this second step was to remove the entries presenting undesired structural features and to create a diversified collection. Inspecting the collection from a medicinal chemistry point of view led us to exclude extremely reactive functions, such as alkylating or acylating features like aliphatic halides, acyl chlorides, epoxides, imines, oximes and acetals. We also excluded Michael acceptors and isocyanates due to their strong electrophilic character. On the other hand, polycyclic and heterocyclic compounds were always preferred when possible. The presence of sp^3-enriched compounds was also encouraged according to the notion that molecules with a pronounced three-dimensional character appear to be more drug-like.[25] Moreover, molecules having a 3D-character may cover a wider portion of extended pockets – such as the ones formed in protein complexes – and could also address the optimization toward different spatial coordinates.[26] Another consideration applied in this phase was the synthetic accessibility of the molecules and the presence of exit points for further diversification. Moreover, in order to keep the reactivity of the molecules under control and at the same time to enhance the synthetic tractability of any eventual hit, we considered the isosteric members of the collection. The carboxylic acid feature was generally favoured in respect to the corresponding boronic acid or nitro group, but the substitution was not strictly enforced, depending on the in-house availability for a given core. For maintaining a high diversity between the cores composing the set, we picked – after visual inspection – one of the three possible positions for mono substituted aromatic rings keeping the other two as backup molecules. The physical availability of the selected entries was evaluated and compounds available in less than 30 mg were discarded. Quality control was applied using uHPLC-MS integrated systems and – when necessary – purification by preparative HPLC was carried out. Applying this workflow, we built up a collection of *circa* 900 compounds. This last set was then further enriched by the design and synthesis of *ca.* 300 additional novel cores based on both natural products

Published on 22 July 2019. Downloaded by Charles University on 7/7/2020 10:09:10 AM.

and already known scaffolds in medicinal chemistry. Fig. 1 shows the workflow applied for the set-up of the Taros fragment library. Currently, the PPI-dedicated section of the Taros fragment collection counts *circa* 1230 entries and is constantly growing. For a statistical analysis of the physicochemical properties, we refer to Fig. S1 and S2.† Finally, for the goals of this project, we selected *circa* 800 fragments that were first combined in cocktails containing five fragments each and then screened against 14-3-3σ applying a multistep approach.

Protein production and purification

14-3-3σ (for differential scanning fluorimetry experiments) or 14-3-3σΔC17 (cleaved after T231 – used for NMR experiments to improve the quality of the NMR spectra) was expressed in *E. coli* BL21 (DE3) cells transformed with a pProExHtb vector carrying the cDNA to express an N-terminally His_6-tagged human 14-3-3σ or 14-3-3σΔC17. An overnight 20 mL preculture in Luria–Bertani (LB) medium was used to inoculate 1 L of culture medium. For the natural abundance proteins, cells were inoculated in 1 L of M9 minimal medium supplemented with 4 g L^{-1} glucose, 1 g L^{-1} ammonium chloride, 5% (v/v) LB medium and 100 μg mL^{-1} ampicillin. For $^{15}N^{2}H$ labelling, the cells were inoculated in 1 L of deuterated M9 minimal medium supplemented with 2 g L^{-1} $^{12}C_6{}^{2}H_7$ glucose, 1 g L^{-1} ^{15}N ammonium chloride, 0.4 g L^{-1} Isogro $^{15}N^{12}C^{2}H$ powder-growth medium (Sigma Aldrich) and 100 μg mL^{-1} ampicillin. Cells were grown at 37 °C to an OD_{600} of 0.9 and induced with 0.5 mM IPTG. Incubation was continued for 12 h at 25 °C for the natural abundance proteins and for 15 h at 28 °C for the $^{15}N^{2}H$ labelled protein. Cells were harvested by centrifugation and lysed with a homogenizer and the proteins were purified using a Ni-NTA column (GE Healthcare). The N-terminal His_6-tag was then cleaved by the TEV protease and the proteins were further dialyzed overnight at 4 °C against the NMR buffer (100 mM sodium phosphate, pH 6.8, 50 mM NaCl), concentrated, aliquoted, flash frozen and stored at −80 °C. Typical yields were in the range of 40 to 80 mg of protein per liter of culture. A detailed protocol can be found in the study of Neves *et al.*[27]

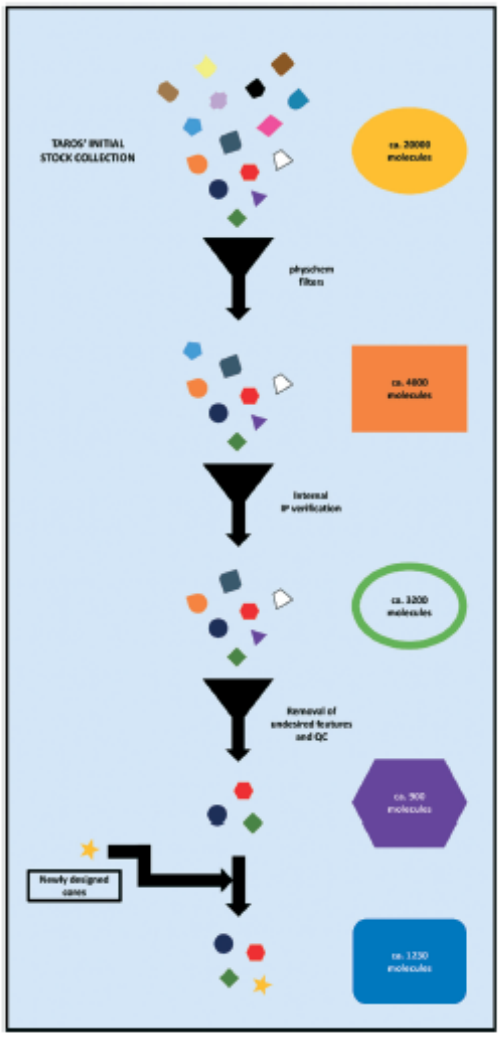

Fig. 1 Workflow applied for setting up the Taros PPI fragment library.

Differential scanning fluorimetry

Differential scanning fluorimetry (DSF) thermal melting points were recorded using a LightCycler® 480 (Roche, Switzerland). Measurements were performed in 96-well plates with samples containing 7 μM 14-3-3σ in the presence or absence of each cocktail (2500 μM per fragment). The buffer contained 100 mM Hepes, pH 7.5, 150 mM NaCl and 4% (v/v) DMSO. The fluorescent probe SYPRO Orange (Sigma Aldrich) was added at a dilution of 1 : 600. The excitation filter for SYPRO Orange was set to 465 nm and the emission filter was set to 580 nm. The temperature was increased from 20 °C to 95 °C at a rate of 0.6 °C per minute. Melting temperature values were determined using the LightCycler® 480 software version 1.5.1.62 by plotting the first derivative of the melting curves (Fig. S3†). All the measurements were performed in triplicate and the deviations of melting temperatures (ΔTm) presented for each cocktail were calculated relatively to three control samples (7 μM 14-3-3σ in the absence of the compound) measured in the same 96-well plate.

WaterLOGSY experiments

WaterLOGSY spectra were acquired in 5 mm tubes (sample volume 530 μL) using a 600 MHz Bruker Avance III HD spectrometer equipped either with a CPQCI cryogenic probe or with a TXI non-cryogenic probe. The spectra were recorded with 32 768 complex data points and with a mixing time of 1.7 s. The number of scans per increment was 384 when the spectrometer was equipped with a cryogenic probe

 This journal is © The Royal Society of Chemistry 2019

Published on 22 July 2019. Downloaded by Charles University on 7/7/2020 10:09:10 AM.

(acquisition time of 35 minutes per experiment) and 1280 when the spectrometer was equipped with a non-cryogenic probe (acquisition time of 118 minutes). The spectra were acquired at 16 °C, in a buffer containing 100 mM sodium phosphate, 50 mM NaCl, pH 6.8 and 10% (v/v) D_2O. The final concentration of DMSO-d_6 was 2% and was kept constant for all the experiments. The spectra were obtained with samples containing 25 μM 14-3-3σΔC17 in the presence or in the absence of each cocktail (500 μM per fragment) or each fragment (at 500 μM). Additional control experiments were performed in the presence of the cocktail/fragment and in the absence of protein. Spectra were collected and processed with Topspin 3.5 (Bruker Biospin, Karlsruhe, Germany).

2D nuclear magnetic resonance experiments

^1H–^{15}N TROSY-HSQC spectra were acquired in 3 mm tubes (sample volume 200 μL) using a 900 MHz Bruker Avance-NEO spectrometer, equipped with a cryoprobe. The spectra were recorded with 3072 complex data points in the direct dimension and 120 complex data points in the indirect dimension, with 128 scans per increment (acquisition time of 4 hours per experiment), at 32 °C, in a buffer containing 100 mM sodium phosphate, 50 mM NaCl, pH 6.8, 1 mM DTT, EDTA-free protease inhibitor cocktail (Roche, Basel, Switzerland) and 10% (v/v) D_2O. The final concentration of DMSO-d_6 was 2% and was kept constant for all the experiments. The spectra were obtained with samples containing 75 μM $^{15}N^2H$ labelled 14-3-3σΔC17 in the presence or in the absence of each cocktail (2000 μM per fragment). Backbone assignments of $^{15}N^2H$ labelled 14-3-3σΔC17 were previously reported.[27] The reference for the ^1H chemical shift was relative to trimethylsilyl propionate (TMSP) or 4,4-dimethyl-4-silapentane-1-sulfonic acid (DSS). ^{15}N chemical shifts were referenced indirectly. Spectra were collected and processed with Topspin 4.0 (Bruker Biospin, Karlsruhe, Germany) and analyzed with Sparky 3.12 (T. D. Goddard and D. G. Kneller, SPARKY 3, University of California, San Francisco). CSPs in the form of chemical shift value modifications (in ppm) on the ^1H–^{15}N TROSY-HSQC were calculated using the following equation:

$$\Delta\delta = \sqrt{\Delta\delta\left(^1H\right)^2 + \left[0.14 \times \Delta\delta\left(^{15}N\right)^2\right]}$$

Results and discussion

Fragment screening strategy

A library of 785 fragments grouped in 157 cocktails of 5 compounds each was screened for binding to 14-3-3σ with the objective of finding low MW starting points for the development of PPI modulators. Initially, ^1H–^{15}N TROSY-HSQC spectra were directly recorded for 55 out of the 157 cocktails. For the screening of the rest of the library, DSF and WaterLOGSY were introduced in order to allow a primary screening of the cocktails before confirmation by ^1H–^{15}N TROSY-HSQC – which is costly and time consuming but offers the additional advantage of identifying the binding pocket. DSF screening was used for 156 out of the 157 cocktails and WaterLOGSY was applied for the 102 cocktails that were not directly screened by ^1H–^{15}N TROSY-HSQC. The cocktails which showed binding by either WaterLOGSY or DSF were further screened by ^1H–^{15}N TROSY-HSQC (secondary screening). The fragments contained in the cocktails showing binding by ^1H–^{15}N TROSY-HSQC were further individually screened initially by WaterLOGSY and finally by ^1H–^{15}N TROSY-HSQC for the determination of the binding site. A diagram illustrating this screening strategy is presented in Fig. 2.

Primary screening by WaterLOGSY

WaterLOGSY is a ligand-based NMR screening method that allows the fast screening of fragment libraries based on the nuclear Overhauser effect (NOE).[28] WaterLOGSY requires a lower amount of protein in comparison with protein-based NMR methods and does not require isotopic labelling of the target. Moreover, this method allows a straightforward hit identification since the NMR signals of binders and non-binders have a different phase in the WaterLOGSY spectrum

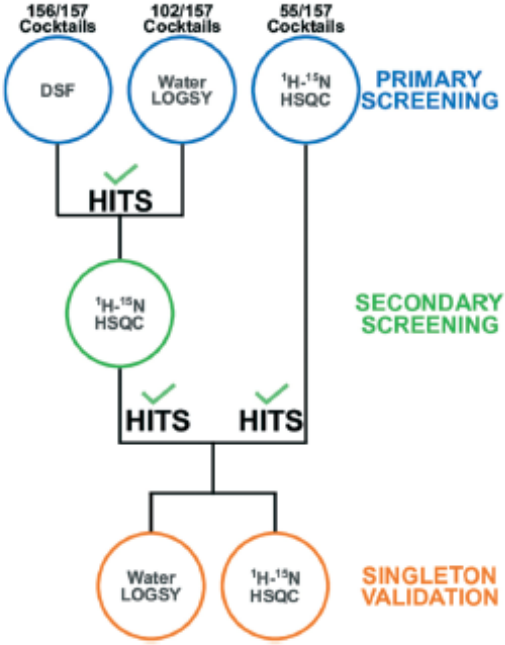

Fig. 2 Workflow of the fragment screening campaign. DSF, WaterLOGSY and ^1H–^{15}N TROSY-HSQC were employed for primary screening. Secondary screening by ^1H–^{15}N TROSY-HSQC was performed for the cocktails that showed binding by either DSF or WaterLOGSY. WaterLOGSY and ^1H–^{15}N TROSY-HSQC were performed for singleton validation.

Published on 22 July 2019. Downloaded by Charles University on 7/7/2020 10:09:10 AM.

(Fig. S4†). WaterLOGSY was performed for the 102 cocktails that were not directly screened by $^{1}H–^{15}N$ TROSY-HSQC. Binding was detected for 43 out of the 102 cocktails, which were selected for secondary screening by $^{1}H–^{15}N$ TROSY-HSQC.

Primary screening by differential scanning fluorimetry

Differential scanning fluorimetry (DSF) is a fast method to screen a fragment library with little material consumption. The principle relies on monitoring the thermal melting curve of the protein upon gradual heating of the protein solution and on the determination of the melting temperature (Tm). A protein-ligand interaction is therefore detected when the binder induces a shift in the melting temperature of the protein.[29] Unlike most proteins, the thermal denaturation profile of 14-3-3σ shows two sigmoidal curves, suggesting that there are two unfolding transitions (Fig. S3†). Both melting temperatures were determined for all the samples and the binding effect was considered significant upon the induction of a thermal shift higher than 1 °C in the sum of both melting temperatures ($\Delta Tm1 + \Delta Tm2 > 1$ °C). After the primary screening, 22 out of the screened 156 cocktails showed a significant thermal shift effect (Table S1†). These cocktails were therefore selected for secondary screening. 15 cocktails out of these 22 also showed binding by WaterLOGSY.

Primary/secondary screening by $^{1}H–^{15}N$ TROSY-HSQC

$^{1}H–^{15}N$ HSQC is the most popular method for protein-based NMR screening. In spite of being more expensive and time-consuming when compared to ligand-based NMR methods, $^{1}H–^{15}N$ HSQC is a more robust method and has the important advantage of identifying the binding site of the ligands.[30] $^{1}H–^{15}N$ TROSY-HSQC was used for the screening of 55 out of 157 cocktails and as a secondary screening technique for the 50 cocktails that showed binding by either WaterLOGSY (43), DSF (22) or both (15). From these, 6 cocktails showed a significant effect on the $^{1}H–^{15}N$ TROSY-HSQC spectrum of 14-3-3σ.

All 6 cocktails were found to be positive by WaterLOGSY and 4 were positive by DSF as well.

False positives in the DSF screening could be due to aggregates of compounds since a considerable part of the hits showed solubility problems at the tested concentration.

Compared to $^{1}H–^{15}N$ TROSY-HSQC, WaterLOGSY also provided a very high hit rate. Probably some of the hits detected were just binding transiently to the protein and were too weak to be detected by $^{1}H–^{15}N$ TROSY-HSQC. Although negative control experiments were performed for all the WaterLOGSY tested cocktails, aggregation cannot be excluded as a source of false positives in this method. It is also possible that some of the WaterLOGSY hits were not confirmed due to the fact that around 15% of the amide resonances of 14-3-3σΔC17 are undetected in the $^{1}H–^{15}N$ TROSY-HSQC.

Confirmation of hits from the cocktails and binding site identification

After the identification and orthogonal validation of 6 hit cocktails, their components were tested as singletons. Thirty singletons were further screened individually by WaterLOGSY. Six out of these 30 singletons (1 per each cocktail) showed a positive effect and were submitted to the final confirmation by $^{1}H–^{15}N$ TROSY-HSQC. Two out of these 6 singletons failed to cause a significant effect on the 2D spectrum of 14-3-3σΔC17. One singleton caused chemical shift perturbations but also induced protein precipitation and was, for this reason, excluded from the screening. Three out of the 6 singletons were successfully confirmed as binders by $^{1}H–^{15}N$ TROSY-HSQC because each produced the same effect by itself on the spectrum as its corresponding cocktail of five. These 3 fragments were therefore validated by both a ligand-based method (Fig. S5–S7†) and a protein-based method (Fig. S8–S10†). Fragments 1 and 2 were seen to bind at the top of 14-3-3 helices αH and αI (Fig. S8, S9,† and 3) and fragment 3 was seen to bind at the dimer interface (Fig. S10† and 3). Interestingly, the cocktails containing the fragments that were seen to bind at the top of helices αH and αI did not produce a significant effect by DSF while the cocktail containing fragment 3 induced a significant thermal shift. This fact suggests that binding at the upper region of the protein does not have an influence on its denaturation. NMR was used for the screening because of its sensitivity to even very weak binders, as expected for fragments. The discrete number of resonances in the $^{1}H–^{15}N$ TROSY-HSQC spectrum affected by the binding, together with the observed fast exchange regime regarding the NMR time scale, gives an estimate of the K_d in the

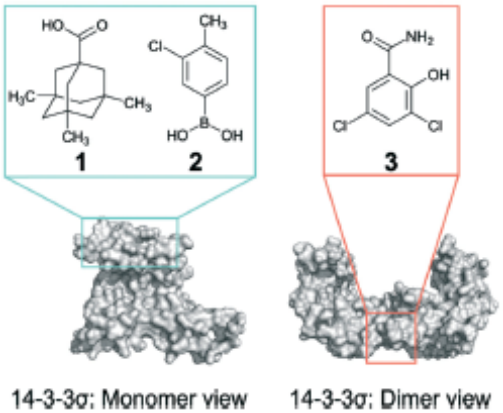

Fig. 3 Identification of the binding sites of the hits by $^{1}H–^{15}N$ TROSY-HSQC. The structures of the hits are represented and their binding sites are shown in the crystal structure of 14-3-3σ (gray surface - PDB ID: 1YZ5). Fragments 1 and 2 induce chemical shift perturbations in resonances corresponding to amino acid residues located on the top of helices αH and αI. Fragment 3 induces chemical shift perturbations in resonances corresponding to amino acid residues located at the dimer interface of 14-3-3σ.

This journal is © The Royal Society of Chemistry 2019

Published on 22 July 2019. Downloaded by Charles University on 7/7/2020 10:59:10 AM.

high μM–mM range.[31] Later stage optimization of the selected fragments should focus on improving the binding affinity.

Conclusions

Here, we discussed a strategy applied in the set-up of a fragment collection dedicated to PPI modulation. The specificity of this type of contacts, involving superficial interactions (no deep pocket) and flexibility at the interface, was taken into account to build the library by loosening the physico-chemical restrictions imposed by the general Rule of Three guidelines. This approach was also derived from the considerations made by Chen and Hubbard[32] about the slight increment of both molecular weight and hydrophobicity in fragment hits modulating protein–protein complexes. The resulting distribution of fragment physico-chemical properties (Fig. S1 and S2†) demonstrates that the described fragment collection indeed meets these criteria and will be valuable for further applications targeting PPI modulation.

In this work, we screened the fragment library on the adapter protein 14-3-3σ using a multi-technique approach. Application of mono- and bi-dimensional NMR coupled with DSF provided us a robust and orthogonally validated dataset of molecules, rapidly excluding false positives and reintegrating false negative hits.

Eventually, we identified three fragment hits binding two different sites from the classic amphipathic groove of 14-3-3σ, where most of the protein partners bind. Nevertheless, some examples in which the protein partners establish contacts with different regions of 14-3-3 are reported.[33–38] In these cases, fragments that bind remotely from the classic amphipathic binding groove represent a unique opportunity for selective modulation of the PPIs.

The hits disclosed by this integrated screening campaign represent a new starting point for modulating the 14-3-3 PPIs and highlight an important opportunity for selectivity improvement towards a specific protein complex.

Conflicts of interest

There are no conflicts to declare.

Acknowledgements

This research is supported by funding from the European Union through the TASPPI project (H2020-MSCA-ITN-2015, grant number 675179). D. V. acknowledges Dr. Martin Corpet for the fruitful scientific discussion. J. F. N., F.-X. C., X. H. and I. L. acknowledge LabEx (Laboratory of Excellence) for financial support on the scope of the DISTALZ consortium (ANR, ANR-11-LABX-009). The NMR facilities were funded by the Nord Region Council, CNRS, Institut Pasteur de Lille, the European Community (ERDF), the French Ministry of Research and the University of Lille and by the CTRL CPER cofunded by the European Union with the European Regional Development Fund (ERDF), by the Hauts de France Regional Council (contract no. 17003781), Métropole Européenne de Lille (contract no. 2016_ESR_05), and French State (contract no. 2017-R3-CTRL-Phase 1). We acknowledge support for the NMR facilities from TGE RMN THC (CNRS, FR-3050) and FRABio (Univ. Lille, CNRS, FR-3688).

Notes and references

1 T. Obsil and V. Obsilova, *Semin. Cell Dev. Biol.*, 2011, 22, 663–672.
2 R. J. Daly, H. Gu, J. Parmar, S. Malaney, R. J. Lyons, R. Kairouz, D. R. Head, S. M. Henshall, B. G. Neel and R. L. Sutherland, *Oncogene*, 2002, 21, 5175–5181.
3 C. Aguilera, V. Fernández-Majada, J. Inglés-Esteve, V. Rodilla, A. Bigas and L. Espinosa, *J. Cell Sci.*, 2006, 119, 3695–3704.
4 S. C. Masters, H. Yang, S. R. Datta, M. E. Greenberg and H. Fu, *Mol. Pharmacol.*, 2001, 60, 1325–1331.
5 K. H. Vousden and C. Prives, *Cell*, 2009, 137, 413–431.
6 N. N. Sluchanko and N. B. Gusev, *J. Alzheimer's Dis.*, 2011, 27, 467–476.
7 L.-G. Milroy, T. N. Grossmann, S. Hennig, L. Brunsveld and C. Ottmann, *Chem. Rev.*, 2014, 114, 4695–4748.
8 M. G. Wuo, A. B. Mahon and P. S. Arora, *J. Am. Chem. Soc.*, 2015, 137, 11618–11621.
9 B. Schumacher, J. Mondry, P. Thiel, M. Weyand and C. Ottmann, *FEBS Lett.*, 2010, 584, 1443–1448.
10 D. Valenti, S. Hristeva, D. Tzalis and C. Ottmann, *Eur. J. Med. Chem.*, 2019, 167, 76–95.
11 A. P. Turnbull, S. M. Boyd and B. Walse, *Res. Rep. Biochem.*, 2014, 4, 13–26.
12 E. Valkov, T. Sharpe, M. Marsh, S. Greive and M. Hyvönen, *Top. Curr. Chem.*, 2012, 317, 145–179.
13 T. V. Magee, *Bioorg. Med. Chem. Lett.*, 2015, 25, 2461–2468.
14 M. Congreve, R. Carr, C. Murray and H. Jhoti, *Drug Discovery Today*, 2003, 8, 876–877.
15 M. P. Williamson, *Prog. Nucl. Magn. Reson. Spectrosc.*, 2013, 73, 1–16.
16 L. Unione, S. Galante, D. Díaz, F. J. Cañada and J. Jiménez-Barbero, *MedChemComm*, 2014, 5, 1280–1289.
17 A. D. Gossert and W. Jahnke, *Prog. Nucl. Magn. Reson. Spectrosc.*, 2016, 97, 82–125.
18 E. Sijbesma, K. K. Hallenbeck, S. Leysen, P. J. de Vink, L. Skóra, W. Jahnke, L. Brunsveld, M. R. Arkin and C. Ottmann, *J. Am. Chem. Soc.*, 2019, 141, 3524–3531.
19 E. Sijbesma, L. Skora, S. Leysen, L. Brunsveld, U. Koch, P. Nussbaumer, W. Jahnke and C. Ottmann, *Biochemistry*, 2017, 56, 3972–3982.
20 S. A. Andrei, F. A. Meijer, J. F. Neves, L. Brunsveld, I. Landrieu, C. Ottmann and L.-G. Milroy, *ACS Chem. Neurosci.*, 2018, 9, 2639–2654.
21 L.-G. Milroy, M. Bartel, M. A. Henen, S. Leysen, J. M. C. Adriaans, L. Brunsveld, I. Landrieu and C. Ottmann, *Angew. Chem., Int. Ed.*, 2015, 54, 15720–15724.
22 S. A. Andrei, P. de Vink, E. Sijbesma, L. Han, L. Brunsveld, N. Kato, C. Ottmann and Y. Higuchi, *Angew. Chem., Int. Ed.*, 2018, 57, 13470–13474.

Published on 22 July 2019. Downloaded by Charles University on 7/7/2020 10:09:10 AM.

high μM–mM range.[31] Later stage optimization of the selected fragments should focus on improving the binding affinity.

Conclusions

Here, we discussed a strategy applied in the set-up of a fragment collection dedicated to PPI modulation. The specificity of this type of contacts, involving superficial interactions (no deep pocket) and flexibility at the interface, was taken into account to build the library by loosening the physico-chemical restrictions imposed by the general Rule of Three guidelines. This approach was also derived from the considerations made by Chen and Hubbard[32] about the slight increment of both molecular weight and hydrophobicity in fragment hits modulating protein–protein complexes. The resulting distribution of fragment physico-chemical properties (Fig. S1 and S2†) demonstrates that the described fragment collection indeed meets these criteria and will be valuable for further applications targeting PPI modulation.

In this work, we screened the fragment library on the adapter protein 14-3-3σ using a multi-technique approach. Application of mono- and bi-dimensional NMR coupled with DSF provided us a robust and orthogonally validated dataset of molecules, rapidly excluding false positives and reintegrating false negative hits.

Eventually, we identified three fragment hits binding two different sites from the classic amphipathic groove of 14-3-3σ, where most of the protein partners bind. Nevertheless, some examples in which the protein partners establish contacts with different regions of 14-3-3 are reported.[33–38] In these cases, fragments that bind remotely from the classic amphipathic binding groove represent a unique opportunity for selective modulation of the PPIs.

The hits disclosed by this integrated screening campaign represent a new starting point for modulating the 14-3-3 PPIs and highlight an important opportunity for selectivity improvement towards a specific protein complex.

Conflicts of interest

There are no conflicts to declare.

Acknowledgements

This research is supported by funding from the European Union through the TASPPI project (H2020-MSCA-ITN-2015, grant number 675179). D. V. acknowledges Dr. Martin Corpet for the fruitful scientific discussion. J. F. N., F.-X. C., X. H. and I. L. acknowledge LabEx (Laboratory of Excellence) for financial support on the scope of the DISTALZ consortium (ANR, ANR-11-LABX-009). The NMR facilities were funded by the Nord Region Council, CNRS, Institut Pasteur de Lille, the European Community (ERDF), the French Ministry of Research and the University of Lille and by the CTRL CPER cofunded by the European Union with the European Regional Development Fund (ERDF), by the Hauts de France Regional Council (contract no. 17003781), Métropole Européenne de Lille (contract no. 2016_ESR_05), and French State (contract no. 2017-R3-CTRL-Phase 1). We acknowledge support for the NMR facilities from TGE RMN THC (CNRS, FR-3050) and FRABio (Univ. Lille, CNRS, FR-3688).

Notes and references

1 T. Obsil and V. Obsilova, *Semin. Cell Dev. Biol.*, 2011, **22**, 663–672.
2 R. J. Daly, H. Gu, J. Parmar, S. Malaney, R. J. Lyons, R. Kairouz, D. R. Head, S. M. Henshall, B. G. Neel and R. L. Sutherland, *Oncogene*, 2002, **21**, 5175–5181.
3 C. Aguilera, V. Fernández-Majada, J. Inglés-Esteve, V. Rodilla, A. Bigas and L. Espinosa, *J. Cell Sci.*, 2006, **119**, 3695–3704.
4 S. C. Masters, H. Yang, S. R. Datta, M. E. Greenberg and H. Fu, *Mol. Pharmacol.*, 2001, **60**, 1325–1331.
5 K. H. Vousden and C. Prives, *Cell*, 2009, **137**, 413–431.
6 N. N. Sluchanko and N. B. Gusev, *J. Alzheimer's Dis.*, 2011, **27**, 467–476.
7 L.-G. Milroy, T. N. Grossmann, S. Hennig, L. Brunsveld and C. Ottmann, *Chem. Rev.*, 2014, **114**, 4695–4748.
8 M. G. Wuo, A. B. Mahon and P. S. Arora, *J. Am. Chem. Soc.*, 2015, **137**, 11618–11621.
9 B. Schumacher, J. Mondry, P. Thiel, M. Weyand and C. Ottmann, *FEBS Lett.*, 2010, **584**, 1443–1448.
10 D. Valenti, S. Hristeva, D. Tzalis and C. Ottmann, *Eur. J. Med. Chem.*, 2019, **167**, 76–95.
11 A. P. Turnbull, S. M. Boyd and B. Walse, *Res. Rep. Biochem.*, 2014, **4**, 13–26.
12 E. Valkov, T. Sharpe, M. Marsh, S. Greive and M. Hyvönen, *Top. Curr. Chem.*, 2012, **317**, 145–179.
13 T. V. Magee, *Bioorg. Med. Chem. Lett.*, 2015, **25**, 2461–2468.
14 M. Congreve, R. Carr, C. Murray and H. Jhoti, *Drug Discovery Today*, 2003, **8**, 876–877.
15 M. P. Williamson, *Prog. Nucl. Magn. Reson. Spectrosc.*, 2013, **73**, 1–16.
16 L. Unione, S. Galante, D. Díaz, F. J. Cañada and J. Jiménez-Barbero, *MedChemComm*, 2014, **5**, 1280–1289.
17 A. D. Gossert and W. Jahnke, *Prog. Nucl. Magn. Reson. Spectrosc.*, 2016, **97**, 82–125.
18 E. Sijbesma, K. K. Hallenbeck, S. Leysen, P. J. de Vink, L. Skóra, W. Jahnke, L. Brunsveld, M. R. Arkin and C. Ottmann, *J. Am. Chem. Soc.*, 2019, **141**, 3524–3531.
19 E. Sijbesma, L. Skora, S. Leysen, L. Brunsveld, U. Koch, P. Nussbaumer, W. Jahnke and C. Ottmann, *Biochemistry*, 2017, **56**, 3972–3982.
20 S. A. Andrei, F. A. Meijer, J. F. Neves, L. Brunsveld, I. Landrieu, C. Ottmann and L.-G. Milroy, *ACS Chem. Neurosci.*, 2018, **9**, 2639–2654.
21 L.-G. Milroy, M. Bartel, M. A. Henen, S. Leysen, J. M. C. Adriaans, L. Brunsveld, I. Landrieu and C. Ottmann, *Angew. Chem., Int. Ed.*, 2015, **54**, 15720–15724.
22 S. A. Andrei, P. de Vink, E. Sijbesma, L. Han, L. Brunsveld, N. Kato, C. Ottmann and Y. Higuchi, *Angew. Chem., Int. Ed.*, 2018, **57**, 13470–13474.

Physico-chemical Filtering

Physico-chemical properties have been calculated by ChemAxon JChem for Excel (version 16.10.1700.1231).

Fragments' quality control and purification

The initial purity of each fragment was analysed by uHPLC-MS integrated systems. For each sample, 100 mg were weighted and dissolved in a mixture of Acetonitrile and Methanol in ratio 1:1. The non-soluble fragments were excluded from the collection. uHPLC-MS checks were performed using uHPLC Agilent Technologies 1290 Infinity coupled with Agilent Technologies 6120 Quadrupole LC/MS, Column: ACQUITY UPLC®BEH C18 1.7 µm, mobile phase: mixture of Acetonitrile + 0.1% Formic Acid and Water + 0.1% Formic Acid. When purity was below the 85% threshold, preparative HPLC was performed using UPLC Agilent Technologies 1260 Infinity coupled with Agilent Technologies 6120 Quadrupole LC/MS, Column: XBridge EH C18 5 µm, 19 mm x 150 mm, mobile phase: mixture of Acetonitrile + 0.1% Formic Acid and Water + 0.1% Formic Acid.

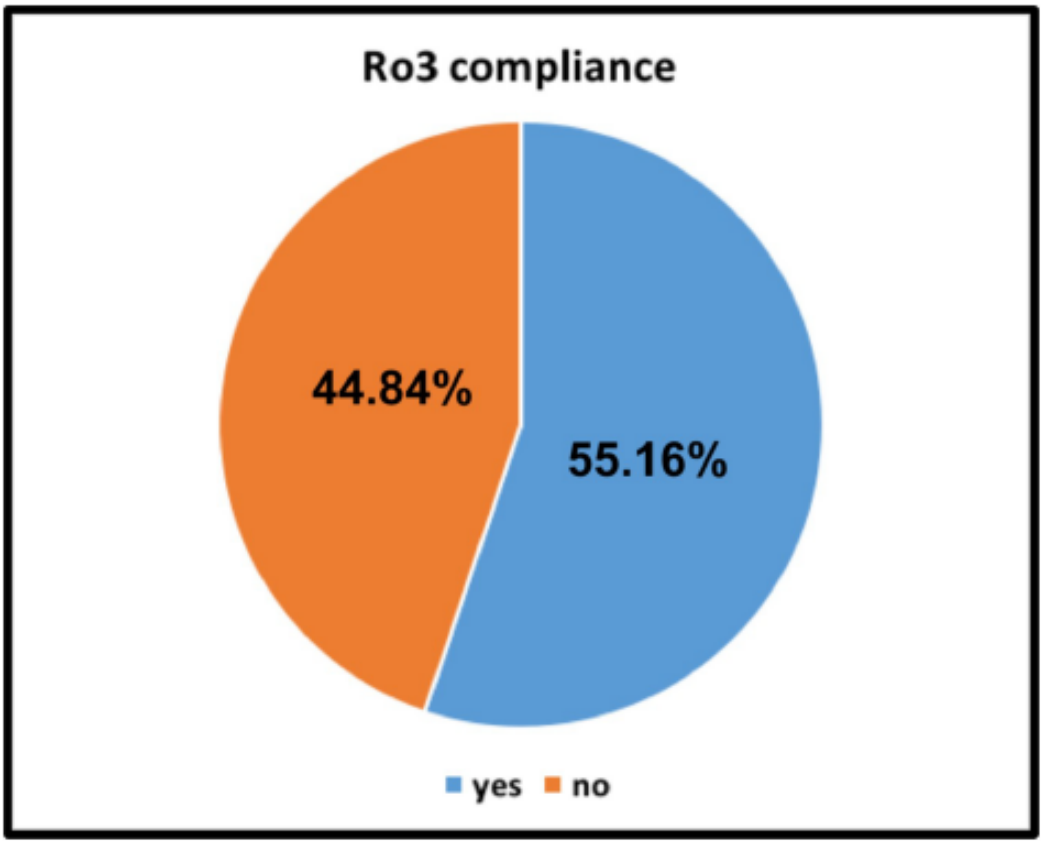

Chart S1. Ro3 compliance of the fragment collection.

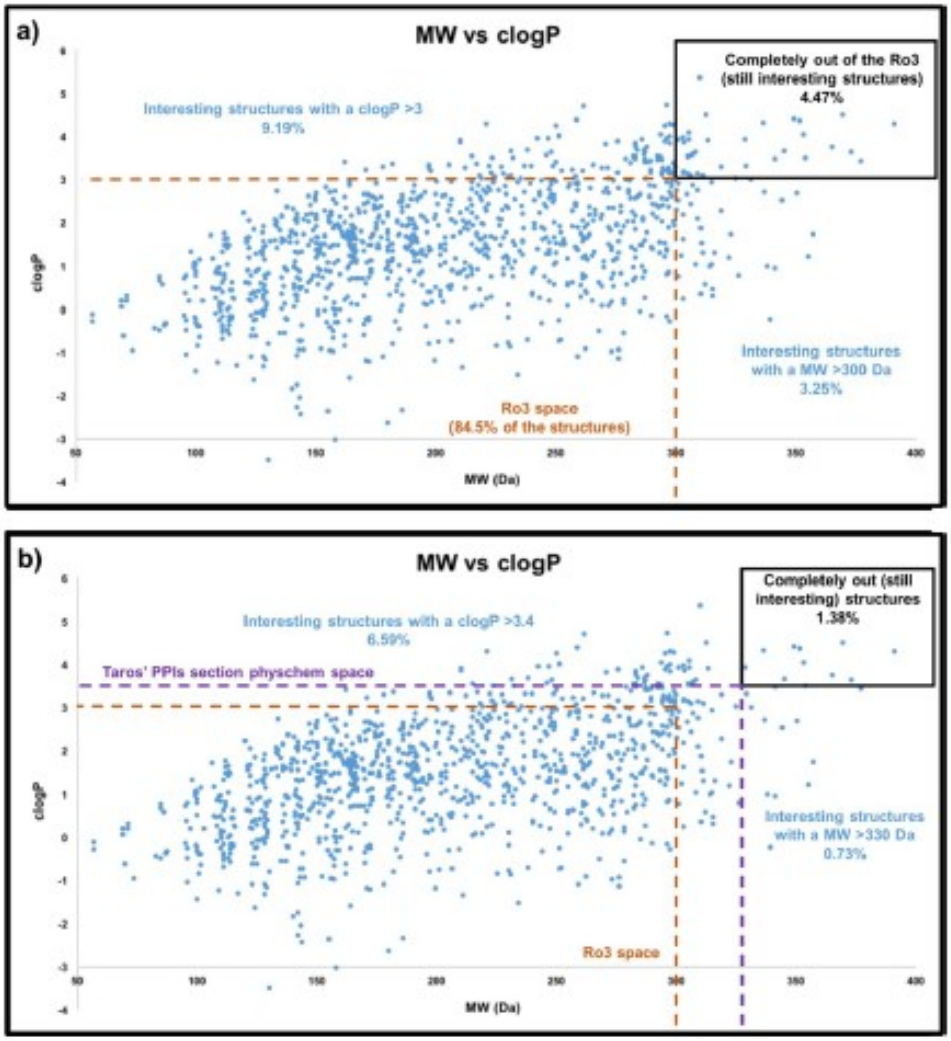

Figure S1. Fragments' MW and clogP distribution. Correlation between MW and clogP considering the classical Rule of Three parameters (A) or the revised limits (MW 330 Da and clogP 3.4) used for setting up the collection (B). Orange dashed line delimitates the Rule of Three (Ro3) space that is included into the wider parameters selected for this particular subset of the Taros' fragment library (purple dashed lines, (B)) while the black box on the top right includes the entries with both MW and clogP out of the Ro3 space (A) or out of the Taros' PPIs physchem space (B). (A) 12% of the structures have at least one parameter out of the rule and only 4% of the entries have both MW and clogP outside of the rule but present promising structures. (B) The percentage of structures with MW or clogP parameters over the settings decrease to 7.3% (compared to (A)) while 1.4% present both MW and clogP over the set limits but nonetheless have attractive structures.

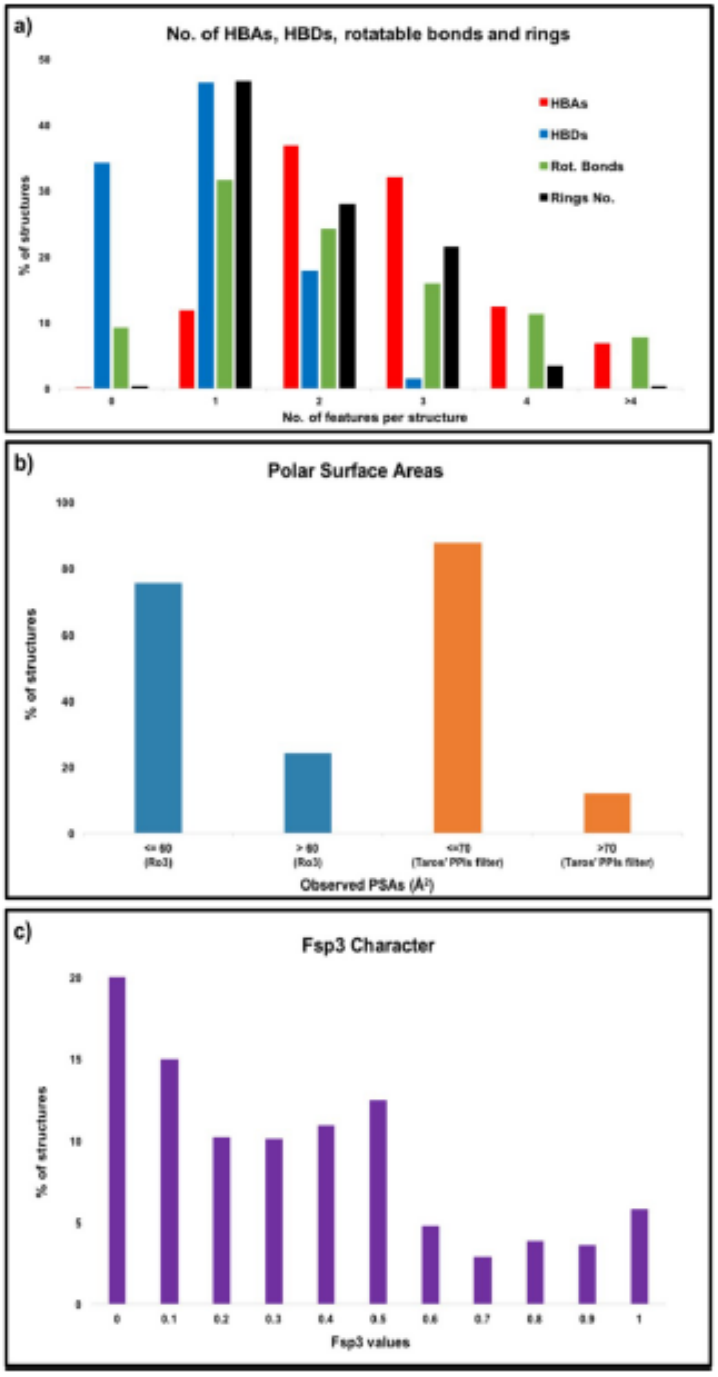

Figure S2. (A) Number of H-bond acceptors (HBAs), donors (HBDs), rotatable bonds (Rot. Bonds) and rings. The totality of the molecules presents no more than 3 HBDs while 80.7% has no more than 3 HBAs. Number of entries with no more than 3 rotatable bonds covers a similar percentage (80.9%). 96.4% of the structures contains no more than 3 rings. (B) Distribution of Polar Surface Areas, according to the Ro3 (cyan) and to the Taros' PPIs section parameters (orange). 75.7% has a PSA value below or equal the 60 Å^2 threshold. According to our parameters (PSA≤70 Å^2) 87.9% of the molecules fit well the requirements. (C) Saturation character (Fsp3) distribution. More than half of the structures (55.8%) present a completely flat core while 28.2% have an intermediate saturation character and 16.1% of them show a fully three-dimensional character.

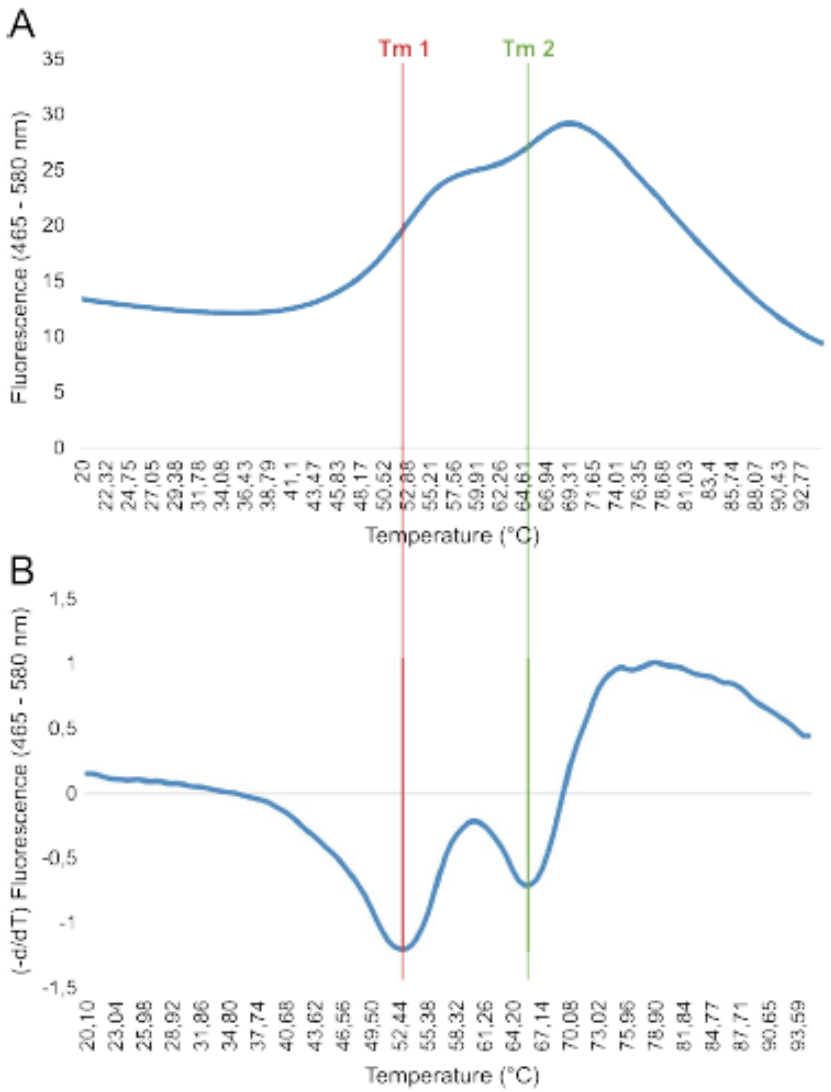

Figure S3. DSF analysis of melting temperatures of 14-3-3σ in the presence of compounds. The melting curve of 14-3-3σ 7 µM in the presence of 4% DMSO is presented in A as the variation of fluorescence (*y* axis) as a function of the temperature (*x* axis). Two different melting temperatures, identified as Tm 1 (in red) and Tm 2 (in green) are observed in the melting curve of the protein. The first derivative of the melting curve is presented in B. The *x* axis represents the temperature, same scale as in A.

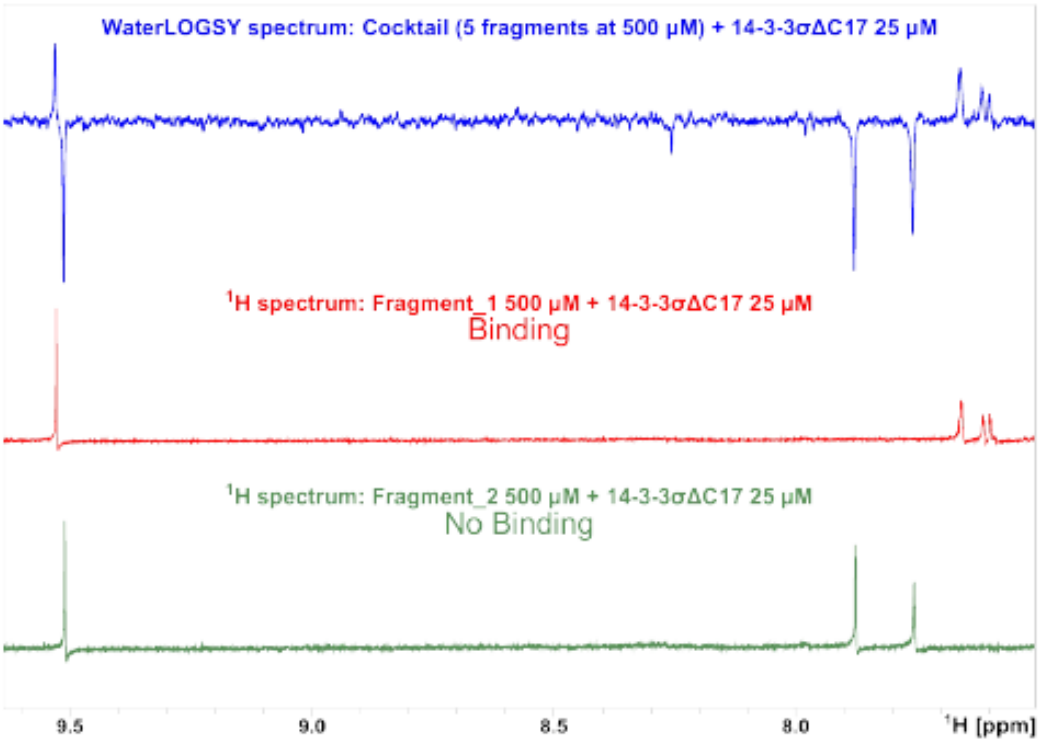

Figure S4. WaterLOGSY allows the determination of which singleton of the cocktail is binding to 14-3-3σΔC17. A WaterLOGSY spectrum of a Cocktail is shown at the top, in blue. A ^{1}H spectrum of a hit singleton (Fragment_1) of the same cocktail is presented below the WaterLOGSY spectrum, in red. Note that the resonances of this molecule are positive in the WaterLOGSY spectrum, showing that this molecule binds to 14-3-3σΔC17. At the bottom, a ^{1}H spectrum of a non-binder singleton (Fragment_2) is shown in green. Note that the resonances of this molecule are negative in the WaterLOGSY spectrum of the cocktail, meaning that this compound does not bind to 14-3-3σΔC17. The three spectra are referenced equally and were acquired in the same conditions.

Table S1. DSF melting temperature data for the screened cocktail library. The average melting temperatures, standard deviations and induced thermal shifts (ΔTm) are reported for each cocktail.

COCKTAIL	Average Tm 1 (°C) n=3	SD Tm 1 (°C) n=3	ΔTm 1 (°C)	Average Tm 2 (°C) n=3	SD Tm 2 (°C) n=3	ΔTm 2 (°C)	ΔTm1 + ΔTm2 (°C)
1	52,54	0,11	-0,31	65,69	0,19	-0,03	0,35
2	53,02	0,06	0,16	66,33	0,06	0,60	0,76
3	52,92	0,15	0,06	66,35	0,25	0,63	0,69
4	52,80	0,11	-0,06	65,82	0,20	0,09	0,15
5	52,73	0,05	-0,13	65,76	0,06	0,03	0,16
6	52,89	0,15	0,03	66,04	0,20	0,31	0,35
7	52,98	0,06	0,13	66,20	0,27	0,47	0,60
8	52,57	0,10	-0,28	65,60	0,09	-0,13	0,41
9	52,54	0,05	-0,32	65,88	0,00	0,15	0,47
10	51,50	0,11	-1,35	66,07	0,10	0,35	1,70
11	-	-	-	-	-	-	-
12	51,57	0,11	-1,29	66,13	0,11	0,41	1,70
13	52,81	0,06	-0,05	65,79	0,17	0,06	0,11
14	52,76	0,10	-0,09	65,82	0,24	0,09	0,19
15	53,11	0,14	0,25	66,23	0,24	0,50	0,75
16	53,17	0,10	0,31	66,20	0,11	0,47	0,78
17	52,95	0,10	0,10	65,95	0,14	0,22	0,32
18	52,64	0,24	-0,22	65,69	0,16	-0,03	0,25
19	53,14	0,28	0,28	66,32	0,22	0,60	0,88
20	53,20	0,14	0,35	66,42	0,14	0,69	1,04
21	52,54	0,20	-0,32	65,73	0,11	0,00	0,32
22	52,98	0,38	0,13	66,20	0,05	0,47	0,60
23	52,95	0,10	0,10	66,13	0,11	0,41	0,50
24	53,11	0,20	0,25	66,39	0,11	0,66	0,91
25	52,67	0,19	-0,19	66,04	0,31	0,31	0,50
26	52,73	0,11	-0,12	66,20	0,11	0,47	0,59
27	53,11	0,20	0,25	66,48	0,05	0,75	1,01
28	53,05	0,10	0,19	66,23	0,24	0,50	0,69
29	52,86	0,00	0,00	66,17	0,00	0,44	0,45
30	53,02	0,14	0,16	66,26	0,17	0,54	0,70
31	52,73	0,20	0,19	66,07	0,10	-0,03	0,22
32	52,67	0,17	0,12	65,76	0,29	-0,35	0,47
33	52,54	0,33	0,00	66,13	0,29	0,03	0,03
34	52,58	0,43	0,03	66,04	0,24	-0,06	0,10
35	52,48	0,10	-0,07	66,04	0,20	-0,06	0,13
36	43,32	0,25	-9,22	65,09	0,11	-1,01	10,23
37	52,94	0,42	0,40	66,04	0,13	-0,06	0,46
38	52,51	0,11	-0,04	65,94	0,11	-0,16	0,20
39	52,32	0,28	-0,22	66,04	0,15	-0,06	0,29
40	52,79	0,45	0,25	65,88	0,10	-0,22	0,47

Table S1. DSF melting temperature data for the screened cocktail library. The average melting temperatures, standard deviations and induced thermal shifts (ΔTm) are reported for each cocktail.

COCKTAIL	Average Tm 1 (°C) n=3	SD Tm 1 (°C) n=3	ΔTm 1 (°C)	Average Tm 2 (°C) n=3	SD Tm 2 (°C) n=3	ΔTm 2 (°C)	ΔTm1 + ΔTm2 (°C)
1	52,54	0,11	-0,31	65,69	0,19	-0,03	**0,35**
2	53,02	0,06	0,16	66,33	0,06	0,60	**0,76**
3	52,92	0,15	0,06	66,35	0,25	0,63	**0,69**
4	52,80	0,11	-0,06	65,82	0,20	0,09	**0,15**
5	52,73	0,05	-0,13	65,76	0,06	0,03	**0,16**
6	52,89	0,15	0,03	66,04	0,20	0,31	**0,35**
7	52,98	0,06	0,13	66,20	0,27	0,47	**0,60**
8	52,57	0,10	-0,28	65,60	0,09	-0,13	**0,41**
9	52,54	0,05	-0,32	65,88	0,00	0,15	**0,47**
10	51,50	0,11	-1,35	66,07	0,10	0,35	**1,70**
11	-	-	-	-	-	-	-
12	51,57	0,11	-1,29	66,13	0,11	0,41	**1,70**
13	52,81	0,06	-0,05	65,79	0,17	0,06	**0,11**
14	52,76	0,10	-0,09	65,82	0,24	0,09	**0,19**
15	53,11	0,14	0,25	66,23	0,24	0,50	**0,75**
16	53,17	0,10	0,31	66,20	0,11	0,47	**0,78**
17	52,95	0,10	0,10	65,95	0,14	0,22	**0,32**
18	52,64	0,24	-0,22	65,69	0,16	-0,03	**0,25**
19	53,14	0,28	0,28	66,32	0,22	0,60	**0,88**
20	53,20	0,14	0,35	66,42	0,14	0,69	**1,04**
21	52,54	0,20	-0,32	65,73	0,11	0,00	**0,32**
22	52,98	0,38	0,13	66,20	0,05	0,47	**0,60**
23	52,95	0,10	0,10	66,13	0,11	0,41	**0,50**
24	53,11	0,20	0,25	66,39	0,11	0,66	**0,91**
25	52,67	0,19	-0,19	66,04	0,31	0,31	**0,50**
26	52,73	0,11	-0,12	66,20	0,11	0,47	**0,59**
27	53,11	0,20	0,25	66,48	0,05	0,75	**1,01**
28	53,05	0,10	0,19	66,23	0,24	0,50	**0,69**
29	52,86	0,00	0,00	66,17	0,00	0,44	**0,45**
30	53,02	0,14	0,16	66,26	0,17	0,54	**0,70**
31	52,73	0,20	0,19	66,07	0,10	-0,03	**0,22**
32	52,67	0,17	0,12	65,76	0,29	-0,35	**0,47**
33	52,54	0,33	0,00	66,13	0,29	0,03	**0,03**
34	52,58	0,43	0,03	66,04	0,24	-0,06	**0,10**
35	52,48	0,10	-0,07	66,04	0,20	-0,06	**0,13**
36	43,32	0,25	-9,22	65,09	0,11	-1,01	**10,23**
37	52,94	0,42	0,40	66,04	0,13	-0,06	**0,46**
38	52,51	0,11	-0,04	65,94	0,11	-0,16	**0,20**
39	52,32	0,28	-0,22	66,04	0,15	-0,06	**0,29**
40	52,79	0,45	0,25	65,88	0,10	-0,22	**0,47**

86	52,80	0,22	0,28	66,04	0,31	0,19	**0,47**
87	53,02	0,06	0,50	66,04	0,45	0,19	**0,69**
88	52,92	0,27	0,40	66,23	0,20	0,38	**0,78**
89	52,70	0,20	0,19	66,20	0,28	0,35	**0,54**
90	52,71	0,41	0,34	65,73	0,29	0,00	**0,34**
91	52,59	0,14	0,22	66,20	0,00	0,47	**0,69**
92	52,65	0,05	0,28	66,26	0,15	0,53	**0,82**
93	52,43	0,09	0,06	65,69	0,11	-0,03	**0,10**
94	52,40	0,14	0,03	65,79	0,05	0,06	**0,09**
95	51,93	0,21	-0,44	65,88	0,14	0,16	**0,60**
96	52,49	0,05	0,12	66,32	0,07	0,60	**0,72**
97	52,40	0,05	0,03	65,82	0,09	0,09	**0,13**
98	52,24	0,17	-0,12	65,91	0,10	0,19	**0,31**
99	52,40	0,05	0,03	65,91	0,32	0,19	**0,22**
100	52,81	0,00	0,44	66,16	0,11	0,44	**0,88**
101	51,87	0,11	-0,50	65,88	0,19	0,16	**0,66**
102	52,52	0,16	0,16	65,82	0,09	0,09	**0,25**
103	52,68	0,28	0,31	66,13	0,33	0,41	**0,72**
104	52,52	0,16	0,16	66,20	0,41	0,47	**0,63**
105	52,46	0,10	0,09	65,91	0,19	0,19	**0,28**
106	52,40	0,05	0,03	66,10	0,19	0,37	**0,41**
107	48,60	0,30	-3,77	66,29	0,17	0,57	**4,34**
108	52,52	0,10	0,16	66,51	0,05	0,78	**0,94**
109	52,49	0,05	0,12	66,26	0,05	0,53	**0,66**
110	52,46	0,10	0,09	65,88	0,05	0,15	**0,25**
111	52,43	0,25	0,06	66,32	0,20	0,60	**0,66**
112	52,49	0,11	0,13	66,16	0,11	0,44	**0,56**
113	52,49	0,14	0,13	66,13	0,24	0,41	**0,53**
114	52,43	0,09	0,06	66,17	0,06	0,44	**0,50**
115	51,74	0,14	-0,63	66,10	0,10	0,38	**1,01**
116	52,81	0,00	0,44	66,45	0,20	0,72	**1,17**
117	52,40	0,20	0,03	66,54	0,36	0,82	**0,85**
118	52,71	0,34	0,35	66,32	0,14	0,60	**0,94**
119	52,52	0,10	0,16	66,54	0,05	0,81	**0,97**
120	52,57	0,17	0,10	66,04	0,15	0,28	**0,38**
121	52,48	0,17	0,00	66,20	0,20	0,44	**0,44**
122	52,60	0,14	0,13	66,07	0,10	0,32	**0,44**
123	50,84	0,19	-1,63	65,22	0,16	-0,53	**2,17**
124	48,54	0,45	-3,94	65,22	0,25	-0,53	**4,47**
125	52,48	0,10	0,00	65,92	0,11	0,16	**0,16**
126	52,64	0,14	0,16	66,39	0,39	0,64	**0,80**
127	51,19	0,11	-1,29	65,82	0,11	0,06	**1,35**
128	52,42	0,11	-0,06	65,82	0,05	0,06	**0,12**
129	52,42	0,24	-0,06	66,04	0,34	0,28	**0,34**
130	50,50	0,49	-1,98	63,87	0,43	-1,89	**3,87**

S9

131	52,29	0,09	-0,19	65,57	0,14	-0,19	**0,38**
132	52,48	0,00	0,00	65,63	0,10	-0,13	**0,13**
133	52,51	0,11	0,03	66,04	0,20	0,28	**0,31**
134	52,70	0,22	0,22	66,35	0,41	0,60	**0,82**
135	52,35	0,05	-0,13	65,75	0,11	0,00	**0,13**
136	52,73	0,05	0,25	66,17	0,16	0,41	**0,66**
137	52,63	0,29	0,16	66,48	0,14	0,73	**0,88**
138	48,76	0,11	-3,71	66,83	0,00	1,07	**4,79**
139	52,54	0,15	0,06	65,85	0,22	0,10	**0,16**
140	52,29	0,00	-0,19	65,85	0,33	0,10	**0,28**
141	52,67	0,10	0,19	66,48	0,14	0,73	**0,92**
142	52,57	0,19	0,09	66,11	0,22	0,35	**0,44**
143	52,45	0,06	-0,03	65,76	0,06	0,00	**0,03**
144	52,79	0,36	0,32	66,32	0,24	0,57	**0,88**
145	52,54	0,05	0,06	66,26	0,17	0,51	**0,57**
146	52,20	0,10	-0,28	65,60	0,09	-0,16	**0,44**
147	50,25	0,11	-2,23	65,98	0,19	0,22	**2,45**
148	52,35	0,14	-0,12	65,98	0,35	0,22	**0,34**
149	48,13	0,02	-4,01	66,45	0,09	0,60	**4,61**
150	51,54	0,32	-0,60	66,14	0,06	0,29	**0,89**
151	52,22	0,46	0,09	66,45	0,34	0,60	**0,68**
152	51,94	0,20	-0,19	65,66	0,19	-0,19	**0,38**
153	51,79	0,36	-0,35	65,79	0,10	-0,06	**0,41**
154	52,10	0,00	-0,04	65,85	0,05	0,00	**0,04**
155	52,14	0,11	0,00	66,18	0,10	0,33	**0,33**
156	52,24	0,05	0,10	65,92	0,11	0,07	**0,17**
157	52,20	0,00	0,06	65,82	0,05	-0,03	**0,09**

S10

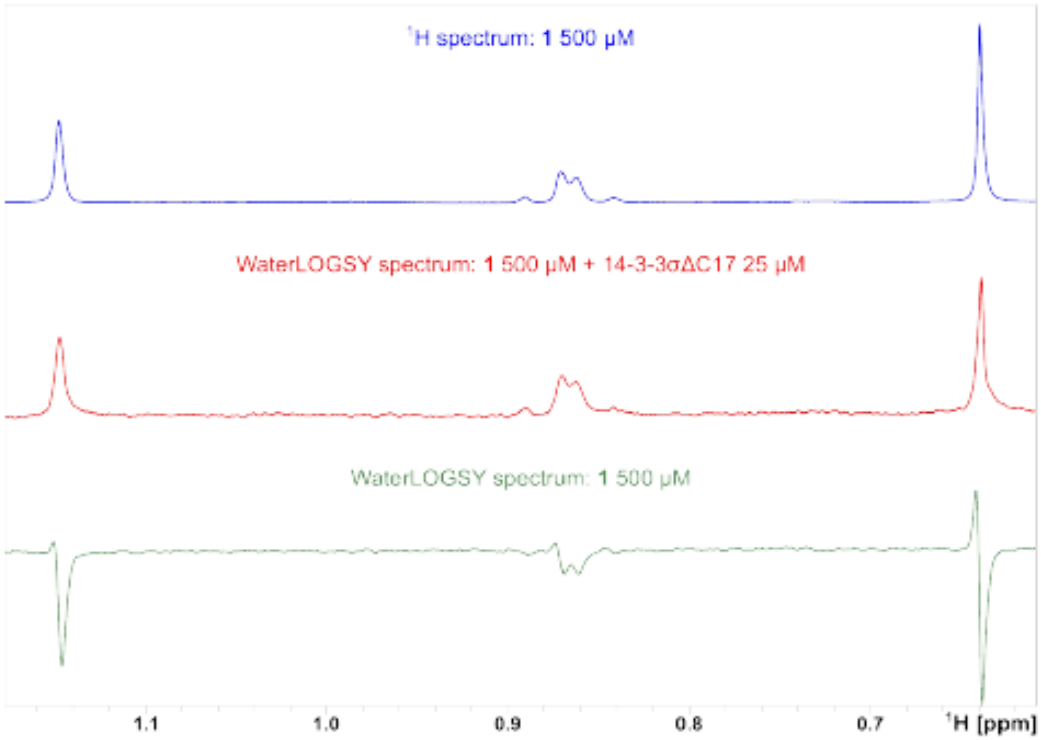

Figure S5. WaterLOGSY detects the binding of 1 to 14-3-3σΔC17. ^{1}H spectrum of 1 500 µM (blue spectrum, on top). The WaterLOGSY spectrum of a solution containing 1 500 µM and 14-3-3σΔC17 25 µM (in red) shows that the NMR signals of 1 are phased positive, indicating binding. The control WaterLOGSY spectrum of a solution containing 1 500 µM alone (in green) shows that in the absence of 14-3-3σΔC17 the NMR signals of 1 500 µM are all phased negative.

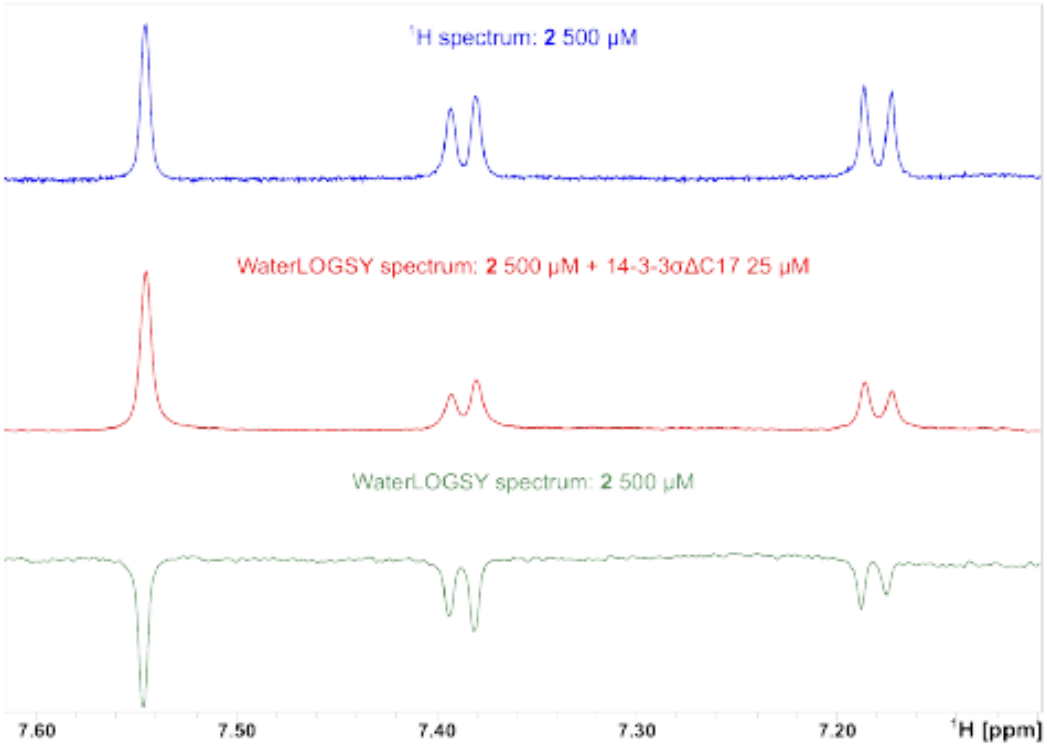

Figure S6. WaterLOGSY detects the binding of **2** to 14-3-3σΔC17. ^{1}H spectrum of **2** 500 µM (blue spectrum, on top). The WaterLOGSY spectrum of a solution containing **2** 500 µM and 14-3-3σΔC17 25 µM (in red) shows that the NMR signals of **2** are phased positive, indicating binding. The control WaterLOGSY spectrum of a solution containing **2** 500 µM alone (in green) shows that in the absence of 14-3-3σΔC17 the NMR signals of **2** 500 µM are all phased negative.

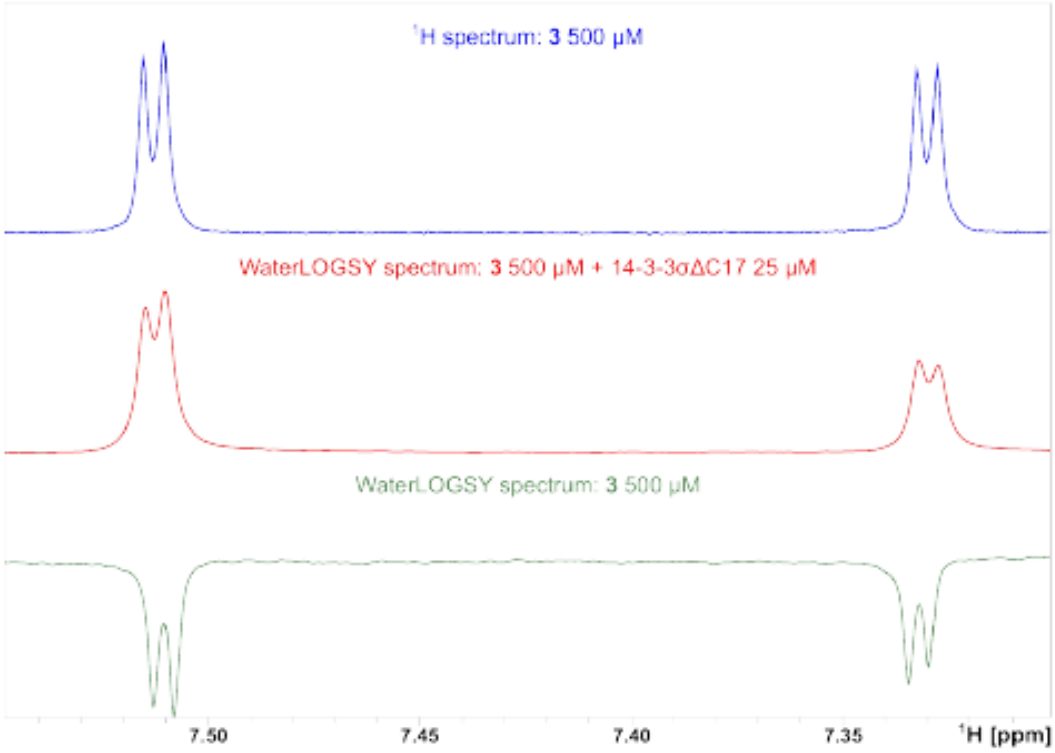

Figure S7. WaterLOGSY detects the binding of 3 to 14-3-3σΔC17. ^{1}H spectrum of 3 500 µM (blue spectrum, on top). The WaterLOGSY spectrum of a solution containing 3 500 µM and 14-3-3σΔC17 25 µM (in red) shows that the NMR signals of 3 are phased positive, indicating binding. The control WaterLOGSY spectrum of a solution containing 3 500 µM alone (in green) shows that in the absence of 14-3-3σΔC17 the NMR signals of 3 500 µM are all phased negative.

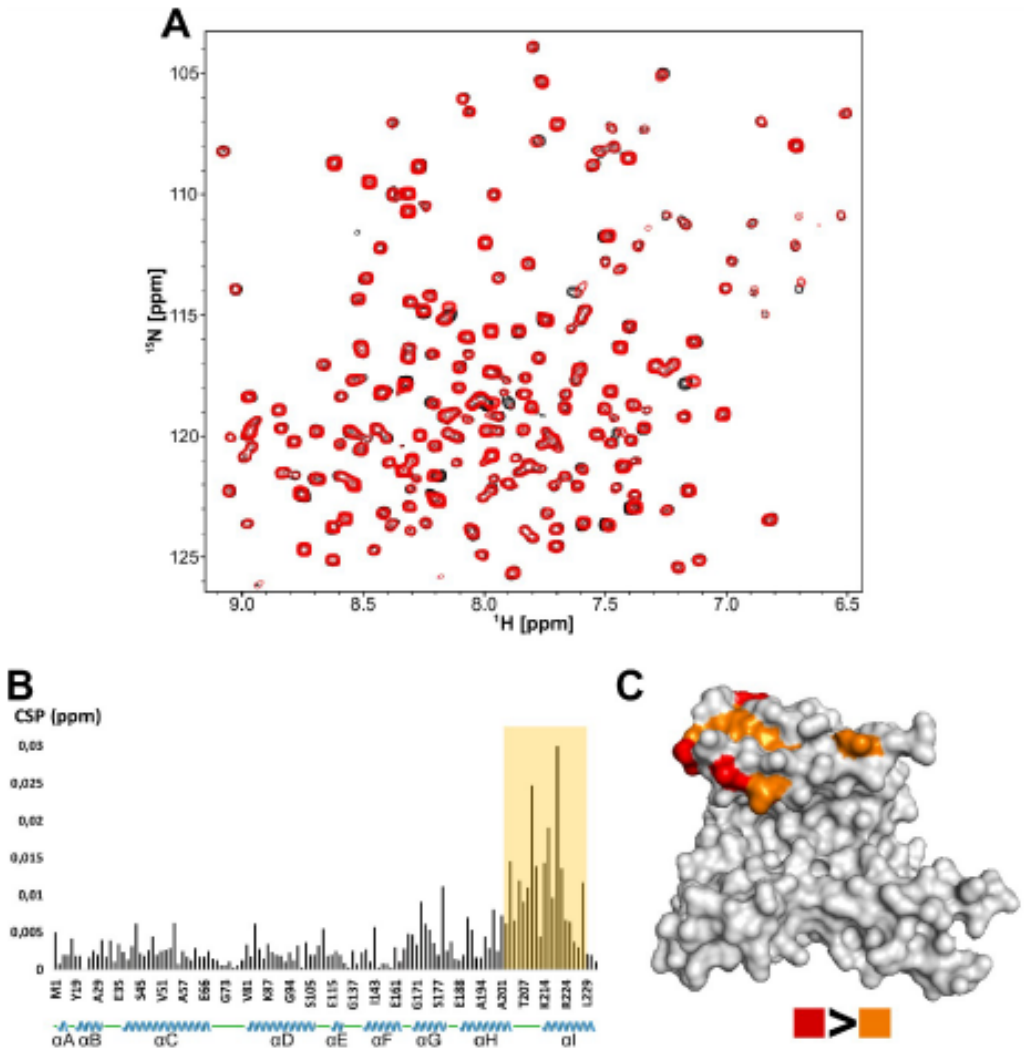

Figure S8. 1 binding site on 14-3-3σΔC17 identified by ^{1}H-^{15}N TROSY-HSQC. (A) Superimposed ^{1}H-^{15}N TROSY-HSQC spectra of ^{15}N^{2}H labelled 14-3-3σΔC17 75 µM in the presence of 2% DMSO-d_6 (v/v) (in black) and **1** 2000 µM (in red). (B) Plot of the CSP values (in ppm) of ^{1}H-^{15}N correlation peaks of 75 µM 14-3-3σΔC17 in the presence of 2000 µM **1** compared to the reference 14-3-3σΔC17 spectrum (75 µM) (*y axis*) versus the amino acid sequence (*x axis*). A total of 128 correlation peak CSP are shown. The *x axis* is not proportional. The helices of 14-3-3σ are identified below the *x axis* as blue cartoons, while disordered regions are represented by green lines. The area highlighted in yellow shows the region of the protein affected by the presence of **1**. (C) Mapping on the crystal structure of 14-3-3σ (PDB ID: 1YZ5) of the amino acid residues corresponding to the 10 most affected resonances by the presence of **1**. The residues corresponding to the 5 most affected resonances are colored in red and an additional 5 are colored in orange.

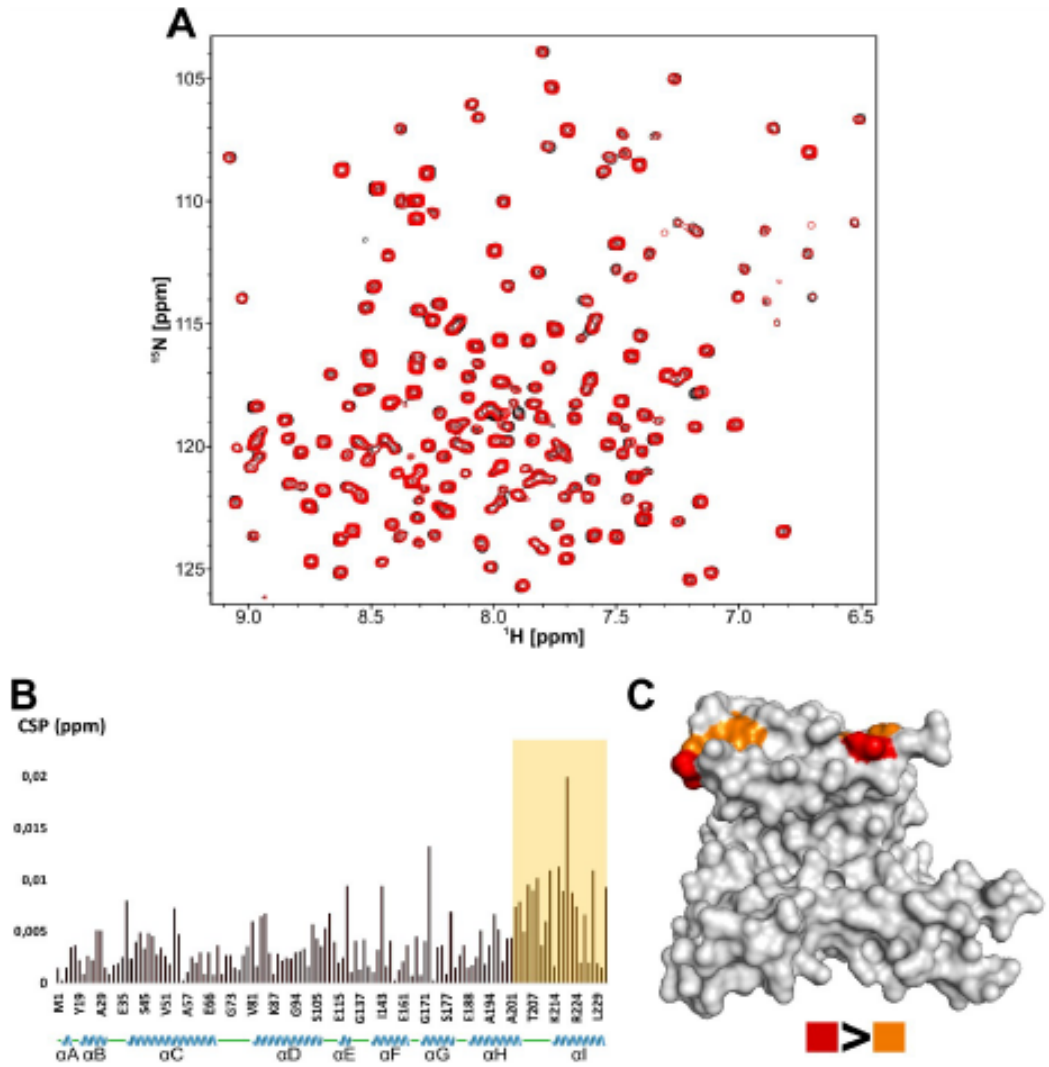

Figure S9. 2 binding site on 14-3-3σΔC17 identified by ^{1}H-^{15}N TROSY-HSQC. (A) Superimposed ^{1}H-^{15}N TROSY-HSQC spectra of ^{15}N^{2}H labelled 14-3-3σΔC17 75 µM in the presence of 2% DMSO-d_6 (v/v) (in black) and 2 2000 µM (in red). (B) Plot of the CSP values (in ppm) of ^{1}H-^{15}N correlation peaks of 75 µM 14-3-3σΔC17 in the presence of 2000 µM 2 compared to the reference 14-3-3σΔC17 spectrum (75 µM) (*y axis*) versus the amino acid sequence (*x axis*). A total of 128 correlation peak CSP are shown. The *x axis* is not proportional. The helices of 14-3-3σ are identified below the *x axis* as blue cartoons, while disordered regions are represented by green lines. The area highlighted in yellow shows the region of the protein affected by the presence of 2. (C) Mapping on the crystal structure of 14-3-3σ (PDB ID: 1YZ5) of the amino acid residues corresponding to the 10 most affected resonances by the presence of 2. The residues corresponding to the 5 most affected resonances are colored in red and an additional 5 are colored in orange.

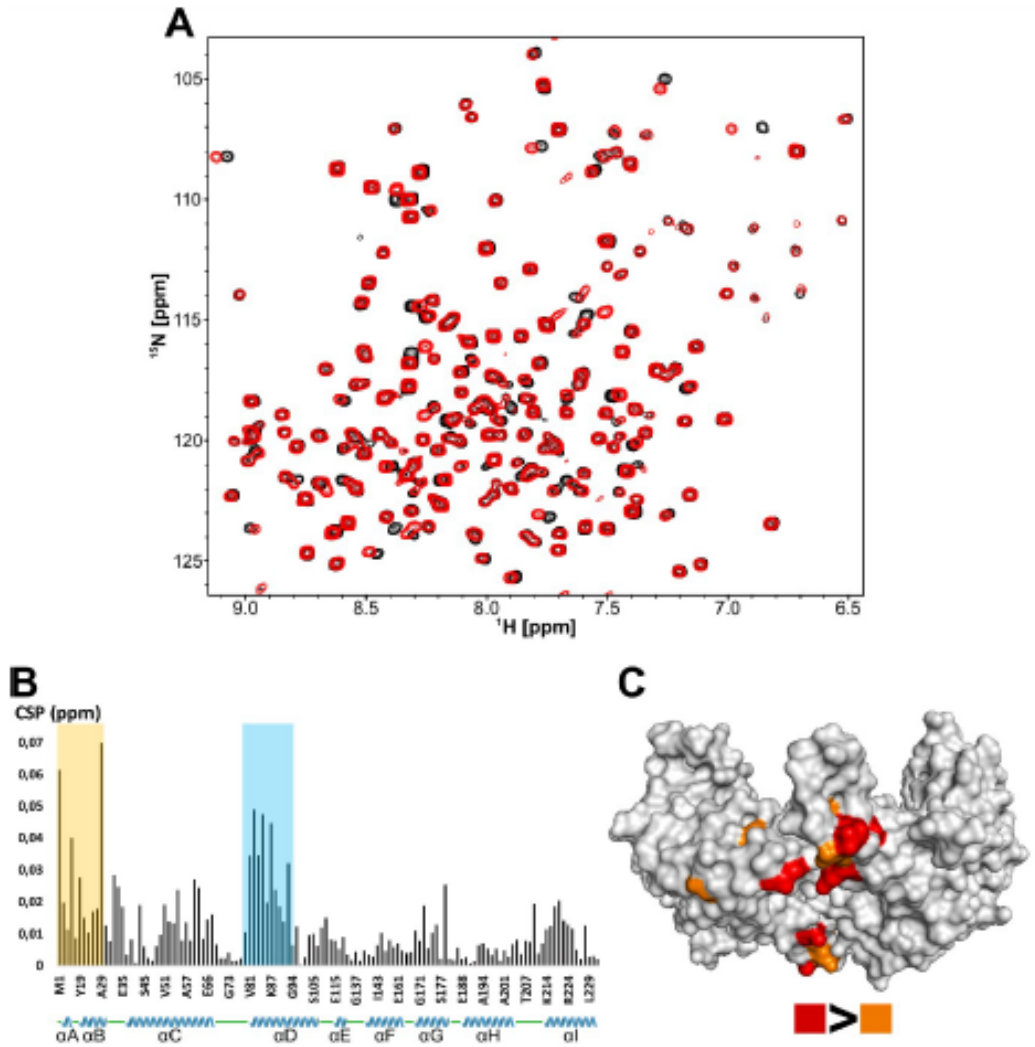

Figure S10. 3 binding site on 14-3-3σΔC17 identified by ^{1}H-^{15}N TROSY-HSQC. (A) Superimposed ^{1}H-^{15}N TROSY-HSQC spectra of ^{15}N^{2}H labelled 14-3-3σΔC17 75 µM in the presence of 2% DMSO-d_6 (v/v) (in black) and 3 2000 µM (in red). (B) Plot of the CSP values (in ppm) of ^{1}H-^{15}N correlation peaks of 75 µM 14-3-3σΔC17 in the presence of 2000 µM 3 compared to the reference 14-3-3σΔC17 spectrum (75 µM) (*y axis*) versus the amino acid sequence (*x axis*). A total of 128 correlation peak CSP are shown. The *x axis* is not proportional. The helices of 14-3-3σ are identified below the *x axis* as blue cartoons, while disordered regions are represented by green lines. The areas highlighted in yellow and blue show the region of the protein affected by the presence of 3. (C) Mapping on the crystal structure of 14-3-3σ (PDB ID: 1YZ5) of the amino acid residues corresponding to the 10 most affected resonances by the presence of 3. The residues corresponding to the 5 most affected resonances are colored in red and an additional 5 are colored in orange.

7.4 Supplement S3

7.4.1 Stabilization of protein-protein interactions between CaMKK2 and 14-3-3 by fusicoccanes

Domenico Lentini Santo, Olivia Petrvalska, Veronika Obsilova, Christian Ottmann, and Tomas Obsil. Stabilization of Protein-Protein Interactions between CaMKK2 and 14-3-3 by Fusicoccins. *ACS Chem. Biol.* 15(11):3060-3071 (2020).

My contribution: Preparation of CaMKK2, 14-3-3γΔC and 14-3-3ξΔC, crystallization of ternary complexes, structure refinement, FP assay for K_D and IC_{50} determination.

pubs.acs.org/acschemicalbiology

Articles

Stabilization of Protein−Protein Interactions between CaMKK2 and 14−3−3 by Fusicoccins

Domenico Lentini Santo, Olivia Petrvalska, Veronika Obsilova, Christian Ottmann,* and Tomas Obsil*

Cite This: https://dx.doi.org/10.1021/acschembio.0c00821

Read Online

ACCESS | Metrics & More | Article Recommendations | Supporting Information

Downloaded via CHARLES UNIV IN PRAGUE on November 13, 2020 at 15:15:33 (UTC).
See https://pubs.acs.org/sharingguidelines for options on how to legitimately share published articles.

ABSTRACT: Ca^{2+}/calmodulin-dependent protein kinase kinase 2 (CaMKK2) regulates several key physiological and pathophysiological processes, and its dysregulation has been implicated in obesity, diabetes, and cancer. CaMKK2 is inhibited through phosphorylation in a process involving binding to the scaffolding 14−3−3 protein, which maintains CaMKK2 in the phosphorylation-mediated inhibited state. The previously reported structure of the N-terminal CaMKK2 14−3−3-binding motif bound to 14−3−3 suggested that the interaction between 14−3−3 and CaMKK2 could be stabilized by small-molecule compounds. Thus, we investigated the stabilization of interactions between CaMKK2 and 14−3−3γ by Fusicoccin A and other fusicoccanes—diterpene glycosides that bind at the interface between the 14−3−3 ligand binding groove and the 14−3−3 binding motif of the client protein. Our data reveal that two of five tested fusicoccanes considerably increase the binding of phosphopeptide representing the 14−3−3 binding motif of CaMKK2 to 14−3−3γ. Crystal structures of two ternary complexes suggest that the steric contacts between the C-terminal part of the CaMKK2 14−3−3 binding motif and the adjacent fusicoccane molecule are responsible for differences in stabilization potency between the study compounds. Moreover, our data also show that fusicoccanes enhance the binding affinity of phosphorylated full-length CaMKK2 to 14−3−3γ, which in turn slows down CaMKK2 dephosphorylation, thus keeping this protein in its phosphorylation-mediated inhibited state. Therefore, targeting the fusicoccin binding cavity of 14−3−3 by small-molecule compounds may offer an alternative strategy to suppress CaMKK2 activity by stabilizing its phosphorylation-mediated inhibited state.

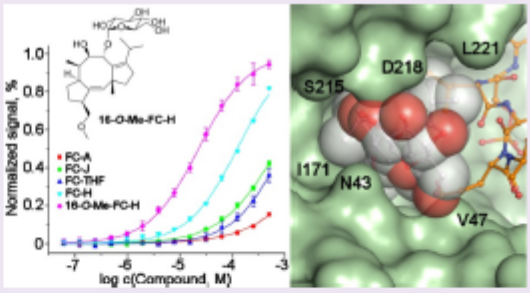

INTRODUCTION

Ca^{2+}/calmodulin-dependent protein kinase kinase 2 (CaMKK2), a member of the Ca^{2+}/calmodulin-dependent kinase (CaMK) family, is a Ser/Thr kinase. As a molecular hub, CaMKK2 regulates several key physiological and pathophysiological processes.[1] CaMK family members respond to increased intracellular concentrations of Ca^{2+} ions by interacting with the Ca^{2+}/calmodulin (Ca^{2+}/CaM) complex. In the inactive state, CaMKs are inhibited by the autoinhibitory segment (AID), which interacts with the kinase domain (KD) and blocks the substrate binding and/or affects the catalytic site structure.[2,3] Ca^{2+}/CaM binding to the region that overlaps with the AID disrupts the interaction between AID and KD, thus relieving autoinhibition.

CaMK kinases (CaMKK1 and CaMKK2) function as upstream elements of the CaMK signaling cascade where they phosphorylate and activate two downstream CaMKs, CaMKI and CaMKIV.[4,5] These two CaMKs, in turn, regulate downstream targets such as CREB, ERK, RAC1, and HDAC5, thereby modulating various processes, including dendritic cell survival, cytokine secretion from T cells, the cell cycle, cell differentiation, and hormone and cytokine production.[1,6,7] In addition, CaMKKs have also been shown to phosphorylate and thus activate Akt/PKB kinase in various cancer cell lines.[8−10] CaMKK2 is also an activator of the AMP-activated protein kinase (AMPK), a crucial regulator of energy homeostasis, inflammation, and autophagy, whose dysregulation has been implicated in chronic diseases, such as obesity, diabetes, and cancer.[11−13] Therefore, the CaMKK2-AMPK signaling pathway connects changes in Ca^{2+} concentration induced by insulin binding to its receptor, inositol 1,4,5-trisphosphate receptor (IP3R) activation, or plasma membrane ion channels to processes that maintain energy levels.[1] Accordingly, the loss of CaMKK2 activity has been shown to protect CaMKK2 null mice from high-fat-diet-induced obesity, insulin resistance, and glucose intolerance.[12] Furthermore, in mouse models of breast cancer, intratumoral myeloid cells showed high expression levels of CaMKK2, and CaMKK2 inhibition suppressed tumor

Received: October 16, 2020
Accepted: October 26, 2020

ACS Publications © XXXX American Chemical Society

Figure 1. Domain structure of human CaMKK2. The positions of regulatory phosphorylation and autophosphorylation sites are indicated by colored asterisks (blue, sites phosphorylated by cAMP-dependent protein kinase; black, sites phosphorylated by glycogen synthase kinase-3 and proline-directed kinases; orange, autophoshorylation sites). Ser^{100} and Ser^{511} are 14−3−3 binding motifs. AAR = autonomous activity region; AID = autoinhibitory region; CBD = Ca^{2+}/CaM-binding domain.

growth by increasing the accumulation of effector CD8+ T cells and immune-stimulatory myeloid subsets.[14] This indicated that CaMKK2 inhibition may serve as a selective way of suppressing AMPK, which is involved in macrophage polarization, while preserving the antitumor functions of CD8+ T cells.

The regulation of CaMKK2 activity is still not fully understood. In addition to Ca^{2+}/CaM-dependent activation, both CaMKKs are further regulated by phosphorylation. cAMP-dependent protein kinase (PKA) partly inhibits both CaMKKs by phosphorylating multiple residues, including two inhibitory sites located N-terminally to the kinase domain and close to the Ca^{2+}/CaM-binding segment (Thr^{108}/Ser^{458} in human CaMKK1 and Thr^{145}/Ser^{495} in human CaMKK2; Figure 1A).[15−17] CaMKK2, in contrast to CaMKK1, also exhibits significant Ca^{2+}/CaM-binding-independent (autonomous) activity, which is inhibited through phosphorylation of three residues located N-terminally to the kinase domain by cyclin-dependent kinase 5, glycogen synthase kinase 3, and cAMP-dependent protein kinase (PKA).[15,18,19] Both CaMKKs are further regulated by 14−3−3 proteins, a family of abundant scaffolding and chaperon proteins expressed in all eukaryotic cells, which are involved in the regulation of a wide range of cellular phenomena including cell-cycle control, signal transduction, protein trafficking, metabolism control, and apoptosis.[20−23] 14−3−3 proteins form very stable dimers with each of the protomers possessing an amphipatic binding groove that accommodates the phosphoserine (pSer)- or phosphothreonine (pThr)-containing motifs of their client proteins.[24,25] Through these binding interactions, 14−3−3 proteins modulate the enzymatic activity and subcellular localization or interactions with other molecules of their binding partners.[22,23,26] Because 14−3−3 proteins play key roles in numerous disease-relevant signaling pathways, they are considered promising targets for pharmacological intervention. Indeed, several small molecules, peptide mimetics, and natural products have already been shown to either disrupt or stabilize specific 14−3−3 protein complexes.[27−32]

Previous studies have shown that 14−3−3 proteins recognize two phosphorylated motifs located within the N- and C-terminal segments of CaMKKs ($pSer^{74}$/$pSer^{475}$ and $pSer^{100}$/$pSer^{511}$ in human CaMKK1 and CaMKK2, respectively) and suggested that this binding interaction slows down the dephosphorylation of inhibitory phosphorylation sites, thus maintaining CaMKKs in the PKA-mediated inhibited state.[33−35] Furthermore, 14−3−3 protein binding directly inhibits CaMKK1 but not CaMKK2, thus indicating that CaMKK isoforms differ in their 14−3−3 protein-mediated regulations.[33−36] The crystal structure of the phosphopeptide containing the CaMKK2 $pSer^{100}$ 14−3−3-binding motif bound to 14−3−3ζ revealed that part of the 14−3−3 ligand binding groove stays empty due to the abrupt change in the direction of the C-terminal part, suggesting that the interaction between the 14−3−3 protein and phosphorylated CaMKKs can be stabilized by small-molecule compounds targeting this region of the 14−3−3 ligand binding groove.[34] Ultimately, this stabilizing interaction may provide an alternative and/or complementary strategy for inhibiting CaMKK activity by stabilizing their phosphorylation-mediated inhibited state.

Here, we investigated the stabilization of protein−protein interactions between CaMKK2 and 14−3−3γ by Fusicoccin A and four other fusicoccanes, diterpene glycosides that share a 5−8−5 ring structure, which have been shown to stabilize several 14−3−3 complexes by filling a gap in the interface of the 14−3−3 ligand binding groove with the 14−3−3 binding motif of the client protein.[28,32,37−39] Our data reveal that two of five fusicoccanes tested in this study considerably increase the binding of the synthetic phosphopeptide containing the $pSer^{100}$ 14−3−3 binding motif of CaMKK2 to 14−3−3γ. Crystal structures of two ternary complexes suggest that the steric contacts between the C-terminal part of the CaMKK2 $pSer^{100}$ 14−3−3-binding motif and the adjacent fusicoccane molecule within the 14−3−3 ligand binding groove are responsible for differences in stabilization potency between the study compounds. Moreover, our data also show that fusicoccanes enhance the binding affinity of phosphorylated full-length CaMKK2 to 14−3−3γ, thus confirming that small-molecule compounds targeting the fusicoccin binding cavity within the 14−3−3 ligand binding groove can be used to stabilize this important protein−protein interaction.

RESULTS

Fusicoccanes Stabilize the Interaction between 14 and 3−3γ and the N-Terminal 14−3−3 Binding Motif of CaMKK2. 14−3−3 proteins recognize three canonical binding motifs: RXX(pS/T)XP (mode I), RXXX(pS/T)XP (mode II), and X(pS/T)X_{1-2}COOH (mode III), where pS/T is phosphoserine or phosphotreonine.[25,38,40,41] These motifs, although optimal, are not absolute because several 14−3−3 binding partners contain significantly different motifs.[42] The previous structural analysis of the $pSer^{100}$ 14−3−3-binding motif of CaMKKs (sequence R^{97}KL-pS-LQE^{103} in human CaMKK2 numbering) bound to 14−3−3ζ revealed that, due to interactions between the side-chains of Gln^{102} and $pSer^{100}$, this motif adopts an unusual conformation, leaving a large part of the 14−3−3 binding groove empty.[34] This is typical of mode III motifs, where the pSer/Thr is located near the C-terminus of the polypeptide chain, and previous studies have

https://dx.doi.org/10.1021/acschembio.0c00821
ACS Chem. Biol. XXXX, XXX, XXX−XXX

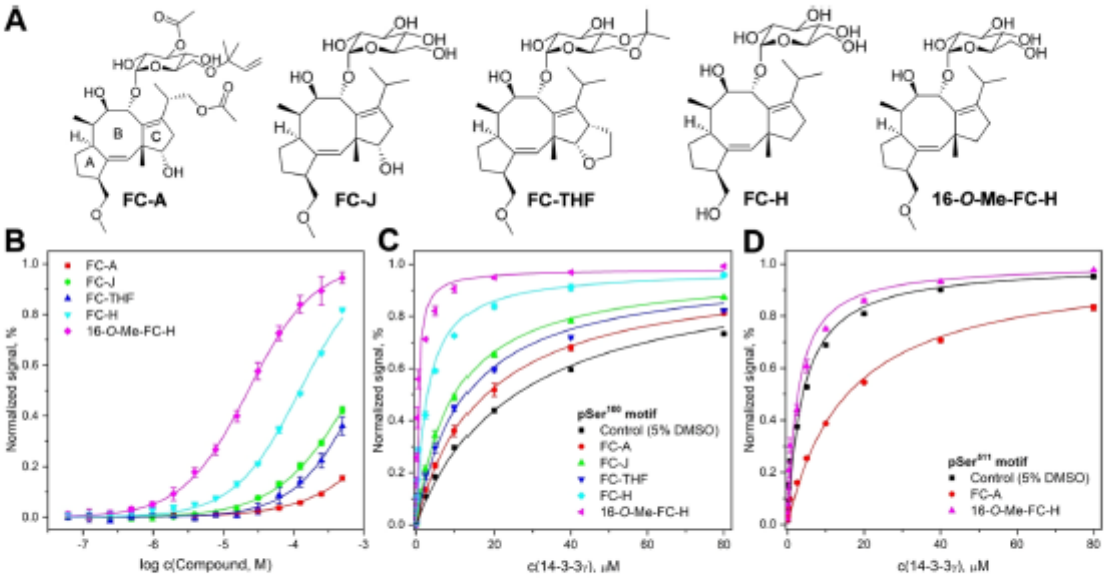

Figure 2. Stabilization of interactions between 14−3−3γ and 14−3−3 binding motifs of CaMKK2 by fusicoccanes. (A) Structures of fusicoccanes used in this study. (B) Fluorescence polarization (FP) measurements of FAM-labeled pepS100 peptide (100 nM) and 14−3−3γ (20 μM) titrated by tested fusicoccanes. Data points are the means ± SD of three experiments. To assess EC_{50} values reflecting the stabilization potency of the study fusicoccanes, the FP data were fitted to a four-parameter dose−response model. (C,D) FP of FAM-labeled pepS100 and pepS511 peptides in the presence of 500 μM of the study fusicoccanes titrated by 14−3−3γ. To determine the apparent K_D values of the peptide:14−3−3γ interaction, the FP data were fitted to a one-site-binding model. Data points are the means ± SD of three experiments.

shown that this gap at the interface between 14−3−3 and the 14−3−3 binding motif of the target protein can be filled by fusicoccin-like compounds, thus stabilizing these complexes.[28,32,37−39] Therefore, we have speculated that the 14−3−3:CaMKK2 complex could also be stabilized by fusicoccin-like compounds.[34]

To test this hypothesis, five fusicoccanes, FC-A, FC-J, FC-THF, FC-H, and 16-*O*-Me-FC-H (Figure 2A), were tested for their ability to stabilize interactions between 14−3−3γ and CaMKK2. FC-A, FC-J, FC-H, and 16-*O*-Me-FC-H are naturally occurring fusicoccanes, and FC-J, FC-H, and 16-*O*-Me-FC-H are intermediates of FC-A biosynthesis.[37,43] These fusicoccanes mainly differ in the ring C modifications, and fusicoccanes with hydroxylated ring C, such as FC-A, preferentially stabilize 14−3−3 complexes with the C-terminal mode III binding motifs.[29,30,32] Moreover, FC-THF, which contains an additional five-membered tetrahydrofuran ring attached to ring C, was designed as an optimal stabilizer for such complexes. Conversely, fusicoccanes whose ring C is not hydroxylated stabilize several 14−3−3 complexes with mode I and mode II binding motifs.[31,44]

The ability of various fusicoccanes to bind to and stabilize the binary complex between 14−3−3γ and the CaMKK2 $pSer^{100}$ 14−3−3 binding motif was investigated by fluorescence polarization (FP) with the synthetic phosphopeptide containing the $pSer^{100}$ motif labeled at the N-terminus by 5-carboxyfluorescein (denoted as FAM-pepS100; Figure 2B,C and Table 1). FC-A stabilized the interaction between human 14−3−3γ (residues 1−235 missing the C-terminal 12-residues-long flexible tail) and FAM-pepS100 only marginally with an EC_{50} of ±5.6 ± 0.9 mM and increased the apparent binding affinity of FAM-pepS100 from a K_D of 25.5 ± 1 μM to 17.1 ± 0.5 μM at a 500 μM concentration. Other fusicoccanes showed a higher potency in stabilizing the 14−3−3γ:FAM-pepS100 complex, with FC-H and 16-*O*-Me-FC-H exhibiting the strongest stabilization effect with EC_{50} values of 123 ± 4 and 23 ± 1 μM, respectively. These two compounds, which lack the hydroxyl group at the cyclopentene ring C, in contrast to

Table 1. Stabilization of the Interaction between Peptides Containing 14−3−3-Binding Motifs of CaMKK and 14−3−3γ by Fusicoccanes

compound	EC_{50}, μM[a]	K_D, μM[b]	factor[c]
	FAM-pepS100 peptide		
control (5% DMSO)		25.5 ± 1	
FC-A	5600 ± 900	17.1 ± 0.5	1.5
FC-J	730 ± 30	9.5 ± 0.5	2.7
FC-THF	930 ± 50	12.3 ± 0.7	2.1
FC-H	123 ± 4	2.8 ± 0.3	9.1
16-O-Me-FC-H	23 ± 1	0.5 ± 0.05	51
	FAM-pepS511 peptide		
control (5% DMSO)		4.0 ± 0.4	
FC-A		15.6 ± 0.9	0.25
16-O-Me-FC-H		2.6 ± 0.3	1.5

[a]The EC_{50} values describing the stabilization potency of the study compounds toward the pepS100:14−3−3γ complex were assessed by FP measurements of FAM-labeled pepS100 peptide (100 nM) and 14−3−3γ (20 μM) titrated with different fusicoccanes. [b]The apparent K_D values of the interaction between the peptide and 14−3−3γ were determined by fluorescence polarization measurements of FAM-labeled pepS100 and pepS511 peptides titrated with 14−3−3γ in the presence of the study fusicoccanes (500 μM). [c]Stabilization factor calculated from the apparent K_D values. Values lower than 1 express destabilization.

https://dx.doi.org/10.1021/acschembio.0c00821
ACS Chem. Biol. XXXX, XXX, XXX−XXX

FC-A and FC-J, enhanced the apparent binding affinity of FAM-pepS100 for 14−3−3γ by a factor of 9.1 and 51, respectively. In addition, the synthetic FC-THF showed a considerably lower stabilization potency than 16-*O*-Me-FC-H, thus corroborating previous evidence that this derivative can only stabilize interactions between 14 and 3−3 and mode III binding sites.[32] The EC_{50} measurements were also performed for the complex between the 14−3−3ζ isoform and FAM-pepS100, revealing EC_{50} values (Figure S3) similar to those assessed for the gamma isoform (Table 1). FC-A exhibited the lowest stabilization potency, whereas FC-H and 16-*O*-Me-FC-H showed the highest stabilization potency, with EC_{50} values in the micromolar range.

Although fusicoccanes are well-known to preferentially stabilize 14−3−3 complexes with mode III binding motifs, we also tested the ability of two compounds, FC-A and 16-*O*-Me-FC-H (as fusicoccanes with hydroxylated and not-hydroxylated ring C, respectively), to stabilize the binary complex between 14−3−3γ and the second 14−3−3 binding motif located at the C-terminus of CaMKK2 (sequence R^{508}SL-pS-AP^{513}) using the FP assay with the synthetic phosphopeptide containing this motif labeled at the N-terminus by 5-carboxyfluorescein (denoted as FAM-pepS511; Figure 2D and Table 1). As expected, no profound stabilization was observed, and the presence of FC-A even substantially destabilized this complex (the K_D value increased from 4 ± 0.4 μM to 15.6. ± 0.9 μM in the presence of 500 μM FC-A). This destabilization is likely caused by the competition between FC-A and the $pSer^{511}$ 14−3−3 binding motif for the same binding site because the previously reported structure of the binary 14−3−3γ:pepS511 complex revealed interactions typical of the mode I motif with a fusicoccin binding pocket fully occupied by the C-terminal portion of the motif.[34]

Structural Basis of Different Stabilization Potencies of Fusicoccanes. In order to understand differences in the ability of fusicoccanes to stabilize interactions between 14−3−3γ and the $pSer^{100}$ motif of CaMKK2, that is, differences in the stabilization potency of fusicoccanes, we solved the crystal structures of ternary complexes between 14−3−3γ, the peptide containing the $pSer^{100}$ motif (pepS100), and FC-A/16-*O*-Me-FC-H. The ternary complexes were prepared by soaking the crystals of the binary 14−3−3γ:pepS100 complex with selected compounds. The soaking reduced, to some extent, the crystal quality, and the soaked crystals diffracted at a maximum resolution of ∼3 Å (Table 2). As expected, both compounds occupy the same part of the 14−3−3 ligand binding groove formed by 14−3−3γ helices H3, H5, H7, and H9 close to the C-terminus of the pepS100 (Figure 3) and interact with 14−3−3γ mainly through hydrophobic interactions. In the 14−3−3γ:pepS100:FC-A complex (Figure 3A−C), the sugar moiety and the hydroxyl group at the B ring of FC-A establish polar contacts with the side chains of the 14−3−3γ residues Asn^{43} and Asp^{218} of the α-helices H3 and H9, respectively. The methoxy group at ring A of FC-A is inserted between 14−3−3γ helices H3 and H5. Its oxygen atom is hydrogen-bonded to the side-chain of 14−3−3γ Lys^{125}, and the terminal *O*-methyl group establishes van der Waals contacts with side chains of 14−3−3γ residues Ser^{46}, Phe^{122}, and Met^{126}. Although there are no polar contacts between FC-A and the pepS100, the hydroxyl group at ring C (marked by a black arrow in Figure 3C) is in van der Waals distance to the side chain of the CaMKK2 residue Glu^{103}. This steric hindrance with the C-terminus of the $pSer^{100}$ motif of CaMKK2 is likely responsible for the shift in the whole pS100pep by ∼1.3 Å within the 14−3−3 binding groove in relation to the position of the peptide in the binary 14−3−3:pepS100 complex structure[34] (Figure 4) and for the negligible potency of FC-A in stabilizing pepS100 binding to 14−3−3γ.

The binding position of 16-*O*-Me-FC-H is similar to that of FC-A, including the hydrogen bonds with the same 14−3−3γ residues (Figure 3D−F). However, 16-*O*-Me-FC-H lacks the hydroxyl group at ring C, which affects the pepS100 conformation differently, and the central part of its molecule, consisting of rings A−C, adopts a more closed conformation. In the presence of 16-*O*-Me-FC-H, the pepS100 is less shifted than in the complex with FC-A (by ∼0.6 Å), and its C-terminal

Table 2. Crystallographic Data Collection and Refinement Statistics

complex	14−3−3γ:pepS100:FC-A (6Y4K)	14−3−3γ:pepS100:16-*O*-Me-FC-H (6Y6B)
wavelength (Å)	0.9184	0.9184
space group	P6(3)22	P6(3)22
unit-cell parameters		
a, *b*, *c* (Å)	225.85, 225.85, 72.96	226.27, 226.27, 72.99
α, β, γ (deg)	90.0, 90.0, 120.0	90.0, 90.0, 120.0
asymmetric unit contents	one dimer of 14−3−3γ with bound phosphopeptides and one molecule of FC-A	one dimer of 14−3−3γ with bound phosphopeptides and one molecule of 16-*O*-Me-FC-H
resolution range (Å)[a]	48.62−3.00 (3.18−3.00)	48.99−3.08 (3.26−3.08)
unique reflections	22485 (3562)	20904 (3285)
data multiplicity	21.83 (21.01)	21.72 (22.04)
completeness (%)	99.8 (99.8)	99.9 (99.7)
$\langle I/\sigma(I)\rangle$	18.91 (1.01)	11.53 (0.69)
R_{meas}[b]	16.5% (304.8%)	28.0% (497.0%)
R_{work}	0.2599 (0.3913)	0.2419 (0.4011)
R_{free}[c]	0.2920 (0.4308)	0.2815 (0.4272)
no. of protein atoms	3482	3634
no. of ligand atoms	48	35
no. of waters	0	0
average B factors (Å^2)		
protein	105.53	113.84
ligand	121.97	119.89
RMS[d] deviations from ideal values		
bond lengths (Å)	0.003	0.001
bond angles (deg)	0.59	0.36
Ramachandran favored (%)	96.11	99.13
Ramachandran allowed (%)	3.89	0.87
Ramachandran outliers (%)	0	0

[a]Values in parentheses are for the highest resolution shell. [b] $R_{meas} = \sum_{hkl}\{N(hkl)/[N(hkl)-1]\}^{1/2} \times \sum_i |I_i(hkl) - \langle I(hkl)\rangle| / \sum_{hkl}\sum_i I_i(hkl)$ where $I(hkl)$ is the intensity of reflection hkl, $\langle I(hkl)\rangle = \frac{1}{N(hkl)}\sum_i I_i(hkl)$, and $N(hkl)$ is the multiplicity. [c]The free *R* value (R_{free}) was calculated using 5% of the reflections, which were omitted from the refinement. [d]RMS, root-mean-square

https://dx.doi.org/10.1021/acschembio.0c00821
ACS Chem. Biol. XXXX, XXX, XXX−XXX

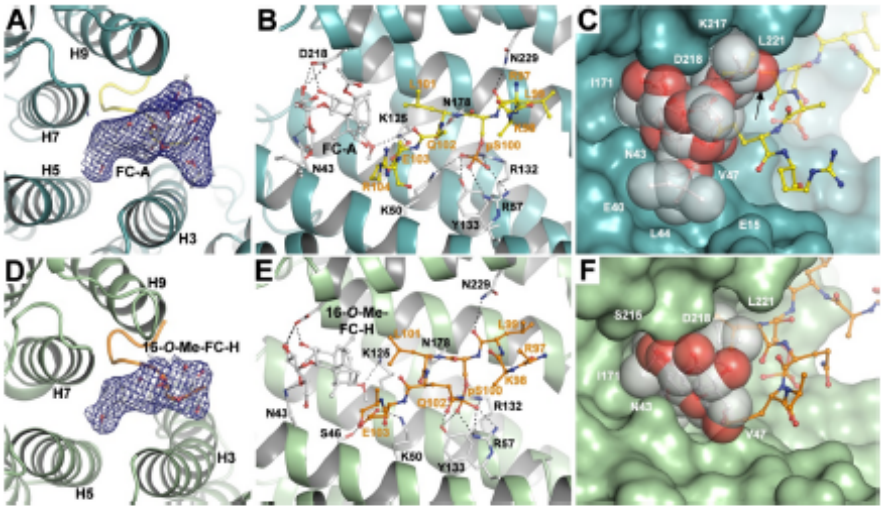

Figure 3. Structural analysis of ternary complexes between 14−3−3γ, the pepS100 peptide, and FC-A/16-*O*-Me-FC-H. (A) FC-A (shown as sticks) bound within the binding groove of 14−3−3γ. The 14−3−3γ and the pepS100 peptide are shown in dark cyan and yellow, respectively. The final $2F_O-F_C$ electron density map is contoured at 0.7σ. (B) Detailed view of contacts between 14−3−3ζ, the pepS100 peptide, and FC-A. The CaMKK2 residues are labeled in orange, and the 14−3−3ζ residues are labeled in black. Polar contacts are indicated by black dotted lines. (C) Detailed view of the FC-A binding site on the interface of the 14−3−3 ligand binding groove (dark cyan surface) and the pepS100 peptide (yellow sticks). FC-A is shown as spheres. Polar contacts are indicated by black dotted lines. The hydroxyl group at the ring C of FC-A, which establishes a steric contact with the side chain of CaMKK2 residue Glu^{103}, is indicated by a black arrow. (D) 16-*O*-Me-FC-H (shown as sticks) bound within the binding groove of 14−3−3γ. The 14−3−3γ and the pepS100 peptide are shown in green and orange, respectively. The final $2F_O-F_C$ electron density map is contoured at 0.7σ. (E) Detailed view of contacts between 14−3−3ζ, the pepS100 peptide, and 16-*O*-Me-FC-H. The CaMKK2 residues are labeled in orange, and the 14−3−3ζ residues are labeled in black. Polar contacts are indicated by black dotted lines. (F) Detailed view of the 16-*O*-Me-FC-H binding site on the interface of the 14−3−3 ligand binding groove (green surface) and the pepS100 peptide (orange sticks). 16-*O*-Me-FC-H is shown as spheres. Polar contacts are indicated by black dotted lines.

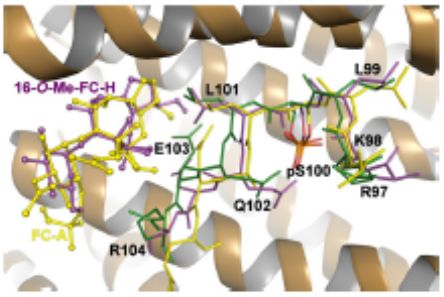

Figure 4. Comparison of the 14−3−3γ:pep100, 14−3−3γ:pepS100:FC-A, and 14−3−3γ:pepS100:16-*O*-Me-FC-H complexes. The pep100 from the binary complex (PDB ID 6EWW[34]) is shown as green sticks. The pep100 and FC-A from the ternary complex are shown as yellow sticks, and the pep100 and 16-*O*-Me-FC-H from the ternary complex are shown as violet sticks.

part is closer to the α-helix H3 of 14−3−3γ, thus enabling the formation of additional polar contacts between the side chain of the pepS100 residue Glu^{103} and side chains of the 14−3−3γ residues Ser^{46} and Lys^{50}. This is likely the reason for the considerably higher potency of 16-*O*-Me-FC-H in stabilizing interactions between pepS100 and 14−3−3γ. FC-H has a lower stabilization potency than 16-*O*-Me-FC-H most likely because the former lacks the terminal *O*-methyl group (Figure 2A), which, as mentioned above, helps to anchor the molecule in the binding pocket through various van der Waals contacts (Figure 3C,F).

Taken together, the comparison between the 14−3−3γ:pepS100:FC-A and 14−3−3γ:pepS100:16-*O*-Me-FC-H structures suggests that the steric contacts between the C-terminal part of the CaMKK2 pSer^{100} 14−3−3 binding motif (residue Glu^{103}) and the hydroxyl group (or the additional five-membered tetrahydrofuran ring) at ring C explain why FC-A, FC-J, and FC-THF show weaker stabilization potencies than FC-H and 16-*O*-Me-FC-H.

Stabilization of the Interaction between Full-Length Phosphorylated CaMKK2 and 14−3−3γ by Fusicoccanes. Subsequently, the ability of fusicoccanes to stabilize the complex between 14−3−3γ and full-length phosphorylated human CaMKK2 was investigated. To this end, the previously reported CaMKK2 T^{145}A/S^{495}A/D^{330}A construct encompassing residues 93−517 and containing both 14−3−3 binding motifs (Ser^{100} and Ser^{511}), the kinase domain, and the Ca^{2+}/CaM binding segment was prepared.[34] Recombinantly expressed CaMKK2$_{93-517}$T^{145}A/D^{330}A/S^{495}A (hereafter referred to as CaMKK2) was phosphorylated in vitro by PKA, and the extent of the phosphorylation reaction was determined by HPLC-MS analysis, which confirmed the stoichiometric phosphorylation of both Ser^{100} and Ser^{511} (Figure S1).

The stability of the complex between the doubly phosphorylated dpCaMKK2 and 14−3−3γ in the absence and presence of selected fusicoccanes was investigated by sedimentation velocity analytical ultracentrifugation (SV-AUC), analyzing mixtures containing a constant concentration

https://dx.doi.org/10.1021/acschembio.0c00821
ACS Chem. Biol. XXXX, XXX, XXX−XXX

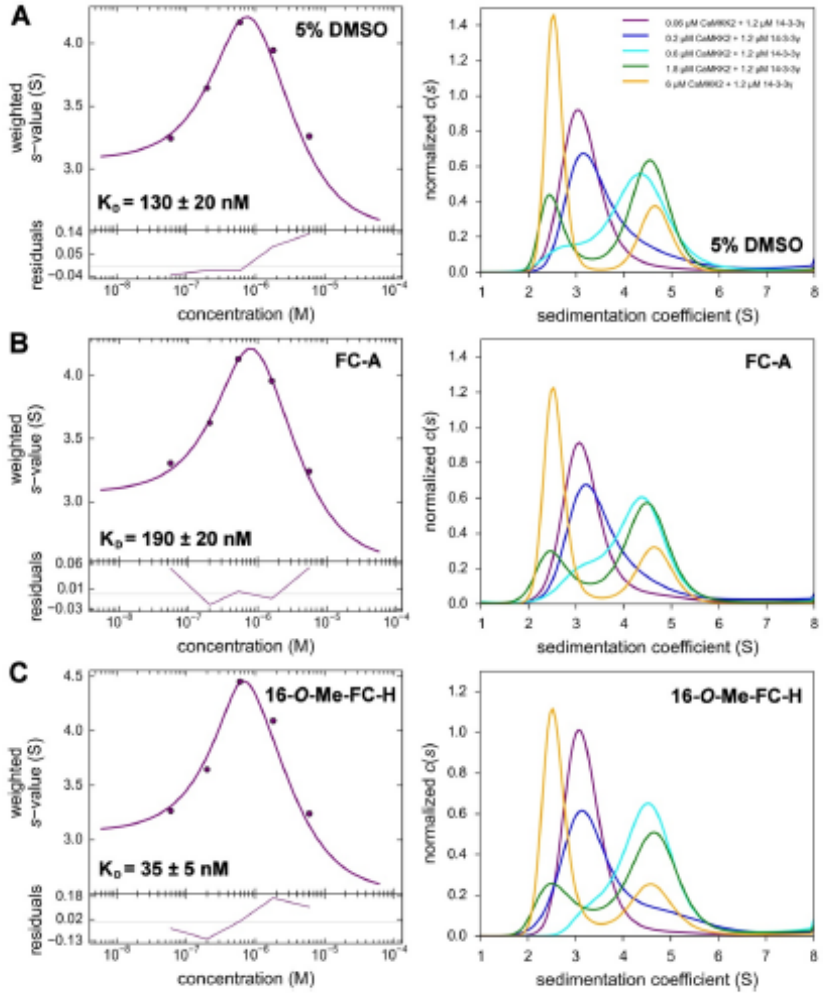

Figure 5. Sedimentation velocity analytical ultracentrifugation analysis of the dpCaMKK2:14−3−3γ complex in the presence of selected fusicoccanes. (A) 14−3−3γ and dpCaMKK2 in the presence of 5% DMSO. (B) 14−3−3γ and dpCaMKK2 in the presence of 500 μM FC-A. (C) 14−3−3γ and dpCaMKK2 in the presence of 500 μM 16-*O*-Me-FC-H. Isotherms of weight-averaged sedimentation coefficients s_w were derived from SV-AUC analysis of mixtures of 1.2 μM 14−3−3γ with 0.06−6 μM dpCaMKK2. The sedimentation coefficient distributions $c(s)$ underlying the s_w data points are shown on the right.

of 14−3−3γ (1.2 μM) and various concentrations of dpCaMKK2 (0.06−6 μM). Both direct modeling of SV-AUC data using the Lamm equation and analysis of the isotherm of weight-averaged sedimentation coefficient s values (s_w isotherm) as a function of dpCaMKK2 concentration in the absence of fusicoccanes revealed an apparent K_D of 130 ± 20 nM when using a binding model assuming a reversible interaction between the 14−3−3γ dimer and one molecule of dpCaMKK2 (left panel in Figure 5A). Normalized continuous sedimentation coefficient distributions $c(s)$ of dpCaMKK2:14−3−3γ mixtures at various molar ratios underlying the s_w data points are shown in the right panel of Figure 5A. Then, similar SV-AUC titrations were performed in the presence of 500 μM FC-A and 16-*O*-Me-FC-H. The resulting s_w isotherms and $c(s)$ distributions are shown in Figure 5B,C. Direct modeling of SV-AUC data and s_w isotherms revealed that 16-*O*-Me-FC-H increased the binding affinity by a factor of ~4 to a K_D value of 35 ± 5 nM (Figure 5C), whereas the presence of FC-A decreased the stability of the dpCaMKK2:14−3−3γ complex to a K_D of 190 ± 20 nM (Figure 5B).

We and others have shown that 14−3−3 binding to phosphorylated CaMKK2 does not directly alter its kinase activity but slows down its dephosphorylation.[34,35] Therefore, stabilization of the dpCaMKK2:14−3−3γ complex by 16-*O*-Me-FC-H was also assessed by comparing the time-dependent dephosphorylation of complexed PKA-phosphorylated CaMKK2 by type 1 protein phosphatase (PP1) in the absence and presence of the compound (Figure 6). Dephosphorylation of CaMKK2 was assessed by downward shift analysis on a

https://dx.doi.org/10.1021/acschembio.0c00821
ACS Chem. Biol. XXXX, XXX, XXX−XXX

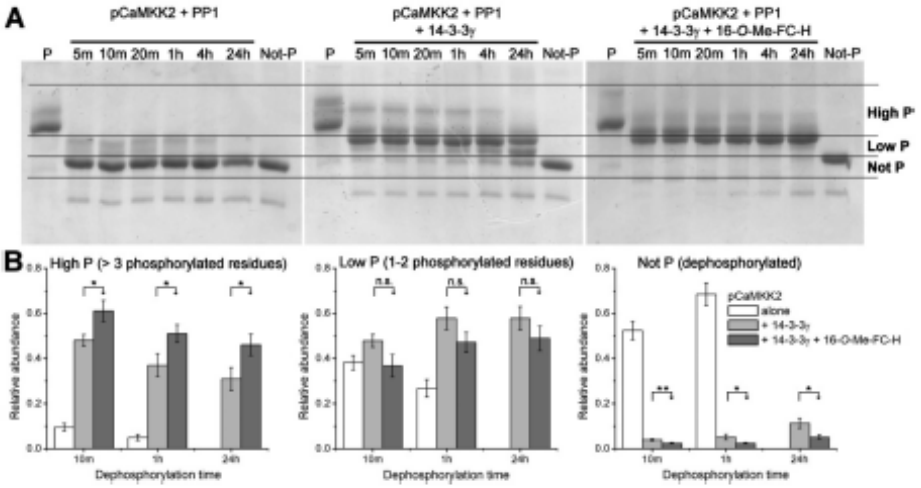

Figure 6. 16-*O*-Me-FC-H slows down the dephosphorylation of PKA-phosphorylated pCaMKK2 in complex with 14−3−3γ. (A) Representative phos-tag SDS-PAGE gels showing the time-dependent dephosphorylation of pCaMKK2 by type 1 protein phosphatase (PP1) in the absence of 14−3−3γ, in the presence of 14−3−3γ, and in the presence of 14−3−3γ and 500 μM 16-*O*-Me-FC-H. The kinase-dead mutant $D^{330}A$ of CaMKK2, with all four sites phosphorylated by PKA, was used to avoid autophosphorylation. Horizontal lines denote CaMKK2 phospho-variants which were quantified (High P, CaMKK2 containing more than three phosphoresidues; Low P, CaMKK2 containing one or two phosphoresidues; Not P, dephosphorylated CaMKK2). The first and the last lanes of each gel contain phosphorylated and not phosphorylated CaMKK2, respectively, as controls. (B) Relative abundances of CaMKK2 phospho-variants after 10-m-, 1-h-, and 24-h-long dephosphorylation of pCaMKK2 by PP1 based on phos-tag SDS-PAGE gels. Results are expressed as mean ± SEM, $n = 3$; $^*p < 0.1$; $^{**}p < 0.05$; n.s., not significant.

phos-tag SDS-PAGE gel.[34] As noted, phosphorylated CaMKK2 is dephosphorylated considerably more slowly when bound to 14−3−3γ than the free enzyme, and dephosphorylation is even slower in the presence of 16-*O*-Me-FC-H, as indicated by the higher abundance of CaMKK2 containing more than three phosphoresidues (Figure 6B, left panel) and by the lower abundance of dephosphorylated CaMKK2 (Figure 6B, right panel).

Moreover, to verify that the enhanced stability of the CaMKK2:14−3−3γ complex does not alter the enzymatic activity of phosphorylated CaMKK2, we also performed kinase activity measurements (Figure S2). These experiments confirmed that the kinase activity of CaMKK2 WT (residues 93−517) is substantially inhibited by the PKA-mediated phosphorylation and that the 14−3−3γ binding does not further affect the already suppressed activity of phosphorylated CaMKK2 WT. In addition, the presence of 16-*O*-Me-FC-H had no significant effect on the enzymatic activity of complexed CaMKK2 WT.

Thus, these data corroborated the results from FP measurements with FAM-labeled phosphopeptides and showed that 16-*O*-Me-FC-H stabilizes the interaction between the phosphorylated full-length CaMKK2 and 14−3−3γ, whereas FC-A decreases the stability of the this complex.

■ DISCUSSION

Protein−protein interactions (PPIs) are difficult to target by small molecule compounds, usually due to their featureless character and absence of well-defined binding pockets.[28,45,46] Nevertheless, various potent small-molecule inhibitors of PPIs have been recently reported, for example, compounds targeting Bcl-x_L:Bak interactions from Abott Laboratories or p53:mDM2 interactions from Johnson & Johnson Pharmaceuticals and Hoffmann-La Roche. Various well-known natural products, such as forskolin and rapamycin, are potent stabilizers of PPIs.[47,48] Another example of a PPI stabilizer is tafamidis, a compound blocking transthyretin misfolding and aggregation by stabilizing its quaternary structure, which has been recently approved for the treatment of neurodegenerative diseases such as transthyretin amyloidosis.[49] 14−3−3 proteins bind to and regulate hundreds of other proteins, including those participating in various disease-relevant signaling pathways, such as protein kinases B-Raf, C-Raf, ASK1, CaMKKs, and LRRK2; transcription factors FOXOs, YAP, and c-Jun; proteins involved in neurodegenerative diseases α-synuclein, δ-catenin, and tau; and apoptosis regulators BAD and Bax. For these reasons, 14−3−3 PPIs are a very attractive target for modulation by small-molecule compounds.[28,50]

Previous studies have shown that CaMKKs have two 14−3−3 binding motifs located at the N- and C-termini bordering the kinase domain.[33,34,36] However, the exact role of 14−3−3 binding in the regulation of CaMKKs is still not fully understood. 14−3−3 binding to CaMKK1 directly inhibits CaMKK activity and blocks dephosphorylation of an inhibitory phosphorylation site Thr^{108}.[33,36] More recent studies focused on CaMKK2 have shown that, similarly to CaMKK1, 14−3−3 binding slows down dephosphorylation of inhibitory PKA phosphorylation sites, albeit without inhibiting the kinase activity.[34,35] Nevertheless, in both cases, 14−3−3 binding maintains CaMKKs in the PKA-mediated inhibited state.

CaMKK-mediated Ca^{2+} signaling plays a key role in metabolic processes, inflammation, and cancer cell growth. Accordingly, CaMKKs are considered promising therapeutic targets for various diseases.[51−56] Yet, despite considerable efforts, no selective CaMKK inhibitor has been developed so far. Therefore, the stabilization of PPIs between CaMKK and 14−3−3 by small molecule compounds may be a plausible

https://dx.doi.org/10.1021/acschembio.0c00821
ACS Chem. Biol. XXXX, XXX, XXX−XXX

alternative and/or complementary strategy for inhibiting CaMKK activity.

The C-terminal 14−3−3 binding motif of CaMKK2 (RSLpS^{511}AP) closely conforms to a canonical "mode I" 14−3−3 binding site (RXX(pS/pT)XP, wherein pS/pT is phosphoserine or phosphothreonine and X is any residue[25,57]), but the N-terminal motif (RKLpS^{100}LQE) has a Gln and not a Pro residue at the position +2 relative to the phosphorylated residue and thus does not match any canonical 14−3−3 binding motif. The role of proline at the +2 position is to introduce a kink in the peptide chain, which consequently leaves the ligand binding groove of the 14−3−3 protein.[25] The recently reported crystal structure of the N-terminal CaMKK2 pSer^{100} 14−3−3-binding motif bound to 14−3−3ζ revealed that the interaction between the side-chain of the Gln residue at +2 and the pSer^{100} residue forces the direction of the peptide chain to change, thus mimicking the role of the Pro residue.[34] As a result, part of the 14−3−3 ligand binding groove, also known as the "fusicoccin-binding site," remains empty, thus resembling complexes with C-terminal mode III 14−3−3 binding motifs (X(pS/T)X$_{1-2}$COOH).

This cavity is targeted by the diterpene glycoside toxin fusicoccin A (FC-A) produced by the phytopathogenic fungus *Phomopsis amygdali*.[58] The molecular target of this compound is the complex between the plasma membrane H$^+$-ATPase and 14−3−3, whose stabilization by FC-A induces a quick acidification of the plant cell wall, opening of the gas-exchange pores (stomata) on the leaf surface, and consequent plant wilt.[38,59] This discovery prompted intensive research on the use of fusicoccanes as stabilizers of 14−3−3 PPIs showing that FC-A and other naturally occurring or synthetic fusicoccanes can stabilize various 14−3−3 complexes, mostly those whose binding partners have the C-terminal mode III 14−3−3 recognition motif, which leaves the fusicoccin-binding site unoccupied.[29−32]

Previous structural studies have revealed that FC-A and other fusicoccanes containing additional groups at ring C (e.g., FC-THF, FC-J, and cotylanin A) can only stabilize 14−3−3 complexes with mode III binding motifs due to steric hindrance between the C-terminal part of mode I and mode II motifs, usually Pro at the +2 position, and groups decorating the ring C.[32] In turn, a few 14−3−3 complexes with mode I and mode II binding motifs (e.g., the 14−3−3 binding motif of C-Raf kinase) are also stabilized by fusicoccanes without additional groups at ring C (e.g., cotylenol and ISIR-005).[31,44] In this study, we have shown that selected fusicoccanes can efficiently stabilize the complex between phosphorylated CaMKK2 and 14−3−3γ. As mentioned above, 14−3−3 proteins recognize two conserved phosphorylated motifs bordering the kinase domain of CaMKKs (Figure 1) with the N-terminal motif functioning as the primary 14−3−3 binding site.[33,34,36] We have previously demonstrated that CaMKK2 with only the N-terminal motif with pSer^{100} binds to 14−3−3γ with a K_D of 1 ± 0.5 μM.[34] The optimized protocol for CaMKK2 phosphorylation by PKA used in this study enabled us to prepare CaMKK2 stoichiometrically phosphorylated at both 14−3−3 binding motifs (Figure S1). SV-AUC analysis revealed that CaMKK2 containing both motifs interacts with 14−3−3γ with a considerably higher binding affinity (K_D = 130 ± 20 nM; Figures 5A), thus confirming that the C-terminal motif also contributes to the overall stability of the CaMKK2:14−3−3γ complex. In addition, our FP binding experiments with synthetic phosphopeptides representing both binding motifs revealed that fusicoccanes, especially 16-*O*-Me-FC-H, can stabilize only the binding of the N-terminal motif containing pSer^{100} (Figure 2B,C and Table 1), thus corroborating a previously published structural analysis of both motifs bound to 14−3−3γ.[34] The crystal structures of ternary complexes with FC-A and 16-*O*-Me-FC-H provided the structural basis for these stabilization potencies (Table 2 and Figure 3). Although FC-A binds to the 14−3−3:pepS100 complex similarly to 16-*O*-Me-FC-H, the steric conflict with the side chain of Glu^{103} from the C-terminal part of pepS100 shifts the whole peptide by 1.3 Å within the binding groove (Figure 4) and is likely responsible for the inability of FC-A to stabilize pepS100 binding to 14−3−3γ, in contrast to 16-*O*-Me-FC-H, which increased the apparent binding affinity of pepS100 toward 14−3−3γ by a factor of 51 (Table 1). Conversely, neither FC-A nor 16-*O*-Me-FC-H were able to enhance the binding of the second pSer^{511} motif to 14−3−3γ (Figure 2D). In fact, FC-A even destabilized this interaction, most likely due to the absence of the fusicoccin-binding cavity because this part of the 14−3−3 ligand binding groove is fully occupied by the C-terminal portion of the pSer^{511} motif.[34] Therefore, the destabilization observed in FC-A may be caused by the competition between FC-A and the pSer^{511} motif for the same binding site. As such, the CaMKK2:14−3−3 complex is yet another example which shows that identifying structural differences between 14 and 3−3 binding motifs within one binding partner may help us design and optimize small molecule PPI stabilizers specific for a selected contact site within the 14−3−3 complex toward achieving "intramolecular target specificity," as previously reported for the stabilization of 14−3−3 complexes with Gab2 and C-Raf.[31,44]

Last, the stabilization potencies of 16-*O*-Me-FC-H and FC-A were tested on the complex between full-length phosphorylated CaMKK2 and 14−3−3γ. SV-AUC measurements revealed an approximately 4-fold increase in the K_D value of the dpCaMKK2:14−3−3γ complex in the presence of 16-*O*-Me-FC-H (Figure 5C). Conversely, in the presence of FC-A, the stability of the dpCaMKK2:14−3−3γ complex decreased (from K_D of 130 ± 20 nM to 190 ± 20 nM), most likely due to the destabilization of the C-terminal motif binding, as indicated by FP measurements with the pepS511 peptide (Figure 2D). In addition, the presence of 16-*O*-Me-FC-H also enhanced the 14−3−3-mediated protection against CaMKK2 dephosphorylation by PP1 (Figure 6), thus confirming the results from our SV-AUC analysis.

In conclusion, our findings show that the interaction between phosphorylated CaMKK2 and 14−3−3γ can be stabilized by fusicoccanes, diterpene glycosides that share a 5−8−5 ring structure, by filling a gap in the interface of the 14−3−3 ligand binding groove with the N-terminal 14−3−3 binding motif of CaMKK2. The steric contacts between the groups decorating the ring C of fusicoccane molecules and the C-terminal part of the 14−3−3 binding motif determine the stabilization potency of these compounds. The increased stability of the CaMKK2:14−3−3γ complex enhances the ability of 14−3−3γ to slow down the dephosphorylation of CaMKK2, which remains in the PKA-mediated inhibited state. Thus, our data provide a mechanistic rationale for the future development of more potent and specific stabilizers of this key protein−protein interaction and ultimately may be used as an alternative and/or complementary strategy for inhibiting CaMKK activity.

https://dx.doi.org/10.1021/acschembio.0c00821
ACS Chem. Biol. XXXX, XXX, XXX−XXX

MATERIALS AND METHODS

Expression and Purification of 14−3−3 Proteins. Human 14−3−3γ (residues 1−235 lacking the C-terminal 12-residues-long flexible tail) was expressed and purified as previously described.[58] Purified 14−3−3γ in a buffer containing 20 mM Tris-HCl (pH 7.5), 150 mM NaCl, 1 mM TCEP, and 10% (w/v) glycerol was concentrated to a final concentration of 30 mg mL^{-1}, frozen in liquid nitrogen, and stored in aliquots at −80 °C (193.15 K).

Expression, Purification, and Phosphorylation of CaMKK2. Human CaMKK2 (residues 93−517) was expressed and purified as previously described.[34] Briefly, the CaMKK2 was expressed as N-terminal His_6-GB1-tagged fusion protein in *E. coli* BL21 (DE3) in autoinduction media for 5 h at 37 °C and then 16 h at 20 °C. This two-step purification procedure included affinity chromatography, His_6-tag cleavage by TEV protease, and size-exclusion chromatography (HiLoad Superdex 75; GE Healthcare) in buffer containing 50 mM Tris-HCl (pH 8), 500 mM NaCl, 5 mM DTT, and 10% (w/v) glycerol. Purified CaMKK2 $D^{330}A$ (contains four PKA sites) and CaMKK2 $T^{145}A/S^{495}A/D^{330}A$ (contains two PKA sites) were phosphorylated in the presence of 0.75 mM ATP and 20 mM $MgCl_2$ by incubation with 2000 and 2700 units of PKA (Promega), respectively, per milligram of protein. After phosphorylation, ATP and PKA were removed by size-exclusion chromatography. The results from the phosphorylation reaction were assessed by HPLC-MS.

Enzyme Activity Measurements. The kinase activity of CaMKK2 was measured as described previously.[61] Briefly, 200 nM CaMKK2 (WT, residues 93−517) was incubated in the presence or absence of 1 mM peptide containing the sequence surrounding the phosphorylation site of AMPK (G^{167}EFLRTSCGSP^{177}) at 30 °C for 60 min, in a reaction solution (25 μL) containing 50 mM HEPES (pH 7.5), 150 mM NaCl, 1 mM DTT, 10 mM $MgCl_2$, 5 μM calmodulin, 1 mM $CaCl_2$, 400 μM ATP, 10% glycerol, 2 μM 14−3−3γ (where needed), 5% DMSO (samples without fusicoccanes), and 0.5 mM FC-A or 16-*O*-Me-FC-H (where needed). ATP consumption was determined using a Kinase-Glo Max luminescent kinase assay kit (Promega, USA). Glow-type luminescence was recorded after 30 min on a luminescence reader (TECAN, Switzerland) using a flat white 96-well plate.

Fluorescence Polarization Binding Assay. Fluorescence polarization measurements were performed using a CLARIOstar microplate reader (BMG Labtech, Germany) on 384-well black low-volume flat-bottom plates (Corning, USA) with 100 nM FAM-pepS100 peptide, sequence FAM-GSLSARKL-pS^{100}-LQER (Pepscan Presto BV, The Netherlands), in buffer containing 10 mM HEPES (pH 7.4), 150 mM NaCl, 0.1% (v/v) Tween 20, and 0.1% (w/v) BSA. Excitation and emission wavelengths were 482 and 530 nm, respectively. In binding affinity (K_D) measurements, the 14−3−3 protein at a concentration of 160 μM, followed by binary dilution series, was incubated for 1 h with 100 nM FAM-pepS100 and 500 μM compound before the fluorescence polarization measurement. To determine the EC_{50} values, a solution containing 100 nM FAM-pepS100 and 20 μM 14−3−3 was titrated with the respective compound. The measured polarization values were normalized using 16-*O*-Me-FC-H as a positive control. To determine K_D and EC_{50} values, the resulting curves were fitted to one-site-binding and dose−response models, respectively, using OriginPro 2018b (OriginLab Corp. MA, USA).

Crystallization, Data Collection, and Structure Determination. The 14−3−3γ protein and the pepS100 peptide (sequence RKL-pSLQER) were mixed in a 1:2 molar stoichiometry in buffer containing 20 mM HEPES (pH 7), 2 mM $MgCl_2$, and 1 mM TCEP. Crystallization was performed using the hanging-drop vapor-diffusion method at 291 K, and the 14−3−3γ:pepS100 binary complex crystals were grown from drops consisting of 2 μL of 16 mg mL^{-1} protein and 4 μL of 100 mM HEPES (pH 7.5), 200 mM $MgCl_2$, 32% (w/v) PEG400, and 1% (v/v) hexafluoro-propanol. Crystals of ternary complexes were prepared by soaking with 0.5 mM FC-A or 16-*O*-Me-FC-H for 3 h at 291 K. Soaked crystals were flash frozen in liquid nitrogen. Data were collected in oscillation mode at beamline 14.2 of the BESSY synchrotron (Berlin, Germany). Diffraction data processing was performed using the packages XDS and XDSAPP.[62,63] Crystal structures of ternary complexes with FC-A and 16-*O*-Me-FC-H were solved by molecular replacement in MOLREP,[64] using the structure of 14−3−3γ (PDB ID: 2B05) as a search model, and refined at a resolution of 3.0 and 3.08 Å, respectively, using the PHENIX package.[65] All structural figures were prepared with PyMOL (https://pymol.org/2/).

Analytical Ultracentrifugation. Sedimentation velocity (SV) experiments were performed using a ProteomLabTM XL-I Beckman Coulter analytical ultracentrifuge, as previously described.[66] Samples were dialyzed against a buffer containing 50 mM Tris-HCl, at pH 7.5, 150 mM NaCl, and 1 mM TCEP before AUC measurements. SV experiments of the 14−3−3γ and pCaMKK2 were conducted at loading concentrations of 1.2 μM and 0.06−6 μM, respectively, in charcoal-filled Epon centerpieces with a 12 mm optical path length at 20 °C, and at a 42 000 rev/min rotor speed (An-50 Ti rotor, Beckman Coulter). Compounds were dissolved in DMSO, the final concentration of DMSO in all samples was 5% (v/v). The concentration of FC-A or 16-*O*-Me-FC-H was 500 μM. All sedimentation profiles were collected with absorbance optics at 280 nm. The calculated distributions were integrated to establish the weight-average sedimentation coefficients corrected to 20 °C and the density of water, $s_{w(20,w)}$. The s_w values were plotted as a function of CaMKK2 concentration to construct s_w isotherms. The resulting isotherms were fitted with an A + B ⇌ AB model, as implemented in the SEDPHAT software package with previously known s_w values of each component. The parameters were verified, and the loading concentrations were corrected using global Lamm-equation modeling, also implemented in the SEDPHAT software.[67,68]

CaMKK2 Dephosphorylation Assay. Phosphorylated CaMKK (residues 93−517) $D^{330}A$ (kinase dead mutant) was dephosphorylated in the presence and absence of 14−3−3γ by protein phosphatase 1 (PP1, catalytic subunit α-isoform from rabbit) as previously described.[34] Briefly, dephosphorylation by PP1 (New England Biolabs, USA) with a specific activity of 80 000 units/mg) was performed at 30 °C in buffer containing 50 mM HEPES (pH 7.5), 100 mM NaCl, 2 mM DTT, 1 mM $MnCl_2$, and 0.01% NP-40. The reaction mixture contained 8 μM pCaMKK2 $D^{330}A$, 16 μM 14−3−3γ (where needed), 500 μM 16-*O*-Me-FC-H (where needed), and PP1 in an optimized molar ratio of 1:1150 (enzyme/substrate). Reactions were stopped after various incubation times (0−24 h) by adding 100 mM β-glycerolphosphate (Sigma-Aldrich, USA), mixing with SDS reducing sample buffer, and boiling for 5 min. Sample analysis was performed using 12% Phos-tag SDS-PAGE with 75 μM Phos-tag (FUJIFILM Wako Pure Chemical Corp., Japan). The gels were quatified using the Image Lab Software for PC, version 6.1 (Biorad, USA).

ASSOCIATED CONTENT

Supporting Information

The Supporting Information is available free of charge at https://pubs.acs.org/doi/10.1021/acschembio.0c00821.

Figures S1−S3 show data concerning the characterization of CaMKK2 phosphorylation at Ser^{100} and Ser^{511} by FT-ICR mass spectrometry, enzyme activity measurements of CaMKK2 in the presence of 14−3−3γ and selected fusicoccanes, and stabilization of interactions between 14 and 3−3ζ and the N-terminal 14−3−3-binding motif of CaMKK2 by fusicoccanes (PDF)

Accession Codes

The atomic coordinates and structure factors of the 14−3−3γ:pepS100:FC-A and 14−3−3γ:pepS100:16-*O*-Me-FC-H complexes were deposited in the Protein Data Bank under accession codes 6Y4K and 6Y6B, respectively.

https://dx.doi.org/10.1021/acschembio.0c00821
ACS Chem. Biol. XXXX, XXX, XXX−XXX

AUTHOR INFORMATION

Corresponding Authors

Christian Ottmann – *Department of Biomedical Engineering, Laboratory of Chemical Biology and Institute for Complex Molecular Systems, Eindhoven University of Technology, 5600 MB Eindhoven, The Netherlands;* orcid.org/0000-0001-7315-0315; Email: c.ottmann@tue.nl

Tomas Obsil – *Department of Physical and Macromolecular Chemistry, Faculty of Science, Charles University, Prague, Czech Republic; Department of Structural Biology of Signaling Proteins, Division BIOCEV, Institute of Physiology of the Czech Academy of Sciences, 252 50 Vestec, Czech Republic;* orcid.org/0000-0003-4602-1272; Email: obsil@natur.cuni.cz

Authors

Domenico Lentini Santo – *Department of Physical and Macromolecular Chemistry, Faculty of Science, Charles University, Prague, Czech Republic*

Olivia Petrvalska – *Department of Physical and Macromolecular Chemistry, Faculty of Science, Charles University, Prague, Czech Republic; Department of Structural Biology of Signaling Proteins, Division BIOCEV, Institute of Physiology of the Czech Academy of Sciences, 252 50 Vestec, Czech Republic*

Veronika Obsilova – *Department of Structural Biology of Signaling Proteins, Division BIOCEV, Institute of Physiology of the Czech Academy of Sciences, 252 50 Vestec, Czech Republic*

Complete contact information is available at: https://pubs.acs.org/10.1021/acschembio.0c00821

Author Contributions

T.O., C.O., and V.O. supervised the project and provided scientific guidance. D.L.S. performed protein expression/purification and FP measurements and crystallized both ternary complexes. O.P. performed protein expression/purification, analytical ultracentrifugation analysis, and dephosphorylation experiments. D.L.S., V.O., and T.O. solved and refined the crystal structures. T.O. and V.O. wrote the manuscript. All coauthors revised the manuscript.

Notes

The authors declare no competing financial interest.

ACKNOWLEDGMENTS

This study was supported by the Initial Training Network, funded by the H2020 Marie Curie Actions of the European Commission under Grant Agreement 675179, and by Czech Science Foundation Grant No. 19-00121S. We acknowledge CMS-Biocev ("Biophysical techniques, Crystallization, Diffraction, Structural mass spectrometry") supported by MEYS CR (LM2018127). We thank N. Kato and Y. Higuchi from the Institute of Scientific and Industrial Research, Osaka University, Japan for fusicoccin derivatives, D. Svec for his help with FP measurements, P. Pompach for his help with MS measurements, and C. V. Melo for proofreading the article.

REFERENCES

(1) Racioppi, L., and Means, A. R. (2012) Calcium/calmodulin-dependent protein kinase kinase 2: roles in signaling and pathophysiology. *J. Biol. Chem. 287*, 31658–31665.

(2) Tokumitsu, H., Ensden, H., and Soderling, T. R. (1995) Characterization of a Ca2+/calmodulin-dependent protein kinase cascade. Molecular cloning and expression of calcium/calmodulin-dependent protein kinase kinase. *J. Biol. Chem. 270*, 19320–19324.

(3) Soderling, T. R., and Stull, J. T. (2001) Structure and regulation of calcium/calmodulin-dependent protein kinases. *Chem. Rev. 101*, 2341–2352.

(4) Tokumitsu, H., Wayman, G. A., Muramatsu, M., and Soderling, T. R. (1997) Calcium/calmodulin-dependent protein kinase kinase: identification of regulatory domains. *Biochemistry 36*, 12823–12827.

(5) Soderling, T. R. (1999) The Ca-calmodulin-dependent protein kinase cascade. *Trends Biochem. Sci. 24*, 232–236.

(6) Colomer, J., and Means, A. R. (2007) Physiological roles of the Ca2+/CaM-dependent protein kinase cascade in health and disease. *Subcell Biochem 45*, 169–214.

(7) Illario, M., Giardino-Torchia, M. L., Sankar, U., Ribar, T. J., Galgani, M., Vitiello, L., Masci, A. M., Bertani, F. R., Ciaglia, E., Astone, D., Maulucci, G., Cavallo, A., Vitale, M., Cimini, V., Pastore, L., Means, A. R., Rossi, G., and Racioppi, L. (2008) Calmodulin-dependent kinase IV links Toll-like receptor 4 signaling with survival pathway of activated dendritic cells. *Blood 111*, 723–731.

(8) Schmitt, J. M., Smith, S., Hart, B., and Fletcher, L. (2011) CaM kinase control of AKT and LNCaP cell survival. *J. Cell. Biochem. 113*, 1514–1526.

(9) Yano, S., Tokumitsu, H., and Soderling, T. R. (1998) Calcium promotes cell survival through CaM-K kinase activation of the protein-kinase-B pathway. *Nature 396*, 584–587.

(10) Gocher, A. M., Azabdaftari, G., Euscher, L. M., Dai, S., Karacosta, L. G., Franke, T. F., and Edelman, A. M. (2017) Akt activation by Ca(2+)/calmodulin-dependent protein kinase kinase 2 (CaMKK2) in ovarian cancer cells. *J. Biol. Chem. 292*, 14188–14204.

(11) Hurley, R. L., Anderson, K. A., Franzone, J. M., Kemp, B. E., Means, A. R., and Witters, L. A. (2005) The Ca2+/calmodulin-dependent protein kinase kinases are AMP-activated protein kinase kinases. *J. Biol. Chem. 280*, 29060–29066.

(12) Anderson, K. A., Ribar, T. J., Lin, F., Noeldner, P. K., Green, M. F., Muehlbauer, M. J., Witters, L. A., Kemp, B. E., and Means, A. R. (2008) Hypothalamic CaMKK2 contributes to the regulation of energy balance. *Cell Metab. 7*, 377–388.

(13) Green, M. F., Anderson, K. A., and Means, A. R. (2011) Characterization of the CaMKKbeta-AMPK signaling complex. *Cell. Signalling 23*, 2005–2012.

(14) Racioppi, L., Nelson, E. R., Huang, W., Mukherjee, D., Lawrence, S. A., Lento, W., Masci, A. M., Jiao, Y., Park, S., York, B., Liu, Y., Baek, A. E., Drewry, D. H., Zuercher, W. J., Bertani, F. R., Businaro, L., Geradts, J., Hall, A., Means, A. R., Chao, N., Chang, C. Y., and McDonnell, D. P. (2019) CaMKK2 in myeloid cells is a key regulator of the immune-suppressive microenvironment in breast cancer. *Nat. Commun. 10*, 2450.

(15) Wayman, G. A., Tokumitsu, H., and Soderling, T. R. (1997) Inhibitory cross-talk by cAMP kinase on the calmodulin-dependent protein kinase cascade. *J. Biol. Chem. 272*, 16073–16076.

(16) Matsushita, M., and Nairn, A. C. (1999) Inhibition of the Ca2+/calmodulin-dependent protein kinase I cascade by cAMP-dependent protein kinase. *J. Biol. Chem. 274*, 10086–10093.

(17) Okuno, S., Kitani, T., and Fujisawa, H. (2001) Regulation of Ca(2+)/calmodulin-dependent protein kinase kinase alpha by cAMP-dependent protein kinase: I. Biochemical analysis. *J. Biochem. 130*, 503–513.

(18) Tokumitsu, H., Iwabu, M., Ishikawa, Y., and Kobayashi, R. (2001) Differential regulatory mechanism of Ca2+/calmodulin-dependent protein kinase kinase isoforms. *Biochemistry 40*, 13925–13932.

(19) Green, M. F., Scott, J. W., Steel, R., Oakhill, J. S., Kemp, B. E., and Means, A. R. (2011) Ca2+/Calmodulin-dependent protein kinase kinase beta is regulated by multisite phosphorylation. *J. Biol. Chem. 286*, 28066–28079.

(20) Pennington, K. L., Chan, T. Y., Torres, M. P., and Andersen, J. L. (2018) The dynamic and stress-adaptive signaling hub of 14–3-3: emerging mechanisms of regulation and context-dependent protein-protein interactions. *Oncogene 37*, 5587–5604.

(21) Gardino, A. K., and Yaffe, M. B. (2011) 14−3-3 proteins as signaling integration points for cell cycle control and apoptosis. *Semin. Cell Dev. Biol.* 22, 688−695.
(22) Sluchanko, N. N., and Gusev, N. B. (2017) Moonlighting chaperone-like activity of the universal regulatory 14−3-3 proteins. *FEBS J.* 284, 1279−1295.
(23) Sluchanko, N. N. (2020) Reading the phosphorylation code: binding of the 14−3-3 protein to multivalent client phosphoproteins. *Biochem. J.* 477, 1219−1225.
(24) Muslin, A. J., Tanner, J. W., Allen, P. M., and Shaw, A. S. (1996) Interaction of 14−3-3 with signaling proteins is mediated by the recognition of phosphoserine. *Cell* 84, 889−897.
(25) Yaffe, M. B., Rittinger, K., Volinia, S., Caron, P. R., Aitken, A., Leffers, H., Gamblin, S. J., Smerdon, S. J., and Cantley, L. C. (1997) The structural basis for 14−3-3:phosphopeptide binding specificity. *Cell* 91, 961−971.
(26) Obsil, T., and Obsilova, V. (2011) Structural basis of 14−3-3 protein functions. *Semin. Cell Dev. Biol.* 22, 663−672.
(27) Watanabe, N., and Osada, H. (2016) Small molecules that target phosphorylation dependent protein-protein interaction. *Bioorg. Med. Chem.* 24, 3246−3254.
(28) Stevers, L. M., Sijbesma, E., Botta, M., MacKintosh, C., Obsil, T., Landrieu, I., Cau, Y., Wilson, A. J., Karawajczyk, A., Eickhoff, J., Davis, J., Hann, M., O'Mahony, G., Doveston, R. G., Brunsveld, L., and Ottmann, C. (2018) Modulators of 14−3-3 Protein-Protein Interactions. *J. Med. Chem.* 61, 3755−3778.
(29) Camoni, L., Di Lucente, C., Visconti, S., and Aducci, P. (2011) The phytotoxin fusicoccin promotes platelet aggregation via 14−3-3-glycoprotein Ib-IX-V interaction. *Biochem. J.* 436, 429−436.
(30) De Vries-Van Leeuwen, I. J., da Costa Pereira, D., Flach, K. D., Piersma, S. R., Haase, C., Bier, D., Yalcin, Z., Michalides, R., Feenstra, K. A., Jimenez, C. R., de Greef, T. F., Brunsveld, L., Ottmann, C., Zwart, W., and de Boer, A. H. (2013) Interaction of 14−3-3 proteins with the estrogen receptor alpha F domain provides a drug target interface. *Proc. Natl. Acad. Sci. U. S. A.* 110, 8894−8899.
(31) Molzan, M., Kasper, S., Roglin, L., Skwarczynska, M., Sassa, T., Inoue, T., Breitenbuecher, F., Ohkanda, J., Kato, N., Schuler, M., and Ottmann, C. (2013) Stabilization of physical RAF/14−3-3 interaction by cotylenin A as treatment strategy for RAS mutant cancers. *ACS Chem. Biol.* 8, 1869−1875.
(32) Anders, C., Higuchi, Y., Koschinsky, K., Bartel, M., Schumacher, B., Thiel, P., Nitta, H., Preisig-Muller, R., Schlichthorl, G., Renigunta, V., Ohkanda, J., Daut, J., Kato, N., and Ottmann, C. (2013) A semisynthetic fusicoccane stabilizes a protein-protein interaction and enhances the expression of K+ channels at the cell surface. *Chem. Biol.* 20, 583−593.
(33) Davare, M. A., Saneyoshi, T., Guire, E. S., Nygaard, S. C., and Soderling, T. R. (2004) Inhibition of calcium/calmodulin-dependent protein kinase kinase by protein 14−3-3. *J. Biol. Chem.* 279, 52191−52199.
(34) Psenakova, K., Petrvalska, O., Kylarova, S., Lentini Santo, D., Kalabova, D., Herman, P., Obsilova, V., and Obsil, T. (2018) 14−3-3 protein directly interacts with the kinase domain of calcium/calmodulin-dependent protein kinase kinase (CaMKK2). *Biochim. Biophys. Acta, Gen. Subj.* 1862, 1612−1625.
(35) Langendorf, C. G., O'Brien, M. T., Ngoei, K. R. W., McAloon, L. M., Dhagat, U., Hoque, A., Ling, N. X. Y., Dite, T. A., Galic, S., Loh, K., Parker, M. W., Oakhill, J. S., Kemp, B. E., and Scott, J. W. (2020) CaMKK2 is inactivated by cAMP-PKA signaling and 14−3-3 adaptor proteins, *J. Biol. Chem.*, DOI: 10.1074/jbc.ra120.013756.
(36) Ichimura, T., Taoka, M., Hozumi, Y., Goto, K., and Tokumitsu, H. (2008) 14−3-3 Proteins directly regulate Ca(2+)/calmodulin-dependent protein kinase kinase alpha through phosphorylation-dependent multisite binding. *FEBS Lett.* 582, 661−665.
(37) de Boer, A. H., and de Vries-van Leeuwen, I. J. (2012) Fusicoccanes: diterpenes with surprising biological functions. *Trends Plant Sci.* 17, 360−368.
(38) Wurtele, M., Jelich-Ottmann, C., Wittinghofer, A., and Oecking, C. (2003) Structural view of a fungal toxin acting on a 14−3-3 regulatory complex. *EMBO J.* 22, 987−994.
(39) Molzan, M., Schumacher, B., Ottmann, C., Baljuls, A., Polzien, L., Weyand, M., Thiel, P., Rose, R., Rose, M., Kuhenne, P., Kaiser, M., Rapp, U. R., Kuhlmann, J., and Ottmann, C. (2010) Impaired Binding of 14−3-3 to C-RAF in Noonan Syndrome Suggests New Approaches in Diseases with Increased Ras Signaling. *Mol. Cell. Biol.* 30, 4698−4711.
(40) Ganguly, S., Weller, J. L., Ho, A., Chemineau, P., Malpaux, B., and Klein, D. C. (2005) Melatonin synthesis: 14−3-3-dependent activation and inhibition of arylalkylamine N-acetyltransferase mediated by phosphoserine-205. *Proc. Natl. Acad. Sci. U. S. A.* 102, 1222−1227.
(41) Coblitz, B., Shikano, S., Wu, M., Gabelli, S. B., Cockrell, L. M., Spieker, M., Hanyu, Y., Fu, H., Amzel, L. M., and Li, M. (2005) C-terminal recognition by 14−3-3 proteins for surface expression of membrane receptors. *J. Biol. Chem.* 280, 36263−36272.
(42) Johnson, C., Crowther, S., Stafford, M. J., Campbell, D. G., Toth, R., and MacKintosh, C. (2010) Bioinformatic and experimental survey of 14−3-3-binding sites. *Biochem. J.* 427, 69−78.
(43) Toyomasu, T., Tsukahara, M., Kaneko, A., Niida, R., Mitsuhashi, W., Dairi, T., Kato, N., and Sassa, T. (2007) Fusicoccins are biosynthesized by an unusual chimera diterpene synthase in fungi. *Proc. Natl. Acad. Sci. U. S. A.* 104, 3084−3088.
(44) Bier, D., Bartel, M., Sies, K., Halbach, S., Higuchi, Y., Haranosono, Y., Brummer, T., Kato, N., and Ottmann, C. (2016) Small-Molecule Stabilization of the 14−3-3/Gab2 Protein-Protein Interaction (PPI) Interface. *ChemMedChem* 11, 911−918.
(45) Arkin, M. R., Tang, Y., and Wells, J. A. (2014) Small-molecule inhibitors of protein-protein interactions: progressing toward the reality. *Chem. Biol.* 21, 1102−1114.
(46) Robertson, N. S., and Spring, D. R. (2018) Using Peptidomimetics and Constrained Peptides as Valuable Tools for Inhibiting Protein(−)Protein Interactions. *Molecules* 23, 959.
(47) Tesmer, J. J., Sunahara, R. K., Johnson, R. A., Gosselin, G., Gilman, A. G., and Sprang, S. R. (1999) Two-metal-Ion catalysis in adenylyl cyclase. *Science* 285, 756−760.
(48) Choi, J., Chen, J., Schreiber, S. L., and Clardy, J. (1996) Structure of the FKBP12-rapamycin complex interacting with the binding domain of human FRAP. *Science* 273, 239−242.
(49) Green, N. S., Palaninathan, S. K., Sacchettini, J. C., and Kelly, J. W. (2003) Synthesis and characterization of potent bivalent amyloidosis inhibitors that bind prior to transthyretin tetramerization. *J. Am. Chem. Soc.* 125, 13404−13414.
(50) Sijbesma, E., Hallenbeck, K. K., Leysen, S., de Vink, P. J., Skora, L., Jahnke, W., Brunsveld, L., Arkin, M. R., and Ottmann, C. (2019) Site-Directed Fragment-Based Screening for the Discovery of Protein-Protein Interaction Stabilizers. *J. Am. Chem. Soc.* 141, 3524−3531.
(51) Massie, C. E., Lynch, A., Ramos-Montoya, A., Boren, J., Stark, R., Fazli, L., Warren, A., Scott, H., Madhu, B., Sharma, N., Bon, H., Zecchini, V., Smith, D. M., Denicola, G. M., Mathews, N., Osborne, M., Hadfield, J., Macarthur, S., Adryan, B., Lyons, S. K., Brindle, K. M., Griffiths, J., Gleave, M. E., Rennie, P. S., Neal, D. E., and Mills, I. G. (2011) The androgen receptor fuels prostate cancer by regulating central metabolism and biosynthesis. *EMBO J.* 30, 2719−2733.
(52) Jin, L., Chun, J., Pan, C., Kumar, A., Zhang, G., Ha, Y., Li, D., Alesi, G. N., Kang, Y., Zhou, L., Yu, W. M., Magliocca, K. R., Khuri, F. R., Qu, C. K., Metallo, C., Owonikoko, T. K., and Kang, S. (2018) The PLAG1-GDH1 Axis Promotes Anoikis Resistance and Tumor Metastasis through CamKK2-AMPK Signaling in LKB1-Deficient Lung Cancer. *Mol. Cell* 69, 87−99 e87.
(53) York, B., Li, F., Lin, F., Marcelo, K. L., Mao, J., Dean, A., Gonzales, N., Gooden, D., Maity, S., Coarfa, C., Putluri, N., and Means, A. R. (2017) Pharmacological inhibition of CaMKK2 with the selective antagonist STO-609 regresses NAFLD. *Sci. Rep.* 7, 11793.
(54) Ohtsuka, S., Ozeki, Y., Fujiwara, M., Miyagawa, T., Kanayama, N., Magari, M., Hatano, N., Suizu, F., Ishikawa, T., and Tokumitsu, H. (2020) Development and Characterization of Novel Molecular

https://dx.doi.org/10.1021/acschembio.0c00821
ACS Chem. Biol. XXXX, XXX, XXX−XXX

Probes for Ca(2+)/Calmodulin-Dependent Protein Kinase Kinase, Derived from STO-609. *Biochemistry 59*, 1701−1710.
(55) Profeta, G. S., Dos Reis, C. V., Santiago, A. D. S., Godoi, P. H. C., Fala, A. M., Wells, C. I., Sartori, R., Salmazo, A. P. T., Ramos, P. Z., Massirer, K. B., Elkins, J. M., Drewry, D. H., Gileadi, O., and Counago, R. M. (2019) Binding and structural analyses of potent inhibitors of the human Ca(2+)/calmodulin dependent protein kinase kinase 2 (CAMKK2) identified from a collection of commercially-available kinase inhibitors. *Sci. Rep. 9*, 16452.
(56) O'Byrne, S. N., Scott, J. W., Pilotte, J. R., Santiago, A. D. S., Langendorf, C. G., Oakhill, J. S., Eduful, B. J., Counago, R. M., Wells, C. I., Zuercher, W. J., Willson, T. M., and Drewry, D. H. (2020) In Depth Analysis of Kinase Cross Screening Data to Identify CAMKK2 Inhibitory Scaffolds. *Molecules 25*, 325.
(57) Rittinger, K., Budman, J., Xu, J., Volinia, S., Cantley, L. C., Smerdon, S. J., Gamblin, S. J., and Yaffe, M. B. (1999) Structural analysis of 14−3-3 phosphopeptide complexes identifies a dual role for the nuclear export signal of 14−3-3 in ligand binding. *Mol. Cell 4*, 153−166.
(58) Squire, G. R., and Mansfield, T. A. (1972) Studies of the mechanism of action of fusicoccin, the fungal toxin that induces wilting, and its interaction with abscisic acid. *Planta 105*, 71−78.
(59) Oecking, C., Eckerskorn, C., and Weiler, E. W. (1994) The fusicoccin receptor of plants is a member of the 14−3-3 superfamily of eukaryotic regulatory proteins. *FEBS Lett. 352*, 163−166.
(60) Obsil, T., Ghirlando, R., Klein, D. C., Ganguly, S., and Dyda, F. (2001) Crystal structure of the 14−3-3zeta:serotonin N-acetyltransferase complex. a role for scaffolding in enzyme regulation. *Cell 105*, 257−267.
(61) Kukimoto-Niino, M., Yoshikawa, S., Takagi, T., Ohsawa, N., Tomabechi, Y., Terada, T., Shirouzu, M., Suzuki, A., Lee, S., Yamauchi, T., Okada-Iwabu, M., Iwabu, M., Kadowaki, T., Minokoshi, Y., and Yokoyama, S. (2011) Crystal structure of the Ca(2)(+)/calmodulin-dependent protein kinase kinase in complex with the inhibitor STO-609. *J. Biol. Chem. 286*, 22570−22579.
(62) Kabsch, W. (2010) Xds. *Acta Crystallogr., Sect. D: Biol. Crystallogr. 66*, 125−132.
(63) Sparta, K. M., Krug, M., Heinemann, U., Mueller, U., and Weiss, M. S. (2016) Xdsapp2.0. *J. Appl. Crystallogr. 49*, 1085−1092.
(64) Vagin, A., and Teplyakov, A. (1997) MOLREP: an automated program for molecular replacement. *J. Appl. Crystallogr. 30*, 1022−1025.
(65) Adams, P. D., Afonine, P. V., Bunkoczi, G., Chen, V. B., Davis, I. W., Echols, N., Headd, J. J., Hung, L. W., Kapral, G. J., Grosse-Kunstleve, R. W., McCoy, A. J., Moriarty, N. W., Oeffner, R., Read, R. J., Richardson, D. C., Richardson, J. S., Terwilliger, T. C., and Zwart, P. H. (2010) PHENIX: a comprehensive Python-based system for macromolecular structure solution. *Acta Crystallogr., Sect. D: Biol. Crystallogr. 66*, 213−221.
(66) Kosek, D., Kylarova, S., Psenakova, K., Rezabkova, L., Herman, P., Vecer, J., Obsilova, V., and Obsil, T. (2014) Biophysical and structural characterization of the thioredoxin-binding domain of protein kinase ASK1 and its interaction with reduced thioredoxin. *J. Biol. Chem. 289*, 24463−24474.
(67) Schuck, P. (2000) Size-distribution analysis of macromolecules by sedimentation velocity ultracentrifugation and lamm equation modeling. *Biophys. J. 78*, 1606−1619.
(68) Dam, J., Velikovsky, C. A., Mariuzza, R. A., Urbanke, C., and Schuck, P. (2005) Sedimentation velocity analysis of heterogeneous protein-protein interactions: Lamm equation modeling and sedimentation coefficient distributions c(s). *Biophys. J. 89*, 619−634.

https://dx.doi.org/10.1021/acschembio.0c00821
ACS Chem. Biol. XXXX, XXX, XXX−XXX

Supplemental data

Stabilization of protein–protein interactions between CaMKK2 and 14-3-3 by fusicoccins

Domenico Lentini Santo[1], Olivia Petrvalska[1,2], Veronika Obsilova[2], Christian Ottmann[3*], and Tomas Obsil[1,2*]

[1] Department of Physical and Macromolecular Chemistry, Faculty of Science, Charles University, Prague, Czech Republic

[2] Department of Structural Biology of Signaling Proteins, Division BIOCEV, Institute of Physiology of the Czech Academy of Sciences, 252 50 Vestec, Czech Republic

[3] Department of Biomedical Engineering, Laboratory of Chemical Biology and Institute for Complex Molecular Systems, Eindhoven University of Technology, P.O. Box 513, 5600 MB, Eindhoven, The Netherlands.

*Corresponding authors: obsil@natur.cuni.cz (T.O.), c.ottmann@tue.nl (C.O.)

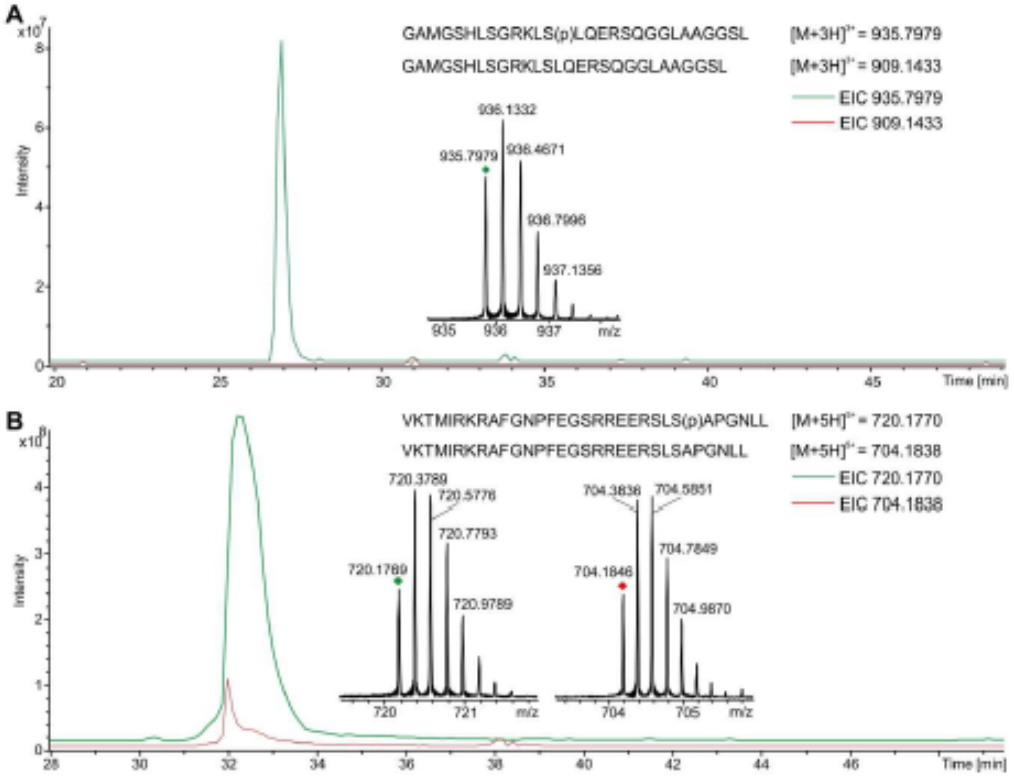

Figure S1. Detection of CaMKK2 Ser^{100} and Ser^{511} phosphorylated peptides by FT-ICR mass spectrometry

(A) Extract ion chromatogram (EIC) of phosphorylated GAMGSHLSGRKL**pS**^{100}LQERSQGGLAAGGSL peptide shown in green, as observed at m/z 935.7979 (3+). The red line represents the EIC of the non-phosphorylated form of the same peptide observed at m/z 909.1433 (3+). The inset shows the zoomed-in, high-resolution MS spectrum of the phosphorylated peptide. (B) Extract ion chromatograms of the phosphorylated VKTMIRKRAFGNPFEGSRREERSL**pS**^{511}APGNLL peptide are shown in green, as observed at m/z 720.177 (5+), and of the non-phosphorylated form, as observed at m/z 704.1838 (5+), are shown in red. The inset shows the zoomed-in, high-resolution MS spectra of phosphorylated and non-phosphorylated peptides. The phosphorylation sites in both peptides were determined based on the collision-induced dissociation spectra.

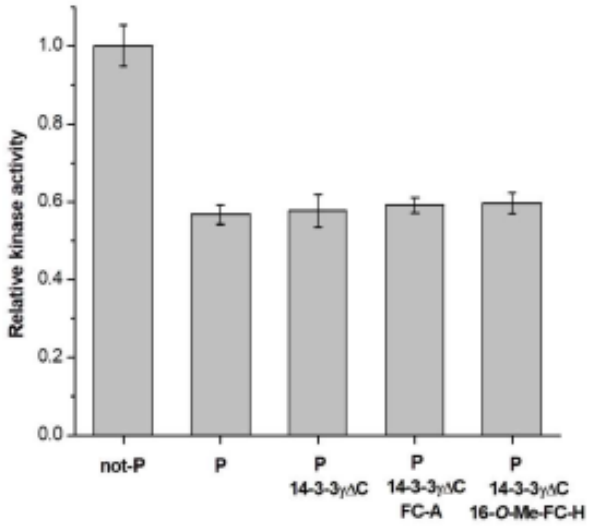

Figure S2. Enzyme activity of CaMKK2 in the presence of 14-3-3γ and selected fusicoccanes

The enzyme activity of CaMKK2 (WT, residues 93–517) was measured using the ADP-Glo™ (Promega, Madison, WI, USA) assay with a synthetic peptide containing the sequence around the phosphorylation site of AMPK (G^{167}EFLRTSCGSP^{177}) as a substrate. The activities were normalized to the non-phosphorylated enzyme activity in the absence of 14-3-3γΔC (the specific activity of not-P CaMKK2 WT was 82 ± 4 nmol.min^{-1}.mg^{-1}). Results are expressed as mean ± S.D., $n = 3$.

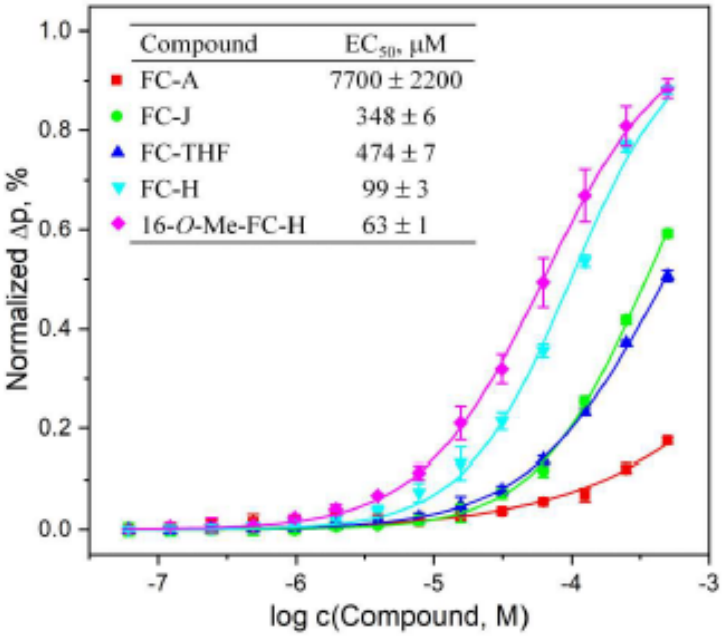

Figure S3. Stabilization of interactions between 14-3-3ζ and the N-terminal 14-3-3-binding motif of CaMKK2 by fusicoccanes

Fluorescence polarization (FP) measurements of the FAM-labeled pepS100 peptide (100 nM) and 14-3-3ζ (20 μM) titrated using the fusicoccanes tested in this study. All data points are the means ± SD of three experiments. To calculate EC_{50} values reflecting the stabilization potency of the study fusicoccanes, the FP data were fitted to a four-parameter dose-response model.